

Kazuhiko Matsumoto *Editor*

Frontiers of Graphene and Carbon Nanotubes

Devices and Applications

 Springer

Frontiers of Graphene and Carbon Nanotubes

Kazuhiko Matsumoto

Editor

Frontiers of Graphene and Carbon Nanotubes

Devices and Applications

 Springer

Editor
Kazuhiko Matsumoto
Osaka University
Osaka, Japan

ISBN 978-4-431-55371-7 ISBN 978-4-431-55372-4 (eBook)
DOI 10.1007/978-4-431-55372-4

Library of Congress Control Number: 2015934009

Springer Tokyo Heidelberg New York Dordrecht London
© Springer Japan 2015

This work is subject to copyright. All rights are reserved by the Publisher, whether the whole or part of the material is concerned, specifically the rights of translation, reprinting, reuse of illustrations, recitation, broadcasting, reproduction on microfilms or in any other physical way, and transmission or information storage and retrieval, electronic adaptation, computer software, or by similar or dissimilar methodology now known or hereafter developed.

The use of general descriptive names, registered names, trademarks, service marks, etc. in this publication does not imply, even in the absence of a specific statement, that such names are exempt from the relevant protective laws and regulations and therefore free for general use.

The publisher, the authors and the editors are safe to assume that the advice and information in this book are believed to be true and accurate at the date of publication. Neither the publisher nor the authors or the editors give a warranty, express or implied, with respect to the material contained herein or for any errors or omissions that may have been made.

Printed on acid-free paper

Springer Japan KK is part of Springer Science+Business Media (www.springer.com)

Preface

The door of a great new era of nano-carbon was opened by the discovery of fullerenes in 1985. Thereafter, new nano-carbon materials, such as carbon nanotubes and graphene were discovered one after the other in 1991 and 2004, respectively, and various kinds of basic and applied research have been developed since then. This book focuses on carbon nanotubes and graphene as representatives of nano-carbon materials, and describes the growth of new technology and applications of new devices. As new devices and as new materials, nano-carbon materials are expected to be world pioneers that could not have been realized with conventional semiconductor materials, and as those that extend the limits of conventional semiconductor performance. This book introduces the latest achievements of nano-carbon devices, processes, and technology growth. It is anticipated that these studies will also be pioneers in the development of future research of nano-carbon devices and materials.

Graphene has extremely high mobility and ultimate thinness of one atomic layer. Using these features of graphene, various types of fundamental research and development of diverse applications have been carried out.

Active research and development of high-frequency transistor applications utilizing the feature of high mobility of graphene is ongoing, and the cutoff frequency of $f_T \sim 500$ GHz has already been realized in the United States. The development of a terahertz oscillator source is another application of high-frequency devices of graphene. The application of graphene research to the transparent electrode as an alternative of indium tin oxide (ITO) by taking advantage of an ultrathin film has been carried out, and there is great potential that can be realized in the near future.

When graphene is applied as a switching transistor of a logic circuit, the problem arises that the transistor current cannot be cut off because of the ambipolar characteristics of graphene. Therefore, the optimal application of graphene FET rather than the application of logic has been sought. Biosensor application is one of the optimal applications of graphene FET which detects the change of current only during the sensing and does not require a cutoff. Furthermore, a higher sensitivity is expected because of the higher mobility of graphene than of other semiconductor materials.

Graphene has a wonderful property, but an optimal growth method for device applications, i.e., that it should be grown directly on the insulating substrate such as SiO_2 , has been difficult. A new growth method to solve this problem has been developed using thermal CVD, laser CVD, and plasma CVD, which are introduced in this book.

Because of the features of very fine structure and high mobility of carbon nanotubes, the formation of new nano devices—development of quantum nano devices, for instance, which could not be attained using conventional semiconductor materials—becomes possible.

For example, the applications and developments of room-temperature-operated single-electron memory, single-electron circuits, and terahertz detection are eagerly anticipated. To realize these devices, it is indispensable to control the growth direction of the carbon nanotube. By using a special substrate such as quartz or sapphire, or using a patterned substrate, it may be said that control of the direction of the growth of carbon nanotubes has been successfully developed.

Moreover, because a thin film of carbon nanotubes can be formed by an inkjet process, the application to flexible devices, transparent devices, and printable devices has been developed. For this to be possible, it is indispensable to separate the semiconductor nanotube and the metallic nanotube. The separation techniques after growth are almost established. For further development of nanotube application, however, the separation growth technique of semiconductors and metallic nanotubes is important.

The vertically grown carbon nanotube-like brush increased the surface area by two to three orders of magnitude or more. By taking advantage of this huge surface area as a working electrode of the electrochemical reaction, the reaction current also increases two to three orders of magnitude or more. This technology can be applied to the electrochemical biosensor in order to drastically enhance its sensitivity.

In addition, a new method for measuring the mass of one molecule, which cannot be attained by conventional methods, may become possible by using the mechanical resonance phenomenon of the carbon nanotube, which has the great advantage of being extremely light.

This book consists of 18 chapters. Chapters 1, 2, 3, 4, 5, 6, 7, and 8 describe new device applications and new growth methods of graphene, and Chaps. 9, 10, 11, 12, 13, 14, 15, 16, 17, and 18, those of carbon nanotubes.

Chapter 1 describes an epitaxial CVD growth method of high-quality, single-layer graphene on a catalyst copper thin film on the sapphire substrate in an atomic-order flat surface.

Chapter 2 explains a new growth method of graphene using a laser CVD, which can grow the graphene directly on the insulating substrate such as SiO_2 and will be applied to future device applications.

Chapter 3 describes a growth method of graphene using a thermal CVD, which can grow the graphene directly on the insulating substrate. It is expected that this method may spread the use of device applications of graphene dramatically.

Chapter 4 explains a growth method of graphene using a plasma CVD, in which carbon atoms pass through the Ni catalyst and grow graphene nanoribbons and graphene on an SiO₂ insulating substrate.

Chapter 5 describes in detail the problem of the interface between the metal and graphene, and the optimal formation method of the ohmic contact of graphene is discussed.

Chapter 6 explains the low-temperature growth method of graphene, and the development of a new fabrication process of graphene FET that does not require a transfer process.

Chapter 7 describes the first application of graphene FET to the biosensor. By modifying the graphene surface, selective protein detection became possible.

Chapter 8 explains recent advances and future trends in graphene terahertz (THz) devices. The ultrafast nonequilibrium carrier dynamics give rise to population inversion and resultant THz gain by stimulated interband photon emission. The science and technology for the creation of current-injection pumped graphene THz lasers are described.

Chapter 9 describes the growth mechanism of carbon nanotubes. It is demonstrated that the initiation of carbon nanotube growth is the formation of a small carbon cap on the fine protrusion of the metal, rather than the traditional growth mechanism where the carbon atom exhausted from catalyst metal forms the nanotube.

Chapter 10 explains the directional control growth of the carbon nanotube. It is demonstrated that carbon nanotubes grow along the ridge of rectangular groove of silicon oxide substrate by the concentrated Casimir force.

Chapter 11 describes the development of the plasma doping method that can dope a fullerene, DNA, and cesium, etc. inside the carbon nanotubes. This method can control the electrical properties of the nanotubes; and solar cells and single-electron transistors, etc. have been successfully created by this method.

Chapter 12 explains stochastic resonant devices that exploit the merits of multichannel carbon nanotube FET. It was demonstrated for the first time that even in solution the present stochastic resonant device can increase the signal–noise ratio by adding noise to a weak input signal.

Chapter 13 describes the application of a vertically aligned carbon nanotube forest for the electrode of the electrochemical reaction for biosensing, which improves the sensitivity by more than two orders of magnitude than the conventional electrode because of the huge surface area of the carbon nanotube forest.

Chapter 14 explains the application of force sensing and mass sensing using the a resonant-frequency shift of a carbon nanotube mechanical resonator, which is expected to provide high sensitivity because of its light weight, high aspect ratio, and extraordinary mechanical properties.

Chapter 15 describes the room-temperature-operated carbon nanotube single-charge quantum nanomemory with a 10 nm carbon nanotube channel wrapped with double insulating layers by accumulating the single charge in the interface states.

The threshold voltage shift and the width of the hysteresis is changed discretely following the number of accumulated charges, and the operation of a single-charge memory at room temperature has been confirmed.

Chapter 16 explains the electrons being conducted through a carbon nanotube channel FET at low temperature, conducted as the resonant tunneling indicating the wave nature and as single-electron tunneling indicating the particulate nature, depending on the magnitude of the tunnel resistance of the depletion layer compared to quantum resistance. Those electron natures can be controlled by the applied gate bias to the FET.

Chapter 17 describes quantum dots formed from a carbon nanotube which are applied to the basic scientific research as an artificial atom. They also are applied to the single-electron transistor, its circuit applications, and the terahertz detection.

Chapter 18 explains the development of flexible transparent circuits and printable devices using the nanotube network formed by the dispersing process.

It is expected that by increasing the advantages and overcoming the weak points of nanocarbon material, a new world that cannot be achieved with conventional materials will be greatly expanded. We strongly hope this book contributes to its development.

In closing, we would like to express our great appreciation for the large contribution of Dr. Yuko Sumino and Ms. Taeko Sato of Springer Japan for their help in editing this book. The work has been completed with the help of these two individuals.

Osaka, Japan

Kazuhiko Matsumoto

Contents

Part I Graphene

1	CVD Growth of High-Quality Single-Layer Graphene	3
	Hiroki Ago	
2	Graphene Laser Irradiation CVD Growth	21
	Yasuhide Ohno, Kenzo Maehashi, and Kazuhiko Matsumoto	
3	Graphene Direct Growth on Si/SiO₂ Substrates	29
	Yasuhide Ohno, Kenzo Maehashi, and Kazuhiko Matsumoto	
4	Direct Growth of Graphene and Graphene Nanoribbon on an Insulating Substrate by Rapid-Heating Plasma CVD	37
	Toshiaki Kato, Rikizo Hatakeyama, and Toshiro Kaneko	
5	Graphene/Metal Contact	53
	Kosuke Nagashio and Akira Toriumi	
6	Low-Temperature Synthesis of Graphene and Fabrication of Top-Gated Field-Effect Transistors Using Transfer-Free Processes for Future LSIs	79
	Daiyu Kondo and Shintaro Sato	
7	Graphene Biosensor	91
	Yasuhide Ohno, Kenzo Maehashi, and Kazuhiko Matsumoto	
8	Graphene Terahertz Devices	105
	Taiichi Otsuji	

Part II Carbon Nanotube (CNT)

9	Carbon Nanotube Synthesis and the Role of Catalyst	125
	Yoshikazu Homma	

10	Aligned Single-Walled Carbon Nanotube Growth on Patterned SiO₂/Si Substrates	131
	Yasuhide Ohno, Takafumi Kamimura, Kenzo Maehashi, Koichi Inoue, and Kazuhiko Matsumoto	
11	Plasma Doping Processes for CNT Devices	143
	Rikizo Hatakeyama, Toshiaki Kato, Yongfeng Li, and Toshiro Kaneko	
12	Stochastic Resonance Effect on Carbon Nanotube Field-Effect Transistors	165
	Yasuhide Ohno, Kenzo Maehashi, and Kazuhiko Matsumoto	
13	Electrochemical Biological Sensors Based on Directly Synthesized Carbon Nanotube Electrodes	179
	Kenzo Maehashi, Kazuhiko Matsumoto, Yuzuru Takamura, and Eiichi Tamiya	
14	Nanomechanical Application of CNT	187
	Seiji Akita	
15	Carbon Nanotube Quantum Nanomemory	201
	Takafumi Kamimura, Yasuhide Ohno, Kenzo Maehashi, and Kazuhiko Matsumoto	
16	Control of Particle Nature and Wave Nature of Electron in CNT	213
	Takafumi Kamimura and Kazuhiko Matsumoto	
17	Quantum-Dot Devices with Carbon Nanotubes	241
	Koji Ishibashi	
18	High-Mobility Thin-Film Transistors for Flexible Electronics Applications	269
	Yutaka Ohno	
	Index	285

About the Authors



Kazuhiko Matsumoto is a professor of Osaka University. He received the B.S. degree from Nagoya Institute of Technology, and M.S., and Ph.D. degrees from Tokyo Institute of Technology in 1976, 1978, 1981, respectively, all in Electronics Engineering. Since 1981, he has been working with Electrotechnical Laboratory, Tsukuba, Japan, where he has been engaged in the field of compound semiconductor devices. In 1988~1990, he was the research associate of the Stanford University in Prof. James S. Harris group. From 1992, he started the research to form nano structure using AFM nano-oxidation process and succeeded in

operating the single electron transistor at room temperature for the first time. From 1999, he is engaged in the research on carbon nanotube devices for the application of ultra-high sensitive bio sensor. From 2003, he is a professor at Osaka University, Osaka, Japan.

He was awarded the Pioneering Research Prize of the Science and Technology Agency of Japan government, the Paper Award of International Conference on Solid State Devices & Materials, the 30th Ichimura Prize, and the Pioneering Research Prize of the Agency of Industrial Science and Technology of Japan government for his work on the room temperature operated single electron transistor.

He is a Fellow of the Japan Society of Applied Physics, and the Research Leader of Center of Innovation (COI) Program of MEXT at Osaka University site.



Hiroki Ago is an associate professor of the Institute for Materials Chemistry and Engineering at Kyushu University, Japan. He received his Ph.D. from Kyoto University in 1997 for experimental and theoretical research on electronic structure of functional materials. After spending 1 year and a half at the Cavendish Laboratory at Cambridge University, he became a researcher of Nanocarbon Research Center of AIST at Tsukuba. In 2003, he moved to Kyushu University. His current research focuses on the controlled synthesis of graphene and related low-dimensional materials as well as experimental investigation of their physical and chemical properties. He received Iijima Award from the Fullerenes, Nanotubes and Graphene Research Society (2006), Young Scientist Award from the Minister of Education, Culture, Sports, Science and Technology (MEXT) (2008), and an Excellent Paper Award from Japanese Society of Applied Physics (2014). Currently, he is an Editorial Board of Scientific Reports (Nature Publishing Group). <http://ago.cm.kyushu-u.ac.jp/>



Kenzo Maehashi He is Professor at Institute of Engineering in Tokyo University of Agriculture and Technology. He received his Master's degree in Engineering from Osaka University. He started to work in the Institute of Scientific and Industrial Research in Osaka University. He received his Ph.D. from Osaka University. He was Associate Professor in the Institute of Scientific and Industrial Research in Osaka University. His research interests are in nanoscale electronic devices and biosensors.



Yasuhide Ohno received the M.S. degree in engineering in 2000, and the Ph.D. in engineering in 2002 from Osaka University, Japan. He is an assistant Professor of The Institute of Scientific and Industrial Research, Osaka University since 2003. He has done research on graphene and carbon nanotube field-effect transistors and their practical device applications.



Takafumi Kamimura is a senior researcher at The National Institute of Information and Communications Technology (NICT). He received his B. S., M. S., and Ph.D. degrees from the Shizuoka University, University of Tsukuba, and Osaka University, respectively, in 2002, 2004, and 2006. After serving as a research fellow of the Japan Society of the Promotion of Science (JSPS) and of the Japan Science and Technology Agency (JST) at the National Institute of Advanced Industrial Science and Technology (AIST) and the Osaka University, Kamimura joined NICT in 2013.



Koichi Inoue is an associate professor in Institute of Scientific and Industrial Research (ISIR), Osaka University, Japan. He received the Ph.D. degree in solid state physics with use of synchrotron radiation from the University of Tokyo, in 1983. He became a research associate at the Department of Physics, Osaka University in 1983 and worked on the optical properties of semiconductors. Since 1990, he has been working on the physics of quantum structures at the Department of Semiconductor Electronics in ISIR.



Rikizo Hatakeyama is presently a professor emeritus at Tohoku University and a research fellow in the Department of Electronic Engineering after retiring from the university as a professor in 2012. He is also a visiting professor at Kyushu University, and lecturers at Yamagata University and Tohoku Gakuin University. He received his B.Eng., M.Eng., and Dr. Eng. Degrees from Tohoku University, Japan, in 1971, 1973, and 1976, respectively. His aim is to create and establish an interdisciplinary field of plasma and nano fusion science & technology. He received a commendation for Science and Technology from the Minister of Education, Culture, Sports, Science and Technology, Japan. He is also a fellow of the Japan Society of Applied Physics.



Toshiro Kaneko is a professor at Department of Electronic Engineering in Tohoku University. He received his B. Eng., M. Eng., and Dr. Eng. Degrees from Tohoku University, Japan, in 1992, 1994, and 1997, respectively. His works are based on giving importance to fundamental plasma physics and realizing novel plasma application to create conjugate materials of nanocarbons, biomolecules, and nanoparticles. He received many honorable awards including Young Scientists' Prize in 2008 [The Commendation for Science and Technology by MEXT] and Chen Ning Yang Award in 2013 [Association of Asia Pacific Physical Societies].



Toshiaki Kato is a Lecturer at the Department of Electronic Engineering at Tohoku University. He received his B.S., M.S., and Dr. Eng. Degrees from the Tohoku University, Japan, in 2003, 2004, and 2007, respectively. Kato obtained a faculty position at Tohoku University in 2007 as an assistant professor and promoted to the current position in 2013.



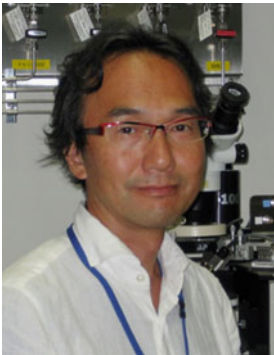
Yongfeng Li is a professor at the School of chemical engineering in China University of Petroleum. He received his B.S. from Jilin Institute of Chemical Technology in 1999, and received his Dr. Eng. Degree from Dalian University of Technology in 2004. After his Ph.D., he started to work in Japan since 2004. In the beginning, he worked as a postdoctoral in the twenty-first century COE program in the department of electronic engineering of Tohoku University from 2004. During 2006–2008 he started to work as a JSPS research fellow. After that, he was employed as an assistant professor in this department and continued to work until 2012. Now he starts to work as a full professor in China University of Petroleum in Beijing. He received many honorable awards due to his research achievements including the Top 100 Excellent Ph.D. Thesis of China in 2007, New Century Excellent Talents in University in 2009 and Recruitment Program of Young Global Experts in 2011.



Akira Toriumi received the B.S. degree in physics, the M.S. and Ph.D. degrees in applied physics from The University of Tokyo. He joined Research and Development Center of Toshiba Corporation in 1983, and moved to Department of Materials Engineering, The University of Tokyo in 2000. His current research interests include materials science and device physics of scaled CMOS both in Si and Ge, and of carbon-based devices. He was in charge of high-k gate stack group in MIRAI Project in Japan from 2001 to 2007. He has authored more than 250 refereed journal/conference publications. He is a fellow of the Japan Society of Applied Physics.



Kosuke Nagashio received the B.E. degree in Materials Science & Engineering from Kyoto University in 1997 and the M.E. and Ph.D. degrees in Materials Engineering from The University of Tokyo in 1999 and 2002, respectively. He is currently an Associate Professor with the Department of Materials Engineering, The University of Tokyo. His research interests presently focus on the crystal growth and the carrier transport for layered materials. Dr. Nagashio is a member of the Japan Society of Applied Physics (JSAP), the Japan Institute of Metals (JIM), the Materials Research Society (MRS) and the IEEE Electron Device Society (EDS).



Shintaro Sato received his master's degree from the Graduate School of Science and Engineering, University of Tsukuba, in 1990. After working for Ushio Inc., he received his Ph.D. from the Department of Mechanical Engineering, University of Minnesota, in 2001. In the same year, he joined Fujitsu Limited. He became a staff researcher in 2002 and a senior researcher of Fujitsu Laboratories Ltd. in 2007. He also worked for Semiconductor Leading Edge Technologies, Inc., between 2006 and 2010. From June 2010 to March 2014, He worked for the National Institute of Advanced Industrial Science and Technology, participating in the

Yokoyama Project supported by the Funding Program for World-Leading Innovative R&D on Science and Technology. He is currently a research manager of Fujitsu Laboratories Ltd. His main research area includes the synthesis and evaluation of nanocarbon materials and their applications to electronics.



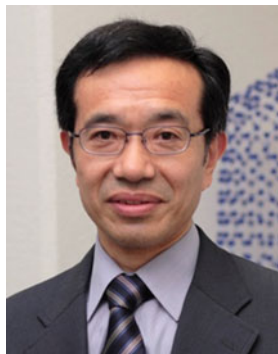
Dr. Daiyu Kondo received M.S. and Ph.D. degrees in Physics from Tohoku University, Sendai, Japan. He joined Nanoelectronics Research Center, Fujitsu Laboratories Ltd., Atsugi, Japan in 2003. He was engaged in research on synthesis and characterization of nanomaterials such as carbon nanotubes and graphene for future carbon electronics including large scale integration interconnects and transistor channels. From 2009 to 2010, he was a visiting researcher, Department of Engineering, University of Cambridge, Cambridge, UK, in which he studied graphene synthesis. From 2011 to 2014, he was seconded to Collaborative Research Team

Green Nanoelectronics Center (GNC), National Institute of Advanced Industrial Science and Technology (AIST), Tsukuba, Japan. He focused on research of nanocarbon interconnects at AIST. Currently, he is a research manager in Innovative Devices Laboratory of Fujitsu Laboratories Ltd.



Taichi Otsuji is a professor at the Research Institute of Electrical Communication (RIEC), Tohoku University, Sendai, Japan. He received the B.S. and M.S. degrees in electronic engineering from Kyushu Institute of Technology, Fukuoka, Japan, in 1982 and 1984, respectively, and the Dr. Eng. degree in electronic engineering from Tokyo Institute of Technology, Tokyo, Japan in 1994. From 1984 to 1999 he worked for NTT Laboratories, Kanagawa, Japan. In 1999 he joined Kyushu Institute of Technology as an associate professor, being a professor in 2002. He joined RIEC, Tohoku University, in 2005. His current research interests

include terahertz electronic and photonic materials/devices and their applications. He is authored and co-authored more than 200 peer-reviewed journals. He was awarded the Outstanding Paper Award of the 1997 IEEE GaAs IC Symposium, and has been an IEEE Electron Device Society Distinguished Lecturer since 2013. He is a Fellow of the IEEE, a senior member of the OSA, and a member of the JSAP, MRS, and IEICE.



Yoshikazu Homma is a professor of Department of Physics and Head of the Nanocarbon Research Division, Research Institute of Science and Technology, Tokyo University of Science. He received his B.S. and M.S. Degrees in physics from Tohoku University, Japan, in 1976 and 1978, respectively, and his Doctor Degree in engineering from the University of Tokyo, Japan, in 1987. Before the present position, he worked for laboratories of Nippon Telegraph and Telephone Public Corporation in 1978–1984 and Nippon Telegraph and Telephone Corporation in 1985–2003. He got Sakaki Award from Microbeam Analysis Committee

141, Japan Society of Promotion of Science, and Seto Award from Japan Society of Electron Microcopy in 2002. He is a fellow of Applied Physics Society of Japan and Surface Science Society of Japan.



Eiichi Tamiya holds a position as full professor at Osaka University. He received his Ph.D. degree from Tokyo Institute of Technology, Science and Engineering School in 1985. He subsequently held positions as research associate at Tokyo Institute of Technology from 1985 to 1987; and as well as a lecturer position at this institute from 1987 to 1988. Later he worked as an associate professor at the University of Tokyo, Research Centre for Advanced Science and Technology (RCAST) from 1988 to 1993. He obtained a full professor position at Japan Advanced Institute of Science and Technology from 1993 to 2007; and then worked as a full professor

at Osaka University from 2007. His research topics are Nanoplasmonic biosensors and biochips. point-of-care (POC) biosensors for medical diagnosis, food safety and environmental protection, biomass based biofuel cell as well as cell-based chips for tissue and stem cell engineering.



Yuzuru Takamura is a professor at Japan Advanced Institute of Science and Technology (JAIST) from 2011. He received his Ph.D. degree from the University of Tokyo in 1995. Then, he held positions as research fellow of Japan Society for the Promotion of Science from 1995 to 1996, research associate at Institute of Space and Astronautical Science, Japan, from 1996 to 1999, Research Associate at The Univ. of Tokyo from 1999 to 2003, and associate professor from 2003 to 2011. His interest includes the study on microfluidics, Micro electronic and mechanical systems and their application to single cell analysis, medical diagnosis, and environmental analysis.



Seiji Akita received his B.S., M.S., and Dr. Eng. degrees from Osaka Prefecture University, Japan, in 1986, 1988, and 1992, respectively. Since 2008, he is a professor at the Department of Physics and Electronics, Graduate School of Engineering, Osaka Prefecture University. His current research interests are nano-electro-mechanical devices consisting of low dimensional materials such as nanocarbon. He received the Nano-probe Technology Award and the Commendation for Science and Technology by the Minister of Education, Culture, Sports, Science and Technology from JSPS and MEXT in 2003 and 2012, respectively.



Koji Ishibashi is a director of the advanced Device Laboratory at RIKEN. He received his B.S. M.S. and Dr. Eng. in electrical engineering from Osaka University, in 1983, 1985 and 1988, respectively. Then, he joined RIKEN as a postdoc and became the director and a chief scientist in 2003. During that time, he stayed at Delft University of Technology in 1996–1997 as a visiting scientist. He is also a visiting professor at Chiba University, Tokyo University of Science and Tokyo Institute of Technology.



Yutaka Ohno is a Professor of EcoTopia Science Institute, and Department of Electrical Engineering and Computer Science, Nagoya University, Japan. He received the B.E., M.E., and Ph.D. degrees from Nagoya University in 1995, 1997, and 2000, respectively. He worked for one year as a Research Scientist of Japan Society for the Promotion of Science when he was a graduate student. He became a research associate in 2000, an assistant professor in 2002, an associate professor in 2008 of the Department of Quantum Engineering, and a professor of EcoTopia Science Institute and Department of Electrical Engineering and Computer Science in 2015, Nagoya University. He was also a Research Scientist of Japan Science and Technology Agency from 2003 to 2007, and a visiting professor of Aalto University, Finland, from 2012 to 2013. He works on transport and optical physics of semiconductor nanostructures and their device applications. He is currently involved in carbon nanotube-based electron devices and their application to healthcare flexible devices.

Part I

Graphene

Chapter 1

CVD Growth of High-Quality Single-Layer Graphene

Hiroki Ago

Abstract To utilize the unique and excellent properties of graphene, synthesis of highly crystalline, large-area graphene is necessary. Among various methods to produce graphene, chemical vapor deposition (CVD) using hydrocarbon molecules in the presence of metal catalyst has shown significant progress due to the large-area availability and low cost. In this section, after a review of the growth methods of graphene with the main focus on CVD, our research on the CVD growth of high-quality graphene over heteroepitaxial metal films and domain structure analysis is presented. Recent development of the CVD growth of single-crystalline graphene as well as large-area growth based on roll-to-roll processes is also reviewed together with future prospect of graphene research.

Keywords CVD • Cu • Epitaxy • Domain boundary • Mobility

1.1 Introduction

Graphene has attracted a significant interest due to its ideal two-dimensional (2D) structure with a single-atom thickness as well as unique linear band dispersion at the K point [1–3]. Graphene shows many excellent properties, high carrier mobility, high optical transparency, high electrical conductivity, and high Young's modulus. These properties and chemical inertness as well as high processability due to 2D structure promise applications in various electronic devices, such as high-frequency transistors, integrated circuits, transparent electrodes, touch panels, and chemical/biochemical sensors. These electronic applications require high-quality, large-area graphene, and synthesis methods of such graphene sheets have shown rapid progress. In this section, chemical vapor deposition (CVD) which is believed to be the most suitable for industrial production is reviewed. Then, our research on graphene CVD using heteroepitaxial metal thin films is described. Finally, recent developments in CVD synthesis are also discussed together with future prospects.

H. Ago (✉)

Institute for Materials Chemistry and Engineering, Kyushu University, Fukuoka, Japan
e-mail: ago@cm.kyushu-u.ac.jp

1.2 Preparation Methods of Graphene

Table 1.1 summarizes preparation methods of graphene. Mechanical exfoliation from graphite first reported by Geim and Novoselov gives highly crystalline graphene flakes which are suitable for physical measurements [4]. However, the size of graphene flakes is limited to several 10 μm or smaller and the thickness is not uniform, thus making industrial production difficult. Thermal annealing of SiC single crystal substrates at 1,500 °C evaporates surface Si atoms, leaving graphene on the SiC surface [5, 6]. Because of the formation of a buffer layer between SiC and graphene, transfer of a graphene sheet from the SiC substrate is difficult, and also SiC wafers are expensive. Instead, graphene devices can be directly made on the SiC substrate, because SiC has a wide bandgap (3.25 eV). For bulk applications, such as composites and conducting paste, graphene oxide (GO) is widely used [7, 8]. A modified Hummers' method is mainly used to prepare GO solutions, but due to the severe oxidation of graphite, it is difficult to completely reduce to graphene. Although GO or reduced GO have many functional groups and defects, they are suitable for applications which require a large quantity of graphene.

Chemical vapor deposition (CVD) utilizes catalytic graphitization over metal catalysts from hydrocarbon feedstock at high temperatures, typically 900-1080 °C. Currently CVD growth is widely used because it can produce large-area, high-quality graphene with relatively low cost [9–13]. In addition, CVD graphene is easily transferrable to other substrates through chemical or electrochemical etching of the metal catalyst substrate, making it useful for flexible electronics. Many electronic applications, such as transistors, touch panels, transparent electrodes, and sensors, have been demonstrated using CVD graphene. In the following, the growth mechanism of CVD graphene is explained.

Table 1.1 Preparation methods of graphene

	Mechanical exfoliation	SiC thermal decomposition	Reduction of GO	CVD
Crystallinity	⊙	⊙-○	×	⊙-○
Size	×	△	⊙	○
Uniformity	×	○	○	⊙-○
Cost	○	×	⊙	○
Advantages	Highly crystalline graphene is obtained by a simple process	It is possible to fabricate devices directly on SiC wafer	Wet process is applicable and suitable for bulk applications	Suitable for low-cost and large-area production, transfer is easy
Disadvantages	Size is small, shape and layer number are not uniform	SiC crystalline substrate is expensive and graphene transfer is difficult	Difficult to completely reduce GO and many defects remain	Metal catalysts and high temperature are required

1.3 CVD Growth Over Metal Catalyst

Growth mechanism largely depends on the metal catalysts used, as illustrated in Fig. 1.1. Because it was well known that carbonization over Ni metal produces graphite flakes, initial CVD growth of graphene was reported on Ni foils [9, 10]. However, for metal films with high carbon solubility, such as Ni and Co, C atoms decomposed from CH₄ molecules are easily dissolved into the metal film and precipitate as grapheme during the final cooling process. The amount of dissolved C atoms is difficult to control so that these metals give nonuniform graphene films with inhomogeneous layer numbers.

In 2009, Ruoff's group discovered that Cu catalyst can produce uniform single-layer graphene (single-layer occupies 95 % of the total area) [11]. As shown in Fig. 1.1b, the dissolution of C atoms into Cu metal is suppressed due to the low carbon solubility, and graphitization proceeds only on the Cu surface, leading to the preferential growth of single-layer graphene [12, 13]. Once the Cu is covered by graphene, the CH₄ decomposition ceases to occur; thus, it is called as "self-limiting mechanism." As single-layer graphene can be synthesized under a wide reaction

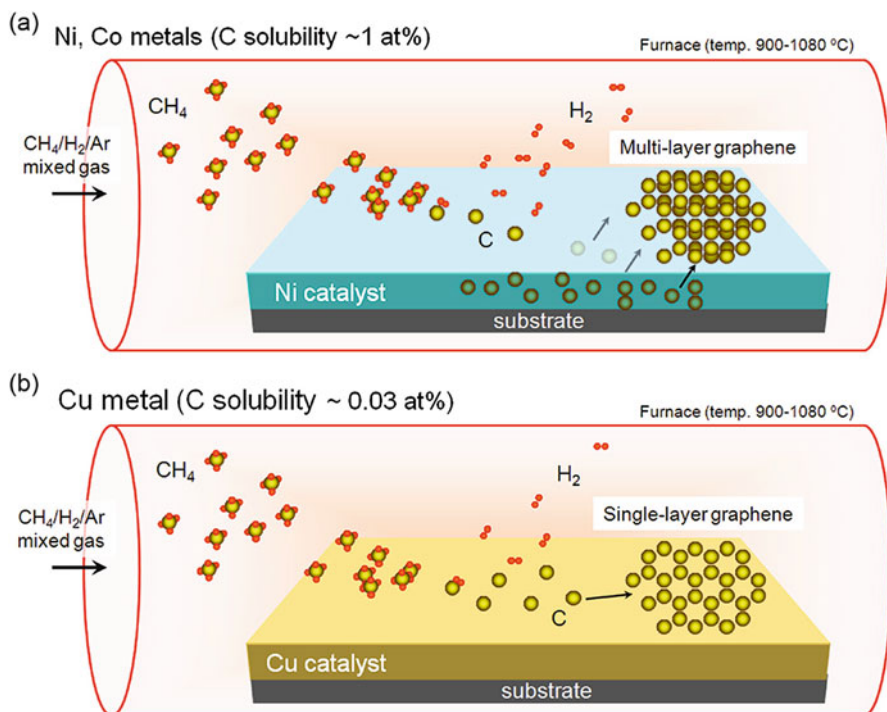


Fig. 1.1 Growth mechanism of graphene sheets on different types of metal catalysts. (a) Inhomogeneous multilayer graphene tends to grow on Ni and Co which has high C solubility. (b) Uniform single-layer graphene can be grown on low C solubility metal, like Cu

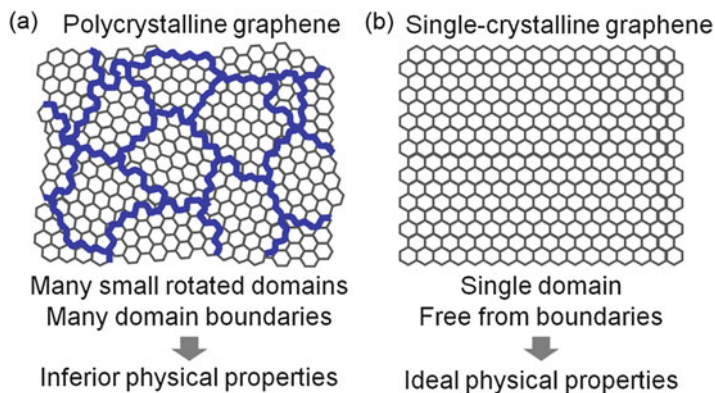


Fig. 1.2 Domain structures of graphene. **(a)** Polycrystalline graphene generally observed for CVD grown samples. *Thick lines* correspond to boundaries. **(b)** Ideal single-crystalline graphene. Single-crystalline graphene is expected to show higher mobility and better mechanical properties than polycrystalline graphene

window, Cu metal, in particular Cu foil, is now widely used as a catalyst for graphene growth. In principle, a simple scale up of both the catalyst substrate and CVD furnace can produce large-area graphene. This was realized by Hong and Ahn's groups which succeeded in synthesizing a 30-in. graphene sheet over Cu foil, and they also reported roll-to-roll transfer to a polymer film [14]. They also effectively demonstrated the potential of CVD graphene by fabricating touch panels using a transferred graphene sheet.

In 2011, Muller's group visualized the domain structure of CVD graphene grown on polycrystalline Cu foil by dark-field transmission electron microscope (DF-TEM). They showed that the CVD graphene is polycrystalline consisting of small domains with a size of 500 nm to several μm , and these domains are randomly rotated [15]. Figure 1.2a is an atomic model of such polycrystalline graphene. Domain boundaries indicated by bold lines scatter charge carriers, thus deteriorating transport property. In addition, mechanical tears are suggested to initiate from these domain boundaries [16]. Therefore, even though one can grow large-area graphene by CVD using large Cu foil, the CVD graphene is a patchwork of small graphene domains, and we cannot expect ideal physical properties from such polycrystalline graphene. Thus, the CVD growth of single-crystalline graphene (Fig. 1.2b) free from boundaries is required for high-performance electronics and other applications. One main reason for the polycrystallinity of CVD graphene (Fig. 1.2a) is that metal catalysts have polycrystalline or amorphous structures. As discussed later, the CVD growth conditions are also important for the graphene's domain structure. Atomic structure and electronic state at domain boundaries are interesting, and different types of boundaries such as linear chains of 5–7 paired rings [15] are observed.

There have been some papers reporting direct growth of graphene on insulating substrates without the use of metal catalysts. This metal- and transfer-free growth

is very attractive for reducing the cost and manufacturing devices, but the graphene grown on insulating substrates has very small domain size around 10 nm [17] and shows much lower mobility and higher sheet resistance than graphene grown on Cu. Thus, it is thought that the metal catalyst plays an essential role in growing a highly developed π -conjugated graphene network.

1.4 CVD Growth Over Heteroepitaxial Co Films

As mentioned above, widely used catalysts are free-standing metal foils and thin metal films deposited on silicon wafers, and these metals have a polycrystalline structure. For high-quality graphene growth by CVD, single-crystalline metal catalysts are expected to be better than polycrystalline metal foils or films. However, as single-crystalline substrates, such as Cu(111) and Ni(111), are very expensive and their sizes are limited, it is not practical to produce graphene on these substrates which require a transfer process that includes chemical metal etching.

We have developed a new method to deposit crystalline metal films epitaxially on single-crystalline oxide substrates, such as sapphire (α -Al₂O₃) and MgO [18–21]. These oxide substrates are much cheaper than Cu(111) and Ni(111) substrates, and currently large sapphire wafers up to 6 in. are available with reasonable price owing to the development of the GaN-based light-emitting diode (LED) industry. This heteroepitaxial CVD approach is illustrated in Fig. 1.3b. Being

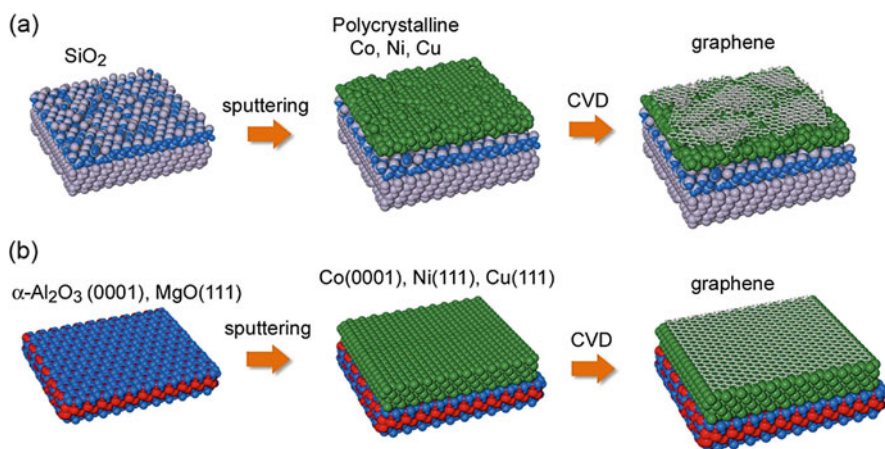


Fig. 1.3 Schematics of the CVD growth of graphene over metal films deposited on SiO₂/Si (a) and single-crystalline substrates (b). (a) Polycrystalline metal catalyst is formed on the SiO₂ surface, which tends to give disordered graphene with broad layer distribution and randomly orientated small domains. (b) Heteroepitaxial metal film (such as Co(0001), Ni(111), or Cu(111)) is expected to assist the growth of uniform, well-defined graphene with controlled orientation

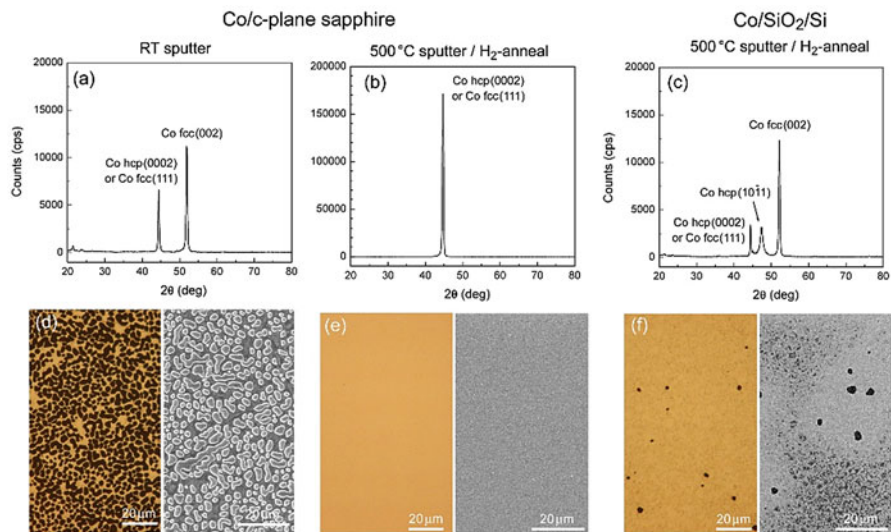


Fig. 1.4 (a–c) XRD profiles of the Co films measured after CVD at 1,000 °C. (d–f) Optical microscope (*left*) and SEM (*right*) images of the Co surfaces obtained after the CVD. (d, e) Co film was sputtered at room temperature on c-plane sapphire and subjected to the CVD. (b, e) Co film was sputtered at 500 °C on c-plane sapphire, annealed at 500 °C in H₂/Ar flow, and then subjected to CVD. (c, f) SiO₂/Si substrate was used instead of sapphire with other experimental conditions identical to those in panels (b, e)

different from conventional polycrystalline metal catalysts or metal foils (Fig. 1.3a), heteroepitaxial metal films are expected to produce graphene with uniform thickness and controlled hexagon orientation.

Figure 1.4 shows x-ray diffraction (XRD) profiles, optical micrographs, and scanning electron microscope (SEM) images of the Co films deposited on sapphire and SiO₂ substrates [18]. It was found that the 200 nm-thick Co film sputtered on sapphire at room temperature is polycrystalline (Fig. 1.4a). This polycrystalline Co film cannot withstand the high temperature CVD process at 1,000 °C, and many pits and holes appeared on the metal surface (Fig. 1.4d). However, high temperature Co sputtering (500 °C) and post-annealing in H₂ significantly improved the crystallinity as well as stability during CVD, as seen in Fig. 1.4b, e. On the other hand, the thin Co film deposited on a Si wafer with 300 nm amorphous oxide layer was polycrystalline and not stable during the CVD process (Fig. 1.4c, f).

Graphene sheets grown on Co/sapphire and Co/SiO₂ were inspected by optical microscope and Raman spectroscopy after transferring onto SiO₂/Si substrates, as shown in Fig. 1.5a–d. The graphene grown on the high temperature-sputtered Co/sapphire showed uniform optical contrast and high 2D/G ratio ($I_{2D}/I_G > 2$), signifying the growth of uniform single-layer graphene (see Fig. 1.5a, b) [22]. In

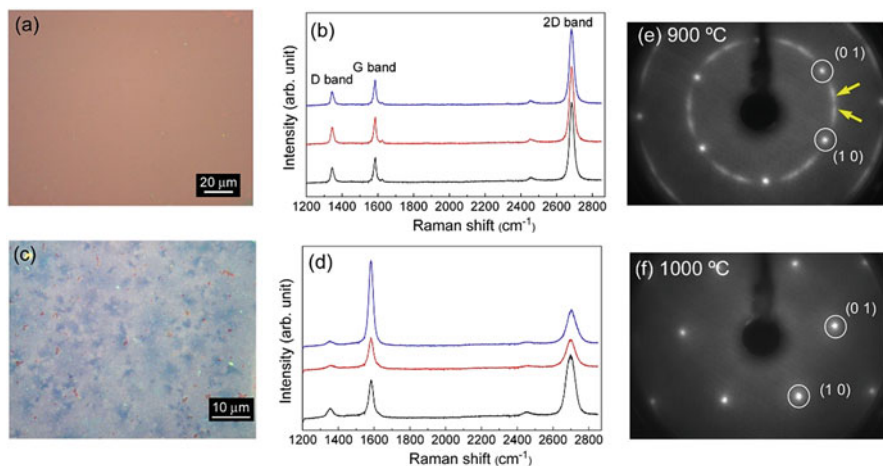


Fig. 1.5 Optical microscope images (a, c) and Raman spectra (b, d) of transferred graphene on SiO₂ [18]. Graphene was grown on Co/sapphire (a, b) and Co/SiO₂ (c, d). (e, f) LEED pattern of graphene/Co/sapphire grown at 900 °C (e) and 1,000 °C (f). Circles in (e) indicate the diffraction from Co lattice; yellow arrows show diffraction from graphene. Graphene grown at 1,000 °C showed only six spots originating in both Co lattice and graphene

contrast, the graphene grown on the Co/SiO₂ showed nonuniform optical contrast and various 2D/G ratios (Fig. 1.5c, d), indicating the formation of multilayer graphene with different layer numbers.

As Co has high C solubility similar to Ni, it was believed that it is difficult to grow uniform single-layer graphene on Co. However, this work demonstrates that Co can catalyze the growth of uniform single-layer graphene when the crystallinity of the Co metal is sufficiently high. The transferred single-layer graphene showed a relatively strong Raman D-band which is originated from defects and domain boundaries in the graphene (see Fig. 1.5b). This D-band may also originate from the strong Co-graphene interaction or small domain size of the graphene sheet.

Orientations of the graphene lattice on the Co(0001) plane is of great interest in terms of the epitaxial graphene growth. To determine the orientation of graphene hexagons, low-energy electron diffraction (LEED) was measured for graphene grown on Co/sapphire substrates. Figure 1.5e, f is the LEED patterns measured for different CVD growth temperatures. The graphene grown at the lower CVD temperature, 900 °C, showed rotated orientations with respect to the underlying Co lattice. At the higher growth temperature of 1,000 °C, the graphene showed a clear set of six diffraction spots, indicating that the graphene hexagon orientation is consistent with the Co lattice. Therefore, our work demonstrates that highly crystalline Co(0001) film is effective not only at growing uniform single-layer graphene but also controlling the graphene's lattice orientation [18].

1.5 CVD Growth Over Heteroepitaxial Cu Films

The heteroepitaxial CVD approach can also be applied to Cu thin films, and like Cu foils, one can grow single-layer graphene on an epitaxial Cu film deposited on sapphire [19, 20]. Conventional Cu foils have slightly misoriented fcc(100) planes due to the rolling process [20]. This fcc(100) has a square lattice and does not match with graphene's sixfold symmetry. Thus, it is interesting to study influence of such fcc(100) plane on the domain structure of CVD graphene.

To understand the effects of the Cu lattice on the domain structure of graphene, CVD graphene grown on heteroepitaxial Cu(111) and Cu(100) lattice was studied [21]. The Cu(111) and Cu(100) films were deposited on MgO(111) and MgO(100), respectively, by high temperature radio-frequency (RF) magnetron sputtering. Both Cu films produced uniform single-layer graphene after the CVD at 1,000 °C, but the domain structures were found to be completely different, as displayed in Fig. 1.6. Here, to investigate nanoscale domain structure, low-energy energy

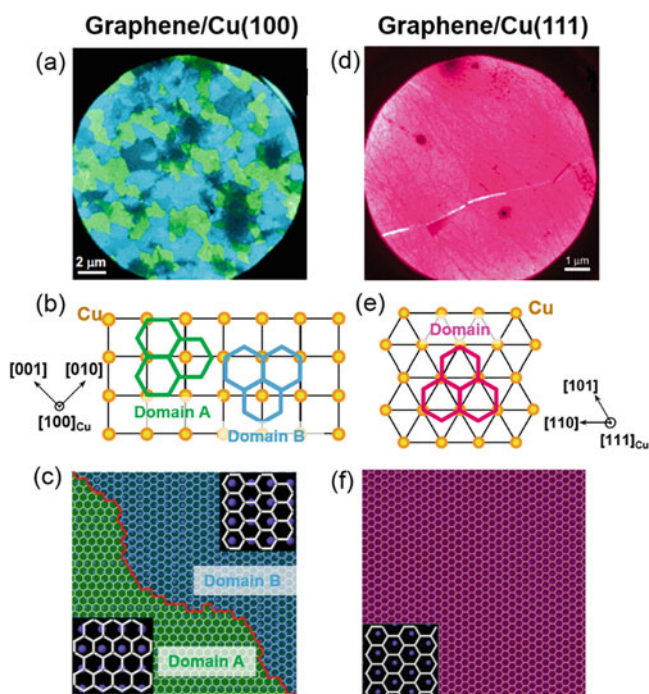


Fig. 1.6 (a) DF-LEEM image of single-layer graphene grown on a Cu(100)/MgO(100). (b) Relative orientation of graphene domains with respect to the square lattice of Cu(100). (c) Schematic of neighboring domains rotated by 30°. (d–f) LEEM image, atomic structure, schematic of graphene on Cu(111)

electron microscope (LEEM) was used, because it can measure a wide area and relative orientation of the graphene to the underlying Cu lattice without use of a transfer process.

Figure 1.6a shows a dark-field LEEM (DF-LEEM) image of single-layer graphene grown on Cu(100) at 1,000 °C. Blue and green colors represent domain orientations, and these two main orientations are rotated by 30°. From the diffraction of the Cu(100) lattice, we can assign the orientation of these two types of domains, A and B (Fig. 1.6b). Graphene's C–C bonds are found to align parallel to one of Cu–Cu bonds of the square lattice. Because of the symmetry mismatch, two types of domains with 30° rotation can grow simultaneously. Note that these two domains (A and B) are crystallographically equivalent. Although the atomic structure cannot be imaged by LEEM, we speculate that domain boundaries should exist between these rotated domains, as illustrated in Fig. 1.6c.

In the case of single-layer graphene grown on Cu(111), the domain orientation is fully consistent with that of the underlying Cu lattice (Fig. 1.6d–f). The threefold symmetry of the Cu(111) lattice allows for the uniform orientation in CVD graphene, as depicted in Fig. 1.6e, leading to epitaxial graphene growth. Within the spatial resolution of LEEM, no domain boundaries were observed. Therefore, this heteroepitaxial CVD approach is expected to be a new approach to grow large-area, single-crystalline graphene.

Transport properties were also studied for the single-layer graphene sheets grown on a Cu(111) thin film and on a conventional Cu foil [20]. Here, the Cu(111) film was deposited on sapphire c-plane, and Cu foil was purchased from Alfa Aesar. After the transfer to SiO₂/Si substrate with a 300 nm thick SiO₂ layer (Fig. 1.7a), graphene was patterned by electron beam lithography and oxygen plasma treatment. Then, a second lithography step was performed to pattern source and drain electrodes for back-gated field-effect transistors (FETs) (Fig. 1.7b).

Transfer characteristics of transistors made with graphene sheets grown on Cu(111) film and Cu foil are compared in Fig. 1.7c. Distribution of two-terminal carrier mobilities measured for different channel widths is displayed in Fig. 1.7d. The mobility was determined based on an equation, $\mu = [(\partial I_d / \partial V_g) L] / (W C_{ox} V_d)$, where L and W are the channel length and width, respectively; V_d is the drain voltage; and C_{ox} is the dielectric constant of SiO₂ (1.15×10^{-4} F/m²). There was no clear width dependence of the mobility after measuring more than 30 devices. The carrier mobility of the graphene grown on Cu film was 1–2 orders of magnitude higher than that of Cu foil. The highest hole mobilities determined for the Cu foil and Cu film are 900 and 2,530 cm²/Vs, respectively. In addition, the carrier mobility values of the graphene grown on Cu foil scatter much more than those on Cu film. We consider that the significant difference in mobilities for different Cu metals probably correlates with difference of the domain structures of graphene/Cu(111) and graphene/Cu foil. In addition, the surface roughness of Cu foil could reduce the carrier mobility because of the damage to graphene during transfer to SiO₂ substrate. Note that the mobility obtained for graphene grown on Cu(111) is still slower than that of exfoliated graphene (10,000 cm²/Vs) [4]. This may be attributed to wrinkles, defects induced by transfer, and undetected boundaries.

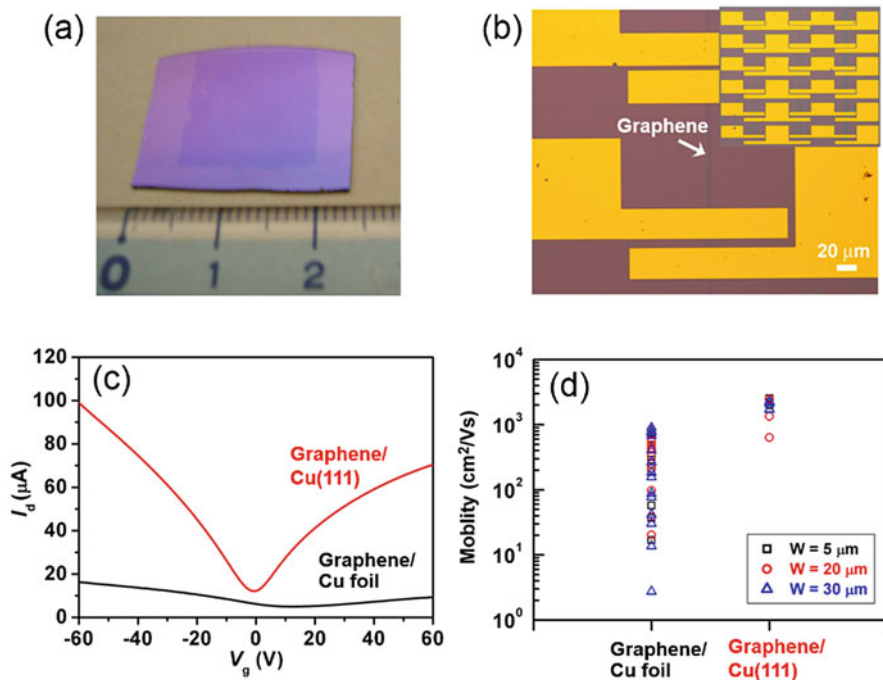


Fig. 1.7 (a) Photograph of single-layer graphene transferred on SiO₂/Si from Cu(111)/sapphire. (b) Micrograph of arrays of graphene FETs. (c) Transfer characteristics of graphene grown on Cu(111) and Cu foil. (d) Distribution of carrier mobilities with different channel widths

1.6 Increasing Graphene Domain Size on Heteroepitaxial Cu Films

Shown in Fig. 1.8 is a schematic model of graphene growth dynamics over Cu metal. There are many surface reactions and processes involved in the graphene growth as follows: (1) Catalytic dehydrogenation of CH₄ feedstock, which leaves CH_x ($x = 0-3$) species adsorbed on the Cu surface. (2) Surface diffusion of the adsorbed C atoms or CH_x. This diffusion is thermally activated and driven by a concentration gradient of these adsorbates. (3) Nucleation of graphene domains. Here grain boundaries and the rough surface of Cu are known to stimulate the graphene nucleation. (4) Growth of graphene domains, which is likely accompanied by edge reconstruction. (5) Coalescence of neighboring graphene domains into a continuous graphene film. (6) Etching of graphene domains by H₂ gas. This is the reverse reaction of the CH₄ decomposition (1) and may be assisted by the Cu surface. (7) During the CVD, evaporation of Cu atoms from the Cu surface also occurs because the growth temperature (1,000–1,080 °C) is close to the melting temperature of Cu (1,084 °C). This is more severe in vacuum CVD (10–1,000 mTor)

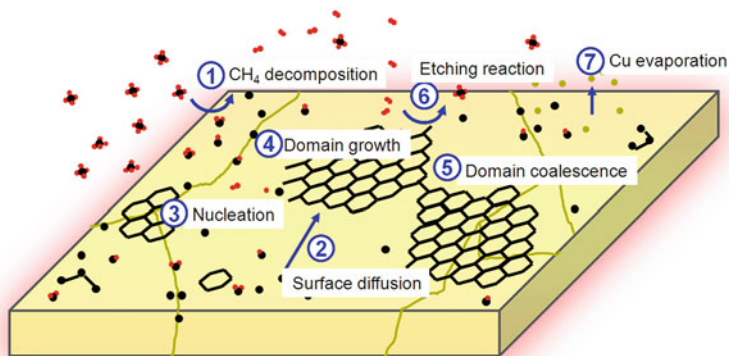


Fig. 1.8 Growth mechanism of single-layer graphene on a Cu metal with grain boundaries

compared with ambient-pressure CVD, and sometimes it contaminates the growth chamber with evaporated Cu. Not only the presence of grain boundaries but also the crystallinity of the Cu catalyst is important in the catalytic graphene growth. This is because (1) the graphene nucleation is associated with the Cu's grain boundary and (2) the orientation of the graphene domain can correlate with the in-plane orientation of the Cu grains.

Recently, a number of papers have been published with an aim to grow large-area “single-crystalline graphene (see Fig. 1.2b).” One main approach is to control the CVD condition and clean and smoothen Cu surface to increase the size of graphene domains. This is done by reducing the CH_4 concentration to 10 ppm and growth at high temperature near the Cu melting temperature ($1,084\text{ }^\circ\text{C}$). The low CH_4 concentration reduces the nucleation density, and the high CVD temperature increases the diffusion length of surface-adsorbed C atoms [13, 23]. Figure 1.9a is scanning electron microscope (SEM) images of large graphene domains realized on an epitaxial Cu(111) film [24]. The growth condition was $1,075\text{ }^\circ\text{C}$ with 10 ppm CH_4 under ambient pressure. One can see that graphene domains (seen as dark contrast) grow with time and they have hexagonal structures. As seen in Fig. 1.9b, each of the hexagonal domains have almost the same orientation, indicating the hexagonal domain growth is consistent with the underlying Cu(111) lattice. From the orientation of the sapphire substrate, it is revealed that these hexagonal domains have zigzag or near zigzag edges (Fig. 1.9c). Such zigzag edges are also interesting in terms of magnetic properties because zigzag edges create nonbonding orbitals that give localized unpaired electrons. Through the optimization of the CVD condition, large graphene domains up to $100\text{ }\mu\text{m}$ size were grown on Cu(111), as shown in Fig. 1.9d [24].

The single-crystalline structure was confirmed by angle-resolved photoelectron spectroscopy (ARPES). Figure 1.9e is the ARPES spectrum of the as-grown graphene domains [24]. A linear band dispersion was observed and graphene was

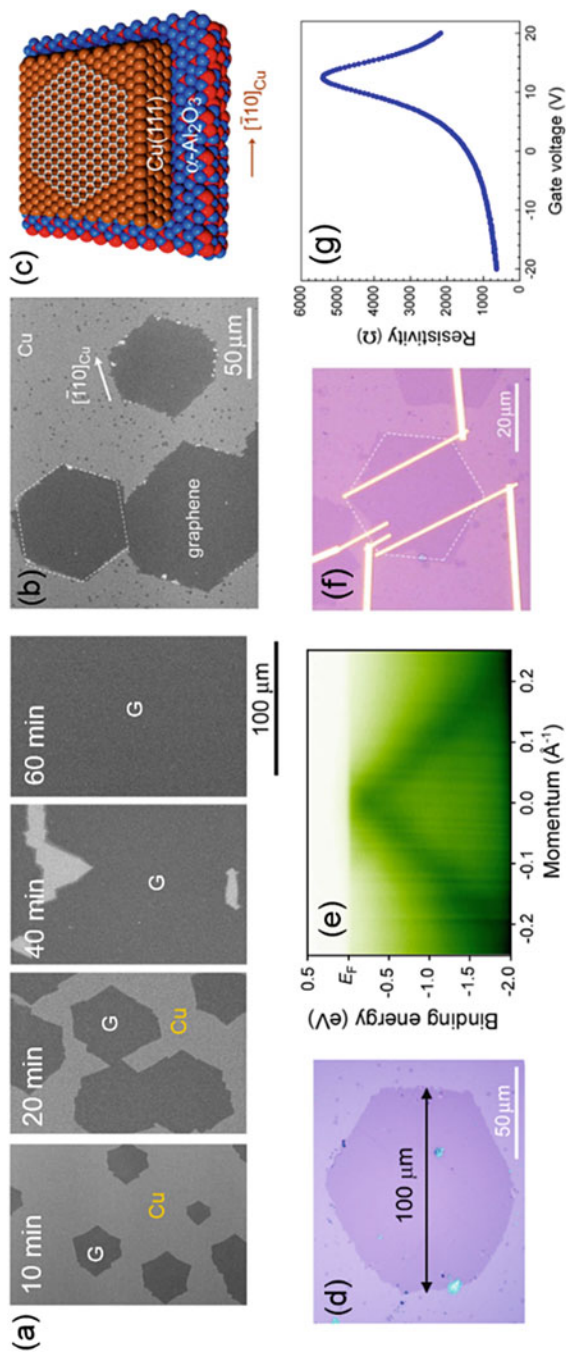


Fig. 1.9 (a) Growth time dependence of graphene domains on Cu(111) thin film. (b) Large hexagonal graphene domains grown with the same orientation. (c) Schematic of a hexagonal domain with zigzag edges on Cu(111)/sapphire. (d) Optical micrograph of a large domain graphene transferred on a SiO_2/Si substrate. (e) Band structure of as-grown graphene domains measured by ARPES. (f) A hexagonal graphene domain contacted with electrodes for four-terminal measurement and (g) the corresponding resistivity measured at room temperature

found to be slightly n-type doped due to the underlying Cu. No orbital hybridization of graphene and Cu was observed, supporting weak graphene-Cu interaction, which may be useful for clean graphene transfer. Carrier mobility was also measured for one of the single-crystalline hexagonal domains by attaching multiple electrodes on a SiO₂/Si substrate. We observed high mobility, reaching 4,000 cm²/Vs, for the device shown in Fig. 1.9f, g. Recently, by careful transfer and impurity removal, we observed a carrier mobility over 20,000 cm²/Vs at 280 K for a hexagonal domain [25]. This mobility value is higher than that of exfoliated graphene (10,000 cm²/Vs), thus signifying the growing of single-crystalline graphene is essential for high-performance electronics.

For realization of large single-crystalline graphene, the seamless connection between neighboring domains with the same orientation becomes important. Figure 1.10a highlights the interface of adjacent domains merged with the same angle. It is interesting to understand the atomic structure of this domain interface. Our recent study suggests that a scattering site exists at the interface of neighboring domains even though the domain orientation is the same [25]. Therefore, further study is necessary to achieve atomic-scale perfect connection of neighboring domains to synthesize single-crystalline graphene based on this approach.

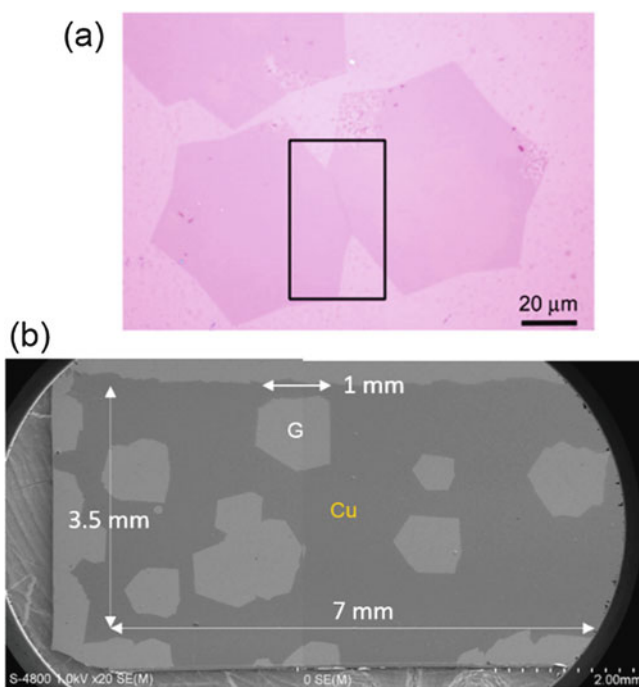


Fig. 1.10 (a) Optical micrograph of adjacent graphene domains merged with the same angle. (b) SEM image of Cu(111) surface with limited graphene nuclei

Recently, the increase of the domain size of graphene has shown rapid progress. The main strategies to grow giant domains are (1) to enhance C surface diffusion by increasing the CVD temperature and (2) to reduce nucleation density as low as possible by making ultrasmooth Cu surface as well as lowering CH₄ concentration. Our epitaxial Cu(111) has several advantages, such as high crystallinity which makes the Cu film more stable than polycrystalline Cu foil, ultrasmooth Cu surface available only by H₂ annealing at high temperature, and suppressed grain boundaries in the epitaxial metal film. Figure 1.10b shows our recent graphene domains with 1 mm size [26]. This size should be sufficient for transistor applications, because this size is much larger than a modern Si transistor. Very recently, a giant graphene domain with 5–10 mm was obtained on Cu foil [27, 28]. Further increase of the domain size might be expected by considering the recent rapid progress of graphene CVD.

1.7 Recent Progress and Future Prospect

Large-scale graphene production is quite important for macroelectronic applications, such as transparent electrodes and touch panels, to replace widely used indium tin oxide (ITO) electrodes. Such large-area graphene has mainly been studied by using Cu foil, and as already mentioned, 30 in. graphene sheets were produced by a Korean group in 2010 [14]. In Japan, a group in AIST used plasma CVD growth to reduce the growth temperature (400 °C) and develop a roll-to-roll production technique [29]. SONY has reported a new method to heat Cu foil by applying a local current and succeeded in producing a 100 m long graphene sheet [30]. This method is expected to reduce the electric power consumption because the graphene growth is limited to the local heating area. Although there are some issues still remaining, such as costs of Cu and transfer processes, graphene is expected as a promising flexible electrode material in a future electronics.

Triggered by the development of graphene research, other two-dimensional inorganic sheets with atomic-scale thickness have attracted recent interests. These materials include hexagonal boron nitride (h-BN) and various transition metal dichalcogenides (TMDCs), such as MoS₂ and WSe₂. Integration of these layered materials is of great interest to derive novel properties and applications. For example, insertion of exfoliated h-BN sheet into the interface between graphene and SiO₂ significantly increases the carrier mobility of graphene FET by a factor of >5 [31]. This result indicates that h-BN is a very good insulating atomic sheet which suppresses the surface roughness and charge impurities present on the SiO₂ surface. TMDCs are layered materials stacked with weak van der Waals interaction so that we can obtain single-layer dichalcogenide sheets either by mechanical exfoliation or CVD. Unique electronic properties are observed for TMDCs with

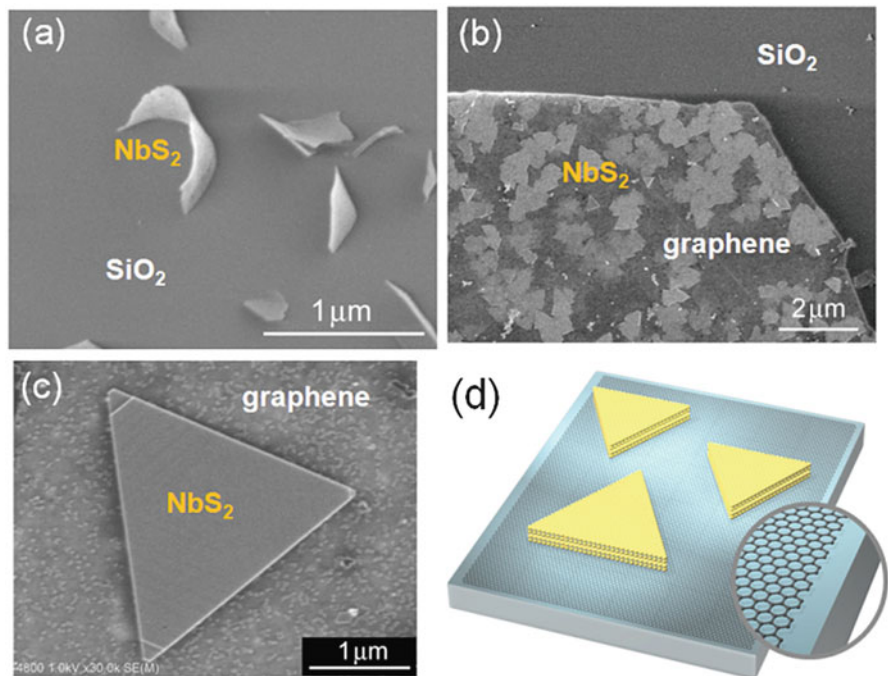


Fig. 1.11 CVD growth of superconducting NbS_2 nanosheets from NbCl_5 and S powder. NbS_2 nanosheets were grown on SiO_2/Si (a) and CVD graphene substrates (b, c). (d) Illustration of the NbS_2 nanosheets on CVD graphene

atomic thickness. For example, bulk MoS_2 has an indirect band gap, but monolayer MoS_2 , a sandwiched structure of single Mo layer with two S layers, shows a direct bandgap, thus giving much stronger photoluminescence than that of bulk MoS_2 [32]. For future development of such two-dimensional materials, integration of different layered materials is very important.

Figure 1.11 shows an example of integration of graphene and TMDCs [33]. NbS_2 is known to become superconductive at low temperature. When grown on a SiO_2/Si substrate by CVD, NbS_2 nanosheets grew normal to the substrate surface (Fig. 1.11a). This structure is not useful for device fabrication. We found that transferred CVD graphene changes the growth mode of NbS_2 nanosheets; laterally oriented nanosheets were obtained only on the graphene surface (Fig. 1.11b–d) [33]. These nanosheets have a faceted structure, as seen in Fig. 1.11c, signifying the growth of crystalline sheet. Other two-dimensional sheets, such as MoS_2 and h-BN, have also been grown on graphene [34–36]. These works are expected to open a new field of novel artificial layered materials with unique electronic, optical, and catalytic properties.

1.8 Summary

In the research of CVD growth of graphene, tremendous development has been observed recently, especially in single-crystalline growth and large-area production technologies. In this section, the mechanism of CVD growth and control of graphene domain structures by CVD are reviewed. Our work demonstrates that it is possible to epitaxially grow single-layer graphene on Cu(111) and Co(0001) with controlled hexagon orientation. This orientation-controlled graphene also allows the epitaxial growth of other 2D atomic sheets.

For electronic applications, the control over layer numbers of graphene is important. For example, transparent electrode application, low sheet resistance comparable to ITO electrodes, $<100 \Omega/\square$ can be achieved only for 3–4 layer graphene after doping. Transistor applications require double-layer graphene to open the bandgap by applying a vertical electric field. Currently multiple transfer is widely used to obtain multilayer graphene to reduce the sheet resistance, but direct growth of layer number-controlled graphene while keeping high quality is desired.

Further development of graphene science and production methods together with integration with other 2D atomic sheets will develop a new type of electronic devices which utilize flexibility, transparency, and high mobility of these unique materials.

Acknowledgments The author acknowledges my group members as well as Prof. M. Tsuji, Dr. H. Hibino, Prof. S. Mizuno, Dr. K. Tsukagoshi, and Dr. K. Ikeda for collaborations. Our work is supported by JSPS funding program for Next Generation World-Leading Researchers (NEXT) and PRESTO-JST.

References

1. Geim AK, Novoselov KS (2009) The rise of graphene. *Nat Mater* 6:183
2. Warner JH, Schaffel F, Rummeli M, Bachmatiuk A (2012) *Graphene: fundamentals and emergent applications*. Elsevier, Oxford
3. Rao CNR, Sood AK (eds) (2013) *Graphene: synthesis, properties, and phenomena*. Wiley, Weinheim
4. Novoselov KS, Geim AK, Morozov SV, Jiang D, Zhang Y, Dubonos SV, Grigorieva IV, Firsov AA (2004) Electric field effect in atomically thin carbon films. *Science* 306:666
5. Berger C, Song Z, Li X, Wu X, Brown N, Naud C, Mayou D, Li T, Hass J, Marchenkov AN, Conrad EH, First PN, de Heer WA (2006) Electronic confinement and coherence in patterned epitaxial graphene. *Science* 312:1191
6. Emtsev KV, Bostwick A, Horn K, Jobst J, Kellogg GL, Ley L, McChesney JL, Ohta T, Reshanov SA, Röhl J, Rotenberg E, Schmid AK, Waldmann D, Weber HB, Seyller T (2009) Towards wafer-size graphene layers by atmospheric pressure graphitization of silicon carbide. *Nat Mater* 8:203
7. Gilje S, Han S, Wang M, Wang KL, Kaner RB (2007) A chemical route to graphene for device applications. *Nano Lett* 7:3394
8. Eda G, Fanchini G, Chhowalla M (2008) Large-area ultrathin films of reduced graphene oxide as a transparent and flexible electronic material. *Nat Nanotechnol* 3:270

9. Yu Q, Lian J, Siriponglert S, Li H, Chen YP, Pei SS (2008) Graphene segregated on Ni surfaces and transferred to insulators. *Appl Phys Lett* 93:113103
10. Reina A, Jia X, Ho J, Nezich D, Son H, Bulovic V, Dresselhaus MS, Kong J (2009) Large area, few-layer graphene films on arbitrary substrates by chemical vapor deposition. *Nano Lett* 9:30
11. Li X, Cai W, An J, Kim S, Nah J, Yang D, Piner R, Velamakanni A, Jung I, Tutuc E, Banerjee SK, Colombo L, Ruoff RS (2009) Large-area synthesis of high-quality and uniform graphene films on copper foils. *Science* 324:1312
12. Mattevi C, Kim H, Chhowalla M (2011) A review of chemical vapour deposition of graphene on copper. *J Mater Chem* 21:3324
13. Ago H, Ogawa Y, Tsuji M, Mizuno S, Hibino H (2012) Catalytic growth of graphene: toward large-area single-crystalline graphene. *J Phys Chem Lett* 3:2228
14. Bae S, Kim H, Lee Y, Xu X, Park JS, Zheng Y, Balakrishnan J, Lei T, Kim HR, Song YI, Kim Y-J, Kim KS, Özyilmaz B, Ahn JH, Hong BH, Iijima S (2010) Roll-to-roll production of 30-inch graphene films for transparent electrodes. *Nat Nanotechnol* 5:574
15. Huang PY, Vargas CSR, Zande AM, Whitney WS, Levendorf MP, Kevek JW, Garg S, Alden JS, Hustedt CJ, Zhu Y, Park J, McEuen PL, Muller DA (2011) Grains and grain boundaries in single-layer graphene atomic patchwork quilts. *Nature* 469:389
16. Kim K, Artyukhov VI, Regan W, Liu Y, Crommie MF, Yakobson BI, Zettl A (2012) Ripping graphene: preferred directions. *Nano Lett* 12:293
17. Sun J, Lindvall N, Cole MT, Teo KBK, Yurgens A (2011) Large-area uniform graphene-like thin films grown by chemical vapor deposition directly on silicon nitride. *Appl Phys Lett* 98:252107
18. Ago H, Ito Y, Mizuta N, Yoshida K, Hu B, Orofeo CM, Tsuji M, Ikeda K, Mizuno S (2010) Epitaxial chemical vapor deposition growth of single-layer graphene over cobalt film crystallized on sapphire. *ACS Nano* 4:7407
19. Hu B, Ago H, Ito Y, Kawahara K, Tsuji M, Magome E, Sumitani K, Mizuta N, Ikeda K, Mizuno S (2012) Epitaxial growth of large-area single-layer graphene over Cu(111)/sapphire by atmospheric pressure CVD. *Carbon* 50:57
20. Orofeo CM, Hibino H, Kawahara K, Ogawa Y, Tsuji M, Ikeda K, Mizuno S, Ago H (2012) Influence of Cu metal on the domain structure and carrier mobility in single-layer graphene. *Carbon* 50:2189
21. Ogawa Y, Hu B, Orofeo CM, Tsuji M, Ikeda K, Mizuno S, Hibino H, Ago H (2012) Domain structure and boundary in single-layer graphene grown on Cu(111) and Cu(100) films. *J Phys Chem Lett* 3:219
22. Ferrari AC, Meyer JC, Scardaci V, Casiraghi C, Lazzeri M, Mauri F, Piscanec S, Jiang D, Novoselov KS, Roth S, Geim AK (2006) Raman spectrum of graphene and graphene layers. *Phys Rev Lett* 97:187401
23. Yu Q, Jauregui LA, Wu W, Colby R, Tian J, Su Z, Cao H, Liu Z, Pandey D, Wei D, Chung TF, Peng P, Guisinger NP, Stach EA, Bao J, Pei SS, Chen YP (2011) Control and characterization of individual grains and grain boundaries in graphene grown by chemical vapour deposition. *Nat Mater* 10:443
24. Ago H, Kawahara K, Ogawa Y, Tanoue S, Bissett MA, Tsuji M, Sakaguchi H, Koch RJ, Fromm F, Seyller T, Komatsu K, Tsukagoshi K (2013) Epitaxial growth and electronic properties of large hexagonal graphene domains on Cu(111) thin film. *Appl Phys Express* 6:75101
25. Ogawa Y, Komatsu K, Kawahara K, Tsuji M, Tsukagoshi K, Ago H (2014) Structure and transport properties of the interface between CVD-grown graphene domains. *Nanoscale* 6:7288
26. Ago H, Kawahara K, Tsuji M, unpublished
27. Yan Z, Lin J, Peng Z, Sun Z, Zhu Y, Li L, Xiang C, Samuel EL, Kittrell C, Tour JM (2012) Toward the synthesis of wafer-scale single-crystal graphene on copper foils. *ACS Nano* 6:9110
28. Hao Y, Bharathi MS, Wang L, Liu Y, Chen H, Nie S, Wang X, Chou H, Tan C, Fallahzad B, Ramanarayan H, Magnuson CW, Tutuc E, Yakobson BI, McCarty KF, Zhang YW, Kim P, Hone J, Colombo L, Ruoff RS (2013) The role of surface oxygen in the growth of large single-crystal graphene on copper. *Science* 342:720

29. Yamada T, Ishihara M, Kim J, Hasegawa M, Iijima S (2012) A roll-to-roll microwave plasma chemical vapor deposition process for the production of 294mm width graphene films at low temperature. *Carbon* 50:2615
30. Kobayashi T, Bando M, Kimura N, Shimizu K, Kadono K, Umezumi N, Miyahara K, Hayazaki S, Nagai S, Mizuguchi Y, Murakami Y, Hobarada D (2013) Production of a 100-m-long high-quality graphene transparent conductive film by roll-to-roll chemical vapor deposition and transfer process. *Appl Phys Lett* 102:23112
31. Dean CR, Young AF, Meric I, Lee C, Wang L, Sorgenfrei S, Watanabe K, Taniguchi T, Kim P, Shepard KL, Hone J (2010) Boron nitride substrates for high-quality graphene electronics. *Nat Nanotechnol* 5:722
32. Wang QH, Zadeh KK, Kis A, Coleman JN, Strano MS (2012) Electronics and optoelectronics of two-dimensional transition metal dichalcogenides. *Nat Nanotechnol* 7:699
33. Ge W, Kawahara K, Tsuji M, Ago H (2013) Large-scale synthesis of NbS₂ nanosheets with controlled orientation on graphene by ambient pressure CVD. *Nanoscale* 5:5773
34. Shi Y, Zhou W, Lu AY, Fang W, Lee YH, Hsu AL, Kim SM, Kim KK, Yang HY, Li LJ, Idrobo JC, Kong J (2012) van der Waals epitaxy of MoS₂ layers using graphene as growth templates. *Nano Lett* 12:2784
35. Yang W, Chen G, Shi Z, Liu CC, Zhang L, Xie G, Cheng M, Wang D, Yang R, Shi D, Watanabe K, Taniguchi T, Yao Y, Zhang Y, Zhang G (2013) Epitaxial growth of single-domain graphene on hexagonal boron nitride. *Nat Mater* 12:792
36. Ago H, Endo H, Solís Fernández P, Takizawa R, Ohta Y, Fujita Y, Yamamoto K, Tsuji M (2015) Controlled van der Waals epitaxy of monolayer MoS₂ triangular domains on graphene, submitted

Chapter 2

Graphene Laser Irradiation CVD Growth

Yasuhide Ohno, Kenzo Maehashi, and Kazuhiko Matsumoto

Abstract We have demonstrated a simple method of directly synthesizing graphene on dielectric surfaces using laser irradiation without a carbon source gas. The position of the graphene synthesis was precisely controlled. Moreover, channels were formed during graphene synthesis by scanning the laser beam across the substrate. The resulting device showed typical ambipolar transport behavior, which indicates that the channel consisted of graphene and that the device acted as a field-effect transistor (FET). Our laser irradiation technique does not require transfer processes and carbon source gases and is a promising method for graphene synthesis and fabricating graphene FETs.

Keywords Laser irradiation • Direct graphene growth • Simple fabrication process

2.1 Introduction

Graphene is a two-dimensional atom-thick crystal consisting of a honeycomb lattice of carbon atoms [1]. Owing to its outstanding mechanical, electrical, thermal, and optical properties, it is a particularly attractive material for future high-performance devices [2–5], such as flexible electronics, solar cells, high-sensitivity sensors, and transparent electrodes [4–6]. Recently, graphene has been fabricated by methods such as mechanical exfoliation, chemical exfoliation, chemical vapor deposition (CVD), and thermal decomposition of SiC [7–12].

Mechanical exfoliation using adhesive tape is the most suitable method for obtaining high-quality graphene. However, the method is inadequate for multiplex handheld chemical and biological sensors for home medical care because the position and size of the graphene cannot be controlled [13].

Y. Ohno (✉) • K. Matsumoto

Institute of Scientific and Industrial Research, Osaka University, Mihogaoka 8-1, Ibaraki, Osaka 567-0047, Japan

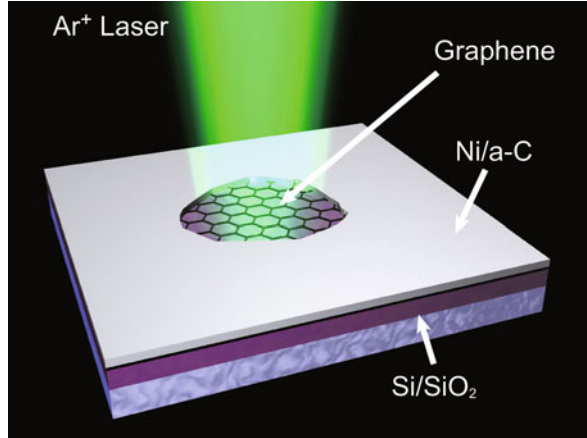
e-mail: ohno@sanken.osaka-u.ac.jp; k-matsumoto@sanken.osaka-u.ac.jp

K. Maehashi

Tokyo University of Agriculture and Technology, Tokyo, Japan

e-mail: maehashi@sanken.osaka-u.ac.jp

Fig. 2.1 Schematic of graphene synthesis by laser irradiation



In contrast, CVD can produce large amounts of high-quality graphene [5]. However, devices such as transparent electrodes or FETs need multistep processes that include growth at high temperatures in an electric furnace and transfer from metal layers to insulators [14]. In particular, the transfer process is complicated and the CVD graphene on insulators often contains cracks, wrinkles, and contaminants [15]. For these reasons, simple techniques for direct graphene synthesis on insulating substrates are required to make fabrication processes shorter and cheaper [16–18]. In this chapter, we report direct graphene synthesis on insulating substrates using laser irradiation (Fig. 2.1).

2.2 Experimental Procedure

An amorphous carbon (a-C) layer and a Ni layer sequentially deposited on a SiO₂/Si substrate were used as a carbon source and a catalyst, respectively. The Ni layer absorbed the laser energy and was heated locally. Therefore, the a-C was only dissolved in the Ni layer in the laser-irradiated area. The Ni layer retracted, indicating that the graphene was synthesized at the desired position on the SiO₂/Si substrates. Moreover, the technique allowed graphene FETs to be fabricated by scanning the laser beam across the substrate. The graphene-channel length and position could be precisely controlled because of the localized laser irradiation and the spot size of the beam. We also demonstrated the ambipolar characteristics of the graphene-channel devices.

A 1-nm-thick a-C carbon source layer and a 20-nm-thick Ni catalyst layer were sequentially deposited on a Si substrate with a thermally grown 300-nm-thick SiO₂ layer using an electron beam evaporator without exposure to ambient conditions. The graphene synthesis was carried out in a vacuum chamber at a pressure of 2.6 Pa. The heater was attached to the back of the substrates, and three different temperatures of 25, 200, and 400 °C were used during the laser irradiation.

A continuous wave Ar-ion laser with a wavelength of 514.5 nm was used to increase the temperature locally on the Ni layer. The substrate was locally irradiated with the laser for 1 min with a laser power density of $9 \text{ mW}/\mu\text{m}^2$. The laser-irradiated area was examined by optical microscopy and Raman spectroscopy (514.5 nm).

2.3 Results and Discussion

Figure 2.2a shows optical microscopy images of the laser-irradiated areas at substrate temperatures of 25, 200, and 400 °C, where the dark circular regions correspond to the laser-irradiated areas. The images show that the laser created holes, exposing the SiO_2/Si substrates under the Ni layer. Raman spectroscopy was measured for the laser-irradiated areas (Fig. 2.2b). The Raman intensities for the samples were normalized to those of the G bands. For comparison, a Raman spectrum for an as-deposited a-C layer with no Ni layer is shown in Fig. 2.2b, which contains broad bands at $1,100\text{--}1,700 \text{ cm}^{-1}$ [16, 17].

After laser irradiation at a substrate temperature of 25 °C, broad D and G bands and a small G' band were observed. This indicates that the Ni layer irradiated with the laser functioned as a catalyst and that the a-C layer was transformed into graphitic carbon. In the Raman spectrum for a substrate temperature of 200 °C, the D, G, and G' bands became narrower than those obtained at 25 °C. However, the intensity ratio of the G to D bands (I_G/I_D) was estimated to be 0.82, which is much smaller than that for conventional CVD or exfoliated graphene [9, 19]. Furthermore, the intensity ratio of the G' to G bands ($I_{G'}/I_G$) was estimated to be 0.20, indicating that graphite-like carbon or defective graphene was directly synthesized on the SiO_2/Si substrate.

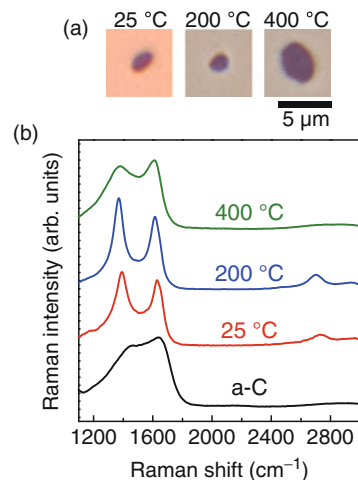
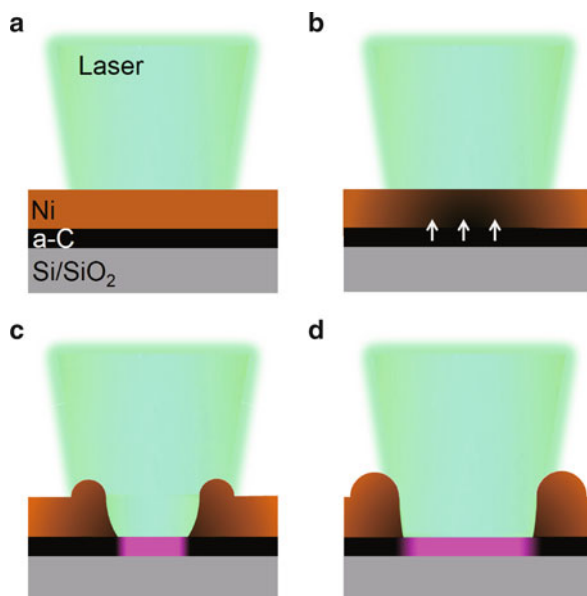


Fig. 2.2 (a) Optical images after laser irradiation at various substrate temperatures, and (b) Raman spectra of as-deposited a-C layer and samples irradiated with a laser at substrate temperatures of 25, 200, and 400 °C

Fig. 2.3 Schematic of graphene-synthesis mechanism. (a) Local annealing of the Ni layer by laser irradiation, (b) dissolution of a-C in the Ni layer, (c) aggregation and retraction of the Ni layer, and (d) direct graphene synthesis on a SiO₂ surface

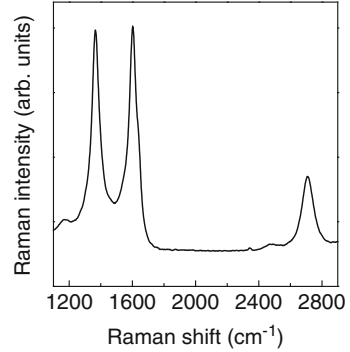


We propose the following mechanism of graphene synthesis by laser irradiation (Fig. 2.3). First, the laser is focused on the Ni layer (Fig. 2.3a). The irradiated region in the Ni layer is annealed, and then the a-C dissolves in the Ni layer (Fig. 2.3b). Because the center of the laser spot has the highest temperature, the Ni layer begins to retract at the center, which forms the holes. Simultaneously, the a-C atoms are segregated from the Ni layer and form graphene because the cooling rate is fast (Fig. 2.3c). As the irradiation time increases, the hole grows larger. Consequently, graphene layers are directly synthesized on the SiO₂ surface by laser irradiation (Fig. 2.3d).

At a substrate temperature of 25 °C, the Ni layer at the interface between the a-C and the Ni layer is not sufficiently annealed during laser irradiation. The Raman spectrum with broad D and G bands (Fig. 2.2b) suggests that some of the carbon is not dissolved in the Ni layer and that the graphitic carbon is formed on the residual a-C layer at a substrate temperature of 25 °C. The Raman spectrum obtained with a substrate temperature of 400 °C is very close to that of the a-C layer (Fig. 2.2b). This is because the size of the hole formed at 400 °C is the largest and is considered to be formed before sufficient amounts of carbon are dissolved in the Ni layer (Fig. 2.2a). Thus, a residual a-C layer appears on the SiO₂/Si substrate, and the Raman spectrum is similar to that of a-C (Fig. 2.2a).

Moreover, H₂ (5 sccm) was introduced into the vacuum chamber during laser irradiation at 9 mW/μm² for 1 min at the substrate temperature of 200 °C. Figure 2.4 shows a Raman spectrum after laser irradiation in H₂ atmosphere,

Fig. 2.4 Raman spectrum for a sample irradiated with a laser in H_2 atmosphere at a substrate temperature of 200°C



revealing that sharper peaks than that at 200°C in a vacuum (Fig. 2.2b) were obtained. The full width at half maximum (FWHM) of the G band was reduced from 97 to 66 cm^{-1} , and that of the G' band was reduced from 125 to 85 cm^{-1} . As a result, the FWHMs of the peaks were reduced by 35% , indicating that the quality of graphene was improved by introducing H_2 . This is probably because the naturally oxidized Ni was reduced by H_2 in the laser-irradiated area, enhancing the Ni-catalyzed reaction. In addition, I_G/I_D and $I_{G'}/I_G$ were estimated to be 1.02 and 0.34 , respectively. It has been reported that the values of $I_{G'}/I_G$ for single-, double-, and triple-layer graphene change to approximately 2 , 1 , and 0.25 , respectively [9]. These results indicate that several layers of graphene were synthesized by introducing H_2 . Since I_G/I_D was still small, the domain size of the graphene layers is considered to be small. However, the method allows precise control over the graphene position and needs no transfer process. Thus, the process is simple and useful for direct graphene synthesis on insulating layers. The sample structures and synthesis conditions must be optimized to obtain high-quality graphene.

Finally, graphene FETs were fabricated using the same graphene-synthesis processes, by scanning the laser beam across the substrate. Figure 2.5a shows a schematic image of the fabrication of a graphene FET. The SiO_2/Si substrate was moved precisely using a motorized stage to form the FET graphene channel. The laser-spot diameter and scan speed of the motorized stage were $2.5\text{ }\mu\text{m}$ and $3\text{ }\mu\text{m}/\text{min}$, respectively, and the substrate temperature of 200°C was used during the laser irradiation. Figure 2.5b shows an optical image of the sample, which shows that the patterned Ni layer was divided into two regions. These Ni regions were used as the source and drain electrodes. Thus, the simple laser-scanning process formed graphene and the device simultaneously. The transfer characteristics of the graphene FET were investigated. Figure 2.5c shows the drain current versus back-gate voltage. The device shows typical ambipolar transport behavior, which indicates that the channel consisted of graphene and that the device acted as an FET.

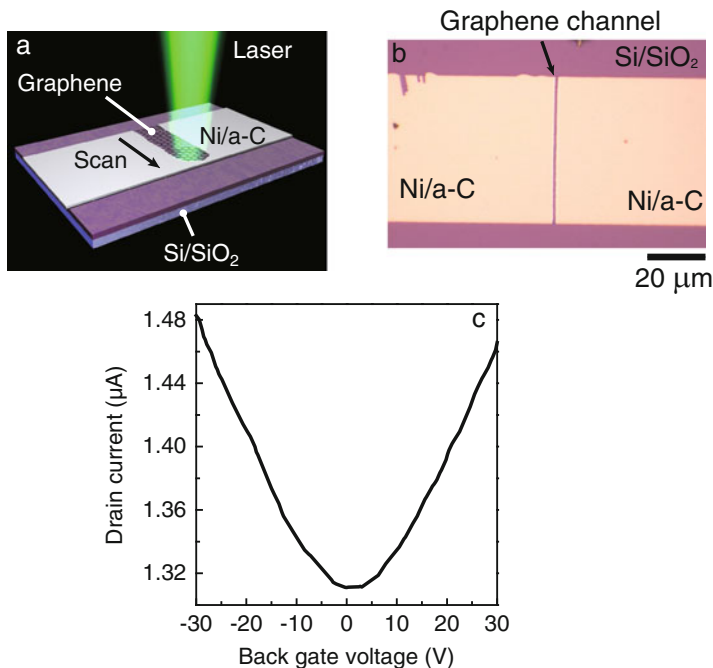


Fig. 2.5 (a) Schematic of graphene-channel formation by scanning the laser beam across the substrate, (b) optical image after graphene-channel formation by laser irradiation, and (c) transfer characteristics of the sample after scanning with the laser beam. The channel length and width were approximately 1.5 and 50 μm , respectively

2.4 Conclusion

We have achieved the direct laser synthesis of graphene on SiO₂ surfaces without using carbon source gases. An a-C layer was introduced between the Ni and SiO₂ layers. The G and G' bands were clearly observed in the Raman spectrum of the laser-irradiated area of the sample, which was attributed to the dissolution of the a-C in the Ni layer and the retraction of the Ni layer. Thus, the position of graphene synthesis was precisely controlled by the laser irradiation method. Moreover, the technique enabled the formation of a graphene channel by scanning the laser beam across the substrate. The electrical measurements revealed typical ambipolar characteristics, indicating that the device acted as an FET. Because the technique does not require carbon source gases and transfer processes, it is a simple and useful method for fabricating graphene FETs.

References

1. Geim AK, Novoselov KS (2007) The rise of graphene. *Nat Mater* 6:183–191
2. Balandin AA, Ghosh S, Bao W, Calizo I, Teweldebrhan D, Miao F, Lau CN (2008) Superior thermal conductivity of single-layer graphene. *Nano Lett* 8:902–907
3. Nair RR, Blake P, Grigorenko AN, Novoselov KS, Booth TJ, Stauber T, Peres NMR, Geim AK (2008) Fine structure constant defines visual transparency of graphene. *Science* 320:1308
4. Lin Y-M, Jenkins KA, Valdes-Garcia A, Small JP, Farmer DB, Avouris P (2009) Operation of graphene transistors at gigahertz frequencies. *Nano Lett* 9:422–426
5. Bae S, Kim H, Lee Y, Xu X, Park JS, Zheng Y, Balakrishnan J, Lei T, Kim HR, Song YI, Kim YJ, Kim KS, Ozyilmaz B, Ahn JH, Hong BH, Iijima S (2010) Roll-to-roll production of 30-inch graphene films for transparent electrodes. *Nat Nanotechnol* 5:574–578
6. Liao L, Lin YC, Bao M, Cheng R, Bai J, Liu Y, Qu Y, Wang KL, Huang Y, Duan X (2010) High-speed graphene transistors with a self-aligned nanowire gate. *Nature* 467:305–308
7. Novoselov KS, Geim AK, Morozov SV, Jiang D, Katsnelson MI, Grigorieva IV, Dubonos SV, Firsov AA (2005) Two-dimensional gas of massless Dirac fermions in graphene. *Nature* 438:197–200
8. Reina A, Jia X, Ho J, Nezich D, Son H, Bulovic V, Dresselhaus MS, Kong J (2009) Large area, few-layer graphene films on arbitrary substrates by chemical vapor deposition. *Nano Lett* 9:30–35
9. Li X, Cai W, An J, Kim S, Nah J, Yang D, Piner R, Velamakanni A, Jung I, Tutuc E, Banerjee SK, Colombo L, Ruoff RS (2009) Large-area synthesis of high-quality and uniform graphene films on copper foils. *Science* 324:1312–1314
10. Yu Q, Lian J, Siriponglert S, Li H, Chen YP, Pei S-S (2008) Graphene segregated on Ni surfaces and transferred to insulators. *Appl Phys Lett* 93:113103
11. Berger C, Song Z, Li X, Wu X, Brown N, Naud C, Mayou D, Li T, Hass J, Marchenkov AN, Conrad EH, First PN, de Heer WA (2006) Electronic confinement and coherence in patterned epitaxial graphene. *Science* 312:1191–1196
12. Li X, Cai W, Colombo L, Ruoff RS (2009) Evolution of graphene growth on Ni and Cu by carbon isotope labeling. *Nano Lett* 9:4268–4272
13. Zaifuddin NM, Okamoto S, Ikuta T, Ohno Y, Maehashi K, Miyake M, Greenwood P, Teo KBK, Matsumoto K (2013) pH sensor based on chemical-vapor-deposition-synthesized graphene transistor array. *Jpn J Appl Phys* 52:06GK04
14. Kim KS, Zhao Y, Jang H, Lee SY, Kim JM, Kim KS, Ahn JH, Kim P, Choi JY, Hong BH (2009) Large-scale pattern growth of graphene films for stretchable transparent electrodes. *Nature* 457:706–710
15. Xu K, Cao P, Heath JR (2009) Scanning tunneling microscopy characterization of the electrical properties of wrinkles in exfoliated graphene monolayers. *Nano Lett* 9:4446–4451
16. Gumi K, Ohno Y, Maehashi K, Inoue K, Matsumoto K (2012) Direct synthesis of graphene on SiO₂ substrates by transfer-free processes. *Jpn J Appl Phys* 51:06FD12
17. Zheng M, Takei K, Hsia B, Fang H, Zhang X, Ferralis N, Ko H, Chueh Y-L, Zhang Y, Maboudian R, Javey A (2010) Metal-catalyzed crystallization of amorphous carbon to graphene. *Appl Phys Lett* 96:063110
18. Koshida K, Gumi K, Ohno Y, Maehashi K, Inoue K, Matsumoto K (2013) Synthesis on silicon oxide surfaces using laser irradiation. *Appl Phys Express* 6:105101
19. Ferrari AC, Meyer JC, Scardaci V, Casiraghi C, Lazzeri M, Mauri F, Piscanec S, Jiang D, Novoselov KS, Roth S, Geim AK (2006) Raman spectrum of graphene and graphene layers. *Phys Rev Lett* 97:187401

Chapter 3

Graphene Direct Growth on Si/SiO₂ Substrates

Yasuhide Ohno, Kenzo Maehashi, and Kazuhiko Matsumoto

Abstract We have demonstrated direct synthesis of graphene on SiO₂ substrates using transfer-free processes. An amorphous layer was sandwiched between a Ni layer and a SiO₂/Si substrate, and then the sample was annealed under the ambient of H₂ and Ar. The measurements using scanning electron microscopy and Raman spectroscopy reveal that Ni islands were formed and that G' band was clearly observed at the region between Ni islands. From the intensity ratio of G band to G' band, multilayer graphene was synthesized owing to retraction of the Ni layer during annealing the sample.

Keywords Graphene direct growth • Anneal • No transfer process

3.1 Introduction

Graphene has ideal two-dimensional structures formed by monolayer of sp²-bonded honeycomb lattice, which shows excellent electrical, mechanical, and chemical properties, such as high carrier mobility, low optical absorption, and excellent thermal strength [1]. Then, graphene is highly expected to be a promising electronic material in the next-generation electronics: field-effect transistors (FETs), high-frequency electronic devices, transparent electrodes, highly sensitive sensors, and so on.

Since their electrical properties are very sensitive for modulation of the surface potentials in graphene channel, ions or proteins were expected to be effectively detected with high sensitivity. In these devices, the single-layer graphene used as a channel in a graphene FET was obtained by mechanical exfoliation using an adhesive tape [2]. The method is suitable to obtain high-quality graphene; however, it is impossible to control size or location of graphene.

Y. Ohno (✉) • K. Matsumoto

Institute of Scientific and Industrial Research, Osaka University, Mihogaoka 8-1, Ibaraki, Osaka 567-0047, Japan

e-mail: ohno@sanken.osaka-u.ac.jp; k-matsumoto@sanken.osaka-u.ac.jp

K. Maehashi

Tokyo University of Agriculture and Technology, Tokyo, Japan

e-mail: maehashi@sanken.osaka-u.ac.jp

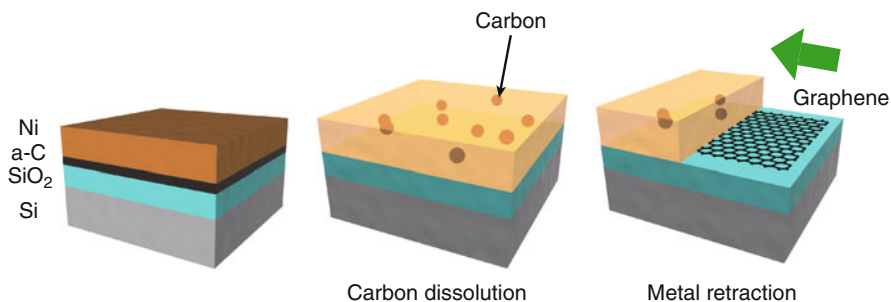


Fig. 3.1 Schematic of transfer-free process to directly synthesize graphene on SiO_2 substrates

Several synthesis methods on graphene have been carried out by different techniques, such as eliminating Si from the surface of single crystal SiC [3, 4], chemically reduced graphene oxide [5], or chemical vapor deposition (CVD) method [6–8]. In particular, CVD on metal substrates has been intensively investigated as an attractive method to synthesize graphene. Nickel and copper are commonly used as metal substrates [9–12]. For growth on Ni substrates, graphene is synthesized at cooling stages. On the other hand, graphene grows on Cu substrates by surface adsorptions of C atoms. For electronic applications such as sensors, existing graphene layer grown using CVD needs a transfer process from a metal substrate to insulating substrates. Recently, transfer processes using various different methods are performed. However, the transfer processes are relatively complicated, and cracks, wrinkles, and contaminations were often observed on graphene surfaces [13]. Therefore, techniques of graphene synthesis directly on insulators have been desired to realize practical devices. Recently, nanographene was directly formed on MgO nanocrystal powder [14]. However, this method might not be suitable for the integration of graphene devices with Si technology.

In this section, we propose a simple method to synthesize graphene directly on insulators by annealing amorphous carbon (a-C) with a metal catalyst. Figure 3.1 shows a schematic of a transfer-free process to directly synthesize graphene on SiO_2 substrates. An a-C layer is sandwiched between a Ni layer and a SiO_2/Si substrate. After annealing the sample, graphene layers will be synthesized on SiO_2 substrates owing to retraction of the Ni layer, as shown in Fig. 3.1.

3.2 Experimental Procedure

An a-C layer was deposited by an electron-beam vacuum evaporator on a Si substrate covered with a thermally grown 280-nm-thick SiO_2 layer. Subsequently, a Ni layer also was deposited by an electron-beam vacuum evaporator, as shown in Fig. 3.1. In this section, we utilized three kinds of samples: Ni layer (10 nm)/a-C (2 nm), Ni layer (30 nm)/a-C (2 nm), and Ni layer (30 nm)/a-C (5 nm). For

comparison, an a-C layer of 2 nm without Ni layer was used. These samples were set into an electrical furnace and then thermally annealed at 750 °C for 10 min in H₂/Ar atmosphere with the ambient of H₂ at 200 sccm and Ar at 100 sccm. After annealing, the samples were investigated by optical microscopy, scanning electron microscopy (SEM), and Raman spectroscopy excited by a He–Ne laser operating at 632.8 nm.

3.3 Results and Discussion

First of all, to investigate effect of Ni layer, only 2-nm-thick a-C layer was deposited on a SiO₂/Si substrate and was annealed at 750 °C for 10 min under the ambient of H₂ and Ar. No change in the surface morphology was obtained after annealing. Figure 3.2a, b show Raman spectra before and after annealing the sample, respectively. As shown in Fig. 3.2a, broad bands (1,100–1,700 cm⁻¹) were observed for as-deposited a-C layer, which is consistent with the previous reported Raman spectrum [14]. After annealing the as-deposited a-C layer at 750 °C, in the Raman spectrum, the peaks of broad D and G bands were obtained. However, no peak of G' band was observed, as shown in Fig. 3.2b.

Next, 2-nm-thick a-C layer was sandwiched between 10-nm-thick Ni layer and a SiO₂/Si substrate. After annealing the sample at 750 °C for 10 min under the ambient of H₂ and Ar, the surface morphology was changed as shown in Fig. 3.3a, b, which correspond to optical microscopy and SEM images, respectively. The microscopy image reveals that islands were observed, whose size and density were estimated to be 100 nm~1 μm and 400,000/mm², respectively. The Ni layer can be easily migrated, and the islands with high density were formed by thermal diffusion of Ni at high temperature because the thickness of the Ni layer was 10 nm. In addition, Raman characterization was also investigated for the sample. At Ni island region, no peaks were obtained. On the other hand, at the region

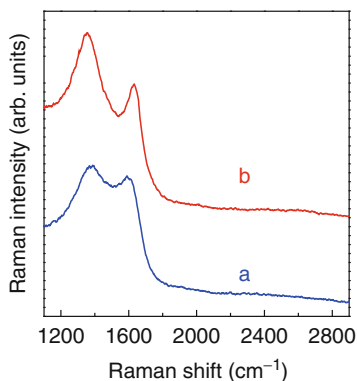
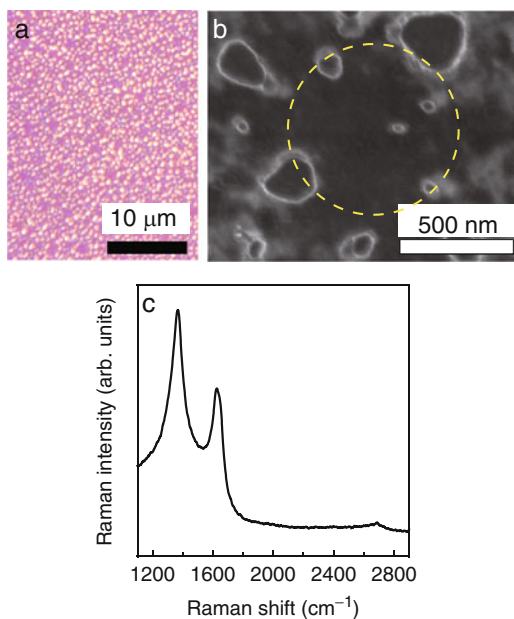


Fig. 3.2 Raman spectra for the sample with only 2-nm-thick a-C layer deposited on SiO₂/Si substrate *a* before and *b* after annealing

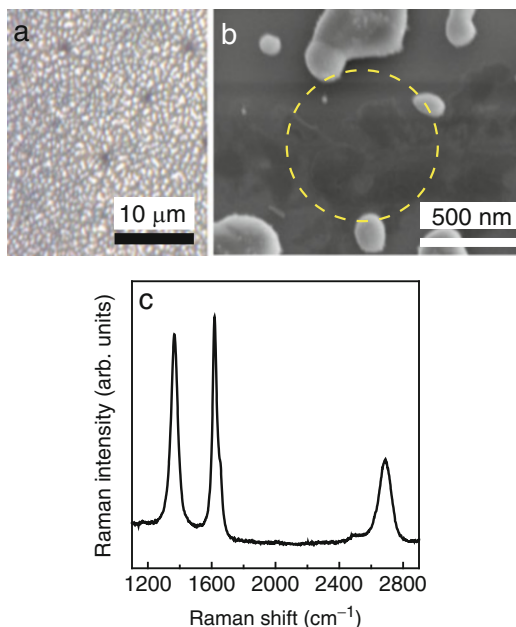
Fig. 3.3 (a) Optical microscopy and (b) SEM images and (c) Raman spectrum after annealing the sample with Ni layer (10 nm) on a-C layer (2 nm)



between Ni islands shown as a dashed line circle in Fig. 3.3b, D and G bands were obtained, whose widths were narrower than that of 2-nm-thick a-C layer shown in Fig. 3.2b. Moreover, a small G' band appeared. These results indicate synthesis of graphitic carbon. Thus, Ni layer could work as a catalyst and could play a role in the graphitization of a-C. However, the intensity ratio (I_D/I_G) of D band to G band was estimated to be 1.6, which is much larger than that for conventional CVD growth of graphene [7]. I_D/I_G is proportional to the amount of structural defects and inversely proportional to the domain size in graphitic materials [15]. Therefore, graphitic-like materials were considered to be synthesized after annealing the sample of Ni layer (10 nm) on a-C layer (2 nm). At high temperature, a-C will be dissolved into Ni layer [11]. For a-C layer of 2 nm with Ni layer of 10 nm, the Ni layer was so thin that Ni can easily migrate and form islands. As a result, before all a-C is taken up into the Ni layer, retraction of Ni layer may occur and graphitic carbon is considered to be synthesized on the residual a-C layer. Thus, Raman spectrum in Fig. 3.3c was obtained.

To improve the graphitization of a-C, a-C layer (2 nm) with a thicker Ni layer (30 nm) was utilized, which was investigated by microscopes and Raman measurements. After annealing at 750 °C for 10 min under the ambient of H₂ and Ar, the surface morphology with high-density Ni islands was obtained as shown in Fig. 3.4a, b, which was similar to the surface morphology of the sample of Ni layer (10 nm) on a-C layer (2 nm) shown in Fig. 3.3a, b. In addition, as shown in Fig. 3.4c, Raman spectroscopy was investigated at the uncovered region between Ni islands shown as a dashed line circle in Fig. 3.4b. The measurement reveals that the peak widths of D and G band peaks became narrower than those of the

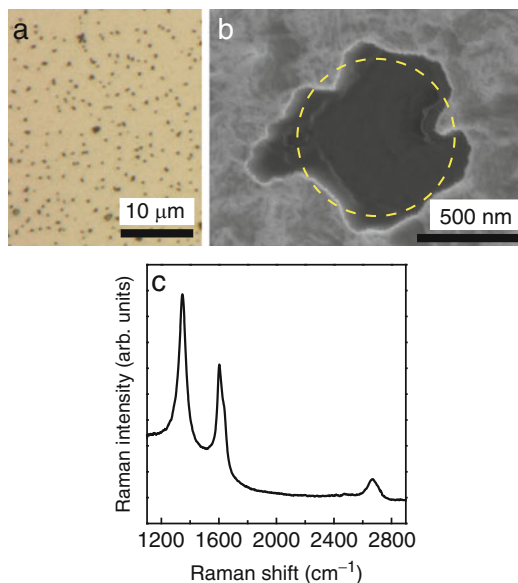
Fig. 3.4 (a) Optical microscopy and (b) SEM images and (c) Raman spectrum after annealing the sample with Ni layer (30 nm) on a-C layer (2 nm)



sample with 10-nm-thick Ni layer and that I_D/I_G was estimated to be 0.85. Thus, the quality of graphitized carbon was improved. In addition, a G' band peak, a signal of sp^2 -hybridized carbon, was clearly observed. The intensity ratio ($I_{G'}/I_G$) of G' band to G band was estimated to be 0.38. It was reported that the $I_{G'}/I_G$ for single, double, and triple layer graphene was changed to be approximately 2, 1, and 0.25, respectively [16]. The results indicate that more than triple layer graphene was synthesized. However, I_D/I_G was still high, resulting from formation of graphene with small domain size. The sample had a thicker Ni layer of 30 nm. Thus, all a-C can be dissolved into the Ni layer at high temperature and then Ni/SiO₂ interface can be formed. Subsequently, when the Ni layer formed Ni islands, multilayer graphene was considered to be synthesized directly on SiO₂ surfaces. For this reason, the sharper D and G band peaks and the clear G' peak were observed, as shown in Fig. 3.4c.

Finally, relatively thicker a-C layer of 5 nm with Ni layer of 30 nm was annealed at 750 °C for 10 min under the ambient of H₂ and Ar. Figure 3.5a, b show optical microscopy and SEM images after annealed, respectively, revealing that pits with high density were observed. As compared to the surface morphology of the sample of Ni layer (30 nm) on a-C layer (2 nm), diffusion of Ni layer was considered to be suppressed. Raman spectroscopy was also measured at the region of a pit, as shown in Fig. 3.5c, revealing that slightly broad G and D bands were obtained and small G' band appeared. Since relatively thicker a-C layer of 5 nm was used, all a-C may not be taken up into the Ni layer of 30 nm at 750 °C for 10 min. As a result, some a-C can exist at the interface between the Ni layer and the SiO₂ surface, resulting in

Fig. 3.5 (a) Optical microscopy and (b) SEM images and (c) Raman spectrum after annealing the sample with Ni layer (30 nm) on a-C layer (5 nm)



the suppression of Ni island formation, as shown in Fig. 3.5a, b. After retraction of some Ni layer, graphitic carbon is considered to be synthesized on the residual a-C layer. Thus, as shown in Fig. 3.5c, the similar Raman spectrum was observed to that of the a-C layer of 2 nm with Ni layer of 10 nm.

In this section, multilayer graphene was synthesized for the sample with Ni layer (30 nm)/a-C layer (2 nm) after annealed at 750 °C for 10 min. For application of sensors, however, single-layer graphene with high quality is necessary to obtain high sensitivity. For this reason, synthesis of monolayer graphene is required. Graphene growth parameters will be optimized by precisely controlling thickness of Ni and a-C layer, annealing temperature, and cooling rate after annealing.

3.4 Conclusion

In this section, we have proposed a simple approach for synthesizing graphene directly on SiO₂ substrates using transfer-free processes. An a-C layer was deposited on a SiO₂/Si substrate, followed by Ni layer deposition, and then the sample was annealed under the ambient of H₂ and Ar. For the Ni layer (30 nm)/a-C (2 nm), island formation of Ni layer and G' band in Raman spectrum were clearly observed. During annealing at high temperature, the a-C was taken up into the Ni layer and then graphene was synthesized directly on SiO₂ surfaces owing to retraction of the Ni layer. From the intensity ratio of G band to 2D band, multilayer graphene was synthesized. By optimizing growth parameters, this method will be useful for fabrication of electronic devices.

References

1. Geim AK, Novoselov KS (2007) The rise of graphene. *Nat Mater* 6:183–191
2. Novoselov KS, Jiang D, Schedin F, Booth TJ, Khotkevich VV, Morozov SV, Geim AK (2005) Two-dimensional atomic crystals. *Proc Natl Acad Sci U S A* 102:10451–10453
3. Berger C, Song Z, Li X, Wu X, Brown N, Naud C, Mayou D, Li T, Hass J, Marchenkov AN, Conrad EH, First PN, de Heer WA (2006) Electronic confinement and coherence in patterned epitaxial graphene. *Science* 312:1191–1196
4. Ohta T, Bostwick A, Seyller T, Horn K, Rotenberg E (2006) Controlling the electronic structure of bilayer graphene. *Science* 313:951–954
5. Navarro CG, Weitz RT, Bittner AM, Scolari M, Mews A, Burghard M, Kern K (2007) Electronic transport properties of individual chemically reduced graphene oxide sheets. *Nano Lett* 7:3499–3503
6. Kwon SY, Ciobanu CV, Petrova V, Shenoy VB, Bareño J, Gambin V, Petrov I, Kodambaka S (2009) Growth of semiconducting graphene on palladium. *Nano Lett* 9:3985–3990
7. Kim KS, Zhao Y, Jang H, Lee SY, Kim JM, Kim KS, Ahn JH, Kim P, Choi JY, Hong BH (2009) Large-scale pattern growth of graphene films for stretchable transparent electrodes. *Nature* 457:706–710
8. Ago H, Ito Y, Mizuta N, Yoshida K, Hu B, Orofeo CM, Tsuji M, Ikeda K, Mizuno S (2010) Epitaxial chemical vapor deposition growth of single-layer graphene over cobalt film crystallized on sapphire. *ACS Nano* 4:7407–7414
9. Reina A, Jia X, Ho J, Nezich D, Son H, Bulovic V, Dresselhaus MS, Kong J (2009) Large area, few-layer graphene films on arbitrary substrates by chemical vapor deposition. *Nano Lett* 9:30–35
10. Li X, Cai W, Colombo L, Ruoff RS (2009) Evolution of graphene growth on Ni and Cu by carbon isotope labeling. *Nano Lett* 9:4268–4272
11. Yu Q, Lian J, Siriponglert S, Li H, Chen YP, Pei SS (2008) Graphene segregated on Ni surfaces and transferred to insulators. *Appl Phys Lett* 93:113103
12. Gao L, Guest JR, Guisinger NP (2010) Epitaxial graphene on Cu(111). *Nano Lett* 10:3512–3516
13. Xu K, Cao P, Heath JR (2009) Scanning tunneling microscopy characterization of the electrical properties of wrinkles in exfoliated graphene monolayers. *Nano Lett* 9:4446–4451
14. Zheng M, Takei K, Hsia B, Fang H, Zhang X, Ferralis N, Ko H, Chueh YL, Zhang Y, Maboudian R, Javey A (2010) Metal-catalyzed crystallization of amorphous carbon to graphene. *Appl Phys Lett* 96:063110
15. Dresselhaus MS, Jorio A, Hofmann M, Dresselhaus G, Saito R (2010) Perspectives on carbon nanotubes and graphene Raman spectroscopy. *Nano Lett* 10:751–758
16. Li X, Cai W, An J, Kim S, Nah J, Yang D, Piner R, Velamakanni A, Jung I, Tutuc E, Banerjee SK, Colombo L, Ruoff RS (2009) Large-area synthesis of high-quality and uniform graphene films on copper foils. *Science* 324:1312–1314

Chapter 4

Direct Growth of Graphene and Graphene Nanoribbon on an Insulating Substrate by Rapid-Heating Plasma CVD

Toshiaki Kato, Rikizo Hatakeyama, and Toshiro Kaneko

Abstract A transfer-free method for growing 2D graphene sheets directly on a SiO₂ substrate has been realized by rapid-heating plasma chemical vapor deposition (RH-PCVD). Using this method, high-quality single-layer graphene sheets with hexagonal domain can be selectively grown between a Ni film and a SiO₂ substrate. Systematic investigations reveal that the relatively thin Ni layer, rapid heating, and plasma CVD are critical to the success of this unique method of graphene growth. By applying this technique, graphene nanoribbon, 1D graphene structure, has also been directly grown on a SiO₂ substrate. Precise control of the site and alignment of narrow (~23 nm) graphene nanoribbons can be realized by directly converting a nickel nanobar into a graphene nanoribbon using rapid-heating plasma CVD. The nanoribbons grow directly between the source and drain electrodes of a field-effect transistor without any posttreatment and exhibit a clear transport gap (58.5 meV) and a high on/off ratio (>10⁴). The process is scalable and completely compatible with existing semiconductor processes and is expected to allow the integration of graphene nanoribbons with silicon technology.

Keywords Graphene nanoribbon • Direct growth • Integration • Plasma CVD

Graphene is a monolayer carbon sheet including high carrier mobility, flexibility, and high optical transmittance. These properties are advantageous if graphene is to be used as a component in electrical devices such as field-effect transistors, solar cells, and various gas and chemical sensors. Chemical vapor deposition (CVD) is one of the most promising methods of growing graphene, which can produce large and relatively high-quality graphene sheets. A graphene layer on an insulating layer, especially on an insulating SiO₂ substrate, is an important structural arrangement used in the fabrication of graphene-based electrical devices. Currently, graphene layers on SiO₂ substrates are fabricated by the following process. First, graphene

T. Kato (✉) • R. Hatakeyama • T. Kaneko
Department of Electronic Engineering, Tohoku University, Sendai 980-8579, Japan
e-mail: kato12@ecei.tohoku.ac.jp

is grown on Ni, Cu, or Co surfaces (foil or deposited films on a substrate). These metal surfaces are necessary for the growth of graphene as they decompose hydrocarbon gases and promote the nucleation of graphene. The graphene layer is then transferred to a SiO₂ substrate using polymer capping and chemical etching techniques. This process can fabricate relatively large-scale graphene sheets on an insulating substrate. However, it is difficult to transfer specific and fine graphene structures, such as graphene nanoribbons or nanoscale patterned graphene, to specific points on a device. This precise placement of graphene is important when fabricating many widely used silicon-based electrical devices. The direct growth of graphene on an insulating substrate is an alternative approach to the above method. It is a challenging method, however, and only a few studies about the direct growth approach have so far been reported [1–3].

In this section, we introduce our recent progresses for the direct growth of graphene using rapid-heating plasma chemical vapor deposition (RH-PCVD). The graphene layer can be made to grow along the interface of the Ni layer and the SiO₂ substrate instead of on top of the Ni layer. The direct fabrication method is completed by removing the Ni layer using a chemical etching process, leaving large area and high-quality single-layer graphene sheets on a SiO₂ substrate [4]. In addition to the usual 2D-graphene sheet, graphene nanoribbon, 1D structure of graphene, can be also directly grown on a SiO₂ substrate by combining RH-PCVD and unique catalytic reaction of Ni nanobar. Since growth site and alignment of graphene nanoribbon are decided by the initial Ni nanobar structure, it is possible to highly integrate graphene nanoribbon devices by our developed novel method [5].

4.1 Direct Growth of 2D Graphene Sheet

Figure 4.1a–d illustrates the basic concept of our approach for growing graphene directly on an insulating substrate. A Ni film was deposited on a SiO₂ (300 nm)/Si by vacuum evaporation (Fig. 4.1a). The graphene growth was realized using a homemade plasma CVD system [6–10] with a mixture of methane and hydrogen gases. The substrate was immediately transferred from outside the electrical furnace to the furnace center, and the substrate temperature increased to the required temperature for growth (typically 600–975 °C) within 1 min. After heating the substrate, radio-frequency power (RF; 13.56 MHz) was supplied to the coils outside of a quartz tube to generate a plasma (Fig. 4.1b). The substrate temperature was immediately decreased after completing the plasma CVD process (Fig. 4.1c). During the cooling process, the graphene layer could be preferentially grown along the interface between the Ni film and SiO₂ substrate. Finally, the deposited Ni film was removed using a conventional chemical etching technique with FeCl₃ or HCl solution (Fig. 4.1d).

Scanning electron microscope (SEM) observations and Raman mapping measurements were carried out for the fabricated materials *before* the Ni film was removed. The detailed growth conditions are as follows: methane to hydrogen

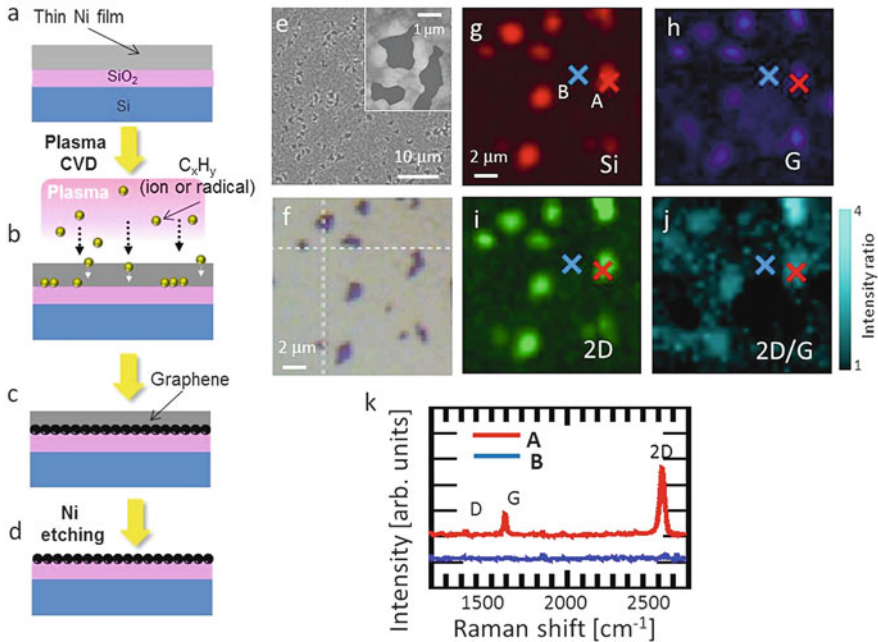


Fig. 4.1 (a–d) A schematic illustration of the basic approach for our method for the direct growth of graphene on a SiO₂ surface. (a) A thin Ni film is deposited on a SiO₂/Si substrate. (b) Plasma CVD is performed. (c) Carbon atoms diffuse in the Ni film and graphene is preferentially grown along the interface between the Ni and SiO₂ layers. (d) Graphene on a SiO₂/Si substrate is realized by removing the Ni film using a chemical etching technique. (e) SEM and (f) optical microscope images of the Ni surface after RH-PCVD. *Inset* in (e) shows a typical high-magnification SEM image of hole-like structures. Integrated Raman intensity maps of the Ni surface after RH-PCVD of the (g) Si-peak, (h) G-peak, (i) 2D-peak, and (j) ratio of the 2D- to G-peak intensity. (k) The raw Raman scattering spectra taken at positions A and B indicated in (g)

mixture ratio of 9:1; substrate temperature, T_{sub} , of 950 °C; growth time, t_{g} , of 30 s; radio-frequency power, P_{RF} , of 110 W; and a Ni film thickness, T_{Ni} , of 55 nm. Hole-like structures were observed over the entire surface of the Ni film (Fig. 4.1e). Figure 4.1f shows an optical microscope image of the Ni film surface. Integrated Raman intensity maps of the Si-peak (512–540 cm⁻¹), the G-peak (1,544–1,626 cm⁻¹), and the 2D-peak (2,577–2,700 cm⁻¹) are shown in Fig. 4.1g–i, respectively. The intensity ratio of the 2D-peak to the G-peak is shown in Fig. 4.1j. It should be noted that Fig. 4.1f–j is described at the same scale and position. Because the strong Si-peak appears only at the hole-like structures, the Ni film should be partially evaporated and the SiO₂ surface appears at the hole-like structures (Fig. 4.1g). The G-peak and 2D-peak are detected only at the hole-like structures (Fig. 4.1h, i), and the intensity of the 2D-peak is much higher than that of the G-peak at the hole-like structures (Fig. 4.1j). This is also confirmed with the raw Raman scattering spectra taken at positions A and B, which describe the hole-like

structures and the top of the flat Ni film, respectively (Fig. 4.1k). The spectrum measured at A (Fig. 4.1k) shows a low D-peak, sharp G-peak, and a high and sharp 2D-peak, which has a high 2D/G intensity ratio (~ 3). These features are consistent with that of a high-quality single-layer graphene sheet. There are three possibilities to realize this unique graphene growth. (1) The hole-like structures of Ni are formed before the graphene growth. (2) The hole-like structure formation and graphene growth happen together. (3) The hole-like structures are formed after the growth of graphene. Based on our systematic investigation, it was found that graphene was not grown when hole-like structures were preformed before the growth. In general, it is known that graphene growth happens during the cooling process. When we follow this model, the formation of Ni hole-like structures after the graphene growth should be difficult because the temperature of the substrate becomes low due to the cooling process. By judging from these reasons, it can be supposed that the hole-like structure formation and graphene growth happen together. The correlation with carbon concentration in Ni, substrate temperature, and melting point of Ni might be the key factors to explain the unique graphene growth. Further study is required to clarify the reason why this unique reaction happens in our system.

After removing the Ni film using a chemical etching process, interestingly, it was found that a high-quality graphene layer was also grown along the interface between the Ni film and the SiO₂ substrate. At the initial growth stage, clear hexagonal domains of graphene were observed (Fig. 4.2a–g). The average hexagonal domain size is about 10–20 μm . Although hexagonal domain growth of graphene has been reported by several groups recently, the growth was limited only on the metal substrates. This is the first result realizing the hexagonal domain growth of graphene directly on the SiO₂ substrate. This hexagonal domain growth indicates the quality of graphene grown with our established method should be relatively high, which is consistent with the low D-peak Raman scattering spectrum shown in Fig. 4.1k. By adjusting the growth conditions, the centimeter-order large-scale graphene layer was also uniformly grown on the SiO₂ substrate (Fig. 4.2h–m), which was confirmed by optical microscopy (Fig. 4.2h), SEM (Fig. 4.2i), integrated Raman intensity mapping of the 2D/G intensity ratio (Fig. 4.2j), atomic force microscopy (AFM) (Fig. 4.2k), transmission electron microscopy (TEM) (Fig. 4.2l), and low Raman scattering spectra randomly taken at the same area shown in Fig. 4.2j (Fig. 4.2m). The continuous dark lines were observed with 0.34 nm space each by TEM observation (Fig. 4.2l). This indicates that the structure of graphene grown by our method is not the stack of the small islands but the continuous one few layer sheets.

To address the mechanism of the growth of graphene along the interface between the Ni and SiO₂ layers, the time evolution of the graphene growth was systematically investigated as a function of initial thickness of the Ni layer, T_{Ni} . When T_{Ni} was small (*e.g.*, 25 nm), the Ni film was easily evaporated and formed nano islands. On the other hand, if the Ni film was relatively thick (*e.g.*, $T_{\text{Ni}} = 85$ nm), the growth between the Ni and SiO₂ layers was initiated after a long period of RH-PCVD (*e.g.*, 20 min). At a suitable thickness ($T_{\text{Ni}} = 55$ nm), hole-like structures were formed after a relatively short growth time (~ 3 min) and graphene was selectively grown

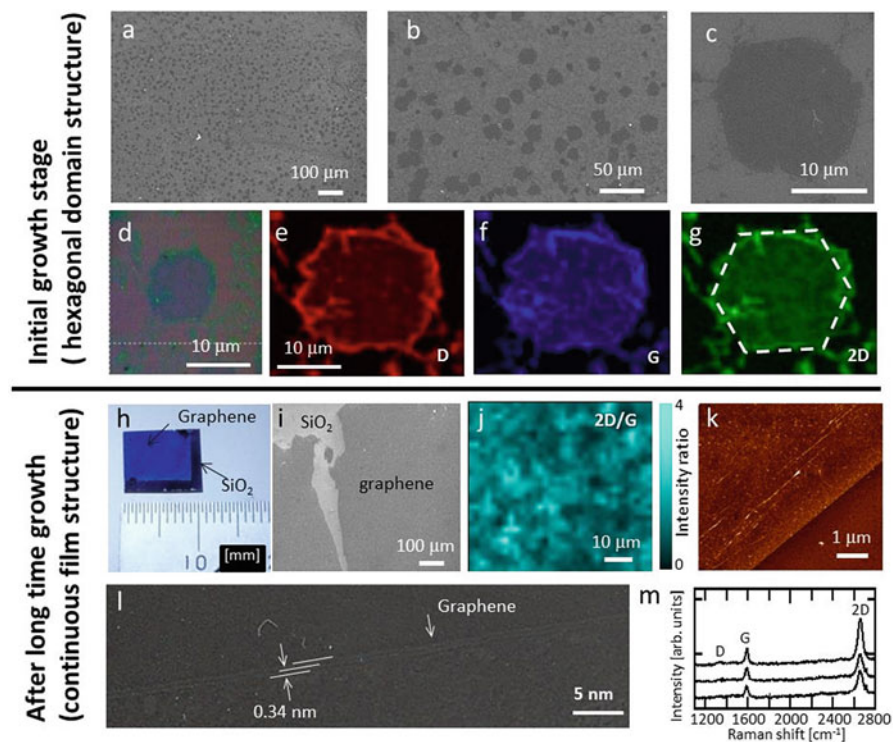


Fig. 4.2 (a–g) Hexagonal domain of graphene directly grown on the SiO₂ substrate. (a) Low-, (b) middle-, and (c) high-magnification SEM images of graphene with hexagonal domain structures. (d) An optical microscope and integrated Raman intensity maps of (e) D-peak, (f) G-peak, (g) 2D-peak of hexagonal domain graphene. (h–m) Uniform graphene in large scale directly grown on the SiO₂ substrate. (h) An optical image, (i) a SEM image, (j) an integrated Raman intensity map of the ratio of the 2D-/G-peak intensity, (k) an AFM image, (l) a TEM image, and (m) typical raw Raman scattering spectra of graphene directly grown on the SiO₂ substrate in large scale

at the interface between the Ni and SiO₂ layers. When the growth time was longer than 5 min, growth occurs on the top layer and at the interface between the layers, and the initial Ni film was converted to nanoislands after a growth period of 20 min, which was similar to the thin Ni layer case (25 nm) where the Ni nanoislands could not be removed even after chemical etching because the graphitic layers covered the Ni nanoislands.

From these experimental results, it is conjectured that the correlation with the evaporation rate of the Ni film (E_{Ni}), the thickness of the film (T_{Ni}), and the diffusion kinetics of the carbon atoms in the Ni film should be important factors for the selective growth of graphene at the interface between the Ni and SiO₂ layers. The following three conditions should be satisfied to realize the selective growth of graphene at the Ni and SiO₂ interface. Here, we describe the carbon density in the Ni film at a distance x from the top of the Ni surface after a growth time

t is $C(x,t)$. The Ni surface is always $x=0$ during the growth. First, the Ni film structure must be maintained during the growth process, *i.e.*, $T_{\text{Ni}} \gg E_{\text{Ni}}t$, where t denotes the growth time. Second, the carbon density at the interface between the Ni and SiO₂ layers ($x=l$) after the growth, $C(l,t)$, must be higher than the threshold density to form graphene, C_{th} , *i.e.*, $C(l,t) > C_{\text{th}}$, $l = T_{\text{Ni}} - E_{\text{Ni}}t$. Third, the carbon density on the surface of the Ni layer ($x=0$) after the growth, $C(0,t)$, must be lower than C_{th} , *i.e.*, $C(0,t) < C_{\text{th}}$. The first condition can be satisfied by adjusting the initial Ni film thickness and the growth time. $C(x,t)$ is given by solving the one-dimensional diffusion equation ($\partial C(x,t)/\partial t = D\nabla^2 C(x,t)$). This solution is $C(x,t) \propto \left(1/\sqrt{4\pi Dt}\right) \exp(-x^2/4Dt)$, where D is a diffusion coefficient. At a specific growth time t_1 , $C(0,t_1) \propto (1/\sqrt{4\pi Dt_1})$ and $C(l,t_1) \propto (1/\sqrt{4\pi Dt_1}) \exp(-l^2/4Dt_1)$, thus $C(0,t_1) > C(l,t_1)$. This indicates that the carbon density on the top of the Ni film is always higher than that at the interface between the Ni and SiO₂ layers, and therefore it is impossible to satisfy the second and third conditions at the same time. In this model, however, it is assumed that the diffusion of carbons starts from $x=0$, *i.e.*, the top of the Ni layer, where the hydrocarbon materials are supplied. This is not accurate for plasma CVD. Plasma involves a large variety of high-energy hydrocarbon ions attacking the Ni surface, and some of these are high enough in energy to penetrate the surface of the Ni film to a certain depth. The penetration of high-energy ions into a solid phase is well-known phenomena as an ion implantation in current Si-based industrial fields. Thus, the position of the highest carbon density in the Ni film is not on the surface but inside the Ni layer. In this case, the diffusion starts from not $x=0$ but $x=l_c$, where l_c is the depth to which hydrocarbons penetrate the Ni surface. If $l_c \gg T_{\text{Ni}}/2$, $C(l,t)$ approaches C_{th} faster than $C(0,t)$, and graphene can be preferentially grown only along the interface between the Ni and SiO₂ layers (Fig. 4.3). It should be mentioned that what we want to focus on in this model is the growth site (top layer of Ni or interlayer between Ni and SiO₂) of graphene. Based on the systematic investigations, it was found that the growth site of graphene was mainly decided by not the temperature but the type of CVD (thermal or plasma), *i.e.*, the selective interlayer growth cannot be realized in any temperature range when we use thermal CVD in our system, and the selective interlayer growth happened only when plasma was generated during the growth. Thus, we do not consider the effects of temperature in this model for simplification. For the construction of further accurate growth model of graphene, it should be necessary to consider the effects of temperature on the growth of graphene.

Another effect of plasma should be a decrease of the Ni layer evaporation rate, E_{Ni} . We also attempted to grow graphene with the same experimental setup except that we used thermal CVD instead of RH-PCVD. However, the Ni film was rapidly evaporated even if the Ni film was 55 nm thick, and graphene growth was not realized. Because the melting temperature of the Ni-C material increases with an increase in the concentration of C, E_{Ni} should also depend on the hydrocarbon flux supplied to the Ni, *i.e.*, Γ_c . In particular, the Ni evaporation rate should decrease with an increase in the supplied hydrocarbon flux. In the case of thermal CVD, Γ_c is

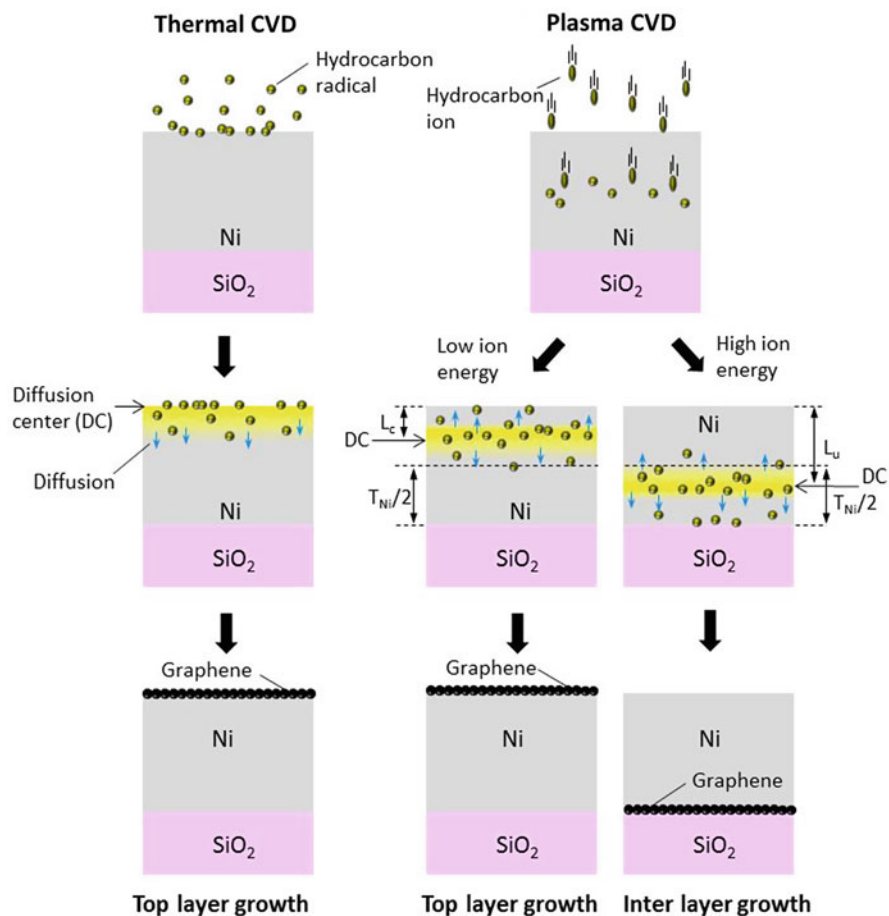


Fig. 4.3 Models for top layer and interlayer growth of graphene with thermal CVD and plasma CVD

mainly dictated by the hydrocarbon gas pressure, whereas Γ_c in plasma CVD should be much higher due to the decomposition of source gases resulting from impacts with the energetic electrons in the plasma. The minimum Ni layer thickness, $T_{Ni, min}$, which satisfies the first condition, is thinner when using plasma CVD than thermal CVD. This thinner Ni structure also allows the second condition to be satisfied. We also used a Cu catalyst instead of the Ni in the RH-PCVD experiment. However, the Cu film was completely transformed to nanoislands, and graphene growth was not realized. This may be due to the lower melting point of Cu compared with that of Ni or it may be due to a difference in the diffusion kinetics of Cu and Ni.

By applying this unique growth technique, the growth of patterned graphene is also possible by forming Ni patterns with a conventional photolithography technique

prior to RH-PCVD. Figure 4.4a, b shows optical microscope images of the patterned Ni film before RH-PCVD and graphene after RH-PCVD followed by chemical etching to remove the Ni film, respectively. Figure 4.4c–f shows the integrated Raman intensity mapping of the Si-, G-, and 2D-peaks and the 2D- to G-peak intensity ratio of directly grown graphene on the SiO₂ substrate. Ribbonlike high-quality graphene (width $\sim 2 \mu\text{m}$) is selectively grown on the SiO₂ substrate, which is also confirmed by the raw Raman scattering spectrum (Fig. 4.4g). It is worthwhile to mention that the 2D/G intensity ratio is almost constant at a relatively high value of ~ 1.8 and the D-peak intensity is very low over the entire patterned area, which

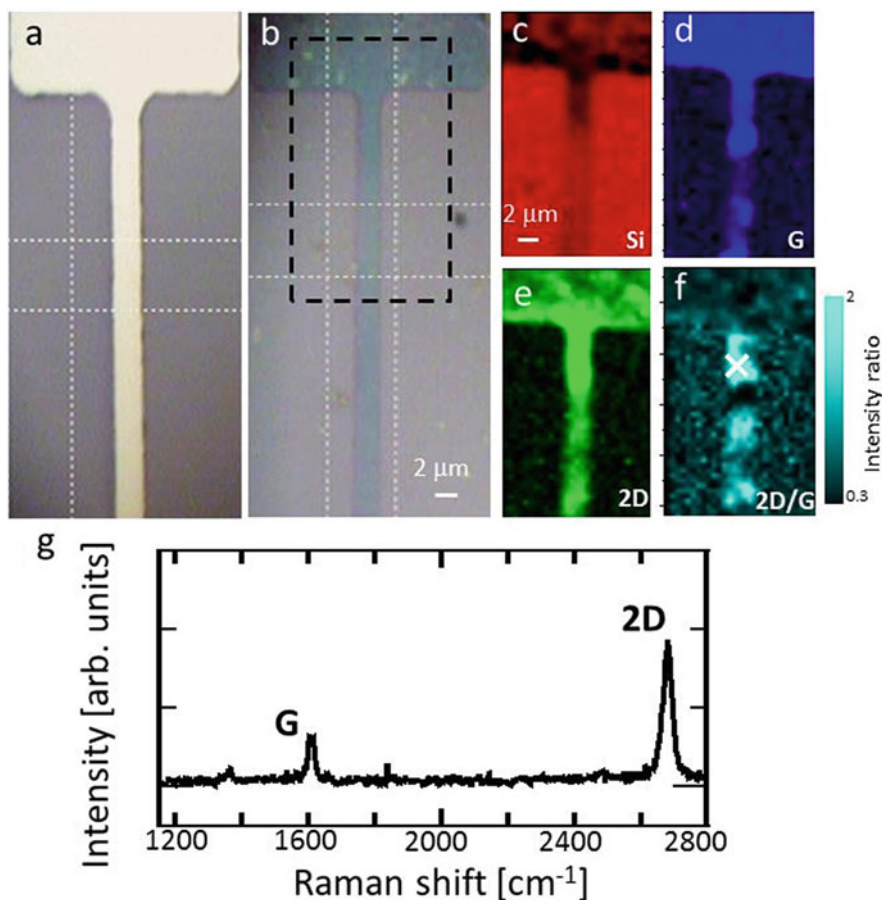


Fig. 4.4 Optical microscope images of (a) before and (b) after the growth ($950 \text{ }^\circ\text{C}$) of graphene on the SiO₂ substrate. (c–f) The integrated Raman intensity maps of the (c) Si-peak, (d) G-peak, (e) 2D-peak, and (f) ratio of the 2D-/G-peak intensities of patterned graphene. The mapping area is indicated by a dotted line in (b). (g) A typical raw Raman scattering spectrum of patterned graphene taken at the position (x) in (f)

indicates that a single layer of patterned and high-quality graphene is realized using this method. A uniform structure of single-layer and high-quality graphene is also obtained even with relatively wide ribbon structures, *e.g.*, width $\sim 20\ \mu\text{m}$.

4.2 Direct Growth of 1D Graphene: Graphene Nanoribbon

Graphene nanoribbons combine the unique electronic and spin properties of graphene with a transport gap that arises from quantum confinement and edge effects. This makes them an attractive candidate material for the channels of next-generation transistors. To date, several graphene nanoribbon production methods based on top-down and bottom-up approaches have been reported [11–16]. Many production-stage challenges for fundamental studies and practical applications remain, including high-yield production, structure (width, length, and edge) control, and large-scale site and alignment control. Recently, some improvements in the graphene nanoribbon yield have been achieved by unzipping carbon nanotubes. The width can also be controlled to a certain degree by using a mild chemical etching process. However, no reliable large-scale methods that can control the site and alignment of graphene nanoribbons with a high on/off ratio have been developed. Although the lithographic method can be used to draw graphene nanoribbon circuits, the area is limited to the micrometer scale, which should be mainly decided by the initial piece of graphene. The growth of single-domain graphene in large scale is still challenging. Graphene nanoribbon device integrations that use the thermal decomposition of SiC have been reported [15]. However, the on/off ratio of graphene nanoribbon devices is low (<30).

In this subsection, we present a new, simple, scalable method based on the bottom-up approach for directly fabricating narrow ($\sim 23\ \text{nm}$) graphene nanoribbon devices with a clear transport gap (58.5 meV) and a high on/off ratio ($>10^4$) [5]. Since our established novel graphene nanoribbon fabrication method, direct conversion of Ni nanobar to graphene nanoribbon (Fig. 4.5a–d), is possible to grow graphene nanoribbons at any desired position on an insulating substrate without any posttreatment, large-scale 2D and 3D integration of graphene nanoribbon devices should be realized, which accelerates the practical evolution of graphene nanoribbon-based electrical applications. Ni nanobar (width 50–100 nm, height 35–85 nm, and length 200–5,000 nm) structures connected to two Ni electrodes (source and drain) were formed on a SiO₂ (300 nm) /Si substrate using a conventional electron beam lithography technique (Fig. 4.5a). The substrate was then rapidly heated to $\sim 900\ ^\circ\text{C}$ for $\sim 1\ \text{min}$, and plasma CVD was performed using a mixture of methane and hydrogen gases (Fig. 4.5b). Following the plasma CVD, the substrate was rapidly cooled to room temperature (Fig. 4.5c, d).

SEM was used to characterize the Ni nanobar structures before (Fig. 4.6a) and after (Fig. 4.6b–g) RH-PCVD. The Ni nanobar structures were partially (Fig. 4.6b, d, e) or fully (Fig. 4.6c, f, g) converted into sheetlike materials (graphene nanoribbons), and the width shrank by up to $\sim 23\ \text{nm}$ after RH-PCVD. Based on

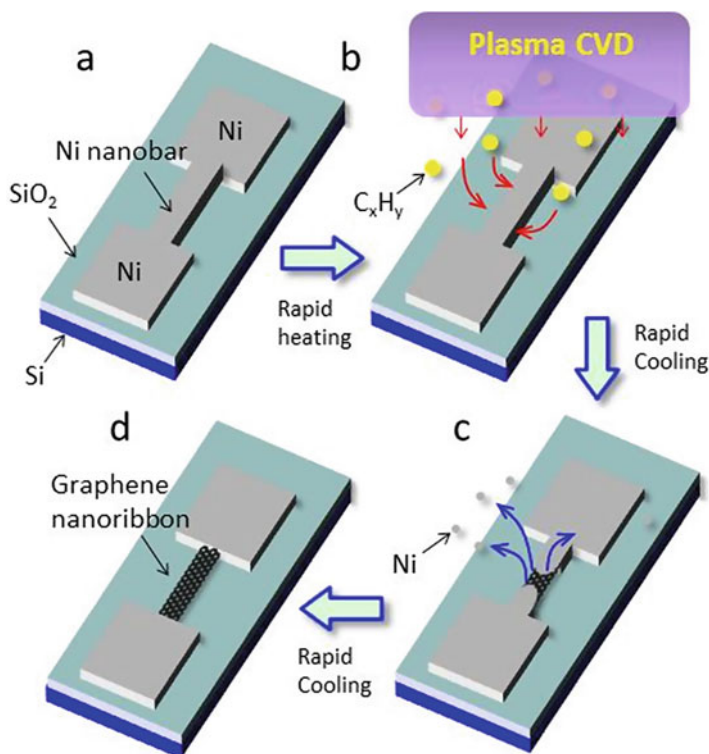


Fig. 4.5 (a–d) A schematic illustration of the Ni nanobar to graphene nanoribbon direct conversion process. The substrate was rapidly heated to desired temperature, and (b) plasma CVD was performed. (c) Nucleation of graphene preferentially starts from the Ni nanobar structure during the cooling process, and (d) finally graphene nanoribbon can be formed

the systematic investigations, a clear correlation was observed between the initial Ni nanobar width and converted graphene nanoribbon width as shown in Fig. 4.6h. The graphene nanoribbon width does not exceed the initial width of Ni nanobar. The conversion efficiency (graphene nanoribbon width/initial Ni nanobar width) was 45–70 %. For the production of relatively narrow (<30 nm) graphene nanoribbons (Fig. 4.6b, c), Ni nanobars with below 50 nm width are necessary. To identify the detailed structures of graphene nanoribbons, Raman mapping measurements were performed. Figure 4.7a, b shows AFM (Fig. 4.7a) and high-magnification SEM (Fig. 4.7b) images of graphene nanoribbon that was used for the Raman mapping measurements. The Ni nanobar structure was fully converted to graphene nanoribbon. The AFM image and height profile (inset of Fig. 4.7a) indicate that the surface and edge of graphene nanoribbon are relatively flat and smooth, respectively. The large height (~60 nm) of graphene nanoribbon may be due to a suspended structure. Figure 4.7c–f shows the integrated Raman intensity mapping of the Si-peak (Fig. 4.7c, 512–540 cm⁻¹), the disorder-related D-peak (Fig. 4.7d, 1,292–

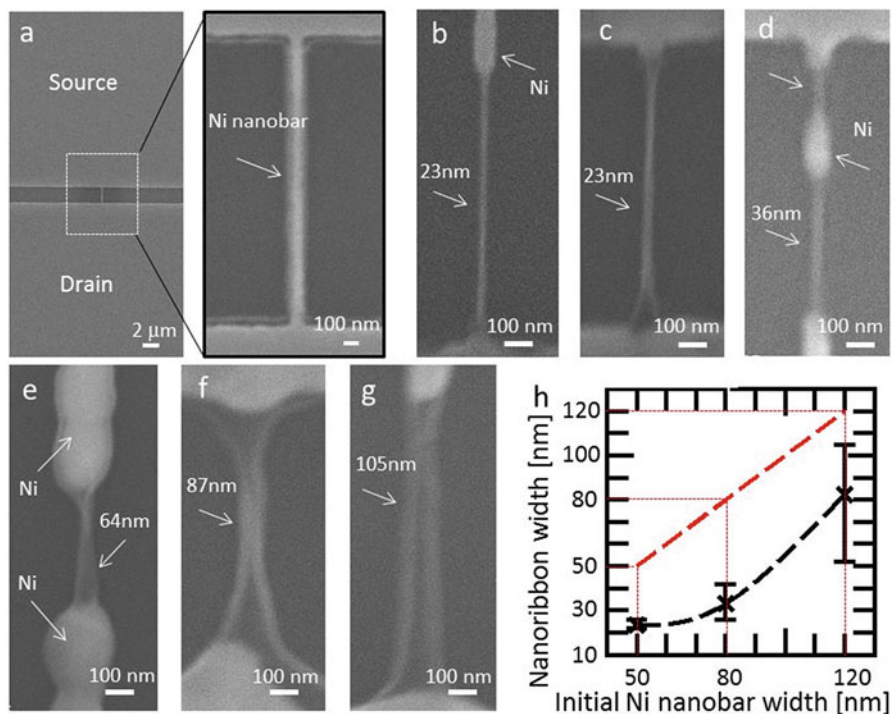


Fig. 4.6 (a) Typical SEM images of patterned Ni electrodes and the Ni nanobar before RH-PCVD. (b–g) SEM images of various graphene nanoribbons converted from (b–d) 50 nm, (e) 100 nm, and (f, g) 120 nm width Ni nanobars. (h) The plot of graphene nanoribbon width as a function of initial Ni nanobar width. The red dash in (h) describes the line satisfying the following correlation; graphene nanoribbon width = initial Ni nanobar width

$1,360\text{ cm}^{-1}$), the graphitic G-peak (Fig. 4.7e, $1,544\text{--}1,626\text{ cm}^{-1}$), and the 2D-peak (an intervalley double-resonance Raman band) (Fig. 4.7f, $2,577\text{--}2,700\text{ cm}^{-1}$). The Si-peak mapping that supports the measurement area was between the two electrodes (Fig. 4.7c). The high-intensity area of the G-, D-, and 2D-peaks appeared as a continuous line between the two electrodes (Fig. 4.7d–f) and matched the structure of graphene nanoribbon well (Fig. 4.7a, b). A typical Raman spectrum of graphene nanoribbon is shown in Fig. 4.7g. A sharp G- and 2D-peak were observed, along with a D-peak. The 2D-peak can be fitted by a single Lorentzian curve (inset of Fig. 4.7g), and the 2D-peak intensity is higher than that of G-peak. These features matched the previously reported Raman scattering spectra of single-layer graphene sheet well. Similar features were observed for the other RH-PCVD samples. Energy-dispersive X-ray spectroscopy (EDX) measurements also indicated that graphene nanoribbons grown by RH-PCVD consisted of carbon, while the Ni signal was below the detection limit.

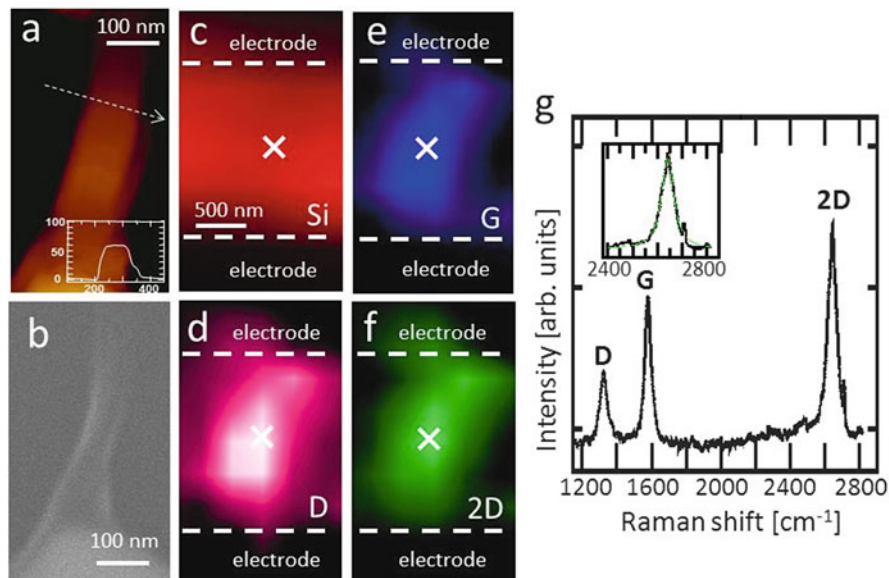


Fig. 4.7 (a) AFM and (b) high-magnification SEM images of graphene nanoribbon used for the Raman mapping measurement. *Inset* of (a) gives a height profile of graphene nanoribbons along with the *dashed line*. (c–f) The integrated Raman intensity mapping of the Si-peak (c, 512–540 cm^{-1}), D-peak (d, 1,292–1,360 cm^{-1}), G-peak (e, 1,544–1,626 cm^{-1}), and 2D-peak (f, 2,577–2,700 cm^{-1}). (g) A typical Raman scattering spectra of graphene nanoribbon taken at the position (X) in c–f. *Inset* in g denotes the raw 2D spectrum (black) and a curve fitted with a single Lorentzian function (green)

In addition to the simple single-channel FET structure as demonstrated above, various complex architectures can also be constructed by predesigning the initial Ni nanostructures. The multi-channel (10–20 graphene nanoribbons (~ 30 nm width and ~ 1 μm length with 1 μm space each)) FET structures (Fig. 4.8a–c) can be formed, which denote the desirable integration of graphene nanoribbons should be possible with RH-PCVD. This is the first time demonstrating a production of complex architectures with bottom-up graphene nanoribbons.

We also performed RH-PCVD on thin (25–85 nm) Ni films. The Raman mapping measurements showed that high-quality suspended graphene sheets were grown by partially evaporating Ni using RH-PCVD. This result also demonstrated that suspended graphene nanoribbons formation using RH-PCVD is reliable. Our systematic investigation revealed that rapid heating, an abundant supply of reactive hydrocarbon, and relatively thin Ni structures are the critical elements for directly converting Ni nanobar structures into graphene nanoribbons. Further detailed growth kinetics will be addressed in future studies.

The electrical properties of the as-grown graphene nanoribbon devices were also measured under the FET configurations. A clear transport gap was obtained from a narrower (less than 30 nm) graphene nanoribbon device. The Ni nanobar

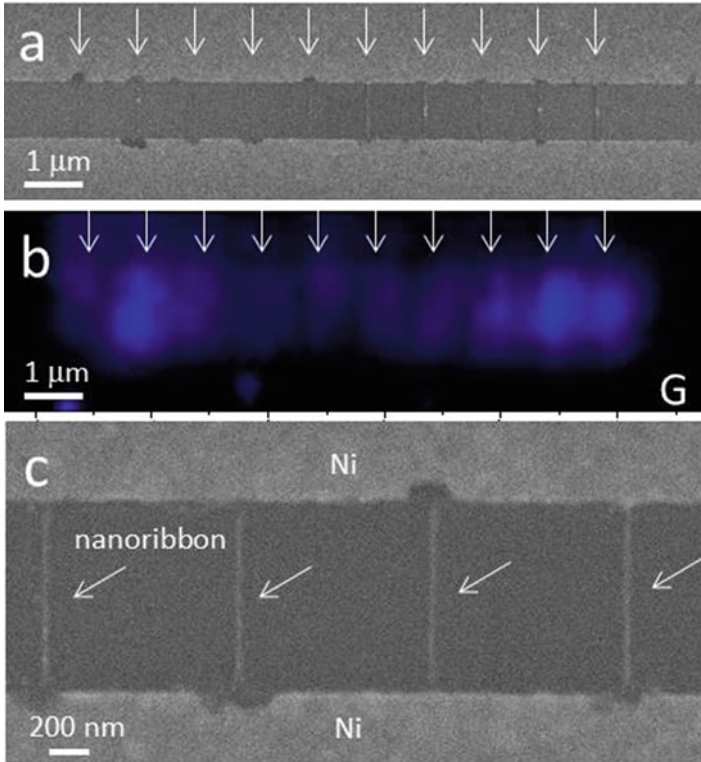


Fig. 4.8 (a) Low- and (c) high-magnification SEM images and integrated Raman intensity mapping of G-peak (b) of multichannel graphene nanoribbon-FET structure

was partially converted into two graphene nanoribbons (with width ~ 23 nm), and a Ni island remained at the center of the channel area (Fig. 4.9a). The source-drain current (I_{ds}) vs. gate bias voltage (V_{gs}) curve showed ambipolar transport characteristics at room temperature (300 K) with an on/off ratio of ~ 16 (red curves in Fig. 4.9b). Notably, when the temperature decreased to 13 K, the on/off ratio increased to 1.5×10^4 (blue curves in Fig. 4.9b). This result is the first indication of a high on/off ratio for the bottom-up-grown graphene nanoribbons. In addition, there was almost no hysteresis in the I_{ds} - V_{gs} curves in any temperature range (Fig. 4.9b), which was probably due to the clean surfaces of as-grown graphene nanoribbons and/or the suspended structures. To estimate the transport gap of graphene nanoribbons, I_{ds} - V_{gs} curves were recorded under different source-drain bias voltages (V_{ds}). The plot of the on/off ratio as a function of the V_{ds} indicated that a high on/off ratio (10^3 - 10^4) was maintained from low V_{ds} up to 50 mV, at which point the on/off ratio began to decrease (Fig. 4.9c). The observed decrement in the on/off ratio was caused by the saturation of I_{on} and the increase of I_{off} .

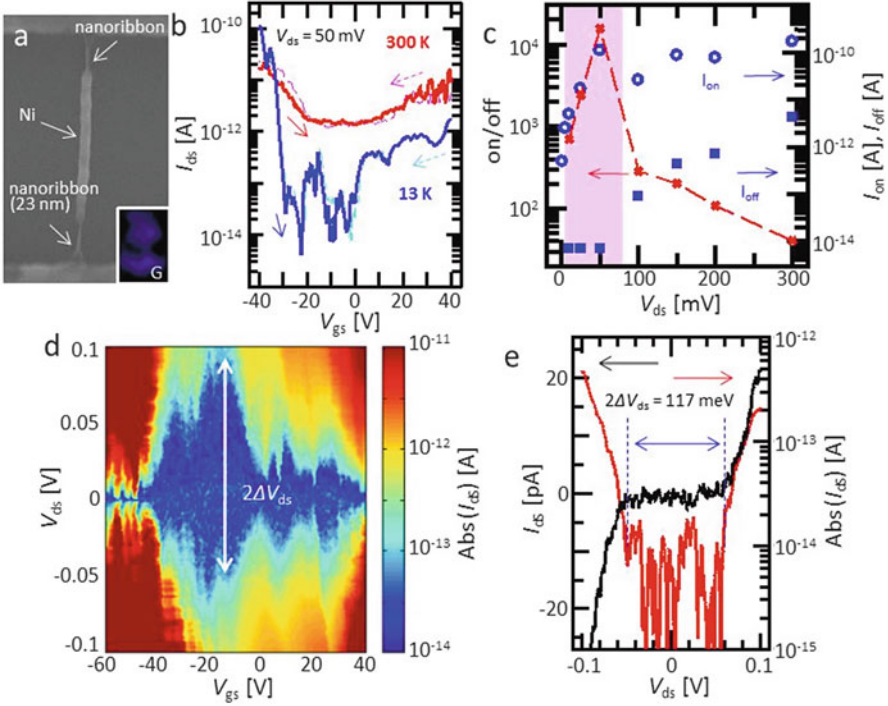


Fig. 4.9 (a) The SEM and (b) I_{ds} - V_{gs} curves of a 23 nm wide graphene nanoribbon device at 300 K and 13 K. (c) The on/off, I_{on} , I_{off} plot as a function of V_{ds} . (d) I_{ds} in logarithmic scale for different V_{gs} and V_{ds} measured at 13 K. (e) The I_{ds} - V_{ds} curves on linear (black) and logarithmic (red) scales for the graphene nanoribbon device with a fixed V_{gs} ($= -16$ V)

This result suggested that the transport gap of the 23 nm graphene nanoribbon was approximately 50 meV.

Low-temperature transport measurements gave further detailed information about the transport gap and its origin. A clear off-current region with diamond-like shapes appeared in the logarithmic-scale I_{ds} contour plots of both V_{gs} and V_{ds} (Fig. 4.9d). The maximum value of the off-current gap in the V_{ds} direction ($2\Delta V_{ds}$) was observed at $V_{gs} = -16$ V (arrow in Fig. 4.9d), where ΔV_{ds} corresponds to the transport gap. ΔV_{ds} was estimated from the I_{ds} - V_{ds} curve at $V_{gs} = -16$ V (Fig. 4.9e) and $\Delta V_{ds} = 58.5$ meV. This value was consistent with the transport gap estimated from Fig. 4.9c. There are several origins of the transport gap in graphene nanoribbons, such as Anderson localization due to edge disorder, a Coulomb blockade in a series of quantum dots, and the intrinsic bandgap of graphene nanoribbons. Because the overlapped coulomb diamond-like features were observed in the graphene nanoribbon device (Fig. 4.9d), the transport gap probably originated from an arrangement of a few quantum dots in parallel and/or in series along the ribbon. The effects of the remaining Ni islands on the transport

properties should also be considered. Because a clear transport gap did not appear in the partially converted graphene nanoribbons with a 39 nm width, there should not have been any significant effects on the graphene nanoribbon transport gap. Therefore, the gap should have been determined mainly by the width or the edge structures of the graphene nanoribbons. Similar features were observed for the other samples grown by RH-PCVD. The field-effect mobilities $\mu = (dG/dV_{gs})(L^2/C_g)$ were calculated for the graphene nanoribbon devices with high on/off ratio ($>10^3$), which were $\sim 40 \text{ cm}^2\text{V}^{-1} \text{ s}^{-1}$ (where G , L , and C_g show conductance, channel length, and gate capacitance, respectively; the $C_g = 1.2\text{--}6 \text{ aF}$ were calculated using three-dimensional electrostatic simulation). In spite of the suspended structure of our graphene nanoribbon devices, the device performances itself are equivalent to that of lithographic graphene nanoribbons or slightly lower than that of graphene nanoribbons prepared by carbon nanotube unzipping. This might be due to a relatively small domain size of our graphene nanoribbons as similar with CVD graphene, which can be improved by enlarging the initial Ni domain size or using other catalysts.

4.3 Conclusions

We have realized and demonstrated an easy and scalable method for the growth of high-quality graphene directly on a SiO_2 substrate. Through systematic investigations, we have shown that a relatively thin Ni layer and the RH-PCVD process are critical for the selective growth of graphene along the interface between the Ni film and the SiO_2 substrate. A new, simple, and scalable method for integrating graphene nanoribbon devices based on a bottom-up approach is also demonstrated. The site- and alignment-controlled growth of graphene nanoribbons with a clear transport gap and a high on/off ratio has been achieved for the first time. This clean and position-controllable graphene nanoribbon growth method could solve the critical issues associated with integrating graphene nanoribbons into practical applications.

Acknowledgment This work was supported by JSPS KAKENHI (23740405, 21654084). We are grateful to Prof. K. Tohji and Mr. K. Motomiya for their help with the EDX measurements.

References

1. Zhang L, Shi Z, Wang Y, Yang R, Shi D, Zhang G (2011) Catalyst-free growth of nanographene films on various substrates. *Nano Res* 4:315–321
2. Ismach A, Druzgalski C, Penwell S, Schwartzberg A, Zheng M, Javey A, Bokor J, Zhang Y (2010) Direct chemical vapor deposition of graphene on dielectric surfaces. *Nano Lett* 10:1542–1548
3. Su C-Y et al (2011) Direct formation of wafer scale graphene thin layers on insulating substrates by chemical vapor deposition. *Nano Lett* 11:3612–3616

4. Kato T, Hatakeyama R (2012) Direct growth of doping-density-controlled hexagonal graphene on SiO₂ substrate by rapid-heating plasma CVD. *ACS Nano* 6:8508–8515
5. Kato T, Hatakeyama R (2012) Site- and alignment-controlled growth of graphene nanoribbons from nickel nanobars. *Nat Nanotechnol* 7:651–656
6. Kato T, Hatakeyama R (2008) Exciton energy transfer assisted photoluminescence brightening from freestanding single-walled carbon nanotube bundles. *J Am Chem Soc* 130:8101–8107
7. Kato T, Hatakeyama R (2008) Kinetics of reactive ion etching upon single-walled carbon nanotubes. *Appl Phys Lett* 92:031502-1-3
8. Kato T, Hatakeyama R (2010) Direct growth of short single-walled carbon nanotubes with narrow-chirality distribution by time-programmed plasma chemical vapor deposition. *ACS Nano* 4:7395–7400
9. Ghorannevis Z, Kato T, Kaneko T, Hatakeyama R (2010) Narrow-chirality distributed single-walled carbon nanotubes growth from nonmagnetic catalyst. *J Am Chem Soc* 132:9570–9572
10. Kato T, Jiao L, Wang X, Wang H, Li X, Zhang L, Hatakeyama R, Dai H (2011) Room-temperature edge functionalization and doping of graphene by mild plasma. *Small* 7:574–577
11. Han MY, Ozyilmaz B, Zhang YB, Kim P (2007) Energy band-gap engineering of graphene nanoribbons. *Phys Rev Lett* 98:206805
12. Li XL, Wang XR, Zhang L, Lee SW, Dai H (2008) Chemically derived, ultrasmooth graphene nanoribbon semiconductors. *Science* 319:1229–1232
13. Jiao LY, Zhang L, Wang XR, Diankov G, Dai H (2009) Narrow graphene nanoribbons from carbon nanotubes. *Nature* 458:877–880
14. Kosynkin DV et al (2009) Longitudinal unzipping of carbon nanotubes to form graphene nanoribbons. *Nature* 458:872–876
15. Sprinkle M et al (2010) Scalable templated growth of graphene nanoribbons on SiC. *Nat Nanotechnol* 5:727–731
16. Cai J et al (2010) Atomically precise bottom-up fabrication of graphene nanoribbons. *Nature* 466:470–473

Chapter 5

Graphene/Metal Contact

Kosuke Nagashio and Akira Toriumi

Abstract The higher the electron mobility is, the stricter the requirement for the contact resistivity becomes, especially for graphene, which has an extremely high electron mobility. Although the ohmic contact due to no bandgap was reported in the supplemental of the first graphene paper, the contact resistivity is intrinsically high due to the small density of states in graphene. In this chapter, the issues concerning metal/graphene interface properties are reviewed, and the guidelines to reduce the contact resistivity are discussed, based on the recent understanding of metal/graphene/substrate interactions.

Keywords Contact resistivity • Density of states • Charge transfer • π - d coupling

5.1 Fundamental Issues Concerning the Carrier Injection

The extremely high electron mobility of graphene severely requires low contact resistivity (ρ_c), especially in miniaturized field effect transistors (FET). Therefore, ρ_c has been measured by many research groups [1–13], and it has been shown that it is necessary to reduce ρ_c by several orders of magnitude from the present status [3]. The high ρ_c at the metal/graphene interface is recognized as a performance killer [1]. To understand the inherent difficulty of the current injection and to further reduce ρ_c , the metal/graphene/substrate interactions for the contact should be addressed because of the monatomic layer, which is completely different from a typical Si junction.

The tunneling current from the metal electrode to graphene is considered from the viewpoint of the electrical transport, as shown in Fig. 5.1. Generally, the tunneling current is proportional to the transmission probability and the density of states (*DOS*) in the metal and graphene, which is inversely proportional to the contact resistance [14, 15]. In terms of the transmission probability, the momentum

K. Nagashio (✉) • A. Toriumi
Department of Materials Engineering, The University of Tokyo, 7-3-1, Hongo, Bunkyo-ku,
Tokyo 113-8656, Japan
e-mail: nagashio@material.t.u-tokyo.ac.jp

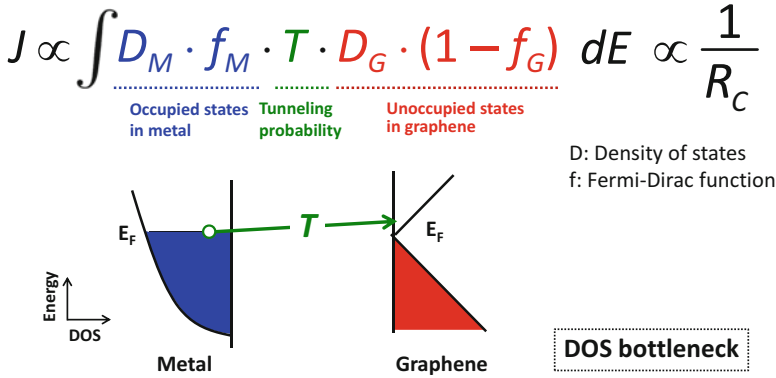


Fig. 5.1 Simple equation for tunneling current, D , f , and T are density of states, Fermi function, and transmission probability, respectively. Schematic of the energy–DOS relation for metal and graphene, showing the DOS bottleneck

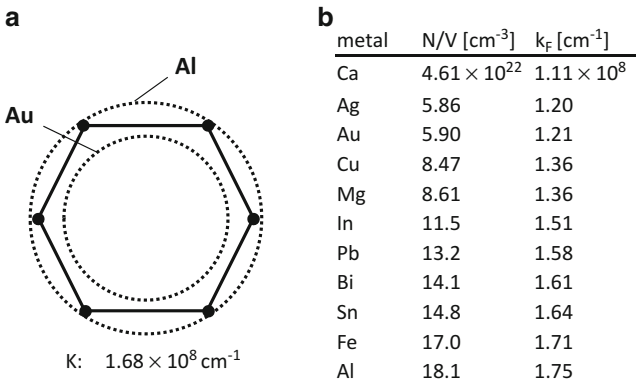


Fig. 5.2 (a) Schematic illustration of Brillouin zone of graphene and Fermi surface of metals (Au and Al) [16]. (b) Carrier densities and wave numbers of the Fermi surfaces for different metals [45]

matching and the distance between graphene and the metal should be considered. The momentum matching between graphene and the metal has been discussed [16] based on the models for metal/metal [17] and metal/semiconductor interfaces [18]. Figure 5.2a compares the 1st Brillouin zone of graphene and the wave number of the Fermi sphere for typical metals [19]. For simplicity, the origin of the momentum is generally redefined as the K point when describing electron transport limited in the graphene channel. In the case of the momentum matching for the current injection from the metal to graphene, however, the Γ point (zero momentum) is taken as the origin. As is evident from the table [19] in Fig. 5.2b, the Fermi wave number of Al is larger than that of Au because the Fermi sphere becomes larger by increasing the carrier density. The momentum of graphene matches well with that of Al but not with that of Au. As a matter of fact, the contact resistance of Al electrode on

graphene is very large because it is easily oxidized due to the small work function, and the Al oxide is often used as a topgate insulator [20]. Although the matching of the Fermi wave numbers alone does not explain the experimental results, it should be taken into consideration in the discussion on the contact resistivity. To describe the metal/graphene distance, the metal electrode is generally formed on the basal plane of graphene. The grain size of the metal deposited on graphene may cause a fluctuation of the metal/graphene distance, which affects ρ_c [12]. Moreover, it has been theoretically reported that the distance between graphene and the metal depends on the metal elements, and this results from the strength of the graphene/metal interaction [21]. However, experimental difficulties associated with determining the distance preclude more detailed discussion.

In terms of the *DOS*, the empty states in graphene as the final state are much fewer than the occupied states in the metal, as shown in Fig. 5.1. Therefore, the small ρ_c is considered to be due to this *DOS* bottleneck, which limits the total performance of graphene device [7]. Increasing in the *DOS* in graphene is not so simple due to the inapplicability of the conventional doping technique such as an ion implantation [22] because the thermodynamically stable C–C bonding prevents the substitutional doping of B or N for C [23]. The *DOS* of graphene in the contact structure, that is, the metal/graphene/SiO₂ structure, differs from the ideal linear *DOS*–energy relationship because the electrical properties of monatomic graphene are easily modified by the environment.

The alteration of the electron dispersion relation in “graphene grown on metals” has been considered so far. A theoretical analysis suggests that the graphene/metal interface can be classified into two groups: a physisorption group (e.g., Au, Ag, Pt) and a chemisorption group (e.g., Ni, Co, Pd) [21, 24]. At the chemisorption interface, it is predicted that the distance between the metal and graphene is shorter than the interlayer distance in graphite and that the *d*-orbitals of the metal are strongly hybridized with the *p_z*-orbitals of graphene (π –*d* coupling), as shown in Fig. 5.3 [25], which results in the destruction of the band structure and an increase in

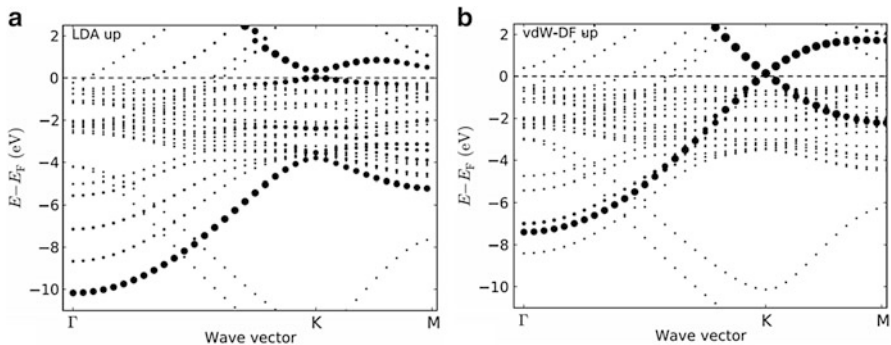


Fig. 5.3 Band structures calculated for graphene on Ni(111) by (a) density functional theory and (b) van der Waals density functional theory [25]. The distance between graphene and Ni is 0.208 nm for (a) and 0.35 nm for (b). Band dispersion depends on the distance

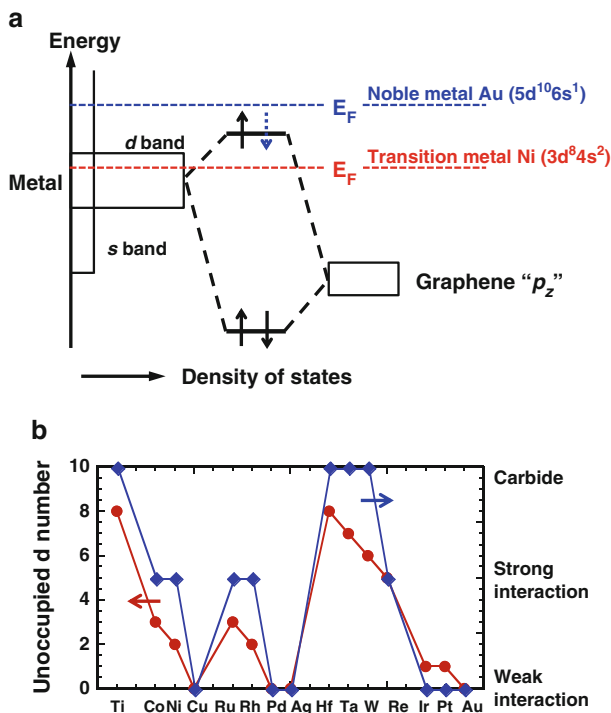


Fig. 5.4 (a) Schematic illustration of the interaction between graphene and metals [28, 29]. (b) The unoccupied d number for metals. These metals are categorized into three types, carbide formation metal, strong interaction metal, and weak interaction metal by Batzill (left axis) [30]. The relation between the unoccupied d number and interaction strength is clearly seen

the DOS in graphene, especially for Ni [26, 27]. The simple explanation of the π - d coupling is shown in Fig. 5.4 [28–30]. The main difference between physisorption and chemisorption metals is the degree of filling in the d -orbitals. For example, the d -orbital is completely filled with electrons for Au and the Fermi level (E_F) for Au is higher than the antibonding states for the π - d coupling. In this case, the antibonding states are completely filled with electrons, which destabilizes the π - d coupling. This is the reason why Au is noble without any reaction. On the other hand, the d -orbital for Ni has still space for two more electrons, which means the antibonding states are not filled with electrons. In this case, the π - d coupling is stabilized. Therefore, the degree of filling in the d -orbitals determines the stability of the antibonding states in the hybridization because a large number of electrons in the antibonding states destabilize the hybridization [28, 29].

However, the metal/graphene/SiO₂ interaction in the device structure might be different from the situation for graphene grown on metal. One possible fact is

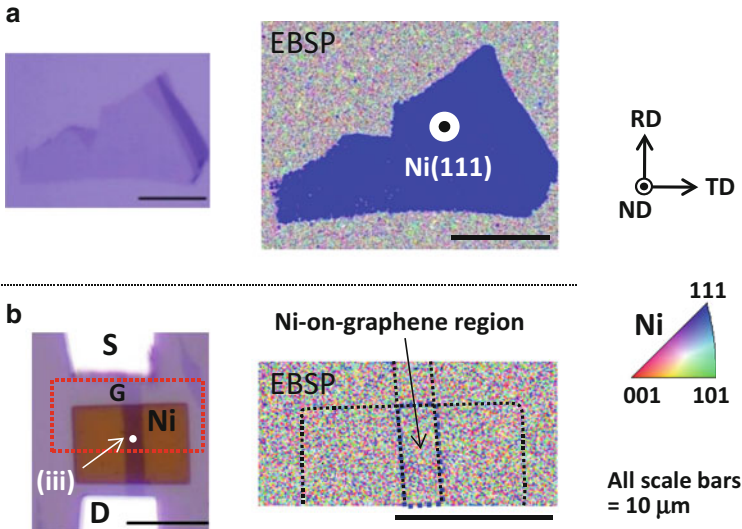


Fig. 5.5 (a) Optical micrograph of graphene on the SiO_2 substrate. The EBSP orientation map of the normal direction (ND) is colored using the inverse pole figure triangle. Both the ND and the transverse direction (TD) show a single color (not shown here), which suggests that Ni(111) grew epitaxially on the graphene. (b) Optical micrograph of the graphene FET device with a Ni electrode on the channel. The EBSP orientation map of the normal direction (ND) is colored using the inverse pole figure triangle

the effect of the resist residue in the device fabrication process. Many researchers have reported that the resist residue is left on graphene [31–33], which should be seriously taken into consideration by recognizing that the activated carbon, whose hydrophobic surface attracts organic materials, is composed of graphene [34]. Indeed, it is shown that resist residue has an influence of the Ni crystallinity deposited on graphene, as shown in Fig. 5.5 [35]. In the case of resist-free Ni deposition, Ni is epitaxially grown on graphene, while Ni is amorphous or forms tiny grains in resist-processed Ni deposition. This difference suggests the importance of the resist-free deposition technique to reveal the intrinsic metal/graphene interaction.

In this chapter, the determination of the *DOS* in graphene in the contact structure using the resist-free metal deposition technique is discussed first because the strength of the metal/graphene/substrate interaction considerably alters the energy-band diagrams at the contact. Then, the contact properties specific to graphene are reviewed by comparison with other junctions such as metal/metal and metal/semiconductor junctions. After summarizing the methods to extract ρ_c , the present status of ρ_c , the correlation between the *DOS* and ρ_c , and possible guidelines for future requirements are addressed.

5.2 Graphene/Metal Interaction

The *DOS* of graphene in a topgate structure with a thin high-*k* oxide layer has been determined by quantum capacitance (C_Q) measurement [36–39]. The C_Q of graphene extracted from the capacitance measurements provides direct information on the *DOS* of graphene because it is regarded as the energy cost of inducing carriers in graphene and is directly related as $C_Q = e^2 \text{DOS}$ [40]. Here, this measurement was applied to the contact structure of the metal/graphene/SiO₂/n⁺-Si stack system [41], in which the model metals, Au (physisorption) and Ni (chemisorption), were deposited by the resist-free process using a handmade mask. Alternatively, the PMMA resist was intentionally spin coated on graphene and removed by acetone before the metal deposition to clarify the effect of the resist residue. Figure 5.6a, b shows the device structure for the *C-V* measurement and its equivalent circuit. Although there are many other techniques such as photoemission spectroscopy [26, 27] and scanning tunneling spectroscopy [42] to extract the *DOS* of graphene, these techniques cannot be applied to the contact structure due to the lack of an available surface of graphene. The C_{Sub} is the series capacitance of SiO₂ and n⁺-Si. The C_Q is introduced in series with C_{sub} in the equivalent circuit ($1/C' = 1/C_{\text{sub}} + 1/C_Q$). The C_{sub} is further introduced in parallel with C' because the area of graphene is not the same as the metal pad area. The SiO₂ thickness of ~3 nm is the critical requirement because C_{sub} should be comparable with C_Q to extract C_Q accurately. Figure 5.6c shows the extracted C_Q of graphene in contact with Ni and Au as a function of the Fermi energy (E_F). The detailed analysis is available in the reference [41]. The right vertical axis indicates the *DOS* calculated by $C_Q = e^2 \text{DOS}$. In addition, the C_Q value obtained for a Y₂O₃ topgate device, in which graphene is sandwiched by the oxides, is also added as a reference in this figure [39].

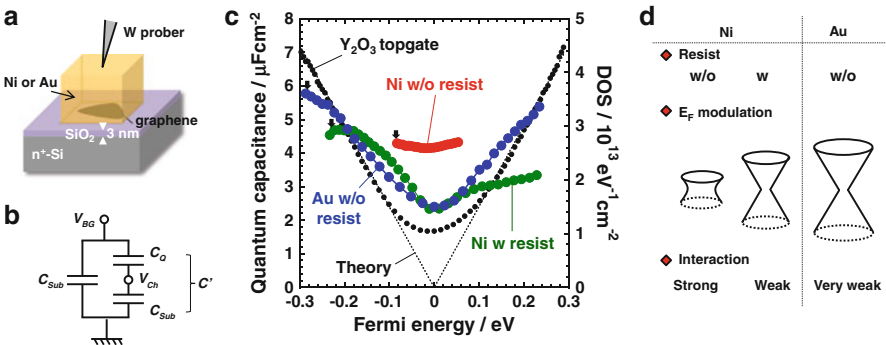


Fig. 5.6 (a) Schematic of the metal/graphene/SiO₂/n⁺-Si device. (b) The equivalent circuit of the device (a). (c) The experimentally extracted C_Q of graphene with the theoretical line. *Solid circles with green, red, and blue colors* represent the resist-processed Ni, the resist-free Ni, and the resist-free Au devices, respectively. The *black circle* represents the C_Q of graphene obtained from the Y₂O₃ topgate device as a reference. The *arrows* indicate the highest *DOS* of the three devices. (d) Summary of the metal/graphene interaction suggested from the C_Q measurements

The resist-processed Ni device shows lightly broken ambipolar E_F modulation, while the DOS for the resist-free Ni device increases near the Dirac point (DP), and the range of E_F modulation is very limited. Although the topgate voltage (V_{TG}) range is the same for all devices, the obtained E_F ranges are different. This result suggests that the resist residue at the graphene/metal interface reduces the graphene/metal interaction considerably. The intrinsic difference between metals in the metal/graphene interaction is discussed with the resist-free process. The C_Q value extracted for the resist-free Au device shows a large ambipolar behavior similar to that of the Y_2O_3 topgate device, which suggests that Au has little influence on the DOS in graphene. Using the resist-free metal deposition technique, it is evident that the interaction of graphene with Ni is much stronger than that with Au. Figure 5.6d summarizes the metal/graphene interaction suggested by the C_Q measurement.

5.3 Energy-Band Diagrams

The ideal case without surface states (interface traps) is considered first. Figure 5.7 shows the energy-band diagrams for (a) metal/semiconductor, (b) metal/metal, and (c) metal/graphene contacts. When a metal and a semiconductor are brought into contact and are connected by an external wire to form a simple circuit, charges flow between the semiconductor and the metal through the external wire for the electrochemical potentials, i.e., E_F , to line up on both sides at the thermal equilibrium.

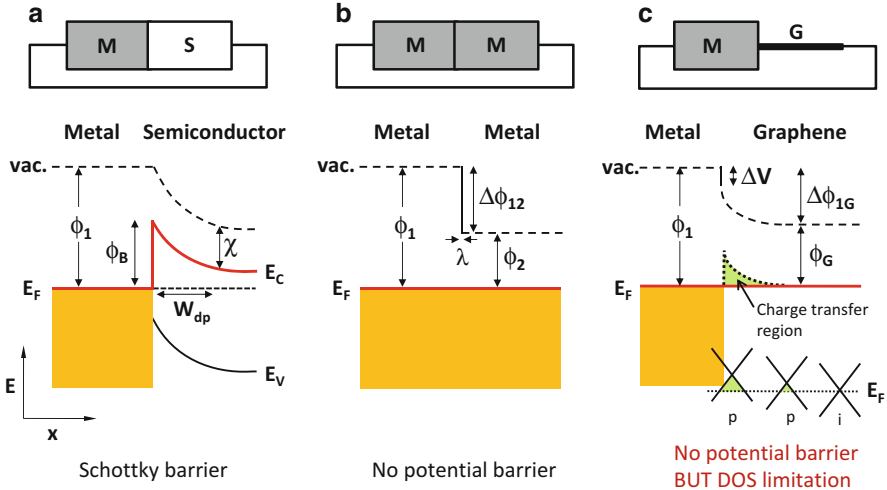


Fig. 5.7 Energy-band diagrams for (a) metal/semiconductor, (b) metal/metal, and (c) metal/graphene contacts. E_C and E_V are the energies for the conduction and valence bands, respectively

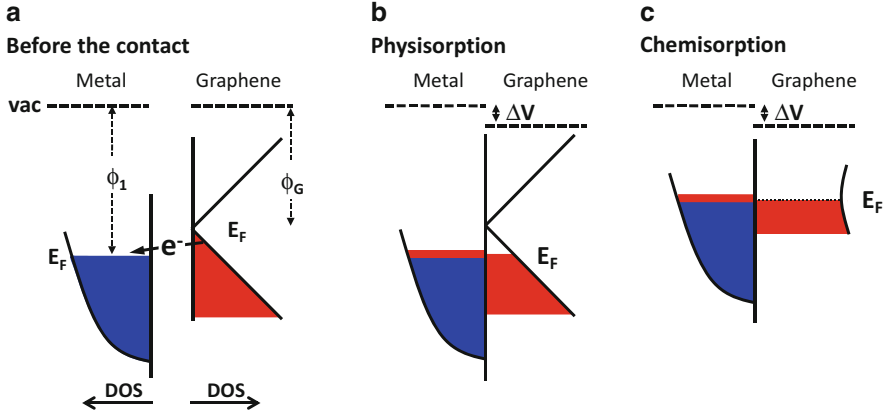


Fig. 5.8 The relation between the *DOS* and the energy “just” at the metal/graphene interface (a) before the contact and after the contact for (b) physisorption metal and (c) chemisorption metal

This builds up the Schottky barrier ($\phi_B = \phi_1 - \chi$) [15], where ϕ_1 and χ are the work function for metal 1 and the electron affinity for the semiconductor, respectively. In terms of the Fermi level pinning at the metal/semiconductor interface [43, 44], the argument over the origin still continues even at present. Here, no Fermi level pinning case is discussed. A depletion layer with a length of W_{dp} is formed because of the much smaller carrier density in the semiconductor. In contrast, the metal/metal contact has no potential barrier. Although the carrier is transferred directly through the metal/metal interface to cancel the difference in work functions, the small redistribution of the electron cloud can screen this potential difference because of the large carrier density. In general, the screening length, expressed as $\lambda = [4\pi \text{DOS}(E_F)]^{-1/2}$, is very short in metals (typically a fraction of a nm) [45]. Therefore, the vacuum level changes sharply at the metal/metal interface.

The case of interest in this work is the metal/graphene contact, which is very similar to the metal/metal contact because graphene is treated as a metal due to its lack of a bandgap. Figure 5.8 shows the relation between the *DOS* and the energy, visualizing the charge transfer process occurring place “just” at the metal/graphene interface for the physisorption case (b) and chemisorption case (c). These schematics were drawn based on the results in Fig. 5.6. It should be noted that the direction of charge transfer does not necessarily correspond to the difference in work functions because of the chemical bonding. The amount of charge transfer gradually decreases from the metal/graphene interface, as shown in Fig. 5.7c. In this case, a very small amount of electron transfer shifts the E_F significantly. It is known that 0.01 electrons per carbon atom would lower the E_F by 0.47 eV [23]. This charge transfer forms the dipole layer at the interface; the potential difference of the dipole layer is expressed as ΔV . Moreover, the very small *DOS* around the E_F for graphene increases the screening length. The resulting long charge transfer region is a unique characteristic of the metal/graphene contact. It is noted that ΔV

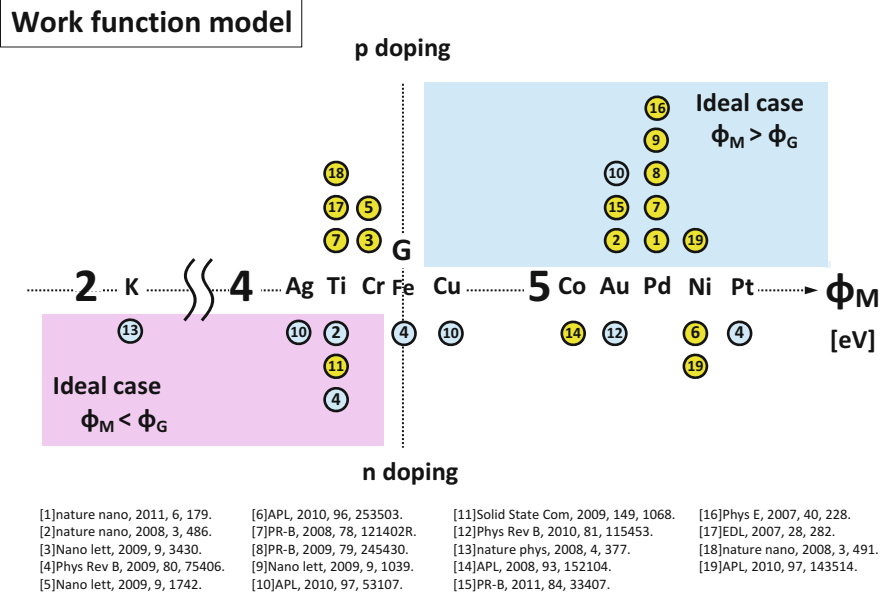


Fig. 5.9 Relationship between work function for various metals and doping polarity in graphene reported in the literature. The ideal doping polarity is hatched based on the work function difference between graphene (4.5 eV) and metals. *Yellow circles* indicate the doping polarity judged from the asymmetry of the current–gate voltage curve, while *gray circles* indicate the doping polarity judged from the DP shift when metal particles are deposited on the graphene channel. The numbers in the *circles* show the references

at the interface depends on the strength of the metal/graphene interaction and is different from $\Delta\phi_{1G} = \phi_1 - \phi_G$, where ϕ_G is the work function of graphene. The charges transferred from graphene to the metal are pulled back by this dipole and then equilibrate with the work function difference. In the case of the metal/metal contact, it is meaningless to separate $\Delta\phi_{12}$ into ΔV at the interface and the potential drop in the charge transfer region because of the short screening length.

The occurrence of the charge transfer is supported by the fact that the DP shifts due to the metal deposition on the graphene channel during the I - V measurement [46]. However, when the data reported so far is summarized in Fig. 5.9, the doping direction is not determined simply by the work function difference between graphene and the metals. The transverse axis is the work function for the metals, and the reported doping polarities are indicated in the longitudinal axis. The hatched regions show the ideal doping polarities for the work function of graphene of 4.5 eV. As mentioned before, the strong interaction between the metals and graphene, i.e., the chemisorption, and the influence of the resist residue could be the reasons. The fact that both polarities are often observed for the same metal, however, suggests that the doping polarity is also affected by the “mixed” interaction among the substrate, metal, and graphene because the surface treatment of SiO_2 also affects the direction

of the charge transfer [35]. Moreover, the length of the charge transfer region was reported as $\sim 0.5 \mu\text{m}$ by the photocurrent, KFM, and nanoESCA experiments [47–49], but the theoretical calculation predicts a length of $\sim 10 \text{ nm}$ [50]. Moreover, the strong graphene/Ni interaction provided by the resist-free metal deposition technique results in a long charge transfer length of $\sim 1.6 \mu\text{m}$ [41]. A detailed study should be further conducted to reveal this discrepancy.

5.4 The p - n Junction Formation

The key feature that originates from the long charge transfer region is the p - n junction that appears near the metal/graphene contact [51]. Figure 5.10 illustrates (a) the schematic of the backgated graphene FET and (b) the band diagram that includes the charge transfer region (hole-doping case) in which the traces of the Dirac point are shown by a broken line, a dash-dotted line, and a dash-double-dotted line for different backgate voltages (V_{BG}). Moreover, the local resistivity for different values of V_{BG} is also schematically shown as a function of position in Fig. 5.10c, where the

Fig. 5.10 (a) Schematic of the graphene FET with the backgate. (b) Schematic of the band diagram showing the charge transfer region (hatched). The traces of the Dirac point for different V_{BG} are indicated by the *broken line*, the *dash-dotted line*, and the *dash-double-dotted line*. The respective resistivities are also shown as a function of position (c). (d) A schematic of the resistivity curves for the cases (*left*) without the charge transfer and (*right*) with the charge transfer. An asymmetric resistivity curve is observed because of the additional resistance produced by the p - n junction

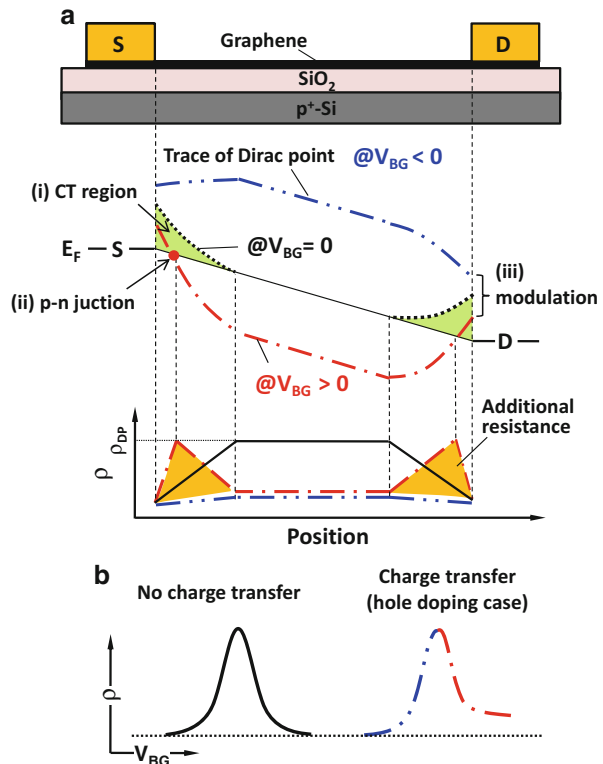
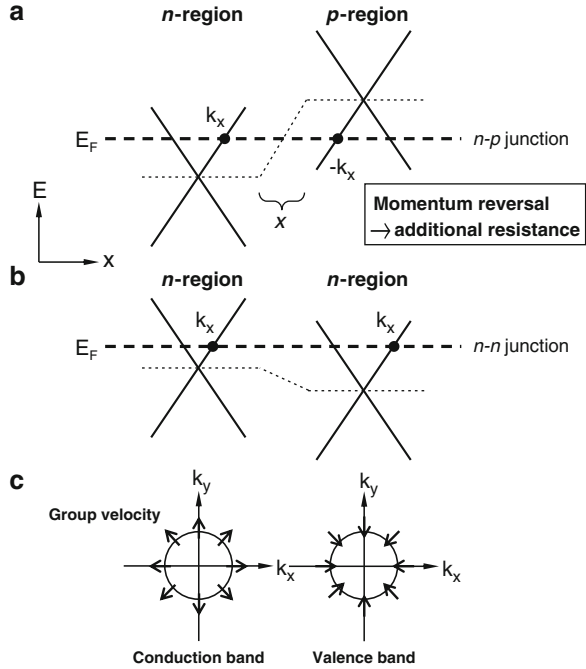


Fig. 5.11 Schematics of electron dispersion relation at (a) n - p junction region and (b) n - n junction region, respectively. The x indicates the width for the potential change. (c) Group velocity for conduction and valence bands



local resistivity at the p - n junction is considered to be the resistivity (ρ_{DP}) at the DP. When a positive V_{BG} is applied to the device, a p - n - p junction is formed near the contact (Fig. 5.10b), resulting in an additional resistance, as shown in Fig. 5.10c. In contrast, the increase in the series resistance is negligible for a negative V_{BG} because no p - n junction is formed (p - p - p junction). Consequently, as shown in Fig. 5.10d, the asymmetric resistivity dependence on V_{BG} is observed due to the increase in the resistance near p - n junctions [51].

In the above discussion on the p - n junction, the diffusive transport is assumed, where the p - n junction width (x) is longer than the mean free path in the graphene channel. When the p - n junction width is shorter than the mean free path in the graphene channel (abrupt junction), the electron advances the p - n junction ballistically, similar to the intra-band tunneling [52]. Figure 5.11 shows the band diagrams for n - p junction and p - n junction near the metal/graphene contact. In Fig. 5.11a, the electron travels from left to right. The group velocity in the n region, which is defined as the slope of the energy-momentum relation (Fig. 5.11c), is also facing right, that is, the wave number is k_x . In the ballistic transport, the direction of the group velocity in the p region does not change, which results in a wave number of $-k_x$ in the p region. Thus, the reversal of the momentum is the additional resistance at the p - n junction for the ballistic case. Moreover, in the experiment of the abrupt p - n junction produced by dual gate control, the additional resistance for an abrupt p - n junction is reported to be higher than that for a diffusive p - n junction [52]. However, the p - n junction formed near the contact will be diffusive due to having

only the backgate control. The additional resistance in Fig. 5.10c is explained by the diffusive p - n junction model.

This origin for the asymmetry was first studied by comparing devices with invasive electrodes crossing the whole graphene channel width and external electrodes connected to the side of the graphene channel [51]. It was shown that the electric transport in the channel with the external electrodes is not affected by the p - n junctions, unlike the invasive electrodes. The increase in the asymmetry with decreasing channel length also supported the existence of the p - n junction [53]. Moreover, the formation of the charge transfer region leads to the band bending, that is, a built-in electric field. The direct evidence of the built-in electric field is provided by a photocurrent experiment in which photoexcitation near the metal/graphene contact generates electron-hole pairs that can be separated by the built-in electric field to produce a net photocurrent [47, 54]. The charge transfer occurs even in the floating condition, i.e., no external wire, which was also confirmed by the generation of the photocurrent near the floating contact [54]. Finally, it is worthwhile to mention that the modulation doping of graphene from the contacts could possibly control the polarity of the channel when the charge transfer length is longer than the channel length, which is a big advantage because the contact doping does not cause additional Coulomb scattering.

In Fig. 5.10b, the E_F in graphene underneath the metal electrode is not pinned because the graphene/metal interaction is weakened in the resist-processed device, and a small E_F modulation is observed even for the resist-free Ni electrode (π - d coupling case) in Fig. 5.6b. Here, for the metal/semiconductor interface, the Fermi level pinning is generally observed, that is, the Schottky barrier heights for many metals are independent of the work function for the metals [43]. The metal-induced gap states (MIGS) [44] model has been discussed. For graphene, intuitively, the Fermi level pinning due to MIGS model will not occur because there is no dangling bond at the basal plane and no bandgap.

5.5 Electron Transport and Contact Resistivity

5.5.1 Current Flow Path at the Metal/Graphene Contact and Contact Resistivity

First, the device structures to extract the contact resistivity and their characteristics are summarized in Fig. 5.12 [55]. In the four-probe measurement (a), the potential along the dotted line is shown. The potential drops at both contacts can be determined by subtracting the channel resistance obtained by the voltage probes from the total resistance. The contact resistance (R_c) measurement by the device structure in (b) is called the transfer length method (TLM). The two-probe resistances are plotted as a function of the channel lengths. When all of the contact and channel properties are assumed to be equal, the intercept at the zero channel length indicates the double of R_c . The last one in (c) is the cross-bridge Kelvin (CBK) structure

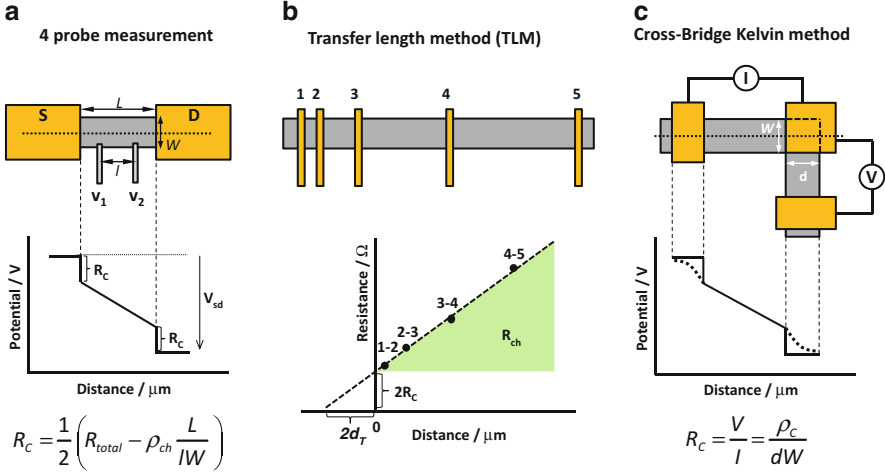
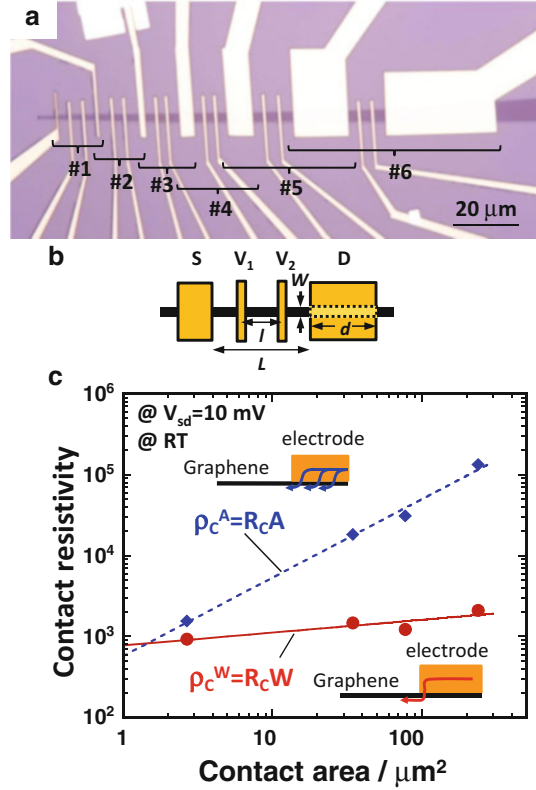


Fig. 5.12 Three kinds of methods to estimate ρ_c . (a) Four-probe measurement, (b) transfer length method, and (c) cross-bridge Kelvin method

in which three electrodes are connected to an L shape channel [56]. A constant current is imposed between the two electrodes on the upper side, while the voltage is measured between the two electrodes on the right side. This method is a type of quasi four-probe measurement. The electrical potential is highest near the contact edge and drops nearly exponentially with the distance, where the $1/e$ distance is indeed defined as the transfer length (d_T), unlike the simple assumption in (a). The voltage measured from the side is the linear average of the potential over the contact length, d . Therefore, ρ_c with an area-normalized unit of Ωcm^2 , which is the physical property of the contact, can be directly measured by a simple equation. However, for the four-point probe and TLM measurements, the assumption of the current flow path (edge or area) is required to determine ρ_c (Ωcm or Ωcm^2) because the current flow path is not clear at the metal/graphene contact. Although the intercept at zero resistance provides the information on d_T in TLM, it is sometimes not very distinct [55].

As mentioned above, the understanding of the current flow path is critical to estimate ρ_c . First, we reveal whether ρ_c is characterized by the channel width (W) or the contact area ($A = Wd$) by using a multiprobe device with different contact areas [3]. All of the data in this section are obtained by the conventional electron beam (EB) lithography technique with an organic resist. In the next section, the resist-free metal deposition technique is applied to obtain ρ_c , and the comparisons of with and without resist residue are addressed. Figure 5.13a shows the four-layer graphene device with six sets of four-probe configurations (#1 – #6). Ni was employed as the contact metal. The devices with different contact areas for the source and the drain were fabricated, and the contact area for the voltage probes was kept constant to avoid uncertain effects from the voltage probes. The R_c was

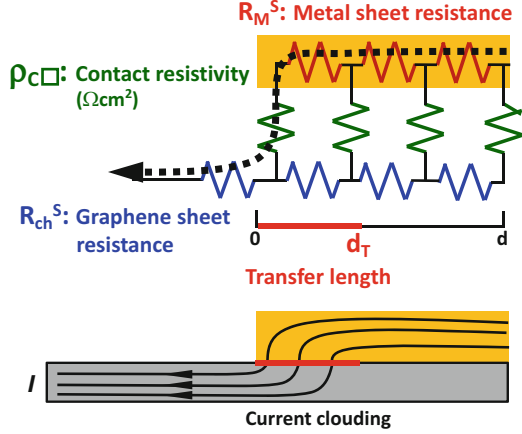
Fig. 5.13 (a) Optical micrograph of the four-layer graphene device with six sets of four-probe configurations (#1–#6). The contact metal is Ni. (b) Schematic of the device. (c) Two types of contact resistivity, $R_c A$ and $R_c W$, extracted by a four-probe measurement from the devices in (a). The unit for $\rho_c = R_c A$ is $\Omega \mu\text{m}^2$, while it is $\Omega \mu\text{m}$ for $\rho_c = R_c W$



calculated by $R_c = 1/2(R_{\text{total}} - R_{\text{ch}} \times L/l)$, where R_{total} is the total resistance between the source and the drain, R_{ch} is the channel resistance between the two voltage probes, L is the length between the source and the drain, and l is the length between the two voltage probes, as shown in Fig. 5.13b. Figure 5.13c shows the relationship between the contact area and two types of contact resistivities, $\rho_c^A = R_c A$ and $\rho_c^W = R_c W$, which were extracted by the four-probe measurements. ρ_c^A increases with increasing contact area, whereas ρ_c^W is nearly constant for all of the devices. This indicates that ρ_c is not characterized by A but W instead, i.e., the current flows mainly through the edge of the graphene/metal contact. In other words, the current crowding takes place at the edge of the contact metal.

Next, to understand the edge conduction in the graphene/metal contact, the current flow path is discussed based on the transmission line model, as shown in Fig. 5.14 [55]. In an equivalent circuit of the transmission line model, there are three types of resistance: the sheet resistance of the metal (R_M^S), the sheet resistance of graphene (R_{ch}^S), and ρ_c . It should be noted that the unit of ρ_c is defined as Ωcm^2 . The edge or area conduction can be presumed by considering the relative magnitudes of R_M^S and R_{ch}^S . Because R_M^S is smaller than R_{ch}^S , it is assumed that the current flows preferentially in the metal to follow the path of least resistance and

Fig. 5.14 Schematic of the transmission line model for the metal/graphene contact



that it enters graphene at the edge of the contact. Although a low value of R_{ch}^S might be expected from the high mobility of graphene, this is not the case because of the much smaller carrier density compared with that of the metal.

In reality, however, the current does not flow just at the contact edge line. Thus, it is quite useful to estimate d_T . The d_T is approximately characterized by the relative magnitude of R_{ch}^S and ρ_c as

$$d_T = \sqrt{\frac{\rho_c}{R_{ch}^S}}, \quad (5.1)$$

where the metal sheet resistance is neglected [55]. Hereafter, the graphene/metal contact is more accurately described by using both ρ_c and d_T instead of the edge-normalized ρ_c . To quantitatively determine ρ_c , the CBK structure is used, as shown in Figs. 5.12c and 5.15a [3]. Figure 5.15b shows ρ_c and d_T as a function of V_{BG} . At a high gate voltage ($n = \sim 5 \times 10^{12} \text{ cm}^{-2}$), ρ_c is $\sim 5 \times 10^{-6} \Omega \text{ cm}^2$. Furthermore, under the assumption that R_M^S is much smaller than R_{ch}^S , the sheet resistance of graphene is required to estimate d_T in Eq. (5.1). Because the sheet resistance of graphene was not available from the two-probe geometry shown in Fig. 5.15a, both the low and high mobilities that were measured previously [57, 58] were used for the present analysis. The apparent contact length is $\sim 4 \mu\text{m}$, but only $\sim 1 \mu\text{m}$ is effective for the current transfer in the present experiment. Because d_T exhibits similar values for devices with the same ρ_c , the current crowding at the contact edge is always observed for the devices with a contact length longer than d_T , as shown in Fig. 5.13c. If the contact length becomes shorter than d_T , a transition from edge conduction to area conduction will occur. With decreasing the contact length, the increase in rc is clearly observed [11, 59].

The mountain-like V_{BG} dependence of ρ_c observed in Fig. 5.15b suggests that the carrier density in graphene underneath the Ni electrode is modulated by V_{BG} .

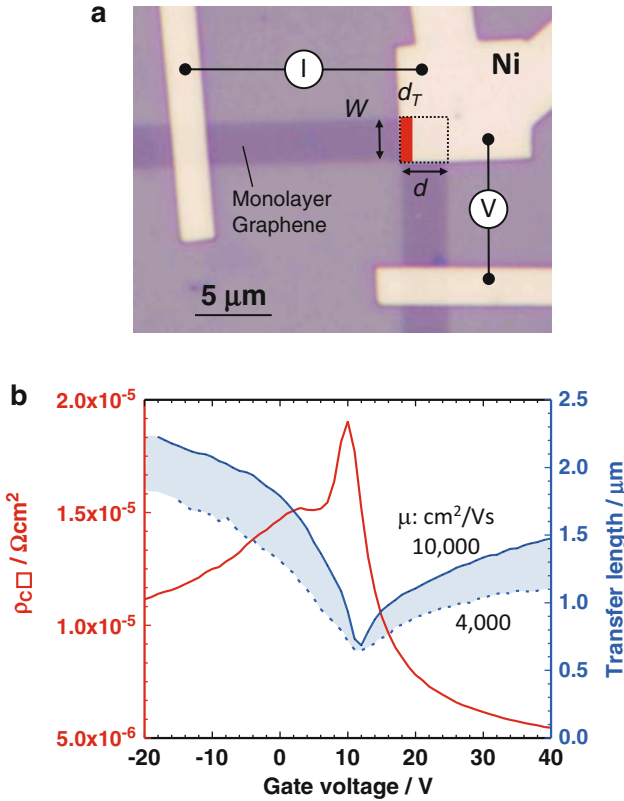


Fig. 5.15 (a) Optical micrograph of the CBK structure for monolayer graphene with a *rectangular shape*. (b) ρ_c and d_T as a function of V_{BG}

This carrier density modulation was first proposed for Ti/Pd/Au contacts because the drain current at the DP increases with increasing V_G , even for a graphene FET device in which the entire channel region is completely covered by the topgate [60–62]. This consideration is supported from the C_Q measurement for the resist-processed Ni electrode case in Fig. 5.6b. Here, the carrier density modulation in graphene just underneath the Ni electrode is revealed by the electron transport measurement as well. Figure 5.16a, b shows the monolayer graphene multiterminal device structure with different Ni electrode lengths (L_M) and the definition of the graphene/metal double-layered structure. Generally, the source–drain current flows through the metal on the graphene channel because the resistivity of the metal is considerably lower than that of graphene. However, with decreasing L_M , the current flows preferentially through graphene due to the contribution of the graphene/metal contact resistance. The resistivities of the graphene/metal double-layered structures with different L_M are measured as a function V_{BG} , as shown in Fig. 5.16c [35]. As L_M becomes shorter, the resistivity of the graphene/metal double-layered structure

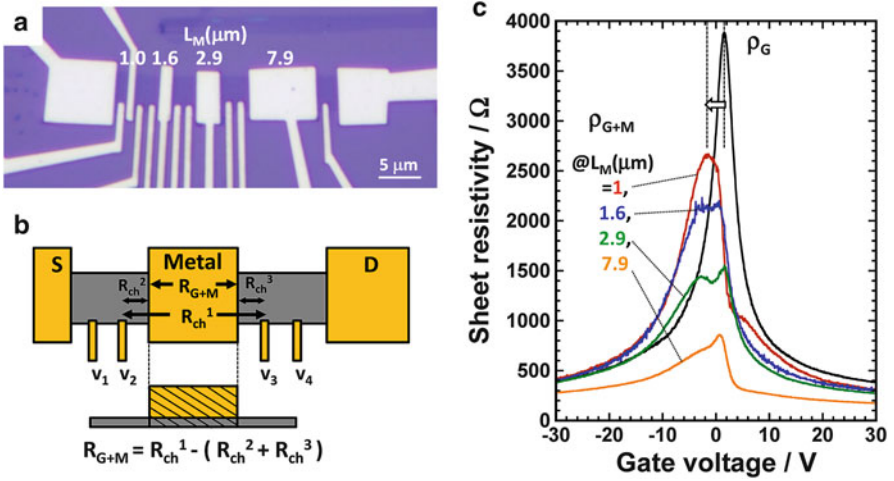


Fig. 5.16 (a) Optical micrograph of the fabricated monolayer graphene FET device showing the four metal electrodes on the graphene channel. The contact metal was Ni, and ohmic contacts were confirmed for all electrodes. (b) Schematic *top* and *side views* of the device for extracting the resistivity of the graphene/metal double-layered structure. (c) Sheet resistivities of intrinsic graphene channel (ρ_G) and graphene/metal double layers with various L_M as a function of V_{BG}

clearly shows ambipolar behavior, especially for $L_M = 1.0 \mu\text{m}$. The carrier density of the metal cannot be modulated because of its large *DOS*. Therefore, the clear carrier density modulation of the graphene/metal double-layered structure is direct experimental evidence of the carrier modulation of graphene underneath the Ni electrode.

In order to understand this experiment more clearly, a simple resistor network model, as shown in Fig. 5.17a, is used to calculate the current flow behavior in the graphene/metal double-layered structure. The sheet resistance of the graphene underneath the metal (R_G^M) is assumed to be identical to the sheet resistance of intrinsic graphene (R_G). The ρ_c and L_M are used as input parameters. As expected, the current flows more preferentially through the graphene for larger ρ_c and shorter L_M , as shown in Fig. 5.17. Therefore, the results in Fig. 5.16c do not mean that the degree of the carrier density modulation of graphene below the metal became more significant with decreasing L_M but that the current flow ratio in the graphene increased with decreasing L_M . It should be noted that this is the case for the resist-processed Ni electrode.

5.5.2 Correlation Between Contact Resistivity and DOS

In this section, the resist-free metal deposition technique is also applied to obtain ρ_c , and the comparisons of with and without resist residue are addressed. TLM

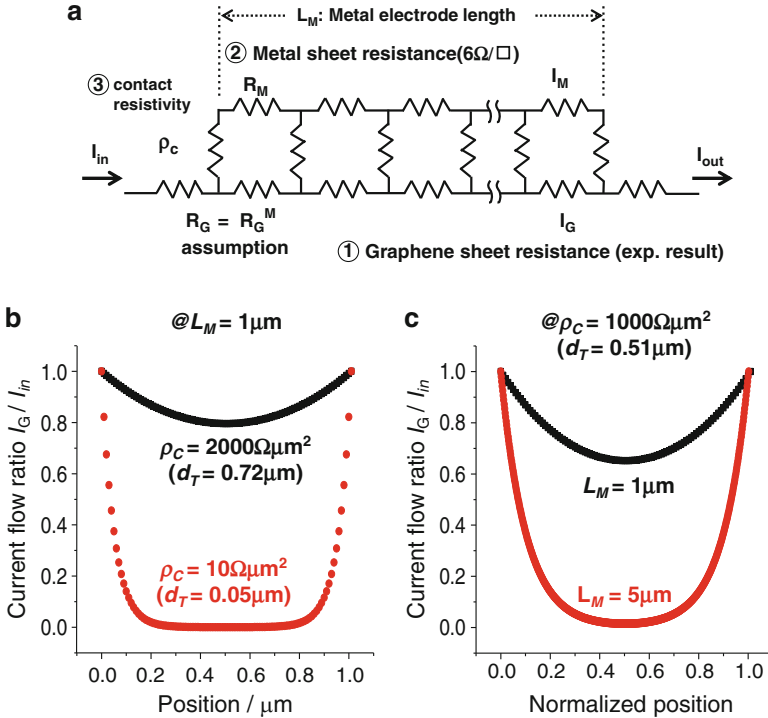


Fig. 5.17 (a) Resistor network model for the device in Fig. 5.16. (a) Current flow ratio in graphene (I_G/I_{in}) calculated at $L_M = 1 \mu\text{m}$ and $V_{BG} = \text{DP}$ for various ρ_c . The larger ρ_c prevents the current from flowing into the metal. (b) Current flow ratio in graphene (I_G/I_{in}) calculated at $\rho_c = 1 \times 10^3 \Omega\mu\text{m}^2$ and $V_{BG} = \text{DP}$ for various L_M . The current flow ratio in graphene increases with decreasing L_M

pattern is selected in this study because CBK requires the manufacturing of the graphene shape. Multielectrodes are deposited onto the long as-transferred graphene ($\sim 50 \mu\text{m}$) using the SiN membrane mask without any resist process, as shown in Fig. 5.18. For the estimation of ρ_c , TLM or four-probe resistance methods are used. The obtained ρ_c values are $\sim 1,500$, $\sim 1,000$, and $\sim 50 \Omega\mu\text{m}$ for the resist-free and resist-processed Ni devices and the resist-free Au device, respectively. Although the considerable improvement of ρ_c was expected by employing the resist-free process for Ni thanks to the increase in the DOS by the π - d coupling, no significant improvement was observed. In contrast, ρ_c for the resist-free Au device was lowest in all the previous reports.

The correlation between the DOS of graphene and ρ_c is addressed. The highest DOS at a high E_F is selected, as shown by arrows in Fig. 5.6b. Figure 5.19 shows the linear relationship between ρ_c and the inverse of the DOS. The reduction of the distance between graphene and the metal due to the lack of resist residue generally leads to the increase in the transmission probability. Because the contribution to ρ_c

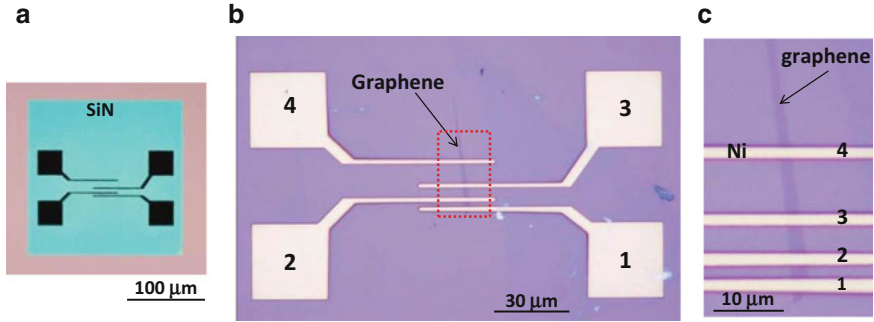
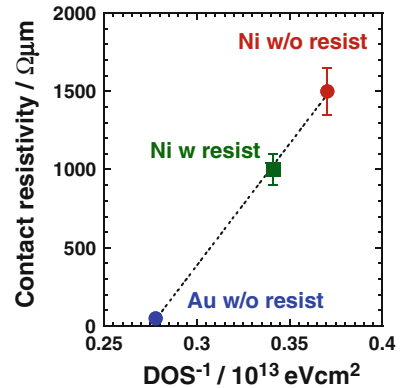


Fig. 5.18 (a) The SiN stencil mask supported by the Si substrate with a 200- μm square window. The TLM pattern was fabricated by the FIB instrument. (b) Optical image of the I - V device with the TLM structure fabricated by the resist-free metal deposition technique. (c) Magnified image of dotted box region in (b)

Fig. 5.19 Relationship between ρ_c and the inverse of the DOS, where the largest DOS, as shown by the arrows in Fig. 5.6b, was selected



by the DOS of graphene and the distance are not separated, the dominant factor to reduce ρ_c is not clear yet. As can be seen from Fig. 5.19, however, it is true that the low ρ_c for the resist-free Au device is due to both the reduction of the graphene/Au distance and the largest DOS achieved by the large E_F modulation.

It should be emphasized that the low ρ_c achieved in the resist-free Au device is not suitable for the topgate device because the DOS of graphene underneath the metal electrode cannot be modulated by the topgate, as shown in Fig. 5.20. When ρ_c is reduced by adjusting V_{BG} , the Dirac point voltage for the V_{TG} sweep is also shifted [63], which is not proper for the device operation. Therefore, we initially expected a large increase in the DOS based on the strong π - d coupling for Ni because this can be used even for the topgate device structure. This, however, is not the case, suggesting that the selection of the contact metal might not help in reducing ρ_c , since the graphene/Ni interaction is expected to be highest in the metals.

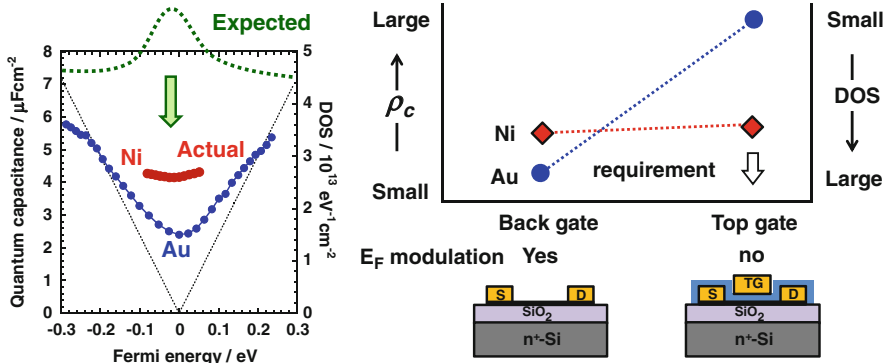


Fig. 5.20 Schematic illustration showing the contact resistivity (*left*) and the DOS (*right*) for the different device structures

Table 5.1 summarizes the ρ_c values reported so far for different metals. There are many reports on ρ_c for different metals. However, the difference in the work function is not obvious in the case of the resist process [12]. The resist residue preserves the graphene's characteristics even underneath the metal electrodes, resulting in the E_F modulation by the backgate bias. Therefore, the notable difference in different metals is blinded.

For the further reduction of ρ_c , there are many attempts. From the viewpoint of the clean interface, the organic-free process using the AlOx layer [6] and the cleaning of graphene surface by the ultraviolet/ozone [64] or O₂ plasma [9] are reported. From the viewpoint of the contact formation, the double contact formation [13, 65, 66], contact area patterning [67], carbide formation [68], the graphitic contact formation [69], and the edge contact [70] are reported. The graphitic contact could be one of the solutions for reducing ρ_c because the DOS of graphite is much larger than that of graphene and because better contact properties have been reported for carbon nanotubes [71]. This process could be useful because the resist residue on graphene will be also converted to graphite.

5.6 The Requirement for Contact Resistivity

Finally, the ρ_c value required for miniaturized graphene FETs is discussed. Consider that the condition on ρ_c is such that the ratio of R_c with R_{ch} becomes less than 10 % because the FET performance should be mainly characterized by R_{ch} . It can be expressed by the following equation:

$$R_c/R_{ch} = \frac{\rho_c}{dW} / R_{ch}^S \frac{L}{W} = \rho_c/R_{ch}^S dL = 0.1. \quad (5.2)$$

Table 5.1 Reported contact resistivity

@300 K		Mechanical exfoliation					CVD			SiC	
Metal	Ni	Pd	Ti	Cu	Au	Graphite	Ti/Pd	Ti	Ti	Pt	
ρ_c Ωcm^2	$\sim 5 \times 10^{-6}$	1.5×10^{-6}		1×10^{-7}	1.4×10^{-7}				1.2×10^{-8}	3×10^{-7}	
Method & ref.	CBK ^[a] , TLM ^[b]	HTA ^[c]		TLM ^[d]	4P ^[e]				TLM ^[b]	TLM ^[o]	
Resist	w	w		w	w/o					O ₂ plasma	
ρ_c $\Omega\mu\text{m}$	500	1,500	250		50	250	150	200	60		
Method & ref.	4P ^[f]	4P ^[g]	TLM ^[i] , 4P ^[j]		TLM ^[g]	4P ^[k]	4P ^[l]	TLM ^[m]	TLM ^[n]		
Resist	w	w/o	w ^[h] , w/o ^[p]	w	w/o	w/o	w/o	Ozone			

References in Table 5.1: [a] K. Nagashio, et al., *APL*, 2010, **97**, 143514. [b] A. Venugopal, et al., *APL*, 2010, **96**, 013512. [c] K. L. Gross, et al., *Nature Nanotech.*, 2011, **6**, 287. [d] C. E. Malec, et al., *Solid State Comm.*, 2011, **151**, 1791. [e] C. E. Malec, et al., *PRB*, 2011, **84**, 033407. [f] K. Nagashio, et al., *IEDM Tech. Dig.*, 2009, 565. [g] R. Ifuku, et al., *APL*, 2013, **103**, 033514. [h] F. Xia, et al., *Nature Nanotech.*, 2011, **6**, 179. [i] S. Russo, et al., *Phys. E*, 2010, **42**, 677. [j] P. Blake, et al., *Solid State Comm.*, 2009, **149**, 1068. [k] K. Nagashio, et al., *IEDM Tech. Dig.*, 2012, 68. [l] A. Hsu, et al., *IEEE EDL*, 2011, **32**, 1008. [m] W. Li, et al., *APL*, 2013, **102**, 183110. [n] J. S. Moon, et al., *APL*, 2012, **100**, 203512. [o] J. A. Robinson, et al., *APL*, 2011, **98**, 053103. [p] L. Wang, et al., *Science*, 2013, **342**, 614

HTA (heat transfer analysis), CBK (cross-bridge Kelvin), TLM (transfer length method), and 4P (4-probe measurement). The contact resistivity is a physical property and should be estimated as the unit of Ωcm^2 . However, the unit of $\Omega\mu\text{m}$ is often used in the literature because of shorter transfer length than the contact length

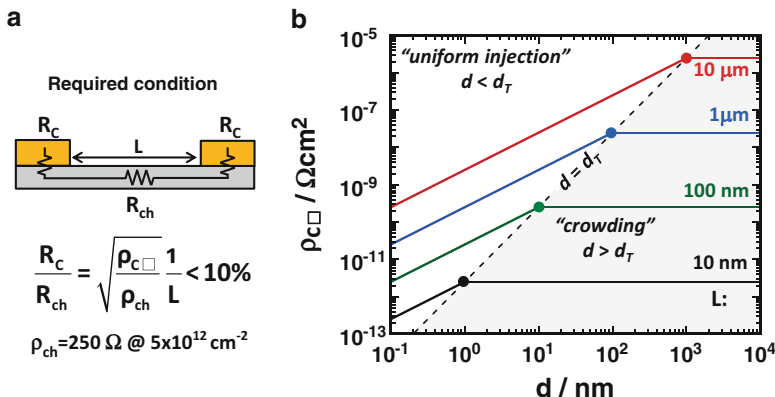


Fig. 5.21 (a) The condition where the contact resistance is negligible, that is, $R_c/R_{ch} = 0.1$. In this calculation, a typical value for $R_{ch}^S = 250 \Omega$ at $\mu = 5,000 \text{ cm}^2 \text{ V}^{-1} \text{ s}^{-1}$ and $n = 5 \times 10^{12} \text{ cm}^{-2}$ was used. (b) The ρ_c required for $R_c/R_{ch} = 0.1$ as a function of d for various L . ρ_c is constant for $d > d_T$ (crowding), while it decreases for $d < d_T$ (uniform injection)

Figure 5.21 shows the ρ_c required for $R_c/R_{ch} = 0.1$ as a function of d for various L . In this calculation, a typical value for $R_{ch}^S = 250 \Omega$ at $\mu = 5,000 \text{ cm}^2 \text{ V}^{-1} \text{ s}^{-1}$ and $n = 5 \times 10^{12} \text{ cm}^{-2}$ was used. The dotted line that indicates the trace of d_T for various L was calculated by Eq. (5.1). It separates the regions of “crowding” and “uniform injection.” It is evident that the requirement of ρ_c becomes more severe when the contact length d becomes smaller than d_T . For a channel length of $10 \mu\text{m}$, the present status of ρ_c for the Ni electrode satisfies the requirement. For the channel length of 100 nm , however, the required ρ_c value is smaller than $10^{-9} \Omega \text{ cm}^2$, which is four orders of magnitude lower than the present value. d_T is on the order of 10 nm . This ρ_c value is smaller than that required for the metal/Si contact ($\sim 10^{-8} \Omega \text{ cm}^2$) because the R_{ch}^S of graphene is lower than that of Si.

5.7 Conclusions and Future Outlook

Is graphene organic or inorganic? It depends on the situation. The research on graphene should be carried out from both sides of organic and inorganic semiconductors. One of the good examples for the organic viewpoint is the fact that the resist residue blinds the intrinsic properties of graphene/metal interaction. In this review, by using the resist-free metal deposition technique, the “intrinsic” physical properties of graphene underneath the metal electrode and the “intrinsic” chemical interaction between graphene and metal are focused. According to the recent researches, one of the effective guidelines to reduce ρ_c is the increase in the DOS of graphene underneath the metal electrode, such as graphitic contact.

Acknowledgements The authors acknowledge the present and former colleagues and students, especially R. Ifuku and T. Moriyama. We thank Drs. Nabatame and Narushima, NIMS, for the fabrication of the SiN membrane masks. We are grateful to Covalent Materials Corporation for kindly providing the Kish graphite. K. N. acknowledges the financial support from the JSPS through its “Funding Program for World-Leading Innovative R&D on Science and Technology (FIRST Program)”, from a Grant-in-Aid for Scientific Research on Innovative Areas and for Young scientists, and from PRESTO, Japan Science and Technology Agency by the Ministry of Education, Culture, Sports, Science and Technology in Japan.

References

1. Nagashio K, Nishimura T, Kita K, Toriumi A (2009) Metal/graphene contact as a performance killer of ultra-high mobility graphene -analysis of intrinsic mobility and contact resistance. *IEDM Tech Dig* 565
2. Blake P, Yang R, Morozov SV, Schedin F, Ponomarenko LA, Zhukov AA, Nair RR, Grigorieva IV, Novoselov KS, Geim AK (2009) Influence of metal contacts and charge inhomogeneity on transport properties of graphene near the neutrality point. *Solid State Commun* 149:1068
3. Nagashio K, Nishimura T, Kita K, Toriumi A (2010) Contact resistivity and current flow path at metal/graphene contact. *Appl Phys Lett* 97:143514
4. Venugopal A, Colombo L, Vogel EM (2010) Contact resistance in few and multilayer graphene devices. *Appl Phys Lett* 96:013512
5. Russo S, Cracuin MF, Yamamoto M, Morpurgo AF, Tarucha S (2010) Contact resistance in graphene-based devices. *Physica E* 42:677
6. Hsu A, Wang H, Kim KK, Kong K, Palacios T (2011) Impact of graphene interface quality on contact resistance and RF device performance. *IEEE Electron Device Lett* 32:1008
7. Nagashio K, Toriumi A (2011) Density-of-states limited contact resistance in graphene field-effect transistors. *Jpn J Appl Phys* 50:070108
8. Xia F, Perebeinos V, Lin Y-M, Wu Y, Avouris P (2011) The origins and limits of metal-graphene junction resistance. *Nat Nanotech* 6:179
9. Robinson JA, LaBella M, Zhu M, Hollander M, Kasarda R, Hughes Z, Trumbull K, Cavalero R, Snyder D (2011) Contacting graphene. *Appl Phys Lett* 98:053103
10. Malec CE, Davidovic D (2011) Vacuum-annealed Cu contacts for graphene electronics. *Solid State Commun* 151:1791
11. Franklin AD, Han S-J, Bol AA, Haensch W (2011) Effects of nanoscale contacts to graphene. *IEEE Electron Device Lett* 32:1035
12. Watanabe E, Conwill A, Tsuya D, Koide Y (2012) Low contact resistance metals for graphene based devices. *Diam Relat Mater* 24:171
13. Franklin AD, Han S-J, Bol AA, Perebeinos V (2012) Double contacts for improved performance of graphene transistors. *IEEE Electron Device Lett* 33:17
14. Wolf EL (2012) *Principles of electron tunneling spectroscopy*. Oxford University Press, New York
15. Sze SM, Ng KK (2007) *Physics of semiconductor devices*. John Wiley & Sons, Hoboken, New Jersey
16. Tersoff J (1999) Contact resistance of carbon nanotubes. *Appl Phys Lett* 74:2122
17. Floyd RB, Walmsley DG (1978) Tunneling conductance of clean and doped Al-I-Pb junctions. *J Phys C: Solid State Phys* 11:4601
18. Heine V (1965) Theory of surface states. *Phys Rev* 138:A1689
19. Burns G (1985) *Solid state physics*. Academic Press, Orlando, Florida
20. Miyazaki H, Odaka S, Sato T, Tanaka S, Goto H, Kanda A, Tsukagoshi K, Ootuka Y, Aoyagi Y (2008) Inter-layer screening length to electric field in thin graphite film. *Appl Phys Express* 1:034007

21. Giovannetti G, Khomyakov PA, Brocks G, Karpan VM, van der Brink J, Kelly PJ (2008) Doping graphene with metal contacts. *Phys Rev Lett* 101:026803
22. Bangert U, Bleloch A, Gass MH, Seepujak A, van den Berg J (2010) Doping of few-layered graphene and carbon nanotubes using ion implantation. *Phys Rev B* 81:245423
23. Yuge K (2009) Phase stability of boron carbon nitride in a heterographene structure: a first-principles stud. *Phys Rev B* 79:144109
24. Khomyakov PA, Giovannetti G, Rusu PC, Brocks G, van den Brink J, Kelly PJ (2009) First-principles study of the interaction and charge transfer between graphene and metals. *Phys Rev B* 79:195425
25. Vanin M, Mortensen JJ, Kelkkanen AK, Garcia-Lastra JM, Thygesen KS, Jacobsen KW (2010) Graphene on metals: a van der Waals density functional study. *Phys Rev B* 81 081408(R)
26. Oshima C, Nagashima A (1997) Ultra-thin epitaxial films of graphite and hexagonal boron nitride on solid surfaces. *J Phys Condens Matter* 9:1
27. Varykhalov A, Sanchez-Barriga J, Shkin AM, Biswas C, Vescovo E, Rybkin A, Marchenko D, Rader O (2008) Electronic and magnetic properties of quasifreestanding graphene on Ni. *Phys Rev Lett* 101:157601
28. Hammer B, Norskov JK (1995) Why gold is the noblest of all the metals. *Nature* 376:238
29. Hammer B, Norskov JK (2000) Theoretical surface science and catalysis—calculations and concepts. *Adv Catal* 45:71
30. Batzill M (2012) The surface science of graphene: metal interfaces, CVD synthesis, nanoribbons, chemical modifications, and defects. *Surf Sci Rep* 67:83
31. Ishigami M, Chen JH, Cullen WG, Fuhrer MS, Willians ED (2007) Atomic structure of graphene on SiO₂. *Nano Lett* 7:1643
32. Cheng Z, Zhou Q, Wang C, Li Q, Wang C, Fang Y (2011) Toward intrinsic graphene surfaces: a systematic study on thermal annealing and wet-chemical treatment of SiO₂-supported graphene devices. *Nano Lett* 11:767
33. Goossens AM, Calado VE, Barreiro A, Watanabe K, Taniguchi T, Vandersypen LMK (2012) Mechanical cleaning of graphene. *Appl Phys Lett* 100:073110
34. Acharya M, Strano MS, Mathews JP, Billinge SJL, Petkov V, Subramoney S, Foley HC (1999) Simulation of nanoporous carbons: a chemically constrained structure. *Philos Mag B* 79:1499
35. Moriyama T, Nagashio K, Nishimura T, Toriumi A (2013) Carrier density modulation in graphene underneath Ni electrode. *J Appl Phys* 114:024503
36. Chen Z, Appenzeller J (2008) Mobility extraction and quantum capacitance impact in high performance graphene field-effect transistor devices. *IEDM Tech Dig* 509
37. Ponomarenko LA, Yang R, Grobachev RV, Blake P, Mayorov AS, Novoselov KS, Katsnelson MI, Geim AK (2010) Density of states and zero landau level probed through capacitance of graphene. *Phys Rev Lett* 105:136801
38. Xu H, Zhang Z, Wang Z, Wang S, Liang X, Peng L-M (2011) Quantum capacitance limited vertical scaling of graphene field-effect transistor. *ACS NANO* 5:2340
39. Nagashio K, Nishimura T, Toriumi A (2013) Estimation of residual carrier density near the Dirac point in graphene through quantum capacitance measurement. *Appl Phys Lett* 102:173507
40. Fang T, Konar A, Xing H, Jena D (2007) Carrier statistics and quantum capacitance of graphene sheets and ribbons. *Appl Phys Lett* 91:092109
41. Ifuku R, Nagashio K, Nishimura T, Toriumi A (2013) The density of states of graphene underneath a metal electrode and its correlation with the contact resistivity. *Appl Phys Lett* 103:033514
42. Li G, Luican A, Andrei EY (2009) Scanning tunneling spectroscopy of graphene on graphite. *Phys Rev Lett* 102:176804
43. Monch W (2004) *Electronic properties of semiconductor interface*. Springer, Berlin
44. Tersoff J (1984) Schottky barrier heights and the continuum of gap states. *Phys Rev Lett* 52:465
45. Ziman JM (1976) *Principles of the theory of solids*. Cambridge University Press, Cambridge

46. Pi K, McCreary KM, Bao W, Han W, Chiang YF, Li Y, Tsai S-W, Lau CN, Kawakami RK (2009) Electronic doping and scattering by transition metals on graphene. *Phys Rev B* 80:075406
47. Xia F, Mueller T, Golizadeh-Mojarad R, Feritag M, Lin Y-M, Tsang J, Perebeinos V, Avouris P (2009) Photocurrent imaging and efficient photon detection in a graphene transistor. *Nano Lett* 9:1039
48. Yu Y-J, Zhao Y, Ryu S, Brus LE, Kim KS, Kim P (2009) Tuning the graphene work function by electric field effect. *Nano Lett* 9:3430
49. Nagamura N, Horiba K, Toyoda S, Kurosumi S, Shinohara T, Oshima M, Fukidome H, Suemitsu M, Nagashio K, Toriumi A (2013) Direct observation of charge transfer region at interfaces in graphene devices. *Appl Phys Lett* 102:241604
50. Khomyakov PA, Starikov AA, Brocks G, Kelly PJ (2010) Nonlinear screening of charges induced in graphene by metal contacts. *Phys Rev B* 82:115437
51. Huard B, Stander N, Sulpizio JA, Goldhaber-Gordon D (2008) Evidence of the role of contacts on the observed electron-hole asymmetry in graphene *Phys Rev B* 78 121402(R)
52. Huard B, Sulpizio JA, Stander N, Todd K, Yang B, Goldhaber-Gordon D (2007) Transport measurements across a tunable potential barrier in graphene. *Phys Rev Lett* 98:236803
53. Nouchi R, Shiraishi M, Suzuki Y (2008) Transfer characteristics in graphene field-effect transistors with Co contacts. *Appl Phys Lett* 93:152104
54. Lee EJJ, Balasubramanian K, Weitz RT, Burghard M, Kern L (2008) Contact and edge effects in graphene devices. *Nat Nanotech* 3:486
55. Schroder DK (2006) Semiconductor material and device characterization. John Wiley & Sons, Hoboken, New Jersey
56. Proctor SJ, Linholm LW, Mazer JA (1983) Direct measurements of interfacial contact resistance, end contact resistance, and interfacial contact layer uniformity. *IEEE Trans Electron Device* 30:1535
57. Nagashio K, Nishimura T, Kita K, Toriumi A (2009) Mobility variations in mono- and multi-layer graphene films. *Appl Phys Express* 2:025003
58. Nagashio K, Nishimura T, Kita K, Toriumi A (2010) Systematic investigation of the intrinsic channel properties and contact resistance of monolayer and multilayer graphene field-effect transistor. *Jpn J Appl Phys* 49:051304
59. Xu H, Wang S, Zhang Z, Wang Z, Xu H, Peng L-M (2012) Contact length scaling in graphene field-effect transistors. *Appl Phys Lett* 100:103501
60. Chen Z, Appenzeller J (2009) Gate modulation of graphene contacts – on the scaling of graphene FETs. *Symp VLSI Tech Dig* 128
61. Berdebes D, Low T, Sui Y, Appenzeller J, Lundstrom MS (2011) Substrate gating of contact resistance in graphene transistors. *IEEE Trans Electron Device* 58:3925
62. Knoch J, Chen Z, Appenzeller J (2012) Properties of metal-graphene contacts. *IEEE Trans Nanotechnol* 11:513
63. Huang B-C, Zhang M, Wang Y, Woo J (2011) Contact resistance in top-gated graphene field-effect transistors. *Appl Phys Lett* 99:032107
64. Li W, Liang Y, Yu D, Peng L, Pernstich KP, Shen T, Hight Walker AR, Cheng G, Hacker CA, Richter CA, Li Q, Gundlach DJ, Liang X (2013) Ultraviolet/ozone treatment to reduce metal-graphene contact resistance. *Appl Phys Lett* 102:183110
65. Gong C, Hinojos D, Wang W, Nijem N, Shan B, Wallace RM, Cho K, Chabal Y (2012) Metal-graphene-metal sandwich contacts for enhanced interface bonding and work function control. *ACS NANO* 6:5381
66. Adamska L, Lin Y, Ross AJ, Batzill M, Oleynik II (2012) Atomic and electronic structure of simple metal/graphene and complex metal/graphene/metal interfaces. *Phys Rev B* 85:195443
67. Smith JT, Franklin AD, Farmer DB, Dimitrakopoulos CD (2013) Reducing contact resistance in graphene devices through contact area patterning. *ACS NANO* 7:3661
68. Nagareddy VK, Nikitina IP, Gaskill DK, Tedesco JL, Myers-Ward RL, Eddy CR, Goss JP, Wright NG, Horsafall AB (2011) High temperature measurements of metal contacts on epitaxial graphene. *Appl Phys Lett* 99:073506

69. Nagashio K, Ifuku R, Moriyama T, Nishimura T, Toriumi A (2012) Intrinsic graphene/metal contact IEDM Tech Dig 68
70. Wang L, Meric I, Huang PY, Gao Q, Gao Y, Tran H, Taniguchi T, Watanabe K, Campos LM, Muller DA, Guo J, Kim P, Hone J, Shepard KL, Dean CR (2013) One-dimensional electrical contact to a two-dimensional material. *Science* 342:614
71. Chai Y, Hazeghi A, Takei K, Chen H-Y, Chan PCH, Javay A, Wong H-SP (2012) Low-resistance electrical contact to carbon nanotubes with graphitic interfacial layer. *IEEE Trans Electron Device* 59:12

Chapter 6

Low-Temperature Synthesis of Graphene and Fabrication of Top-Gated Field-Effect Transistors Using Transfer-Free Processes for Future LSIs

Daiyu Kondo and Shintaro Sato

Abstract High-quality graphene synthesis by chemical vapor deposition (CVD) on a substrate has been achieved recently. Although synthesized graphene is often transferred to another substrate for electrical measurements, this transfer process may not be appropriate for applications using a large substrate, including large-scale integrated circuits (LSIs). Therefore, it is desirable that graphene channels are formed directly on a substrate without such transfer processes. Furthermore, graphene should be formed at low temperature to avoid possible adverse effects on the substrate.

In this study, thickness-controlled growth of few-layer and multilayer graphene was demonstrated at 650 °C by the thermal CVD method, and top-gated field-effect transistors (FETs) were fabricated directly on a large SiO₂/Si substrate without using graphene-transfer processes. Graphene was synthesized on patterned Fe films. The iron was subsequently etched after both ends of the graphene were fixed by source and drain electrodes, leaving the graphene channels bridging the electrodes all over the substrate. Top-gated FETs were then made after covering the channels with HfO₂. The fabricated devices exhibit ambipolar behavior and can sustain a high-density current. The growth mechanism of graphene was also investigated. In addition, a novel technique for synthesizing graphene directly on insulating substrate is also described.

Keywords Graphene • Chemical vapor deposition • Transistor • Interconnect • Transfer-free process

D. Kondo (✉) • S. Sato (✉)
AIST, Tsukuba, Japan

Fujitsu Laboratories Ltd., Atsugi, Japan
e-mail: kondo.daiyu@jp.fujitsu.com; sato.shintaro@jp.fujitsu.com

6.1 Introduction

Graphene has been attracting much attention since a report on its electrical properties was published in 2004 [1]. It has unique properties arising from its peculiar electronic band structure, and an extraordinary high carrier mobility of $200,000 \text{ cm}^2/\text{Vs}$ has been reported for it [2]. In addition, graphene has excellent mechanical and thermal properties [3, 4]. These properties make graphene a promising material for future nanoelectronics.

One of the promising applications of graphene is in field-effect transistors (FETs). Many studies using exfoliated graphene as a transistor channel have been reported [5–10], and a field-effect mobility of $8,600 \text{ cm}^2/\text{Vs}$ [8, 10] and an intrinsic cutoff frequency of 427 GHz [9] have been reported for top-gated transistors. However, for real-world applications, use of exfoliated graphene is not practical. From this point of view, synthesis of graphene by chemical vapor deposition (CVD) on a substrate has been attempted [8, 10–15]. In these studies, graphene was synthesized on a metal catalyst film (Ni or Cu) deposited on an insulating substrate and/or a metal catalyst foil and transferred to another substrate for electrical measurements. The source gas for CVD was mainly CH_4 and the growth temperature was $800\text{--}1,000 \text{ }^\circ\text{C}$. These studies are an important step toward making electronics using graphene a reality. However, the transfer process may not be appropriate for applications using a large substrate, including large-scale integrated circuits (LSIs) and large-screen displays. We believe that graphene channels should be formed directly on a substrate without such transfer processes. Furthermore, lower-temperature synthesis of graphene is required for substrates which are vulnerable to heat.

6.2 Low-Temperature Synthesis of Graphene with Chemical Vapor Deposition

In this section, we explain the synthesis of few-layer and multilayer graphene by thermal CVD method at low temperature [16]. As the source gas, C_2H_2 diluted by Ar was used, which is well known to be suitable for low-temperature synthesis of nano-carbon materials, such as carbon nanotubes. The CVD chamber was a cold-wall type with a heating stage. The total gas pressure was 1 kPa and the substrate temperature was $650 \text{ }^\circ\text{C}$, which was measured with a thermocouple bonded onto a Si substrate. As a catalyst, an Fe film was deposited onto a SiO_2/Si substrate by conventional magnetron sputtering. The concentration of C_2H_2 , growth time, and Fe thickness were changed to optimize the growth conditions. The partial pressure of C_2H_2 ranged from 0.002 to 5 Pa. The growth time was varied from 1 to 20 min. The catalyst thickness was varied from 5 to 500 nm. The synthesized graphene was characterized by transmission electron microscopy (TEM) and Raman spectroscopy.

A few-layer graphene and multilayer graphene with various thicknesses were obtained by changing the partial pressure of C_2H_2 and growth time. The thickness as a function of the product of partial pressure and growth time is shown in Fig. 6.1a.

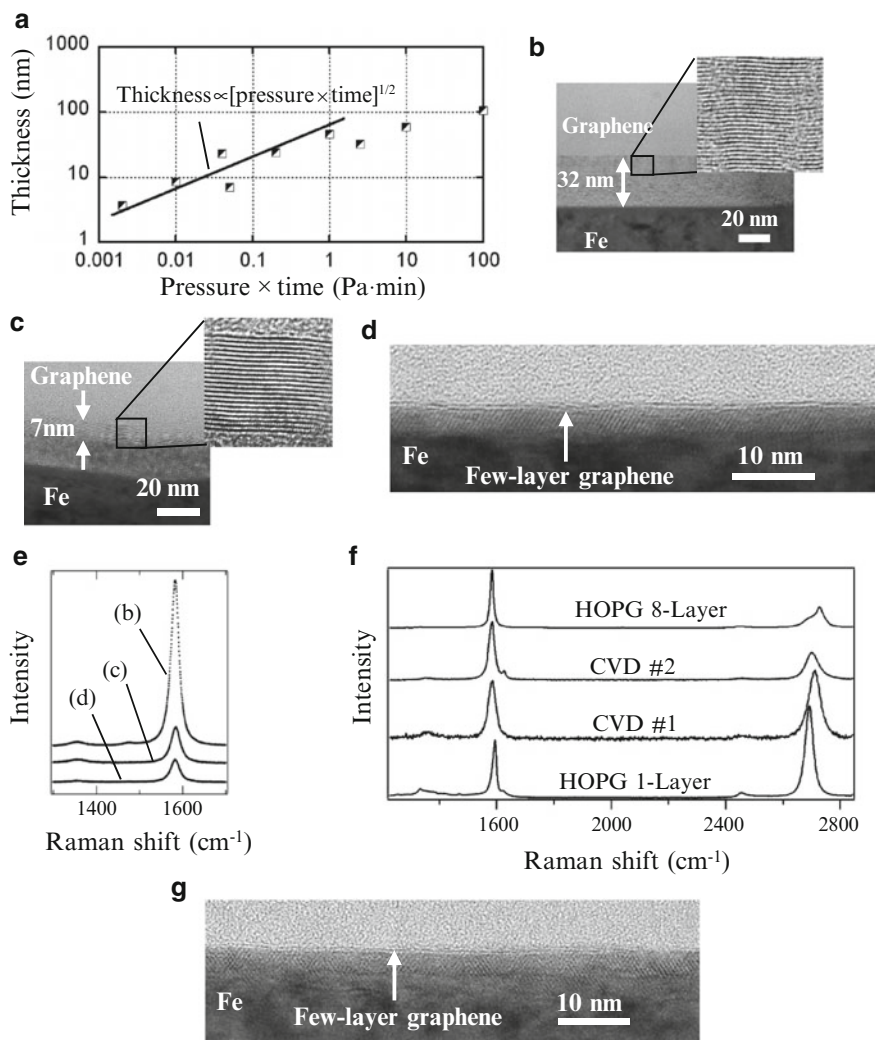


Fig. 6.1 (a) Dependence of graphene thickness on the product of partial pressure of C_2H_2 and growth time (*square symbols*). A fitted line for the square-root dependence is also shown. (b) Cross-sectional TEM image of 32-nm-thick multilayer graphene, (c) 7-nm-thick multilayer graphene, and (d) few-layer graphene. (e) Raman spectra of graphene samples shown in (b), (c), and (d). (f) Raman spectra of few-layer graphene at two different locations on the substrate (CVD #1, 2), together with spectra for single-layer graphene (HOPG 1-Layer) and 8-layer graphene (HOPG 8-Layer) exfoliated from HOPG. (g) Cross-sectional TEM image of few-layer graphene synthesized at 590 °C

In this case, the Fe thickness was 200 nm. The graphene thickness appears to be proportional to the square root of the product up to about 50 nm, as shown by the line in Fig. 6.1a. A similar dependency can be seen in the Deal-Grove model for SiO₂ growth by thermal oxidation of Si [17]. In this model, when the oxide film is thick, the thickness is proportional to the square root of the product of growth time and O₂ concentration at the surface. This dependence is caused by diffusion of O₂ in the oxide film. Similarly, our results suggest that the graphene growth may be governed by the diffusion of the source gas in the synthesized graphene (possibly at the grain boundaries). Cross-sectional TEM images of 32-nm- and 7-nm-thick multilayer graphene and few-layer (mostly bilayer) graphene are shown in Fig. 6.1b–d, respectively. Their Raman spectra with an excitation wavelength of 514.5 nm are shown in Fig. 6.1e. The partial pressure, growth time, and catalyst thickness for the few-layer graphene were 0.002 Pa, 1 min, and 500 nm, respectively. The ratio of the G band intensity to the D band intensity (G/D ratio) was ~40 for the multilayer graphene, while that for the few-layer graphene was ~15. The empirical equation by Cançado et al. [18] suggests that the crystallite size of the multilayer graphene shown in Fig. 6.1b is around 700 nm. There is a tendency for thicker multilayer graphene to exhibit a higher G/D ratio. This might be because the graphene at the interface with Fe tends to have more defects, although this issue has not been raised in previous studies [8, 10–13]. The Raman spectra including the G, D, and 2D bands for few-layer graphene are shown in Fig. 6.1f, along with those for graphene exfoliated from HOPG. The two lines for CVD graphene are typical spectra obtained at different positions on a substrate with a size of ~2 cm × 3 cm. The graphene shown in Fig. 6.1d was mostly bilayer over a cross-sectional TEM sample with a width of ~2 μm. The variations in the 2D band suggest those in the number of layers, as in cases with a Ni catalyst, where the number of layers varied from 1 to around 10 [8, 10, 11]. However, it is difficult to conclude it only from the Raman spectra, and further analyses would be required.

Although the synthesis temperature above may not be low enough to be accepted in the present Si LSI technology, there are ongoing efforts to lower the synthesis temperature of few-layer and multilayer graphene [19–23, 26]. Actually, we obtained few-layer graphene on a 200-nm Fe film at a lower temperature of 590 °C, as shown in Fig. 6.1e [19, 22, 26]. Furthermore, synthesis of few-layer graphene was recently performed with Au-Ni alloy [20] and Ni [21] as a catalyst at 450 and 460 °C, respectively. Graphene obtained at lower temperature tends to be more defective than that at higher temperature according to Raman analyses. Synthesizing high-quality graphene at low temperature would be a next important task for realizing LSIs utilizing graphene.

We have also found that the use of Fe films thinner than 10 nm tends to result in carbon nanotubes being formed. A schematic diagram showing the obtained products as a function of the catalyst thickness (x) is shown in Fig. 6.2 [19, 22, 26]. This phase diagram was obtained at 620 °C. It is possible to classify the products into five categories: (I) CNTs lying on the substrate, (II) vertically aligned CNTs, (III) vertically aligned CNTs combined with multilayer graphene on their top, (IV) nonuniform multilayer graphene, and (V) uniform multilayer graphene. Although

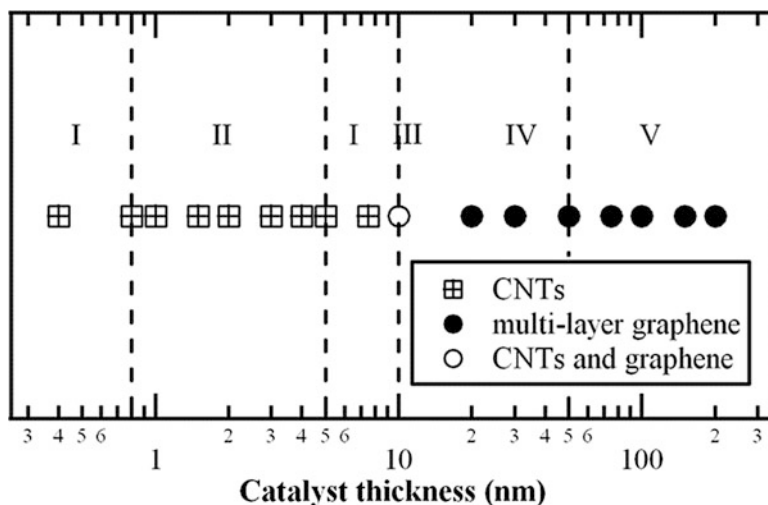


Fig. 6.2 A schematic diagram showing the obtained products as a function of the catalyst thickness

the products in the two catalyst-thickness ranges ($x < 0.8$ nm and $5 < x < 10$ nm) are classified into category I, their appearances are a little different from each other: there seems to be a larger number of CNTs for the thickness of $5 < x < 10$ nm. At an Fe thickness of 10 nm shown as a category III, vertically aligned CNTs with a flat structure on their top were obtained. The flat structure was found to be multilayer graphene as reported previously. This observation implies that transition from CNTs to multilayer graphene occurs at a catalyst thickness of around 10 nm. In category V, the thickness of the multilayer graphene depended on that of the Fe film and synthesis conditions including the temperature.

6.3 Fabrication of Top-Gated Field-Effect Transistors Without Using Transfer Processes

In this section, we propose a novel method to fabricate transistors directly on an insulating substrate using transfer-free processes. The procedures for fabrication of a top-gated graphene FET are illustrated in Fig. 6.3. First, Fe films with channel patterns were formed on a SiO_2/Si substrate by conventional photolithography and lift-off processes. Graphene was then grown on the patterned Fe films by thermal CVD as described above. After synthesis, Au (300 or 50 nm)/Ti (10 nm) source and drain electrodes were formed by electron-beam evaporation at both ends of the patterned graphene, under which the Fe films still remained. The Fe films were then removed by wet etching using dilute HCl and/or FeCl_3 solution, leaving suspended or partially suspended graphene channels bridging the two electrodes all

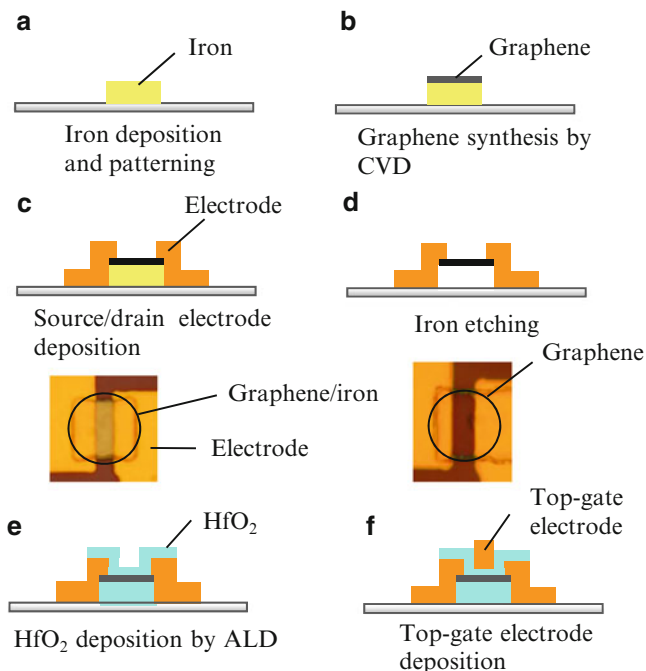


Fig. 6.3 (a)–(f) Fabrication process of a top-gated FET. The optical microscopy images of the device before and after etching the iron film are also shown

over the substrate. Graphene was usually formed on the side walls of the patterned Fe film, but the Fe film was still etched away, probably via the interface of the graphene and the substrate. In some cases, we removed the graphene on the side walls by applying O_2 plasma before etching the Fe film. The graphene channels were subsequently covered by a HfO_2 layer with a typical thickness of 70 nm by atomic layer deposition (ALD) at 250 °C using tetrakis (dimethyl) amino hafnium (TDMAH) and H_2O as precursors. Finally, top-gate electrodes of Au (50 nm)/Ti (10 nm) were formed. Incidentally, fabrication of top-gated transistors using CVD graphene by transfer-free processes has been reported recently [24]. However, in the method reported, the electrode materials are the same as the catalyst materials. In contrast, our method uses electrode materials different from the catalyst, resulting in better etching selectivity and compatibility with smaller-sized device fabrication.

In Fig. 6.4, another fabrication process we suggest is also shown, which does not have to remove graphene on the side walls of catalyst films. First, graphene was grown on Fe film deposited all over a SiO_2/Si substrate by thermal CVD. Graphene with the Fe film was then patterned for channel fabrication by conventional photolithography, followed by argon ion milling and reactive ion etching. After isolation of graphene channel, the process was almost the same as that shown in Fig. 6.3.

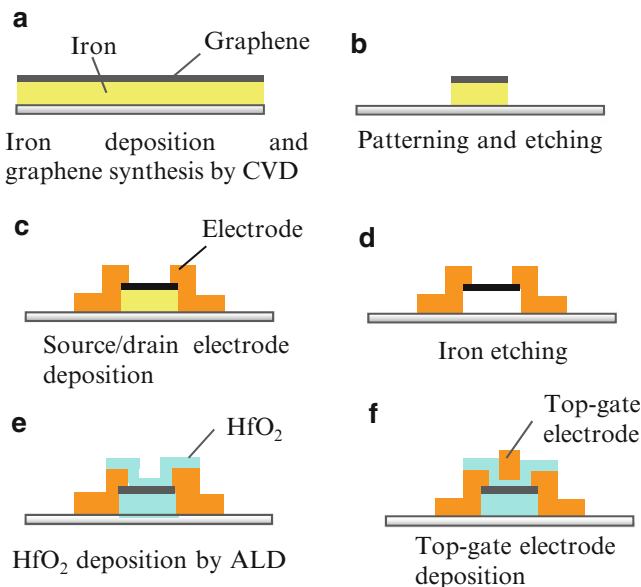


Fig. 6.4 (a)–(f) Alternative fabrication process of a top-gated FET

Graphene transistors were fabricated on a substrate as large as 75 mm in diameter, but our method can be applied to much larger substrates. An optical microscope image of a device is shown in Fig. 6.5a. Optical microscope images of a few-layer graphene channel connecting two electrodes are also shown. The pictures were taken before and after removal of the Fe film. In Fig. 6.5b, a schematic diagram of the cross section of a device and a cross-sectional TEM image are shown. The suspended graphene channel covered by HfO₂ film on both sides can be seen. Measurement of the top-gated FETs was performed at room temperature. A typical result is shown in Fig. 6.5c. The graphene channel was synthesized using the conditions for the few-layer graphene shown in Fig. 6.1d. The transconductance of this device is 10 mS/mm. Since the measured dielectric constant for HfO₂ is 16, the field-effect mobility is estimated to be 110 cm²/Vs. We also obtained devices with a transconductance as high as 22 mS/mm and a field-effect mobility of 230 cm²/Vs. The contact resistances between the graphene channel and the electrodes were *not* subtracted for this calculation. These values are of the same order as the field-effect mobilities of back-gated devices with early CVD graphene [11, 12]. The field-effect mobility is actually not as good as that of top-gated FETs using exfoliated graphene by Farmer et al. [7], although Lin et al. [6] reported a value similar to ours. The lower mobility is partly because the quality of the graphene synthesized by low-temperature CVD is not as good as that of exfoliated graphene. In addition, it is possible that the Fe etching and HfO₂ deposition processes damaged the channels. In order to observe the variations of graphene channels, the sheet resistivities of 38 graphene channels were measured. The average sheet resistivity was 1.2 kΩ at the

Fig. 6.5 (a) An optical microscopy image of a top-gated graphene FET. (b) Schematic diagram of the cross section of a device and a cross-sectional TEM image. (c) Drain current as a function of the top-gate voltage (channel length (L), $3\ \mu\text{m}$; channel width (W), $2\ \mu\text{m}$; drain voltage, $1.4\ \text{V}$; HfO_2 thickness, $70\ \text{nm}$). (d) Stability of the resistance of a 7-nm -thick graphene channel ($L = 1\ \mu\text{m}$, $W = 2\ \mu\text{m}$)

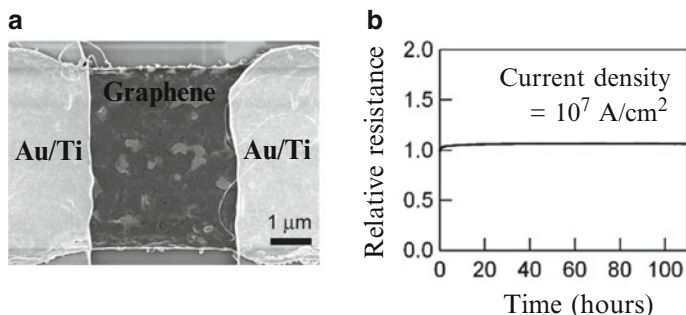
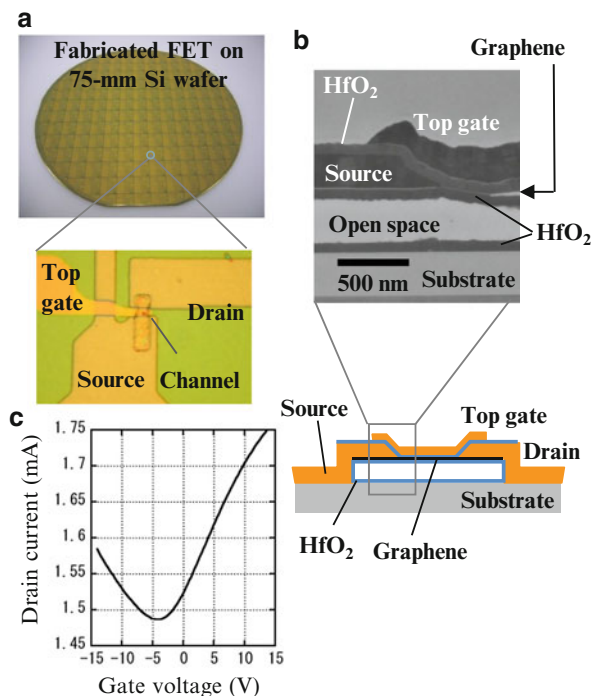


Fig. 6.6 (a) An SEM image of a graphene interconnect. (b) Stability of the resistance of a 7-nm -thick graphene channel ($L = 1\ \mu\text{m}$, $W = 2\ \mu\text{m}$)

Dirac point, with a standard deviation of $1.1\ \text{k}\Omega$. The variations were considered to be caused by those in the number of layers and/or those in the contact resistance. Incidentally, the current density in graphene was $\sim 10^8\ \text{A}/\text{cm}^2$ for the device shown in Fig. 6.5c, assuming a graphene thickness of $\sim 1\ \text{nm}$.

To confirm the robustness of graphene as wiring, a current with a density of $10^7\ \text{A}/\text{cm}^2$ was applied to a 7-nm -thick graphene channel. Figure 6.6a shows the SEM image before removal of Fe catalyst underneath graphene. The resistance was stable over 100 h as shown in Fig. 6.6b, suggesting that graphene is a robust

wiring material. In such applications, Fe catalyst has an advantage over Ni or Cu, because it can easily form thick multilayer graphene suitable for interconnects at lower temperature. Incidentally, very recently, intercalated multilayer graphene interconnects with resistivity of the same order as Cu were demonstrated. The interconnects also exhibited better high-current reliability than Cu [31].

6.4 Direct Synthesis of Graphene on the Substrate and Its Fabrication Process

In this section, we propose a novel method to grow graphene directly on an insulating substrate and, therefore, fabricate transistors using transfer-free processes. The procedures for fabrication of a top-gated graphene FET are illustrated in Fig. 6.7 [19, 22, 26]. First, Fe films with channel patterns were formed on a SiO₂/Si substrate by conventional photolithography and lift-off processes. By optimizing the CVD condition, graphene was grown on and underneath the patterned Fe films at the same time. After synthesis, the Fe films were removed by wet etching using dilute HCl and/or FeCl₃ solution, leaving graphene on the substrate. After removal of the Fe films, the device fabrication process was performed in the same manner as explained above. This fabrication process seems to be easier and more suitable for the present Si LSI processes. However, the quality of graphene synthesized underneath the catalyst film is much worse than that synthesized on the film possibly due to difficulty in the precipitation of carbon at the interface between the catalyst film and SiO₂/Si substrate. Recently, direct synthesis of graphene on the substrate using

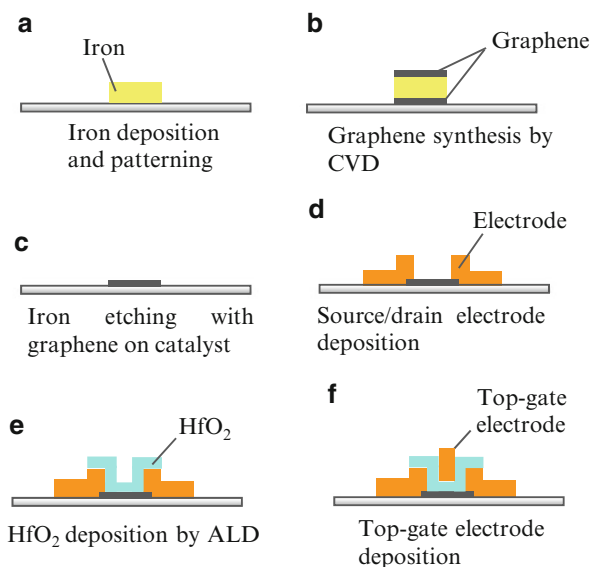


Fig. 6.7 (a)–(f) New fabrication process of a top-gated FET

different approaches has been reported, in which the quality of graphene has been improving gradually [19, 22, 25–30]. Further research regarding direct synthesis of graphene on the substrate will be required.

6.5 Summary

Top-gated field-effect transistors (FETs) utilizing CVD-synthesized graphene were fabricated directly on a large SiO₂/Si substrate by transfer-free processes. The graphene was synthesized at 650 °C and the thickness was controlled by the partial pressure of C₂H₂ and the growth time. The fabricated devices exhibit ambipolar behavior, whose transconductance was as high as 22 mS/mm. In addition, graphene can sustain a high-density current, being a promising material for future LSI wiring. Direct synthesis of graphene on the insulating substrate was also demonstrated.

References

1. Novoselov KS, Geim AK, Morozov SV et al (2004) Electric field effect in atomically thin carbon films. *Science* 306:666–669
2. Bolotin KI, Sikes KJ, Jiang Z et al (2008) Ultrahigh electron mobility in suspended graphene. *Solid State Commun* 146:351–355
3. Lee C, Wei X, Kysar JW et al (2008) Measurement of the elastic properties and intrinsic strength of monolayer graphene. *Science* 321:385–388
4. Balandin AA, Ghosh S, Bao W et al (2008) Superior thermal conductivity of single-layer graphene. *Nano Lett* 8:902–907
5. Lemme MC, Echtermeyer TJ, Baus M, Kurz H (2007) A graphene field effect device. *IEEE Electron Device Lett* 28:282
6. Lin Y-M, Jenkins KA, Valdes-Garcia A et al (2009) Operation of graphene transistors at gigahertz frequencies. *Nano Lett* 9:422–426
7. Farmer DB, Chiu H-Y, Lin Y-M et al (2009) Utilization of a buffered dielectric to achieve high field-effect carrier mobility in graphene transistors. *Nano Lett* 9:4474–4478
8. Kim S, Nah J, Jo I et al (2009) Realization of a high mobility dual-gated graphene field-effect transistor with Al₂O₃ dielectric. *Appl Phys Lett* 94(062107)
9. Cheng R, Bai J, Liao L et al (2012) High-frequency self-aligned graphene transistors with transferred gate stacks. *PNAS* 109:11588–11592
10. Kim KS, Zhao Y, Jang H et al (2009) Large-scale pattern growth of graphene films for stretchable transparent electrodes. *Nature* 457:706–710
11. Reina A, Jia X, Ho J et al (2009) Large area, few-layer graphene films on arbitrary substrates by chemical vapor deposition. *Nano Lett* 9:30–35
12. Wei D, Liu Y, Wang Y et al (2009) Synthesis of N-doped graphene by chemical vapor deposition and its electrical properties. *Nano Lett* 9:1752–1758
13. Piner R, Velamakanni A, Jung I et al (2009) Large-area synthesis of high-quality and uniform graphene films on copper foils. *Science* 324:1312–1314
14. Ago H, Ito Y, Mizuta N et al (2010) Epitaxial chemical vapor deposition growth of single-layer graphene over cobalt film crystallized on sapphire. *ACS Nano* 4:7407–7414
15. Hayashi K, Sato S, Ikeda M et al (2012) Selective graphene formation on copper twin crystals. *J Am Chem Soc* 134:12492–12498

16. Kondo D, Sato S, Yagi K et al (2010) Low-temperature synthesis of graphene and fabrication of top-gated field effect transistors without using transfer processes. *Appl Phys Express* 3:025102
17. Deal BE, Grove AS (1965) General relationship for the thermal oxidation of silicon. *J Appl Phys* 36:3770
18. Cançado LG, Takai K, Enoki T et al (2006) General equation for the determination of the crystallite size L_a of nanographite by Raman spectroscopy. *Appl Phys Lett* 88:163106
19. Kondo D, Sato S, Yagi K et al (2011) The 72nd autumn meeting of The Japan Society of Applied Physics, Yamagata, Japan
20. Weatherup RS, Bayer BC, Blume R et al (2011) In situ characterization of alloy Catalysts for low-temperature graphene growth. *Nano Lett* 11:4154–4160
21. Lahiri J, Miller T, Adamska L et al (2011) Graphene growth on Ni(111) by transformation of a surface carbide. *Nano Lett* 11:518–522
22. Kondo D, Yagi K, Sato M et al (2011) Selective synthesis of carbon nanotubes and multi-layer graphene by controlling catalyst thickness. *Chem Phys Lett* 514:294–300
23. Yamazaki Y, Wada M, Kitamura M et al (2012) Low-temperature graphene growth originating at crystalline facets of catalytic metal. *Appl Phys Express* 5:025101
24. Levendorf MP, Ruiz-Vargas CS, Garg S et al (2009) Transfer-free batch fabrication of single layer graphene transistors. *Nano Lett* 9(2009):4479–4483
25. Rummeli MH, Bachmatiuk A, Scott A et al (2010) Direct low temperature nano-graphene synthesis over a dielectric insulator. *ACS Nano* 4:4206–4210
26. Kondo D, Sato S, Yagi K et al (2011) 24th international microprocesses and nanotechnology conference, Kyoto, Japan
27. Ding X, Ding G, Xie X et al (2011) Direct growth of few layer graphene on hexagonal boron nitride by chemical vapor deposition. *Carbon* 49:2522–2525
28. Yan Z, Peng Z, Sun Z et al (2011) Growth of bilayer graphene on insulating substrates. *ACS Nano* 5:8187–8192
29. Su C-Y, Lu A-Y, Wu C-Y et al (2011) Direct formation of wafer scale graphene thin layers on insulating substrates by chemical vapor deposition. *Nano Lett* 11:3612–3616
30. Kato T, Hatakeyama R (2012) Site- and alignment-controlled growth of graphene nanoribbons from nickel nanobars. *Nat Nanotechnol* 145:1–6
31. Kondo D, Nakano Y, Zhou B et al (2013) Intercalated multi-layer graphene grown by CVD for LSI interconnects. *IEEE International Interconnect Technology Conference*, Kyoto, Japan

Chapter 7

Graphene Biosensor

Yasuhide Ohno, Kenzo Maehashi, and Kazuhiko Matsumoto

Abstract Since the electrical characteristics of graphene field-effect transistors (FETs) are very sensitive for their environmental condition, the graphene FETs have high potential for chemical and biological sensors. In this chapter, the electrical detection of biomolecules and ions by graphene FETs was described. The graphene FETs can be operated in the buffer solution by top-gate operation from a reference electrode without any passivation film. And their transconductance was more than 200 times larger than that of the conventional back-gate operation in vacuum. The drain current increased with increasing the solution pH. And the graphene FETs detected the charges in proteins. To detect the specific protein, aptamers were functionalized on the graphene surface. As results, aptamer-modified graphene FETs detected the target molecule, and their sensitivity was comparable to other aptamer-based biosensors.

Keywords Graphene FET biosensors • Electrical-double layer • Aptamer • pH sensor • Electrical detection

7.1 Introduction

Electrical detection of biomolecules using nanomaterial-based devices grows in importance owing to the advent of the aging society in recent years, because these devices can be downsized for use at home or outside. Silicon-nanowire- [1] and carbon-nanotube (CNT)-based biosensors [2–4] have been reported by many researchers over the past decade. In particular, the CNT is one of the strongest candidates for highly sensitive biological sensors owing to its large surface-area-to-volume ratio. However, CNT-based biosensors have some major problems for

Y. Ohno (✉) • K. Matsumoto

Institute of Scientific and Industrial Research, Osaka University, Mihogaoka 8-1, Ibaraki, Osaka 567-0047, Japan

e-mail: ohno@sanken.osaka-u.ac.jp; k-matsumoto@sanken.osaka-u.ac.jp

K. Maehashi

Tokyo University of Agriculture and Technology, Tokyo, Japan

e-mail: maehashi@sanken.osaka-u.ac.jp

sensing application since their electrical characteristics strongly depend on their chirality, i.e., some devices show semiconducting characteristics and other devices show metallic characteristics. In addition, the absolute value of the typical drain current (I_D) in a buffer solution is 10~30 nA if the CNT channel is single. Because the oxidization of electrodes and an analyte or water electrolysis should be prevented, a large voltage cannot be applied in any buffer solution. This small I_D is often comparable to the leakage current between the reference electrode and the channel (several nA). This indicates that the electrical characteristics of CNT field-effect transistors in a buffer solution are susceptible to noise. Recently, network CNTs [5] or aligned CNT [6, 7] devices have been investigated for the sensors to solve these problems. However, it is difficult to grow only semiconducting CNTs at present.

7.2 Principle of Graphene Biosensor

Graphene [8], monolayer or few-layer graphite, may solve these problems [9–11]. It has an extremely high carrier mobility with a large sheet carrier concentration and is chemically stable. Its electrical characteristics are very sensitive to its environmental conditions, and it also has a high potential for use in chemical and biological sensors. The electrical characteristic of the graphene FET shows clear ambipolar characteristic, and this ambipolar characteristic can be explained by the Fermi level shift in the band structure of graphene. Figure 7.1 shows the schematic of the gate voltage dependence of the drain current (I_D - V_{TG}) characteristic and its band structure. The Fermi level can be controlled by applying the gate voltage, resulting in the field effect of the I_D . This Fermi level shift can be obtained by access of charges. Generally, ions and proteins have charges in the solution. Therefore, when positively (negatively) charged molecules are attached on the graphene surface, the Fermi level will increase (decrease), resulting in the shift of the transfer characteristic in

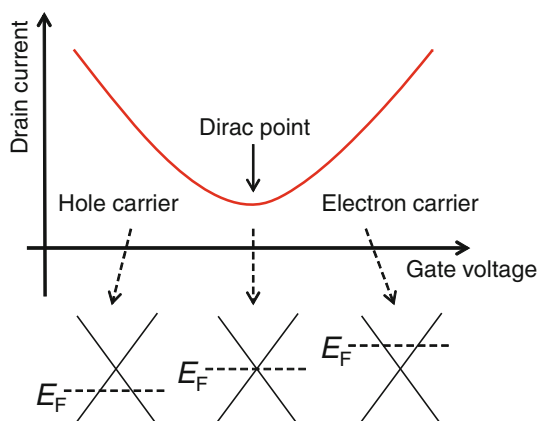
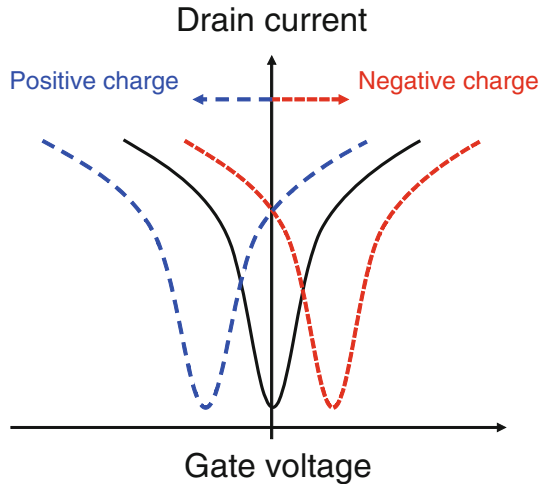


Fig. 7.1 Schematic of transfer characteristic of typical graphene FET and the band structure for each part

Fig. 7.2 Schematic of transfer characteristic after introducing analyte



negative (positive) gate voltage direction as shown in Fig. 7.2. We can detect the proteins or ions by I_D change of the graphene FET.

There are many advantages to use graphene FETs as biosensors compared with CNT-based biosensors. The charge sensitivity of the graphene FET is still high because the surface-area-to-volume ratio of the graphene is higher than that of the bulk material. And the graphene is chemically stable. One of the most important advantages of using a graphene channel is its large potential window. To detect the biomolecules in the solution, the biosensors have to be sunk in the solution. For conventional semiconductor materials such as Si or GaAs, they need a passivation film to avoid the oxidization. This is because these materials are easily oxidized in a solution under low voltage. On the other hand, graphene is the carbon material and is not easily oxidized in the solution due to its large potential window. As a result, the graphene FET-based biosensors can be used in the solution without any passivation film. For CNT-based biosensors, which have almost the same potential window, the highest sensitivity will be obtained for the device with a single carbon-nanotube channel. However, this CNT-FET shows very low drain current in the solution (several nA). The drain current value of the graphene FET shows more than 1,000 times larger than that of the CNT-FET. Therefore, higher signal/noise ratio is obtained for the graphene FETs.

7.3 Device Fabrication

To obtain a higher sensitivity, monolayer graphene flakes were only used as the channel of the FETs in this work since the carrier mobility of the graphene FETs strongly depends on their layer number and the highest mobility can be obtained for the monolayer graphene. The monolayer graphene flakes were obtained by

micromechanical exfoliation using kish graphite and a clear adhesive tape and identified by Raman spectroscopy. The gold source and drain electrodes were formed by conventional electron beam lithography, e-beam evaporation, and lift-off procedure. The distance between the source and drain electrodes was approximately $4\ \mu\text{m}$.

7.4 Result and Discussions

7.4.1 Electrical Double Layer

When the small voltage is applied between two electrodes in solution, ions around electrodes are attracted to the electrodes, resulting in the formation of the electrical double layer. In this case, the electric potential in the solution shows rapid increase as shown in Fig. 7.3. Therefore, this electrical double layer acts as a gate insulator. The thickness of the electrical double layer, which is called as Debye length, depends on the temperature and ion strength. For example, the Debye length of the 10 mM buffer solution at room temperature is approximately 5 nm. In the buffer solution, top-gate voltage can be applied from a Ag/AgCl reference electrode, and the reference electrode should be used in this solution-gated system to reduce the environmental effect as shown in Fig. 7.4.

Initially, we investigated the transport behaviors of graphene FETs in the solution to confirm the electrical double layer. Because the thickness of the electrical double layer is very thin (5 nm) compared with the back-gate insulator (SiO_2 , 280 nm), top-gate voltage can be effectively applied to the graphene channel. To measure the

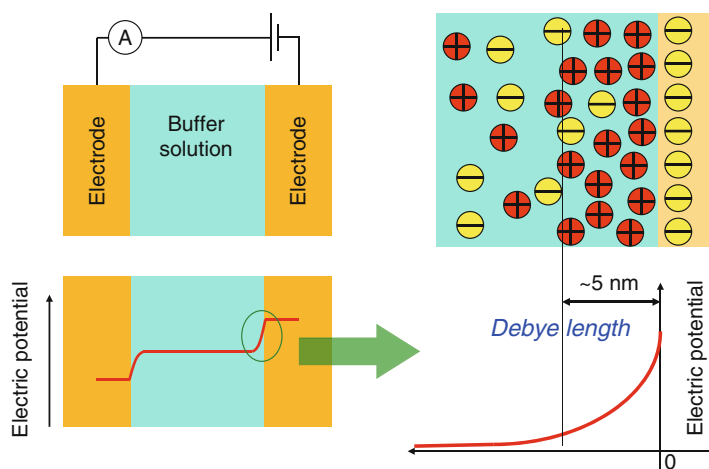


Fig. 7.3 Conceptual diagram of the electrical double layer

Fig. 7.4 Conceptual diagram of measurement setup

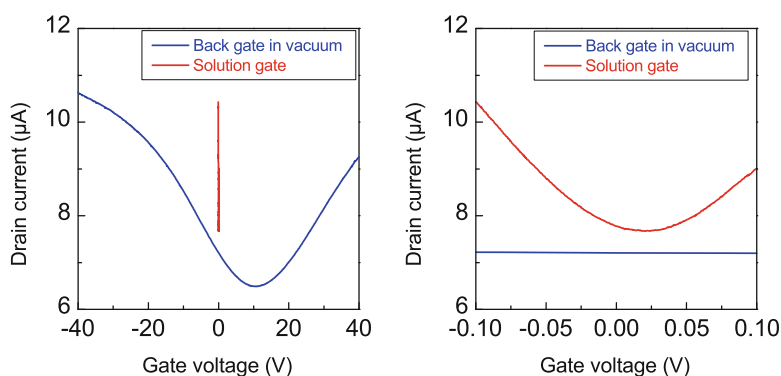
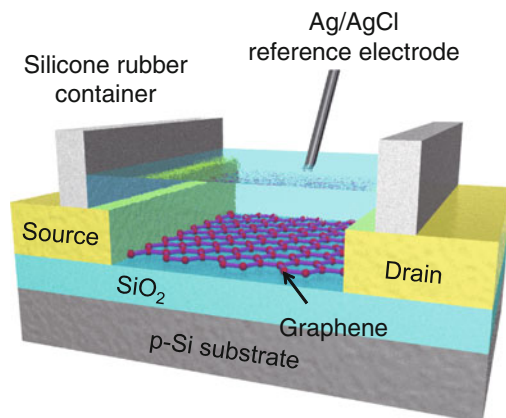


Fig. 7.5 Transfer characteristics of a graphene FET for back- and top-gate operations. *Right figure* shows the enlarged view of the *left figure* from -0.1 to 0.1 V

back-gate operation, the graphene FETs were put in the vacuum chamber with a probing station, and then the chamber was evacuated to 1×10^{-3} Pa. To remove the oxygen effect to the electrical characteristic, the graphene FETs were annealed 200°C for 1 h before measurement. The measurement was carried out at room temperature. For the solution-gated system, the graphene FETs were immersed in the phosphate buffer solution (PBS, pH 6.8), and a silicone rubber well was placed on the graphene FETs to allow the surface of the graphene channel to be filled with several buffer solutions and analytes for electrical measurement and sensing. The electrical characteristics of the GFETs were measured by a semiconductor parameter analyzer using a two-terminal measurement.

Figure 7.5 shows the I_D versus V_{TG} characteristics of a graphene FET. Ambipolar electric field-effect characteristics of a graphene FET were observed for both back-gate and top-gate operations, indicating that the electric field was applied on the graphene. For the back-gate operation, we have to apply the back-gate voltage of more than 20 V to obtain the clear field effect of the I_D . On the other hand, the clear

field effect can be observed by only 0.1 V of the top-gate voltage. Transconductance ($g_m = \partial I_D / \partial V_G$) were estimated to be 0.14 and 36 μS from Fig. 7.5, respectively. The g_m value of the graphene FET under top-gate operation was more than 250 times larger than that of the back-gate operation. These results show that the very thin gate insulator film was formed on the graphene surface.

7.4.2 Solution pH Sensing

The dependence of the transfer characteristics and conductance of graphene FETs on pH were evaluated. Figure 7.6 shows conductance plotted as a function of V_{TG} for a graphene FET in various electrolytes at various pH values from 4.0 to 7.8. The Dirac points of the graphene FET shifted in a positive detection with increasing pH. This behavior indicates that graphene FETs can detect the pH value by the electrical characteristics. A plot of the time-dependent conductance for a graphene FET at $V_{\text{TG}} = -80\text{ mV}$ in pH values from 4.0 to 8.2 is shown in Fig. 7.7. Every 10 min, either a 10 mM PBS at pH 6.8 or a 10 mM borate buffer solution at pH 9.3 was added to increase the pH. It is concluded that the increased conductance can be

Fig. 7.6 I_D as a function of top-gate voltage of a graphene FET at pH 4.0, 4.9, 5.8, and 7.2

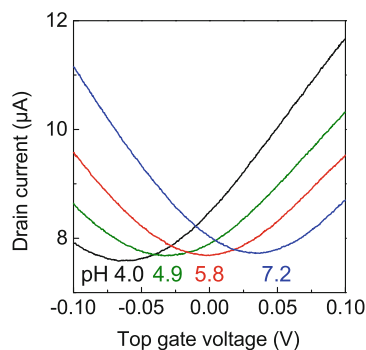
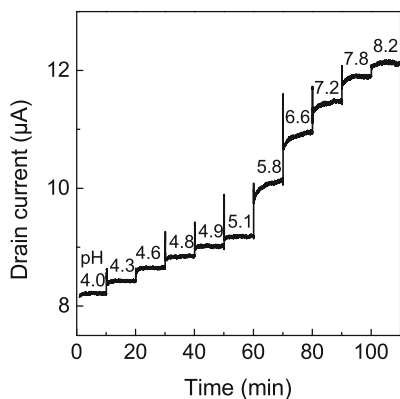


Fig. 7.7 I_D versus time data of a GFET for pH values from 4.0 to 8.2



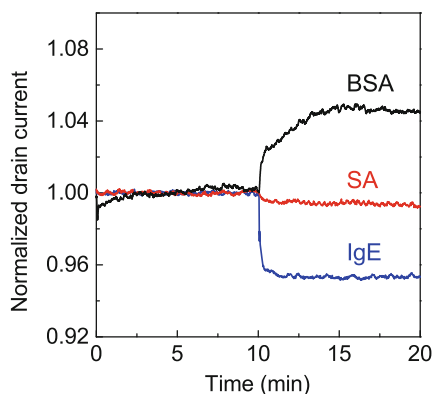
attributed to the increased negative charge around the graphene channel, because the hole is the carrier in this condition. Increased conductance has also been observed in carbon-nanotube pH sensors, which has been interpreted as the attachment of hydroxide ions that act as electron scavengers. We believe these phenomena can occur on the graphene channel and the results indicate that graphene FETs can be used as pH sensors.

7.4.3 Protein Adsorption Detecting

From the solution pH detection, we confirmed that the graphene FETs can detect the charges in the solution. This indicates that graphene FETs can also detect the proteins because a protein consists of one or many chains of amino acid. And an amino acid has both of amine ($-\text{NH}_2$) and carboxylic acid ($-\text{COOH}$) functional groups. Therefore, proteins have positive or negative charges in the solution owing to the electrolytic dissociation of these functional groups. The isoelectric point (pI) of a protein is defined as the solution pH at which the protein does not have net electrical charges. In this experiment, there are three kinds of proteins. One is human immunoglobulin E (IgE), and the others are bovine serum albumin (BSA) and streptavidin (SA).

Figure 7.8 shows the time course of normalized I_D of graphene FETs with bare graphene channel in the 10 mM PBS at pH 6.8. After 10 min, 100 nM IgE, BSA, and SA were introduced into the graphene channel. I_D increased after adding BSA. On the other hand, I_D decreased after adding IgE and SA. The difference in the drain current change can be explained by the difference in the isoelectric point of these proteins. The pI of BSA and SA are 5.3 and 7.0, respectively. That is to say, SA is positively charged and BSA is negatively charged in phosphate-buffered solution at pH 6.8. The evaluation of the pI of IgE molecules is complicated by the fact that each immunoglobulin generally has a rather large range of pI. For example, the isoelectric point of IgG is 6.5~9.5 [12, 13]. Since the I_D decreased after adding the

Fig. 7.8 Time course of I_D for aptamer-modified graphene FET. At 10, 30, and 50 min, respectively, BSA and SA (nontarget proteins) and IgE (target protein) were injected into the aptamer-modified graphene channel



IgE molecules, we believe that the positively charged part of the IgE molecule was detected by bare and aptamer-modified graphene FETs. Although the binding part of the IgE molecules should be investigated, these results show that all proteins can be electrically detected using a graphene FET with a bare graphene channel.

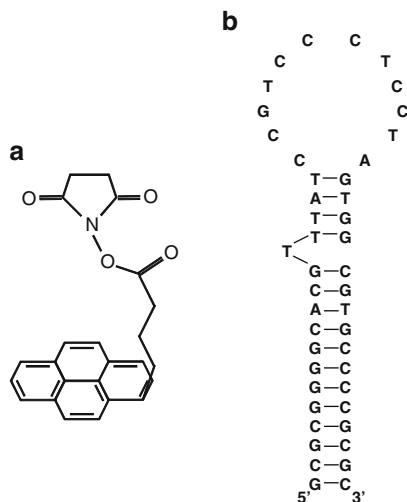
7.4.4 Specific Protein Sensing

To detect a specific biomolecule, receptor-modified graphene FETs are required, where the receptor is the molecular recognition materials such as an antibody or enzyme. It should be noticed that there are two requirements for the functionalization of receptors on FET-based biosensors. One is that the height of the receptor must be less than that of the electrical double layer because mobile charges in a transistor's channel are not affected by charged molecules located more than a Debye length away. Although an antibody is often used in the conventional biosensors, the height of the antibody is approximately 10 nm. If we obtained 10-nm-thick Debye length, less than 100 μM buffer solution is prepared. However, the thin concentration buffer solution has a weak buffering effect. A smaller size of the receptor is needed in this case. And the other requirement is that the functionalization process should be carried out without introducing defects on the graphene surface because these defects lead to the degradation of the electrical characteristics.

In this experiment, IgE is the target molecule. To meet these requirements, aptamer- and pyrene-based linker materials were used. Aptamers are artificial oligonucleotides produced in vitro. Hence, they are less expensive than antibodies but are very stable [14–16]. The greatest benefit of using aptamers is that they are smaller than the Debye length. The height of the anti-IgE aptamer used in this work is approximately 3 nm. As a result, protein–aptamer reactions are expected to occur inside the electrical double layer. And to modify the aptamer to graphene surface without introducing defects, 1-pyrenebutanoic acid succinimidyl ester (PBASE) was used as a linker (Fig. 7.9a). This linker material is often used for carbon-nanotube functionalization [17]. The pyrenyl group of the linker interacts strongly with the basal plane of graphite via π -stacking, and the succinimide part strongly reacts with the amino base [18, 19].

Functionalization process of the aptamers on the graphene surface was carried out as follows. After rinsing with methanol and 10 mM phosphate-buffered solution at pH 6.8, the device was immersed in a 1 nM solution of IgE aptamers in phosphate-buffered solution for 12 h at room temperature. Anti-IgE aptamer DNA oligonucleotides (D17.4ext) with 5'-amino modification were custom-synthesized by Fasmac Corp. (Kanagawa, Japan), and the base sequence was 5'-NH₂ GCG CGG GGC ACG TTT ATC CGT CCC TCC TAG TGG CGT GCC CCG CGC -3' (Fig. 7.9b). Finally, 100 mM ethanolamine was added to the channel of the GFET for 1 h to deactivate and block the excess reactive groups remaining on the graphene surface.

Fig. 7.9 (a) Molecular structure of 1-pyrenebutanoic acid succinimidyl ester, (b) anti-IgE aptamer D.17.4ext used in this work



Atomic force microscopy was carried out to confirm the functionalization of the graphene with IgE aptamers. Figure 7.10 shows AFM images and height profiles of the graphene FET in air before and after IgE aptamer functionalization, respectively. Before functionalization, an approximately 0.3- to 0.5-nm-thick graphene channel was observed, which indicates that the graphene channel is a single layer. After aptamer functionalization, the height of the channel apparently increased to approximately 3~4 nm, indicating that the functionalization with IgE aptamers occurred only on the graphene surface.

The effects of the IgE-aptamer functionalization of the graphene surface were also observed through electrical measurements. Figure 7.11 shows the drain current (I_D) versus the top-gate voltage (V_{TG}) characteristics at a drain voltage (V_D) of 0.1 V for a graphene FET in PBS before and after functionalization with IgE aptamers. Increased I_D was observed after functionalization. Because the carriers in the graphene channel are holes under these conditions, this increased I_D comes from an increase in negative charge density on the graphene channel. These results show that the IgE aptamers were successfully immobilized in the graphene channel because the aptamers (oligonucleotides) are always negatively charged in the solution due to the ionized hydroxyl of phosphoric acid. Thus, it must be emphasized that the graphene FET can electrically detect the existence of the oligonucleotides on its surface. Moreover, the slopes of the I_D - V_{TG} curves were almost identical, indicating that no defects were introduced on the graphene surface by the functionalization process.

Next, we measured specific sensing characteristics of the aptamer-modified graphene FET. Figure 7.12 shows the time dependence of I_D for an aptamer-modified graphene FET at a V_D of 0.1 V and a V_{TG} of 0.1 V in phosphate-buffered solution at pH 6.8. After 10 and 30 min, respectively, 100 nM nontarget proteins, namely, BSA and SA, were added to the buffer solution, and the target human IgE protein

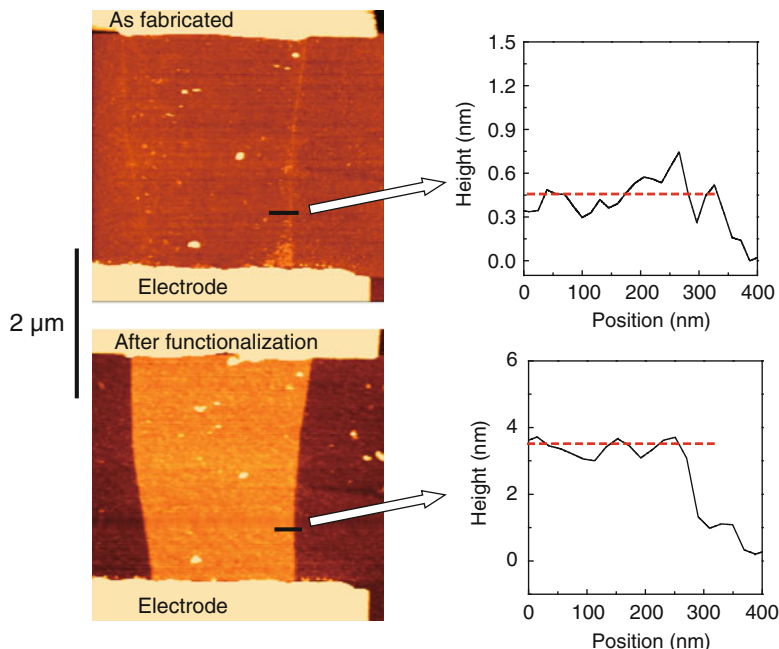
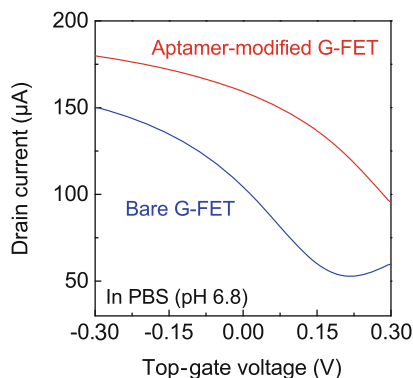


Fig. 7.10 AFM image of graphene FET before and after functionalization. *Inset* shows the height profile of the graphene channel marked by a *solid line*. *Red dashed lines* indicate the average height

Fig. 7.11 I_D - V_{TG} characteristics of the graphene FET in 10 mM PBS before and after functionalization with IgE aptamers



(100 nM) was added after 50 min. To accelerate the reaction between IgE aptamers and IgE protein, the solution was stirred for several tens of seconds after adding each analyte. When the target protein was introduced into the graphene channel, the I_D suddenly decreased. In this case, it can be considered that the positively charged IgE molecules were connected to the negatively charged IgE aptamers, resulting in a decrease in I_D . In contrast, upon addition of nontarget proteins, I_D of the aptamer-modified graphene FET remained almost constant. Therefore, the

Fig. 7.12 Time course of I_D for aptamer-modified graphene FET. At 10, 30, and 50 min, respectively, BSA and SA (nontarget proteins) and IgE (target protein) were injected into the aptamer-modified graphene channel

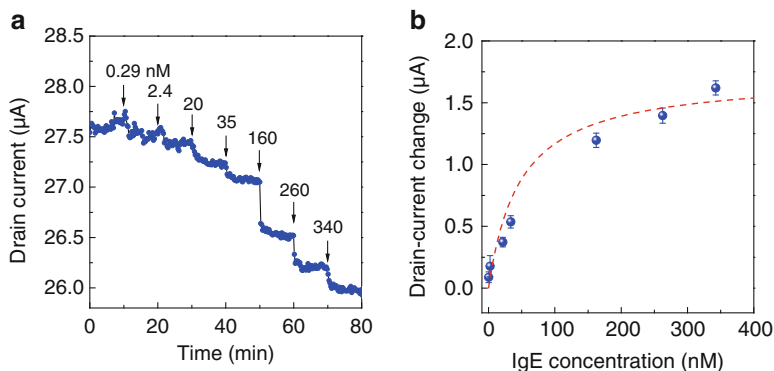
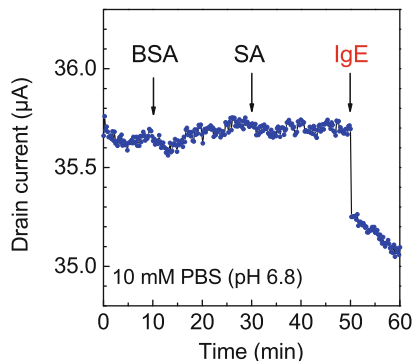


Fig. 7.13 (a) Time course of I_D for aptamer-modified graphene FET. At 10-min intervals, various concentrations of IgE were injected. (b) Drain current change versus IgE concentration. Red dashed line shows the fitted curve of the Langmuir adsorption isotherm with $K_D = 47$ nM

results shown in Figs. 7.8 and 7.12 indicate that the nonspecific binding of nontarget proteins was successfully suppressed in the aptamer-modified graphene FET.

Using aptamer-modified graphene FETs, we estimated the dissociation constant (K_D) between IgE aptamer and IgE protein by monitoring I_D at various IgE concentrations. The target IgE protein at concentrations of 0.29, 2.4, 20, 35, 160, 260, and 340 nM was introduced into an aptamer-modified graphene FET while monitoring I_D in real time (Fig. 7.13a). I_D decreased stepwise after injection of the target IgE at each concentration. Figure 7.13b shows the net drain current change (ΔI_D) plotted as a function of IgE concentration. ΔI_D sharply increased with increasing IgE concentration from 0.29 to 160 nM, while ΔI_D gradually became saturated above 160 nM. The data indicate that the reaction between IgE aptamer and IgE protein in the graphene channel follows the Langmuir adsorption isotherm given by

$$\Delta I_D = \frac{\Delta I_{D\max} C_{\text{IgE}}}{K_D + C_{\text{IgE}}},$$

where ΔI_{Dmax} and C_{IgE} are the saturated net drain current change and the concentration of IgE protein, respectively. From the fitted curve shown in Fig. 7.13b (dashed line), ΔI_{Dmax} and K_D were estimated to be $1.8 \mu A$ and 47 nM , respectively, indicating a high affinity between the IgE aptamer and IgE protein.

Aptamer-based immunosensors have been intensively investigated in recent years. Liss et al. developed aptamer-based quartz crystal microbalance biosensors with K_D of several nM [20]. Mendonsa et al. reported aptamer–IgE reactions using capillary electrophoresis, and their average K_D was 29 nM [21]. Katilius et al. investigated a fluorescent signaling aptamer and fitted the IgE concentration dependence with $K_D = 46 \text{ nM}$ [22]. Aptamer-modified immunosensors using carbon-nanotube FETs were reported by Maehashi et al. with K_D of 1.9 nM [3]. Turgeon et al. studied aptamer equilibria using gradient micro-free-flow electrophoresis with K_D of 48 nM [23]. Our result ($K_D = 47 \text{ nM}$) is comparable with these previous results. Thus, the present graphene FET has sufficiently high sensitivity to estimate dissociation constants for receptor and ligand reactions.

7.5 Conclusion

Graphene FET-based chemical and biological sensors were demonstrated. The graphene FETs showed good gate transfer characteristics in electrolytes; their transconductances were more than 250 times larger than those obtained under vacuum. Clear pH-dependent drain current change was observed, indicating the potential for use of graphene FETs in pH sensors. The drain current was also changed by protein adsorption and the changes depend on the charge type in proteins. To realize specific protein detection, aptamers were modified on the graphene surface. AFM observation and electrical characteristics show the aptamers could be functionalized on the graphene surface without introducing defects. The aptamer-modified graphene FETs detected only the target protein, and the dissociation constant obtained from this experiment was comparable to those of other aptamer-based biosensors. These results indicate that graphene FETs are promising candidates for the development of real-time chemical and biological sensors.

References

1. Cui Y, Wei Q, Park H, Lieber CM (2001) Nanowire nanosensors for highly sensitive and selective detection of biological and chemical species. *Science* 293:1289–1292
2. Star A, Gabriel JCP, Bradley K, Gru G (2003) Electronic detection of specific protein binding using nanotube FET devices. *Nano Lett* 3:459–463
3. Maehashi K, Katsura T, Kerman K, Takamura Y, Matsumoto K, Tamiya E (2007) Label-free protein biosensor based on aptamer-modified carbon nanotube field-effect transistors. *Anal Chem* 79:782–787

4. Saito R, Fujita M, Dresselhaus G, Dresselhaus MS (1992) Electronic structure of graphene tubules based on C₆₀. *Phys Rev B* 46:1804–1811
5. Ishikawa FN, Chang H-K, Curreli M, Liao H-I, Olson CA, Chen PC, Zhang R, Roberts RW, Sun R, Cote RJ, Thompson ME, Zhou C (2009) Label-free, electrical detection of the SARS virus N-protein with nanowire biosensors utilizing antibody mimics as capture probes. *ACS Nano* 3:1219–1224
6. Palaniappan A, Goh WH, Tey JN, Wijaya IPM, Moochhala SM, Liedberg B, Mhaisalkar SG (2010) Aligned carbon nanotubes on quartz substrate for liquid gated biosensing. *Biosens Bioelectron* 25:1989–1993
7. Okuda S, Okamoto S, Ohno Y, Maehashi K, Inoue K, Matsumoto K (2012) Horizontally aligned carbon nanotubes on a quartz substrate for chemical and biological sensing. *J Phys Chem C* 116:19490–19495
8. Geim AK, Novoselov KS (2007) The rise of graphene. *Nat Mater* 6:183–191
9. Mohanty N, Berry V (2008) Graphene-based single-bacterium resolution biodevice and DNA transistor: interfacing graphene derivatives with nanoscale and microscale biocomponents. *Nano Lett* 8:4469–4476
10. Ohno Y, Maehashi K, Yamashiro Y, Matsumoto K (2009) Electrolyte-gated graphene field-effect transistors for detecting pH and protein adsorption. *Nano Lett* 9:3318–3322
11. Ohno Y, Maehashi K, Matsumoto K (2010) Label-free biosensors based on aptamer-modified graphene field-effect transistors. *J Am Chem Soc* 132:18012–18013
12. Chiodi F, Åke Sidéén, Ösby E (1985) Isoelectric focusing of monoclonal immunoglobulin G, A and M followed by detection with the avidin-biotin system. *Electrophoresis* 6:124–128
13. Prin C, Bene MC, Gobert B, Montagne P, Faure GC (1995) Isoelectric restriction of human immunoglobulin isotypes. *Biochim Biophys Acta* 1243:287–289
14. Tuerk C, Gold L (1990) Systematic evolution of ligands by exponential enrichment: RNA ligands to bacteriophage T4 DNA polymerase. *Science* 249:505–510
15. Robertson DL, Joyce GF (1990) Selection in vitro of an RNA enzyme that specifically cleaves single-stranded DNA. *Nature* 344:467–468
16. Ellington AD, Szostak JW (1990) In vitro selection of RNA molecules that bind specific ligands. *Nature* 346:818–822
17. Chen RJ, Zhang Y, Wang D, Dai H (2001) Noncovalent sidewall functionalization of single-walled carbon nanotubes for protein immobilization. *J Am Chem Soc* 123:3838–3839
18. Jaegfeldt H, Kuwana T, Johansson G (1983) Electrochemical stability of catechols with a pyrene side chain strongly adsorbed on graphite electrodes for catalytic oxidation of dihydronicotinamide adenine dinucleotide. *J Am Chem Soc* 105:1805–1814
19. Katz EJ (1994) Application of bifunctional reagents for immobilization of proteins on a carbon electrode surface: oriented immobilization of photosynthetic reaction centers. *Electroanal Chem* 365:157–164
20. Liss M, Petersen B, Wolf H, Prohaska E (2002) An aptamer-based quartz crystal protein biosensor. *Anal Chem* 74:4488–4495
21. Mendonsa SD, Bowser MT (2004) In vitro selection of high-affinity DNA ligands for human IgE using capillary electrophoresis. *Anal Chem* 76:5387–5392
22. Katilius E, Katiliene Z, Woodbury NW (2006) Signaling aptamers created using fluorescent nucleotide analogues. *Anal Chem* 78:6484–6489
23. Turgeon RT, Fonslow BR, Jing M, Bowser MT (2010) Measuring aptamer equilibria using gradient micro free flow electrophoresis. *Anal Chem* 82:3636–3641

Chapter 8

Graphene Terahertz Devices

Taiichi Otsuji

Abstract In this section, recent advances and future trends in graphene terahertz (THz) devices are described. First, the fundamental basis of optoelectronic properties of graphene is introduced. Second, ultrafast nonequilibrium carrier dynamics in optically pumped graphene is described, giving rise to population inversion and resultant THz gain by stimulated interband photon emission. Third, graphene active plasmonics are described in which plasmon dispersion and modes are theoretically addressed, leading to one important aspect of giant THz gain by stimulated interband photon emission in inverted graphene. Fourth, science and technology toward the creation of current-injection-pumped graphene THz lasers are described. Fifth, some other important functional devices including THz modulators and photodetectors/mixers are described. Finally, trends and the future of graphene THz devices are summarized.

Keywords Graphene • Terahertz • Plasmon • Laser

8.1 Introduction

The groundbreaking discovery of graphene [1–3] triggered the research and development of graphene-based electronic, optoelectronic, and terahertz (THz) photonic devices [4–8]. In this section, recent advances and future trends in graphene THz devices are described. Ultrafast nonequilibrium carrier dynamics and phonon properties in graphene can originate a very small gain in the broadband THz frequency range [9, 10], which may open the way to create the THz lasers [11–15] but is inefficient to compete against the strong losses in the THz range. Graphene plasmons, quanta of the collective charge-density waves excited by two-dimensional carriers in graphene, can dramatically increase the light (THz photons) and matter (graphene) interaction [6, 7, 16, 17], leading to “giant THz gain” [18–20].

Very recently we have succeeded in the observation of the giant THz gain in monolayer graphene pumped by a femtosecond infrared laser [21, 22], which

T. Otsuji (✉)

Research Institute of Electrical Communication, Tohoku University, Sendai, Japan

e-mail: otsuji@riec.tohoku.ac.jp

includes the following four important processes: (1) population inversion of graphene carriers by optical pumping; (2) stimulated interband THz photon emission by impinging THz photons; (3) excitation of surface plasmons by the impinging THz photons, giving rise to propagation of surface plasmon polaritons (SPPs) and producing the giant amplification of the THz SPPs; and (4) conversion of the SPPs to the THz photons, eventually yielding strongly amplified THz photons. As a consequence, what is really exciting and important is how to implement such plasmonic structures into a real graphene laser device structure.

The physics of plasmons and SPPs behind the real graphene materials has yet been under studying so that it could also be an important aspect of this section. First, the fundamental basis of optoelectronic properties of graphene is introduced. Second, ultrafast nonequilibrium carrier dynamics in optically pumped graphene is described, giving rise to population inversion and resultant THz gain by stimulated interband photon emission. Third, graphene active plasmonics are described in which plasmon dispersion and modes are theoretically addressed, leading to one important aspect of giant THz gain by stimulated interband photon emission in inverted graphene. Fourth, science and technology toward the creation of current-injection-pumped graphene THz lasers are described. Fifth, some other important functional devices including THz modulators and photodetectors/mixers are described. Finally, trends and the future of graphene THz devices are summarized.

8.2 Optoelectronic Properties of Graphene for THz Active Device Applications

8.2.1 Optical Conductivity in Graphene

Optical conductivity in graphene is determined by the interband and intraband transition processes of carriers and is derived from the Kubo formula as follows [23, 24]:

$$\begin{aligned}\sigma(\omega) &= \sigma_{\text{inter}}(\omega) + \sigma_{\text{intra}}(\omega) \\ &= \frac{ie^2\omega}{\pi} \int_0^\infty \frac{f(\varepsilon - \varepsilon_F) - f(-\varepsilon - \varepsilon_F)}{(2\varepsilon)^2 - (\varepsilon + i\delta)^2} d\varepsilon + \frac{ie^2\varepsilon_F}{\pi\hbar^2(\omega + i/\tau_m)},\end{aligned}\quad (8.1)$$

where e is the elementary charge, $f(\varepsilon)$ is the Fermi–Dirac distribution function, ε_F is the Fermi energy, \hbar is the reduced Planck’s constant, δ is the broadening parameter for the interband transition, and τ_m is the momentum relaxation time. This gives the important aspects of the frequency dependence of the conductivity profiles described as follows.

Due to the gapless and linear energy spectra of electrons and holes in graphene, interband optical absorption exhibits the flat response with a universal absorption

coefficient $\alpha = \pi e^2 / (c\hbar) \approx 1/137 \approx 2.3\%$ over broadband photon energies from submillimeter waves to near ultraviolet when the photon energies exceed twice the Fermi energy $2\varepsilon_F$ where c is the speed of light in vacuum [25]. When the photon energy $\hbar\omega$ is smaller than $2\varepsilon_F$, the optical absorption is prohibited due to the Pauli's state blocking. Thus in general the real part of the interband optical conductivity $\text{Re}\sigma_{\hbar\omega}^{\text{inter}}$ at photon energy $\hbar\omega$ is given by the universal quantum conductivity $e^2/(4\hbar)$ and the carrier distribution function $f(\hbar\omega)$ as follows:

$$\text{Re}\sigma_{\hbar\omega}^{\text{inter}} = \frac{e^2}{4\hbar} (1 - 2f(\hbar\omega)). \quad (8.2)$$

On the other hand, intraband conductivity follows the Drude-like dependence with parameters $\omega\tau_m$; the real part of the intraband conductivity $\text{Re}\sigma_{\hbar\omega}^{\text{intra}}$ is derived as follows:

$$\text{Re}\sigma_{\hbar\omega}^{\text{intra}} \approx \frac{(\ln 2 + \varepsilon_F/2k_B T) e^2}{\pi\hbar} \frac{k_B T \tau_m}{\hbar(1 + \omega^2\tau_m^2)}, \quad (8.3)$$

where k_B is the Boltzmann constant and T is the temperature.

Figure 8.1 plots the real part of the conductivity. The THz frequency range is an intersection region where intraband (interband) conductivity decreases (increases) with increasing frequency [26]. When graphene is doped, intraband Drude conductivity shifts upward, whereas the Pauli's state-blocking-limited roll-off frequency of the interband conductivity shifts upward. Thus THz conductivity can be substantially modulated by doping carriers which could be performed by the electrostatic gating. This in turn makes graphene active THz functional devices such as photodetectors [27], intensity modulators [28, 29], filters [30], etc. It is worth to note that according to Eq. (8.2), when graphene is optically pumped, $\text{Re}\sigma_{\hbar\omega}^{\text{inter}}$ could take a negative value when $f(\hbar\omega) > 0.5$. Generally, optical pumping is performed with photon energies $\hbar\omega$ larger than $2\varepsilon_F$. Therefore, the condition $f(\hbar\omega) > 0.5$ means that the carrier population is inverted [9]. This effect and application to THz lasers will be discussed in detail later.

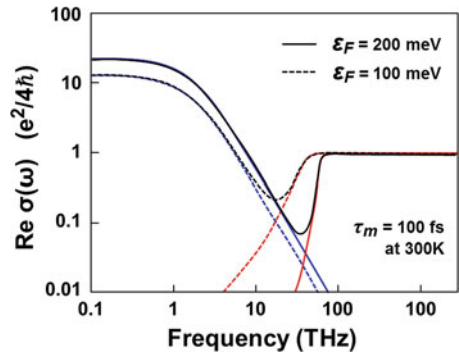


Fig. 8.1 Real part of the conductivity in graphene. *Red lines*, $\text{Re}\sigma_{\hbar\omega}^{\text{inter}}$; *blue lines*, $\text{Re}\sigma_{\hbar\omega}^{\text{intra}}$

8.2.2 Nonequilibrium Carrier Dynamics and Negative Dynamic Conductivity in Optically Pumped Graphene

The honeycomb lattice of graphene is formed with strong in-plane covalent bonds of carbons having a low atomic mass, giving rise to extremely high optical phonon energies, ~ 198 meV ($1,600$ cm^{-1}) at the Brillouin zone center [31, 32]. Thanks to this extremely high optical photon energy, carrier–phonon interaction makes ultrafast energy relaxations for excited carriers through intravalley, intervalley, intraband, and interband scattering [33–37]. Carrier relaxation and recombination dynamics in optically pumped graphene are schematically shown in Fig. 8.2. After the electrons and holes are first photogenerated, collective excitations due to carrier–carrier scattering result in ultrafast carrier quasi-equilibration within a time scale of 10–100 fs in which the total energy distribution of electrons and holes changes to Fermi-like distributions, respectively [33–35]. Then, carriers in the high-energy tails of their distributions emit optical phonons, cooling the entire population and accumulating around the Dirac points. Because of the fast intraband relaxation (picosecond or less) and relatively slow interband recombination ($\gg 1$ ps) of photoelectrons/holes, a large excess of electrons and holes builds up just above and below the Dirac points (in a wide THz frequency range). As a consequence, with sufficiently intense excitation, a population inversion can be achieved [37, 38], leading to stimulated emission of THz radiation [21, 22].

Interband carrier–carrier scattering like Auger-type recombination and impact-ionization-type carrier multiplication processes are major recombination/generation processes in narrow-gap semiconductors but have been thought to be theoretically forbidden in graphene [39]. They may, however, take place due to higher-order many-body effects and/or imperfections of crystal qualities [40–45], which could also extremely modify the carrier relaxation dynamics, limiting population inversion in fs-scale very short time and hence preventing the negative conductivity. Recent experimental works demonstrate such aspects on the carrier relaxation dynamics [41–45] particularly in case of defect-originated symmetry breaking and/or lattice deformation caused by extremely high-field excitation. One should take care in synthesizing and processing high-quality graphene to yield the population inversion.

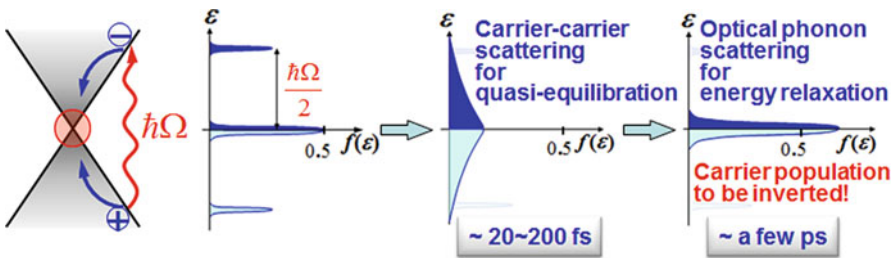


Fig. 8.2 Carrier relaxation and recombination dynamics in optically pumped graphene

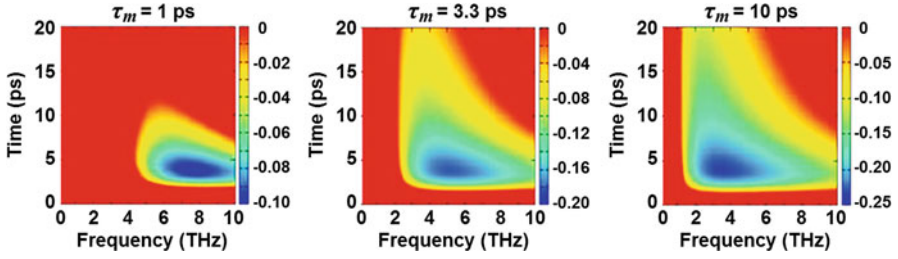


Fig. 8.3 Numerically simulated temporal evolution of the real part of the dynamic conductivity $\text{Re}[\sigma(\omega)]$ (normalized to the minimum quantum conductivity $e^2/4\hbar$) in graphene photoexcited with 0.8-eV, 80-fs pump fluence $8 \mu\text{J}/\text{cm}^2$ (average intensity $1 \times 10^8 \text{ cm}^2$) at the time of 0 ps having different momentum relaxation times τ_m of 1, 3.3, and 10 ps. Any positive values of $\text{Re}[\sigma(\omega)]$ are clipped to the zero level (shown with red color) to focus on the negative-valued region

The nonequilibrium relaxation dynamics of both the electrons and the holes can be characterized by the Fermi–Dirac function with carrier temperature T_c and quasi-Fermi energy ε_F [37]. The time evolutions of these quantities after graphene is pumped at $t = 0$ with an optical pulse are numerically calculated [37]. By using these quantities, the time evolution of THz conductivity is calculated as shown in Fig. 8.3 [14, 38]. At sufficiently strong excitation, the interband stimulated emission of photons can prevail over the intraband (Drude) absorption. In this case, the real part of the dynamic conductivity of graphene, $\text{Re}[\sigma_\omega]$, can be negative in THz range due to the gapless energy spectrum. This effect can be exploited in graphene-based THz lasers with optical or current-injection pumping [9, 10, 12]. Graphene photonic lasers with the Fabry–Pérot resonators based on dielectric or slot-line waveguides were proposed for lasing the THz photons [11, 46, 47]. Stimulated emissions of THz [21, 22] and near-infrared photons [48] from population-inverted graphene were observed experimentally.

8.3 Graphene Active Plasmonics for THz Device Applications

Collective excitation of 2D plasmons in graphene mediates strong light–matter interaction and hence can provide unique features in their response to THz electromagnetic radiation, such as extremely high absorption as well as giant THz gain [6–8, 16, 18–20, 49–53]. This is because the plasmons have an extremely slow-wave nature whose group velocity is comparable to the Fermi velocity which is $\sim 1/300$ of the speed of light in vacuum so that they could interact with matter under propagation by orders of magnitude stronger than what photons can do directly. The mode frequencies (resonant frequencies) of plasmons are defined by the structural dimensions (plasmon cavity size), effective permittivity depending on materials, and group velocity depending on the density of carriers. As a consequence, plasmons

can strongly modulate the optical (THz) conductivity, giving rise to the possibility of various active plasmonic THz devices.

8.3.1 Dispersion and Modes of Graphene Plasmons

The dispersion relations for plasmons have been formulated in various graphene structures [16–18, 50, 53–56]. In particular, gated plasmons are of major concern for use in practical frequency-tuned device applications. The dispersion relation and the damping rate for gated graphene plasmons are theoretically revealed; it holds a superlinear dispersion in which the gate-to-graphene distance d and the momentum relaxation rate (collision frequency) deform the linear dispersion relations (Fig. 8.4a) [18, 21, 32]. The plasmon phase velocity is proportional to the 1/4 power of the gate bias and of d , which is quite different from those in conventional semiconductors.

Semiclassical Boltzmann equations derive the hydrodynamic kinetics of electron–hole plasma wave dynamics [17]. Intrinsic graphene and/or photoexcited graphene hold equi-density of electrons and holes so that bipolar e - h modes of plasmons are excited. Due to the freedoms of e - h motions, e - h plasma waves and charge-neutral sound-like waves are excited (Fig. 8.4b). The e - h plasmons are strongly damped whereas the e - h sound-like waves are survived. On the other hand, doped graphene holds a large fraction on the majority and minority carriers. The plasma waves originated from the minority carriers are strongly damped, resulting in unipolar modes of plasmons originated from the majority carriers.

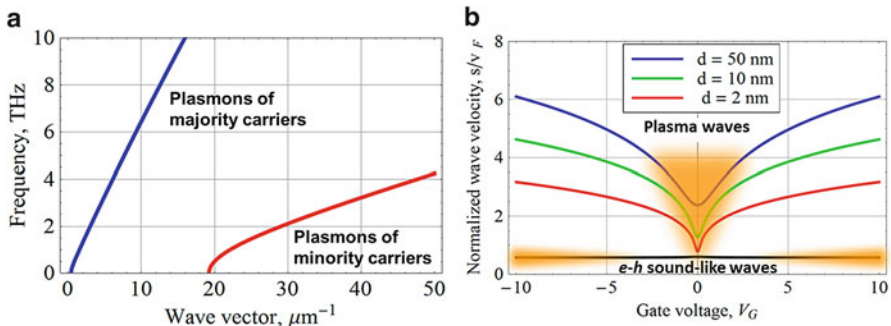


Fig. 8.4 (a) Dispersion relation of gated plasmons in doped graphene. (b) Plasma wave velocity versus gate bias for undoped graphene with different gate–graphene distances d . Black line corresponds to the electron–hole sound-like waves in the vicinity of the neutrality point. Regions of strong damping are filled

8.3.2 Giant THz Gain by Stimulated Plasmon Emission in Inverted Graphene

It is noted that the negative THz conductivity in optically pumped monolayer graphene is limited to or below the universal quantum conductivity ($e^2/4\hbar$) as seen in Eq. (8.2). This is because the absorption of THz photons that can contribute to the stimulated photon emission is only made possible via an interband transition process with absorbance limited to $\pi e^2/\hbar c \approx 2.3\%$ [25]. To overcome this limit, using the plasmons in graphene is very promising. There are several factors to exploit the graphene plasmons: (1) the excitation and propagation of the plasmons along population-inverted graphene [18, 19], (2) the resonant plasmon absorption in structured graphene like microribbon arrays [20] as well as microdisk arrays [57], and (3) the superradiant THz emission mediated by the plasmons [19].

As compared with the lasing associated with the stimulated emission of photons, the stimulated emission of plasmons by the interband transitions in population-inverted graphene can be a much stronger emission process [18–20]. Nonequilibrium plasmons in graphene can be coupled to the TM modes of electromagnetic waves resulting in the formation and propagation of the surface plasmon polaritons (SPPs) [19]. The SPP gain in pumped graphene can be very high due to a small group velocity of the plasmons and strong confinement of the plasmon field in the vicinity of the graphene layer. The propagation index ρ of the graphene SPP along the z coordinate derived from Maxwell's equations is

$$\sqrt{n^2 - \rho^2} + n^2 \sqrt{1 - \rho^2} + \frac{4\pi}{c} \sigma_\omega \sqrt{1 - \rho^2} \sqrt{n^2 - \rho^2} = 0, \quad (8.4)$$

where n is the substrate refractive index and σ_ω is the graphene conductivity [19]. When $n = 1$, ρ becomes

$$\rho = \sqrt{1 - \frac{c^2}{4\pi^2 \sigma_\omega^2}}. \quad (8.5)$$

Thus the absorption coefficient α is obtained as the imaginary part of the wave vector along the z coordinate: $\alpha = \text{Im}(q_z) = 2\text{Im}(\rho \cdot \omega/c)$. Figure 8.5 plots the calculated value of α for a monolayer graphene on a SiO₂/Si substrate ($\text{Im}(n) \sim 3 \times 10^{-4}$) at 300 K. To drive graphene in the population inversion with a negative dynamic conductivity, quasi-Fermi energies are parameterized at $\varepsilon_F = 10, 20, 30, 40, 50,$ and 60 meV and a carrier momentum relaxation time $\tau_m = 3.3$ ps is assumed [22]. The results demonstrate giant THz gain (negative values of absorption) on the order of 10^4 cm^{-1} . An increase in the substrate refractive index and, consequently, stronger localization of the surface plasmon electric and magnetic fields result in markedly larger gain, i.e., negatively larger absorption coefficient. Waveguiding the THz emitted waves with less attenuation is a critical key issue to create a graphene THz laser.

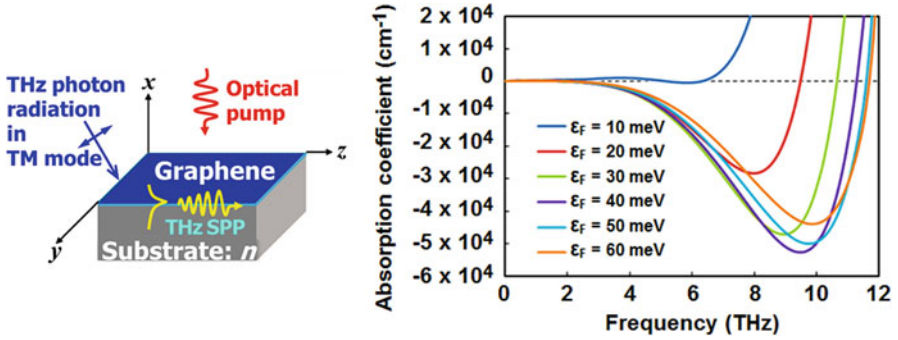


Fig. 8.5 Simulated absorption coefficient for monolayer graphene on a SiO_2/Si substrate ($\text{Im}(n) \sim 3 \times 10^{-4}$) at 300 K. To drive graphene in the population inversion with a negative dynamic conductivity, quasi-Fermi energies are parameterized at $\epsilon_F = 10, 20, 30, 40, 50,$ and 60 meV and a carrier momentum relaxation time $\tau_m = 3.3$ ps is assumed

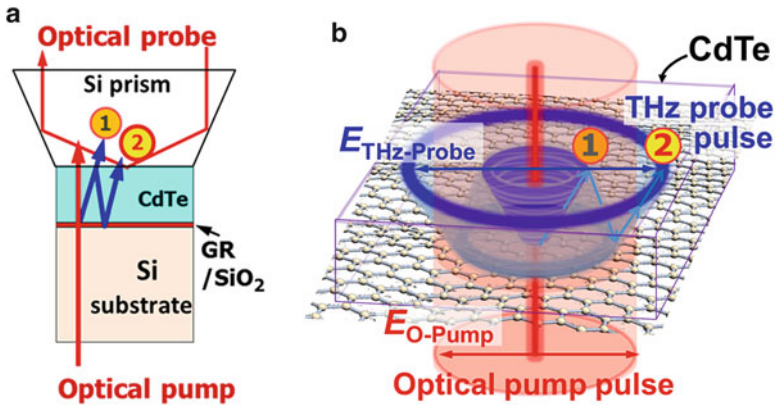


Fig. 8.6 Experimental setup of the time-resolved optical pump, THz probe, and optical probe measurement based on a near-field reflective electro-optic sampling. **(a)** Cross-sectional image of the pump/probe geometry and **(b)** birds view showing the trajectories of the optical pump and THz probe beams. The polarization of the optical pump and THz probe pulse are depicted with *red* and *dark-blue* arrow, respectively

We conducted optical pump, THz probe, and optical probe measurement at room temperature for intrinsic monolayer undoped graphene on a SiO_2/Si substrate [22]. The experimental setup is shown in Fig. 8.6. An 80-fs (in FWHM), 20-MHz repetition, 1,550-nm fiber laser was utilized as the optical pump and probe pulse source. The pumping laser beam, being linearly polarized, was focused with a beam diameter of about $120 \mu\text{m}$ onto the sample and the CdTe from the back side, while the probing beam is cross-polarized and focused from the top side. The CdTe can rectify the optical pump pulse to emit the envelope THz probe pulse. The emitted primary THz beam grows along the Cherenkov angle to be detected at the CdTe top surface as the primary pulse (marked with “①” in Fig. 8.6) and then reflects to the

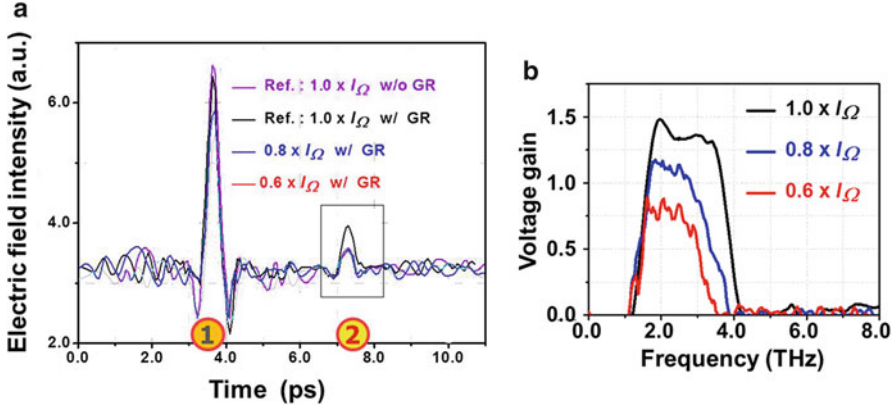


Fig. 8.7 (a) Measured temporal responses of the THz photon echo probe pulse (designated with “②”) for different pumping intensities I_{Ω} (3×10^7 W/cm²), $0.8 \times I_{\Omega}$, and $0.6 \times I_{\Omega}$. (b) Corresponding voltage gain spectra of graphene obtained by Fourier transforming the temporal responses of the secondary pulse measured at graphene flake, normalized to that at the position without graphene

graphene sample. When the substrate of the sample is conductive, the THz probe pulse transmitting through graphene again reflects back to the CdTe top surface, which is electro-optically detected as a THz photon echo signal (marked with “②” in Fig. 8.6). Figure 8.7a shows the temporal responses measured for different pumping pulse intensities of up to 3×10^7 W/cm² (pump fluence $2.4 \mu\text{J}/\text{cm}^2$, almost one order below the Pauli’s blocking) [22]. It is clearly seen that the peak obtained on graphene is more intense than that one obtained on the substrate without graphene and that the obtained gain factor exceeds the theoretical limit given by the quantum conductance by more than one order of magnitude as was measured in Ref. [21]. The Fourier-transformed gain spectra (Fig. 8.7b) are well reproduced and showed similar pumping intensity dependence with the results in Ref. [21].

We observed the spatial distribution of the THz probe pulse under the linearly polarized optical pump and THz probe pulse conditions at the maximum pumping intensity [22]. The optical probe pulse position was changed step by step to measure the in-plane spatial distributions of the THz probe pulse radiation. Observed field distributions for the primary pulse and the secondary pulse intensity are shown in Fig. 8.8 [22]. The primary pulse field is situated along the circumference with diameter $\sim 50 \mu\text{m}$ concentric to the center of optical pumping position. The secondary pulse (THz photon echo) field, on the contrary, is concentrated only at the restricted spot area on and out of the concentric circumference with diameter $\sim 150 \mu\text{m}$ where the incoming THz probe pulse takes a TM mode being capable of exciting the SPPs in graphene. The observed field distribution reproduces the reasonable trajectory of the THz echo pulse propagation inside of the CdTe crystal as shown in Fig. 8.6 when we assume the Cherenkov angle of 30 deg. which was determined by the fraction of the refractive indices between infrared and THz frequencies.

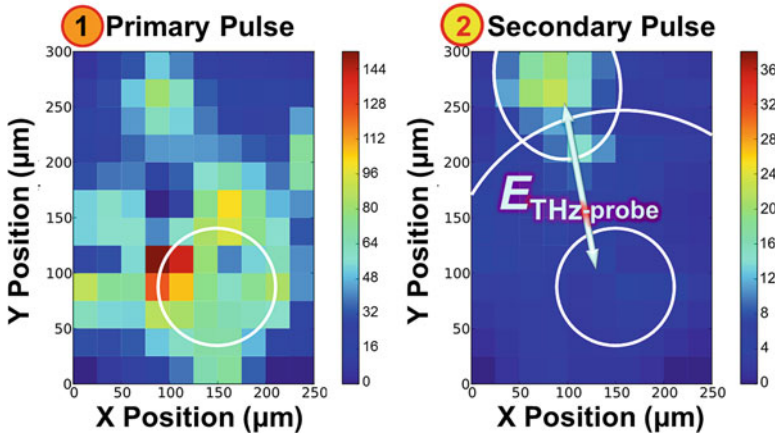


Fig. 8.8 Spatial field distribution of the THz probe pulse intensities. The primary pulse shows nonpolar distribution, whereas the secondary pulse shows a strong localization to the area in which the THz probe pulse is impinged to a graphene surface in the TM modes

How to couple the incoming/outgoing THz pulse photons to the surface plasmons in graphene is considered. One possibility of the excitation of SPPs by the incoming THz probe pulse is the spatial charge-density modulation at the area of photoexcitation by optical pumping. The pump beam having a Gaussian profile with diameter $\sim 120 \mu\text{m}$ may define the continuum SPP modes in a certain THz frequency range as seen in various SPP waveguide structures [58]. After short propagation on the order of $\sim 10 \mu\text{m}$, the SPPs approach the edge boundary of illuminated and dark area so that they could mediate the THz electromagnetic emission. The plasmon group velocity in graphene (exceeding the Fermi velocity) and propagation distance give a propagation time of the order of 100 fs. According to the calculated gain spectra shown in Fig. 8.7b, the gain enhancement factor could reach or exceed ~ 10 at the gain peak frequency 4 THz, which is dominated in the optically probed secondary pulse signals.

8.4 Toward the Creation of Current-Injection-Pumped Graphene THz Lasers

8.4.1 Lateral *p-i-n* Junction in Dual-Gate Graphene-Channel FETs

Optical pumping suffers from a significant heating of the electron-hole plasma and the optical phonon system, which suppresses the formation of population inversion [12, 59]. In the case of optical pumping with the sufficiently low photon energy,

however, the electron–hole plasma can be cooled down [12, 38, 59]. Another important parameter is the optical phonon decay time τ_o^{decay} which stands for the thermal conductivity of the material. A longer τ_o^{decay} (like suspended free-standing graphene) suppresses the carrier cooling, preventing from population inversion and thus from the negative conductivity [12]. Current-injection pumping is the best solution to substantially reduce the pumping threshold because electrical pumping can serve any pumping energy below the order of “meV” when a p - i - n junction is formed like semiconductor laser diodes. A dual-gate structure can make a p - i - n junction in the graphene channel as shown in Fig. 8.9a [10, 12]. Gate biasing controls the injection level, whereas the drain bias controls the lasing gain profiles (photon energy and gain). To minimize undesired tunneling current that lowers the injection efficiency, the distance between the dual-gate electrodes must be sufficiently long. Typical calculated conductivities are plotted in Fig. 8.9b [12]. Compared to the results for optical pumping shown in Fig. 8.4, the advantage of current injection is clearly seen. Waveguiding the THz emitted waves with less attenuation is another key issue. We theoretically discover the amplification of SPPs when traveling along the graphene-channel waveguide under population inversion [19].

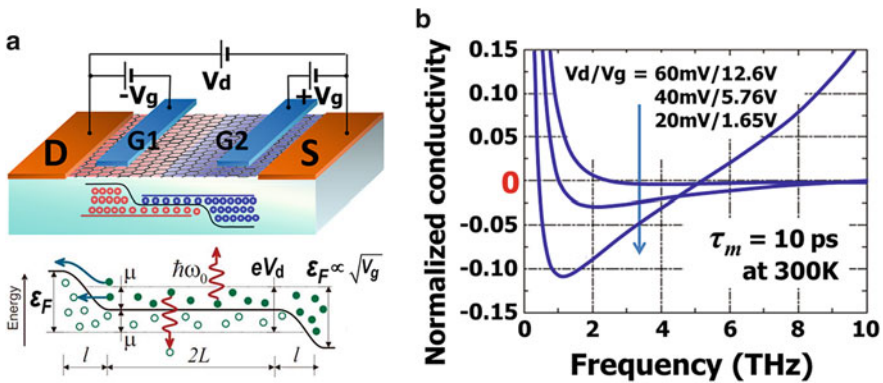


Fig. 8.9 (a) Schematics of the dual-gate field-effect transistor structure and corresponding band diagram for electrically pumping graphene to create current-injection THz lasers. Opposite biases on the two gates, G1 and G2, create an effective p - i - n lateral junctions. A small bias between drain D and source S injects electrons and holes from under the gates into the intrinsic region between the gates. Sufficient injection will create population inversion in this region and thus the possibility of optical gain for photons of energy $\hbar\omega_0$. μ is the quasi-Fermi energy in the intrinsic section given by the drain–source bias, whereas μ_i is the Fermi energy of the p -type and n -type region given by the dual-gate biases. (b) Simulated real parts of the terahertz conductivities (negative values corresponding to gain) of monolayer graphene at 300 K. The axis unit is normalized to the universal quantum conductivity $e^2/4\hbar$

8.4.2 Plasmonic THz Lasing and Superradiance in Dual-Grating Gate G-FETs

The amplification of THz wave by stimulated generation of resonant plasmons in a planar periodic array of graphene plasmonic microcavities (PA-GPMC) as shown in Fig. 8.10a has been theoretically derived [20]. Graphene microcavities are confined between the contacts of the metal grating located on a flat surface of a dielectric substrate. Suppose that the graphene is optically or electrically pumped. Figure 8.10b shows the contour map of the calculated absorbance as a function of the quasi-Fermi energy (which corresponds to the pumping strength and hence the population inversion) and the THz wave frequency for the PA-GPMC with period $L = 4 \mu\text{m}$ and the length of each microcavity $a = 2 \mu\text{m}$ [20]. With increasing ε_F , the energy gain can balance the energy loss so that the net energy loss becomes zero, $\text{Re}[\sigma(\omega)] = 0$, with corresponding graphene transparency. Above the graphene transparency line, the THz wave amplification at the plasmon resonance frequency is several orders of magnitude stronger than away from the resonances (the latter corresponding to the photon amplification in population-inverted graphene [9, 10, 12]).

At a certain value of the quasi-Fermi energy, the amplification coefficient at the plasmon resonance tends toward infinity with corresponding amplification linewidth shrinking down to zero as shown in Fig. 8.11a [20]. This corresponds to plasmonic lasing in the PA-GPMC in the self-excitation regime. The plasmons in different graphene microcavities oscillate in phase (even without the incoming

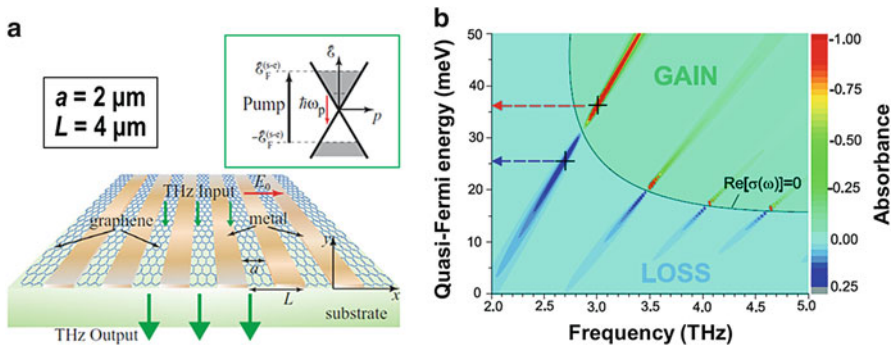


Fig. 8.10 (a) Schematic view of the array of graphene micro-/nanocavities. The incoming electromagnetic wave is incident from the top at normal direction to the structure plane with the polarization of the electric field across the metal grating contacts. The energy band structure of pumped graphene is shown schematically in the inset. (b) Contour map of the absorbance as a function of the quasi-Fermi energy and the frequency of incoming THz wave for the array of graphene microcavities with period $L = 4 \mu\text{m}$ and the length of a graphene microcavity $a = 2 \mu\text{m}$. The electron scattering time in graphene is $\tau_m = 10^{-12}$ s. Blue and red arrows mark the quasi-Fermi energies for the maximal absorption and for the plasmonic lasing regime, respectively, at the fundamental plasmon resonance

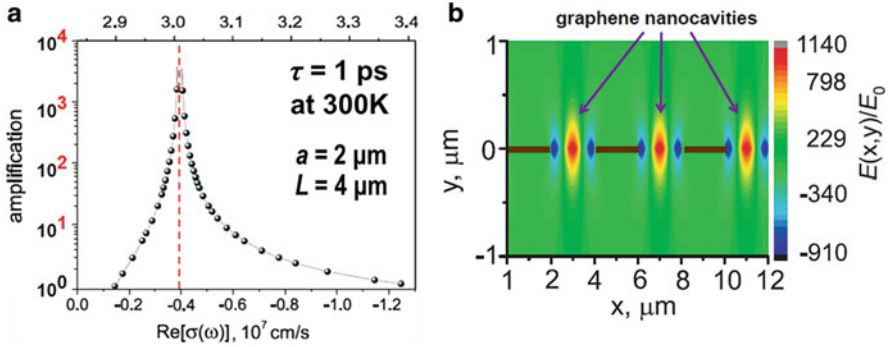


Fig. 8.11 (a) The variation of the power amplification coefficient along the first-plasmon-resonance lobe. (b) Distribution of the normalized induced in-plane electric field at the moment of time corresponding to the maximal swing of plasma oscillations in the graphene microcavities at the fundamental plasmon amplification resonance

electromagnetic wave) because the metal contacts act as synchronizing elements between adjacent graphene microcavities (applying a mechanical analogy, one may think of rigid crossbars connecting oscillating springs arranged in a chain) as shown in Fig. 8.11b. Therefore, the plasma oscillations in the PA-GPMC constitute a single collective plasmon mode distributed over the entire area of the array, which leads to the enhanced *superradiant* electromagnetic emission from the array.

8.5 Some Other Functional Devices

8.5.1 Graphene THz Modulators

The modulation of optical conductivity can work for the modulation of transmittance/reflectance of incoming photons as mentioned in Sect. 8.2. The first demonstration of a graphene optical modulator was performed in the infrared optical frequency region by using interband absorption in a double-layer graphene capacitor structure [60]. On the other hand, THz intensity modulators based on intraband absorption in graphene have been proposed and experimentally demonstrated by the group of Jena which is probably the first real “THz” application of graphene [28, 29]. The device exploits the electrical tuning of *intraband* Drude conductivity for making transmittance modulation to the THz electromagnetic radiation. They experimentally demonstrated a fairly high modulation index of up to $\sim 70\%$ by utilizing a simple structure of a back gate bias planar graphene capacitor in which the back gate electrode acts as a THz reflector [29]. It is also theoretically demonstrated that by introducing plasmonic effects with patterned graphene ribbon arrays, the modulation index could become 100% [57].

8.5.2 Graphene THz Detectors and Photomixers

Graphene-channel field-effect transistors (FETs) can originate a lateral p - i - n junction at the source and/or drain ohmic metal contact portions depending on the fractions of the work functions of the metal electrodes and graphene and on the gate biasing condition, which can be exploited as p - i - n photodetectors [61, 62]. At optical frequencies, excellent photodetection performance with high-frequency bandwidth beyond 40 GHz was demonstrated by the group of IBM [61]. Due to the gapless energy spectra of graphene, such a p - i - n junction can work for detection of THz radiation. Various novel device structures like dual-gate FETs as well as graphene sandwich have been proposed, and their superiority of the responsivity and high-frequency performances were analytically studied [27, 63].

On the other hand, the THz detectors using the resonant excitation plasma oscillations in the standard heterostructures like high-electron-mobility transistor with a gated 2D electron (or hole) plasma in its channel, proposed by Dyakonov and Shur [64], were also extensively studied theoretically and successfully fabricated and analyzed. The operation of these detectors is associated with the rectified component of the current due to the nonlinearity of the 2D electron plasma oscillations. At the plasma resonances when the THz signal frequency is approaching to the resonant plasma frequency and its harmonics, the responsivity of such detectors becomes fairly high. Plasma resonant phenomena in the gated graphene layer (GL) structures can also be used for the THz detection providing the enhanced performance.

One of the most prospective versions of the GL-based THz detectors exploiting the resonant excitation of the plasma waves can be realized using double-GL structures. In these structures, each GL plays the role of the gate for another GL. Such double-GL structures were fabricated and experimentally studied recently [65, 66]. Since the tunneling current between GLs exhibits pronounced nonlinear voltage dependence [3], the double-GL structures can also be used in different devices exploiting the plasma waves.

8.6 Conclusion

Recent advances and future trends in graphene THz devices are described. Gapless and linear energy spectra of electrons and holes in graphene produce unique features of THz dynamic conductivities which can be substantially modulated by electrostatic gate biasing in an FET structure, leading to various functional devices such as photodetectors, modulators, mixers, filters, etc. Ultrafast carrier relaxation and recombination dynamics of relativistic Dirac fermions in gapless linear band structures of optically or electrically pumped graphene give rise to negative dynamic conductivity in a wide THz range. This will open a new paradigm to create solid-state THz emitters and lasers using graphene but is inefficient to compete against the strong losses in the THz range. Two-dimensional plasmons in

graphene can dramatically enhance the light–matter interaction in THz frequency range, drastically improving the quantum efficiency and hence leading to higher output power of graphene THz amplifying and emitting devices. Plasmonic gain in graphene can exceed 10^4 cm^{-1} in a wide THz range which is four orders of magnitude higher than photonic gain in graphene. This gain enhancement effect of the surface plasmon polaritons on THz stimulated emission in optically pumped graphene has recently been experimentally verified. Graphene nanoribbon arrays locked between metallic grating fingers can promote strong stimulated emission of cooperative plasmon modes. Due to strong confinement of the plasmon modes in graphene microcavities and superradiant nature of electromagnetic emission from the array of the plasmonic microcavities, the amplification of THz wave enhances by several orders of magnitude at the plasmon resonance frequencies, resulting in superradiant THz lasing when the plasmon gain in graphene balances the sum of the dissipative and radiative damping of plasmon modes in the array of graphene microcavities. These new findings can lead to the creation of new types of plasmonic THz emitters and lasers operating up to room temperature.

Acknowledgments The author thanks V. Ryzhii, M. Ryzhii, A. Satou, S.A. Boubanga Tombet, V.V. Popov, A. Dubinov, Y.V. Aleshkin, V. Mitin, D. Svintsov, I. Semenikin, V. Vyurkov, M.S. Shur, E. Sano, T. Watanabe, T. Fukushima, S. Chan, T. Suemitsu, H. Fukidome and M. Suemitsu for their extensive contributions.

References

1. Novoselov KS, Geim AK, Morozov SV, Jiang D, Zhang Y, Dubonos SV, Grigorieva IV, Frisov AA (2004) Electric field effect in atomically thin carbon films. *Science* 306:666
2. Novoselov KS, Geim AK, Morozov SV, Jiang D, Katsnelson MI, Grigorieva IV, Dubonos SV, Firsov A (2005) Two-dimensional gas of massless Dirac fermions in graphene. *Nature* 438:197
3. Kim P, Zhang Y, Tan Y-W, Stormer HL (2005) Experimental observation of the quantum Hall effect and Berry's phase in graphene. *Nature* 438:201
4. Geim AK, Novoselov KS (2007) The rise of graphene. *Nat Mater* 6:183
5. Schwierz F (2010) Graphene transistors. *Nat Nanotech* 5:487–496
6. Bonaccorso F, Sun Z, Hasan T, Ferrari AC (2010) Graphene photonics and optoelectronics. *Nat Photon* 4:611–622
7. Bao Q, Loh KP (2012) Graphene photonics, plasmonics, and broadband optoelectronic devices. *ACS Nano* 6:3677–3694
8. Grigorenko AN, Polini M, Novoselov KS (2012) Graphene plasmonics. *Nat Photon* 6:749–759
9. Ryzhii V, Ryzhii M, Otsuji T (2007) Negative dynamic conductivity of graphene with optical pumping. *J Appl Phys* 101:083114
10. Ryzhii M, Ryzhii V (2007) Injection and population inversion in electrically induced p–n junction in graphene with split gates. *Jpn J Appl Phys* 46:L151
11. Ryzhii V, Dubinov A, Otsuji T, Mitin V, Shur MS (2010) Terahertz lasers based on optically pumped multiple graphene structures with slot-line and dielectric waveguides. *J Appl Phys* 107:054505
12. Ryzhii V, Ryzhii M, Mitin V, Otsuji T (2011) Toward the creation of terahertz graphene injection laser. *J Appl Phys* 110:094503

13. Otsuji T, Boubanga Tombet SA, Satou A, Fukidome H, Suemitsu M, Sano E, Popov V, Ryzhii M, Ryzhii V (2012) Graphene materials and devices in terahertz science and technology. *MRS Bull* 37:1235–1243
14. Otsuji T, Boubanga Tombet SA, Satou A, Fukidome H, Suemitsu M, Sano E, Popov V, Ryzhii M, Ryzhii V (2012) Graphene-based devices in terahertz science and technology. *J Phys D Appl Phys* 45:303001
15. Otsuji T, Boubanga Tombet S, Satou A, Ryzhii M, Ryzhii V (2013) Terahertz-wave generation using graphene: Toward new types of terahertz lasers. *IEEE J Select Top Quant Elect* 19:8400209
16. Ryzhii V, Satou A, Otsuji T (2007) Plasma waves in two-dimensional electron-hole system in gated graphene heterostructures. *J Appl Phys* 101:024509
17. Svintsov D, Vyurkov V, Yurchenko S, Otsuji T, Ryzhii V (2012) Hydrodynamic model for electron-hole plasma in graphene. *J Appl Phys* 111:083715
18. Rana F (2008) Graphene terahertz plasmon oscillators. *IEEE Trans Nanotechnol* 7:91–99
19. Dubinov AA, Aleshkin YV, Mitin V, Otsuji T, Ryzhii V (2011) Terahertz surface plasmons in optically pumped graphene structures. *J Phys Condens Matter* 23:145302
20. Popov VV, Polischuk OV, Davoyan AR, Ryzhii V, Otsuji T, Shur MS (2012) Plasmonic terahertz lasing in an array of graphene nanocavities. *Phys Rev B* 86:195437
21. Boubanga-Tombet S, Chan S, Watanabe T, Satou A, Ryzhii V, Otsuji T (2012) Ultrafast carrier dynamics and terahertz emission in optically pumped graphene at room temperature *Phys. Phys Rev B* 85:035443
22. Watanabe T, Fukushima T, Yabe Y, Boubanga Tombet SA, Satou A, Dubinov AA, Ya Aleshkin V, Mitin V, Ryzhii V, Otsuji T (2013) The gain enhancement effect of surface plasmon polaritons on terahertz stimulated emission in optically pumped monolayer graphene. *New J Phys* 15:075003
23. Falkovsky L, Varlamov A (2007) Space-time dispersion of graphene conductivity. *Eur Phys J B* 56:281
24. Ando T, Zheng Y, Suzuura H (2002) Dynamical conductivity and zero-mode anomaly in honeycomb lattices. *J Phys Soc Jpn* 71:1318–1324
25. Nair RR, Blake P, Grigorenko AN, Novoselov KS, Booth TJ, Stauber T, Peres NMR, Geim AK (2008) Fine structure constant defines visual transparency of graphene. *Science* 320:1308
26. Sensale-Rodriguez B, Yan R, Liu L, Jena D, Xing HG (2013) Graphene for reconfigurable terahertz optoelectronics. *Proc IEEE* 101:1705–1716
27. Ryzhii V, Ryabova N, Ryzhii M, Baryshnikov NV, Karasik VE, Mitin V, Otsuji T (2012) Terahertz and infrared photodetectors based on multiple graphene layer and nanoribbon structures. *Opto-Elect Rev* 20:15–25
28. Sensale-Rodriguez B, Yan R, Kelly MM, Fang T, Tahy K, Hwang WS, Jena D, Liu L, Xing HG (2012) Broadband graphene terahertz modulators enabled by intraband transitions. *Nat Comm* 3:780
29. Sensale-Rodriguez B, Yan R, Rafique S, Zhu M, Li W, Liang X, Gundlach D, Protasenko V, Kelly MM, Jena D, Liu L, Xing HG (2012) Extraordinary control of terahertz beam reflectance in graphene electro-absorption modulators. *Nano Lett* 12:4518–4522
30. Ju L, Geng B, Horng J, Girit C, Martin M, Hao Z, Bechtel HA, Liang X, Zettl A, Ron Shen Y, Wang F (2011) Graphene plasmonics for tunable terahertz metamaterials. *Nat Nanotech* 6:630–634
31. Maultzsch J (2004) Double-resonant Raman scattering in graphite: Interference effects, selection rules, and phonon dispersion. *Phys Rev B* 70:155403
32. Suzuura H, Ando T (2008) Zone-boundary phonon in graphene and nanotube. *J Phys Soc Jpn* 77:044703
33. Dawlaty JM, Shivaraman S, Chandrashekhara M, Rana F, Spencer MG (2008) Measurement of ultrafast carrier dynamics in epitaxial graphene. *Appl Phys Lett* 92:042116
34. George PA, Strait J, Dawlaty J, Shivaraman S, Chandrashekhara M, Rana F, Spencer MG (2008) Ultrafast optical-pump terahertz-probe spectroscopy of the carrier relaxation and recombination dynamics in epitaxial graphene. *Nano Lett* 8:4248

35. Breusing M, Ropers C, Elsaesser T (2009) Ultrafast carrier dynamics in graphite. *Phys Rev Lett* 102:086809
36. Rana F, George PA, Strait JH, Dawlaty J, Shivaraman S, Chandrashekhara M, Spencer MG (2009) Carrier recombination and generation rates for intravalley and intervalley phonon scattering in graphene. *Phys Rev B* 79:115447
37. Satou A, Otsuji T, Ryzhii V (2011) Theoretical study of population inversion in graphene under pulse excitation. *Jpn J Appl Phys* 50:070116
38. Satou A, Ryzhii V, Kurita Y, Otsuji T (2013) Threshold of terahertz population inversion and negative dynamic conductivity in graphene under pulse photoexcitation. *J Appl Phys* 113:143108
39. Foster MS, Aleiner IL (2009) Slow imbalance relaxation and thermoelectric transport in graphene. *Phys Rev B* 79:085415
40. Rana F (2007) Electron-hole generation and recombination rates for coulomb scattering in graphene. *Phys Rev B* 76:155431
41. Strait JH, Wang H, Shivaraman S, Shields V, Spencer M, Rana F (2011) Very slow cooling dynamics of photoexcited carriers in graphene observed by optical-pump terahertz-probe spectroscopy. *Nano Lett* 11:4902–4906
42. Winzer T, Knorr A, Malic E (2010) Carrier multiplication in graphene. *Nano Lett* 10:4839–4843
43. Obraztsov PA, Rybin MG, Tyurnina AV, Garnov SV, Obraztsova ED, Obraztsov AN, Svirko YP (2011) Broadband light-induced absorbance change in multilayer graphene. *Nano Lett* 11:1540–1545
44. Winzer T, Malic E (2012) Impact of Auger processes on carrier dynamics in graphene. *Phys Rev B* 85:241404(R)-1-5
45. Tani S, Blanchard F, Tanaka K (2012) Ultrafast carrier dynamics in graphene under a high electric field. *Phys Rev Lett* 99:166603-1-5
46. Dubinov AA, Aleshkin VY, Ryzhii M, Otsuji T, Ryzhii V (2009) Terahertz laser with optically pumped graphene layers and Fabry–Perot resonator. *Appl Phys Express* 2:092301
47. Ryzhii V, Ryzhii M, Satou A, Otsuji T, Dubinov AA, Aleshkin VY (2009) Feasibility of terahertz lasing in optically pumped epitaxial multiple graphene layer structures. *J Appl Phys* 106:084507
48. Li T, Luo L, Hupalo M, Zhang J, Tringides MC, Schmalian J, Wang J (2012) Femtosecond population inversion and stimulated emission of dense dirac fermions in graphene. *Phys Rev Lett* 108:167401
49. Hwang EH, Das Sarma S (2007) Dielectric function, screening, and plasmons in two-dimensional graphene. *Phys Rev B* 75:205418
50. Jablan M, Buljan H, Soljačić M (2009) Plasmonics in graphene at infrared frequencies. *Phys Rev B* 80:245435
51. Koppens FHL, Chang DE, García de Abajo FJ (2011) Graphene plasmonics: a platform for strong light-matter interactions. *Nano Lett* 11:3370
52. Rana F, Strait JH, Wang H, Manolatu C (2011) Ultrafast carrier recombination and generation rates for plasmon emission and absorption in graphene. *Phys Rev B* 84:045437
53. Nikitin AY, Guinea F, Garcia-Vidal FJ, Martin-Moreno L (2012) Surface plasmon enhanced absorption and suppressed transmission in periodic arrays of graphene ribbons. *Phys Rev B* 85:081405(R)
54. Wunsch B, Stauber T, Sols F, Guinea F (2006) Dynamical polarization of graphene at finite doping. *New J Phys* 8:318
55. Brey L, Fertig HA (2007) Elementary electronic excitations in graphene nanoribbons. *Phys Rev B* 75:125434
56. Popov VV, Bagaeva TY, Otsuji T, Ryzhii V (2010) Oblique terahertz plasmons in graphene nanoribbon arrays. *Phys Rev B* 81:073404
57. Sensale-Rodriguez B, Yan R, Zhu M, Jena D, Liu L, Xing HG (2012) Efficient terahertz electro-absorption modulation employing graphene plasmonic structures. *Appl Phys Lett* 101:261115

58. He X-Y, Wang Q-J, Yu S-F (2012) Numerical study of gain-assisted terahertz hybrid plasmonic waveguide. *Plasmonics* 7:571–577
59. Ryzhii V, Ryzhii M, Mitin V, Satou A, Otsuji T (2011) Effect of heating and cooling of photogenerated electron–hole plasma in optically pumped graphene on population inversion. *Jpn J Appl Phys* 50:094001
60. Liu M, Yin X, Zhang X (2012) Double-layer graphene optical modulator. *Nano Lett* 12:1482–1485
61. Xia F, Mueller T, Lin Y-M, Valdes-Garcia A, Vouris P (2009) Ultrafast graphene photodetector. *Nat Nanotech* 4:839–843
62. Mueller T, Xia F, Avouirs P (2010) Graphene photodetectors for high-speed optical communications. *Nat Photon* 4:297–301
63. Ryzhii M, Otsuji T, Mitin V, Ryzhii V (2011) Characteristics of p-i-n terahertz and infrared photodiodes based on multiple graphene layer structures. *Jpn J Appl Phys* 50:070117
64. Dyakonov M, Shur M (1996) Plasma wave electronics: novel terahertz devices using two dimensional electron fluid. *IEEE Trans Elect Dev* 43:1640–1646
65. Britnell L, Gorbachev RV, Jalil R, Belle BD, Schedin F, Mishchenko A, Georgiou T, Katsnelson MI, Eaves L, Morozov SV, Peres NMR, Leist J, Geim AK, Novoselov KS, Ponomarenko LA (2012) Field-effect tunneling transistor based on vertical graphene heterostructures. *Science* 335:947–950
66. Ryzhii V, Otsuji T, Ryzhii M, Shur MS (2012) Double graphene-layer plasma resonances terahertz detector. *J Phys D Appl Phys* 45:302001

Part II
Carbon Nanotube (CNT)

Chapter 9

Carbon Nanotube Synthesis and the Role of Catalyst

Yoshikazu Homma

Abstract This chapter describes the synthesis of single-walled carbon nanotubes (SWCNTs) by chemical vapour deposition (CVD). Nanoparticles called catalyst are indispensable to grow SWCNTs. Although commonly used catalyst species are iron-group metals, Fe, Co and Ni, they are not limited to metals but also encompass nonmetallic species. The essential role of the catalyst particle is to provide a large curvature surface for the formation of cap structure that includes five-membered rings and acts as the nucleus of SWCNT.

Keywords Catalyst • CVD • VLS

9.1 Introduction

Carbon nanotubes (CNTs) are rolled-up graphene with nanometre diameter. CNTs are synthesised using carbon source in solid, liquid or vapour phases. Since carbon solids have high vaporisation temperatures, high-temperature methods, such as arc discharge [1] and laser ablation [2], are necessary. Arc discharge is also applied to the CNT synthesis using liquid phase carbon sources such as sucrose solution [3]. On the other hand, vapour phase synthesis has more versatility in source gas, temperature and growth control. In particular for device applications of directly grown CNTs, chemical vapour deposition (CVD) is widely used. Another important aspect of CNT synthesis is use of catalysts. While multiwalled CNTs (MWCNTs) can be synthesised without using catalysts by the arc-discharge method, nanoparticles called catalyst are indispensable to grow single-walled CNTs (SWCNTs) that are single cylinders composed of graphene. The reason why nanoparticles are necessary is discussed in the following section. In short, while graphene nucleates on a flat surface, nucleation of CNT requires a surface with a large curvature.

Y. Homma (✉)

Department of Physics, Tokyo University of Science, Tokyo, Japan

e-mail: homma@rs.tus.ac.jp

© Springer Japan 2015

K. Matsumoto (ed.), *Frontiers of Graphene and Carbon Nanotubes*,

DOI 10.1007/978-4-431-55372-4_9

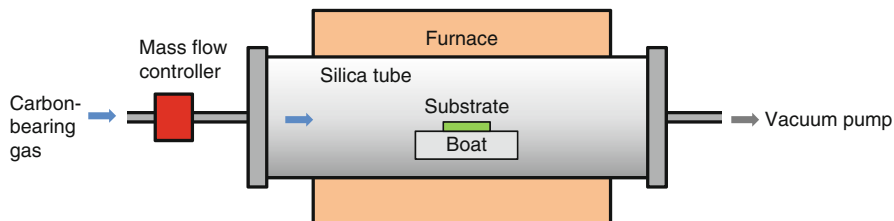


Fig. 9.1 CVD apparatus

9.2 CVD Growth

Vapour phase growth has been used as the synthesis method of carbon fibres. It has been intensively studied for SWCNT synthesis since 1998 [4]. Because carbon atoms are supplied by decomposition of source gas molecules, it is called chemical deposition. The source gases commonly used are hydrocarbons such as methane, ethane, ethylene and acetylene or alcohols such as ethanol and methanol. Those gas species are decomposed thermally or with assistance of plasma or hot filament. The presence of metal catalyst can promote the decomposition. Figure 9.1 is a schematic drawing of a typical thermal CVD apparatus. The key point of the CVD apparatus is the control of source gas flow, pressure and temperature. It is not necessarily a horizontal furnace type like Fig. 9.1. Vertical or cold wall types are also used. In CVD methods, by controlling the catalyst particle size, SWCNTs can be selectively grown. Also, by controlling the catalyst particle distribution or by using appropriate substrates, growth direction of individual SWCNTs can be controlled (see Chap. 10). Basically, an individual SWCNT grows from a catalyst particle in CVD.

9.3 Roll of Catalyst

Common catalyst species are iron-group metals, iron (Fe), cobalt (Co) and nickel (Ni) [5], which are known to have a catalytic function in assisting carbon feedstock cracking and producing graphite layers on a bulk material surface [6]. For these species, a widely accepted growth model is based on the vapour–liquid–solid (VLS) mechanism as the analogue of semiconductor nanowire growth from gold eutectic alloys [7]. As shown in Fig. 9.2, carbon-bearing molecules are catalytically decomposed on the surface of the catalyst, which is supposed to be in the liquid phase, resulting in the dissolution of carbon atoms into the catalyst particles. Upon supersaturation of carbon concentration in a particle, carbon atoms precipitate from the catalyst, leading to the formation of tubular carbon networks around or on the catalyst. From the viewpoint of carbon solubility and carbide phase formation in the carbon–metal binary phase diagram, Fe, Co and Ni should be the elements capable of catalysing SWCNT growth.

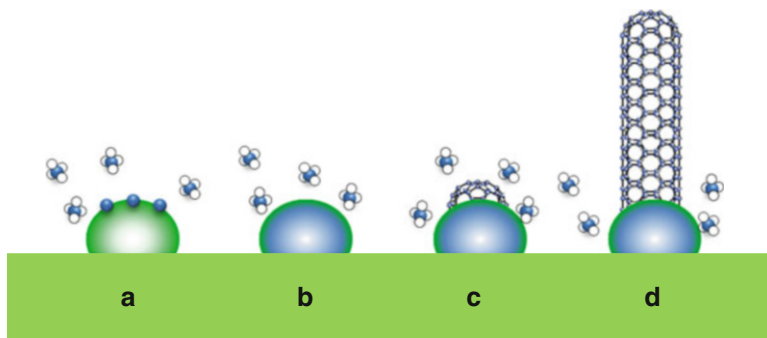


Fig. 9.2 SWCNT formation process. (a) Decomposition of carbon-bearing gas molecule on the catalyst surface. (b) Dissolution of carbon atoms into the catalyst. (c) Nucleation of cap. (d) Extension of SWCNT

However, it should be noted that a liquid phase is not essential for the VLS mechanism. Recent in situ transmission electron microscopy (TEM) observations have revealed that multiwalled CNTs grow continuously from crystalline Fe_3C particles at 600°C [8]. Although the Fe_3C particle shows clear lattice fringes, the crystal structure occasionally fluctuates during CVD, indicating that the particles are near their melting point. A similar result has been reported for germanium nanowire growth with a gold catalyst [9]. At just below the melting point, the solid particle might have a high density of vacancies, which allows efficient diffusion of carbon atoms. The point is carbon uptake into the metal particles and carbon precipitation from the carbon–metal eutectic alloy, i.e. continuous carbon supply from the bulk of nanoparticle is the key to the SWCNT growth.

Recently, many other species have been reported to yield SWCNTs [10, 11]: gold (Au), silver (Ag), copper (Cu), and aluminium (Al), as well as palladium (Pd) and platinum (Pt) that were used in the high-temperature synthesis such as arc-discharge method. Catalysts are not limited to metals but also encompass nonmetallic species, such as silicon (Si), germanium (Ge), silicon carbide (SiC) and alumina (Al_2O_3) [12, 13]. Even nanodiamond and fullerene have been reported to have the ability to catalyse CNT growth under limited conditions [14, 15]. Those materials barely have catalysis of hydrocarbon/alcohol decomposition or graphite formation. Therefore, the functions of catalyst in SWCNT formation need to be reconsidered.

Without nanoparticles, SWCNT formation never occurs. This implies a surface with a large curvature is necessary for SWCNT formation. Considering that SWCNTs have a cap at the opposite end to a catalyst particle, the nanoparticle surface should act as a template for the cap structure. The basic idea of this cap nucleation is that small graphene islands are self-formed without catalysis. The size of the island needs not be large and such a small graphene island is easily formed. In an early growth stage of a small graphene island on a Ni surface, a graphene island including a five-membered ring was shown to be energetically more favourable than a graphene island composed of all six-membered rings [16]. A similar sp^2 -bonded

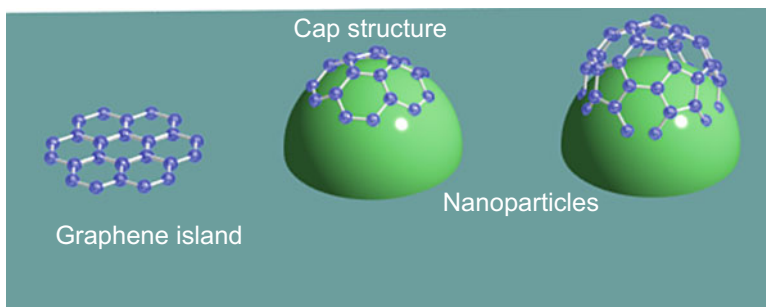


Fig. 9.3 The effect of nanoparticle on cap nucleation

island with five-membered rings (a cap) was shown to be formed following the diffusion of carbon atoms on a 1-nm iron particle surface by ab initio molecular dynamics simulations [17]. When a graphene island with five-membered rings is partially formed on a nanoparticle, it lifts off the particle surface except for the edge of the island and it becomes an SWCNT cap, as shown in Fig. 9.3.

For the continuous growth of SWCNT, carbon atoms need to be supplied to the tube edge. The edge of SWCNT is chemically active and acts as the incorporation site for carbon atoms. The interaction between the carbon atoms at the cap edge and the catalyst surface should not be so strong as to prevent incorporation of carbon atoms, but not too weak as to maintain an open end of the SWCNT [18]. In this respect, the VLS mechanism is a very efficient way to grow SWCNTs. The growth rate of SWCNT is the highest for iron catalyst. Vertically aligned growth and gas-flow-guided growth, both of which need a high growth rate, are almost exclusively achieved with iron and cobalt catalysts. The growth rate of SWCNT from nonmetal catalysts is generally low.

References

1. Iijima S (1991) Helical microtubules of graphitic carbon. *Nature* 354:56
2. Thess A, Lee R et al (1996) Crystalline ropes of metallic carbon nanotubes. *Science* 273:483
3. Aikawa S, Kizu T, Nishikawa E, Kioka T (2007) Carbon nanomaterial synthesis from sucrose solution without using graphitic electrodes. *Chem Lett* 36:1426
4. Kong J, Soh H et al (1998) Synthesis of single single-walled carbon nanotubes on patterned silicon wafers. *Nature* 395:878
5. Kong J, Cassell AM, Dai H (1998) Chemical vapor deposition of methane for single-walled carbon nanotubes. *Chem Phys Lett* 292:567
6. Hamilton JC, Blakely JM (1980) Carbon segregation to single crystal surfaces of Pt, Pd and Co. *Surf Sci* 91:199
7. Gavillet J, Loiseau A et al (2001) Root-growth mechanism for single-wall carbon nanotubes. *Phys Rev Lett* 87:275504
8. Yoshida H, Takeda S et al (2008) Atomic-scale in-situ observation of carbon nanotube growth from solid state iron carbide nanoparticles. *Nano Lett* 8:2082

9. Kodambaka S, Tersoff J et al (2007) Germanium nanowire growth below the eutectic temperature. *Science* 316:729
10. Takagi D, Homma Y et al (2006) Single-walled carbon nanotube growth from highly activated metal nanoparticles. *Nano Lett* 6:2642
11. Yuan D, Ding L et al (2008) Horizontally aligned single-walled carbon nanotube on quartz from a large variety of metal catalysts. *Nano Lett* 8:2576
12. Takagi D, Hibino H et al (2007) Carbon nanotube growth from semiconductor nanoparticles. *Nano Lett* 7:2272
13. Liu H, Takagi D et al (2008) Growth of single-walled carbon nanotubes from ceramic particles by alcohol chemical vapor deposition. *Appl Phys Express* 1:014001
14. Takagi D, Kobayashi Y, Homma Y (2009) Carbon nanotube growth from diamond. *J Am Chem Soc* 131:6922
15. Yu X, Zhang J et al (2010) From opened C₆₀ to single-walled carbon nanotubes. *Nano Lett* 10:3343
16. Fan X, Buczko R et al (2003) Nucleation of single-walled carbon nanotubes. *Phys Rev Lett* 90:145501
17. Raty JY, Gygi F et al (2005) Growth of carbon nanotubes on metal nanoparticles: a microscopic mechanism from ab initio molecular dynamics simulations. *Phys Rev Lett* 95:096103
18. Ding F, Larsson P et al (2008) The importance of strong carbon-metal adhesion for catalytic nucleation of single-walled carbon nanotubes. *Nano Lett* 8:463

Chapter 10

Aligned Single-Walled Carbon Nanotube Growth on Patterned SiO₂/Si Substrates

Yasuhide Ohno, Takafumi Kamimura, Kenzo Maehashi, Koichi Inoue, and Kazuhiko Matsumoto

Abstract Horizontally aligned single-walled carbon nanotubes (SWNTs) were fabricated on patterned SiO₂/Si substrates with groove-and-terrace or half-cylinder structures by electron-beam lithography and reactive ion etching. Scanning electron microscopy observation reveals that the SWNTs were aligned in the direction parallel to the patterned structures and were preferentially grown along the edges of terraces or along the sidewalls of the half cylinders. The results are consistent with calculations obtained using the Casimir–Polder potential between the SWNTs and the patterned substrates. Using aligned SWNTs as multichannels, carbon nanotube field-effect transistors (CNT-FETs) were fabricated on the patterned SiO₂/Si substrates. This method will be promising to control the directions of the SWNTs on SiO₂/Si substrates.

Keywords Horizontally aligned carbon nanotubes growth • Patterned substrate • Casimir–Polder potential

Y. Ohno (✉) • K. Inoue • K. Matsumoto
Institute of Scientific and Industrial Research, Osaka University, Mihogaoka 8-1, Ibaraki,
Osaka 567-0047, Japan
e-mail: ohno@sanken.osaka-u.ac.jp; inoue-k@sanken.osaka-u.ac.jp;
k-matsumoto@sanken.osaka-u.ac.jp

T. Kamimura
Institute of Scientific and Industrial Research, Osaka University, Mihogaoka 8-1, Ibaraki, Osaka
567-0047, Japan

Advanced ICT Research Institute, National Institute of Information and Communications
Technology, 4-2-1 Nukui-Kitamachi, Koganei, Tokyo 184-8795, Japan
e-mail: Kamimura@nict.go.jp

K. Maehashi
Tokyo University of Agriculture and Technology, Tokyo, Japan
e-mail: maehashi@sanken.osaka-u.ac.jp

10.1 Introduction

Single-walled carbon nanotubes (SWNTs) are one of the most promising materials for the fabrication of nanoscale devices or microelectrodes owing to their unique mechanical, chemical, and electrical properties. In particular, carbon nanotube field-effect transistors (CNT-FETs), in which semiconducting SWNTs are used as channels, are expected to find applications as highly integrated CNT-based circuits and highly sensitive label-free sensors. In order to realize such devices, it is necessary to fabricate high-performance CNT-FETs with high-current outputs.

Well-aligned, very dense SWNT arrays are expected to be used as channels for high-performance CNT-FETs with high-current outputs. Using conventional photolithography and the metal lift-off process, catalyst particles can be precisely positioned on these arrays. From these particles, it is possible to grow SWNTs. In general, however, the growth direction of SWNTs on SiO_2/Si substrates is difficult to control since SiO_2 is an amorphous material. In recent years, SWNTs have been aligned in a specific direction on sapphire or single-crystal quartz substrates [1–4]. SWNTs are grown along periodic steps or in a specific crystallographic direction. Furthermore, it has been demonstrated that aligned SWNTs on sapphire or single-crystal quartz substrates can be transferred to flexible substrates. Complementary metal oxide semiconductor logic gates were also fabricated on plastic substrates [5,6]. On the other hand, thin SiO_2 films act as electric insulators with high chemical stability, and SiO_2/Si substrates are useful for the fabrication of back-gated FETs. As a result, CNT-FETs on SiO_2/Si substrates have been investigated. Thus, the control of the SWNT growth direction on SiO_2/Si substrates is still desired for the fabrication of nanodevices using conventional Si processes, which are suitable for mass production of highly integrated devices, resulting in price reduction. Moreover, CNT nanodevices can be combined with Si-integrated circuits. In this study, we demonstrated the formation of aligned SWNTs on patterned SiO_2/Si substrates using electron-beam (EB) lithography and reactive ion etching (RIE) techniques.

10.2 Experimental Procedure

Two types of patterned SiO_2/Si substrate were fabricated by EB lithography and RIE techniques. The first type has groove-and-terrace structures, as shown in Fig. 10.1a, and the other type has half-cylinder structures, as shown in Fig. 10.1b. The fabrication of the patterned SiO_2/Si substrates is as follows. A p^+ -type Si wafer with a thermally oxidized SiO_2 (300 nm) layer was used as a substrate. After coating the SiO_2 layer with an EB resist (ZEP520A), lines were patterned by EB lithography. The SiO_2 layer was etched by the RIE technique using CF_4 gas after developing the EB resist. Figure 10.1c, d shows cross-sectional scanning electron microscopy (SEM) images of typical patterned substrates with groove-and-terrace and half-cylinder structures, respectively. The height of the terraces was controlled by etching time during the RIE process. Subsequently, a 0.5-nm-thick Co catalyst

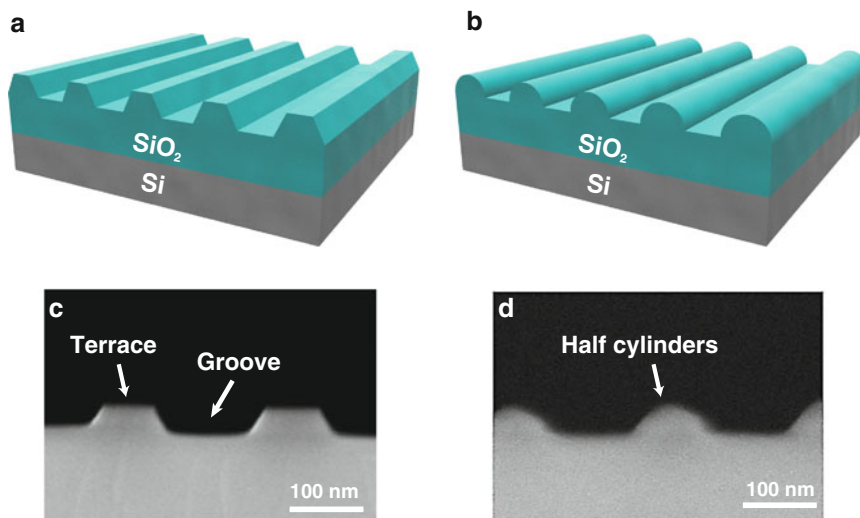


Fig. 10.1 Schematic illustration of patterned SiO₂/Si substrates: (a) groove-and-terrace and (b) half-cylinder structures. Cross-sectional SEM images on the SiO₂/Si patterned substrates with (c) groove-and-terrace and (d) half-cylinder structures

was patterned on the substrates by conventional photolithography. Finally, SWNTs were synthesized by thermal chemical vapor deposition at 900 °C for 10 min, using C₂H₅OH as a source gas.

10.3 Results and Discussion

10.3.1 Direction Control Growth

The SWNTs grown on the patterned SiO₂/Si substrates with groove-and-terrace structures were observed by SEM. Figure 10.2a shows an SEM image of the SWNTs on the patterned and planar SiO₂/Si substrates. The inset of Fig. 10.2a shows a schematic illustration of the SiO₂/Si substrate shown in Fig. 10.2a. As is shown in the SEM image, the SWNTs started to grow from the top and bottom of the patterned catalyst area. The distance between the patterned catalyst areas was estimated to be 50 nm. The left-hand side in the SEM image corresponds to a flat surface area, revealing that the SWNTs grew in a random direction. In contrast, the right-hand side of the image corresponds to the patterned area with groove-and-terrace structures, as shown in Fig. 10.1a, c. The height and width of the terraces were estimated to be approximately 40 and 100 nm, respectively. The SEM image in Fig. 10.2a reveals that the SWNTs were aligned on the patterned areas in the direction parallel to the groove-and-terrace structures. Note that the SWNT growth direction was not affected by the direction of gas flow during SWNT

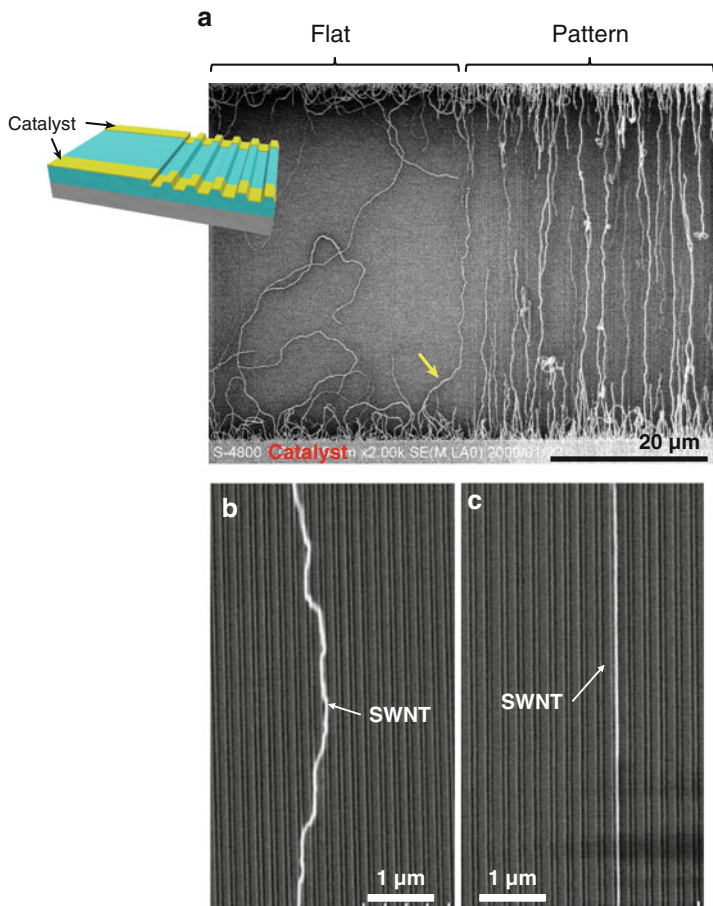


Fig. 10.2 (a) SEM image of SWNTs on the patterned SiO_2/Si substrate with groove-and-terrace structures. The left and right sides correspond to the flat and patterned areas, respectively. The *inset* is a schematic illustration of the substrate. (b) and (c) Magnified SEM images of SWNTs

synthesis [7]. One SWNT, indicated by the arrow in Fig. 10.2a, started growing from the catalyst on the flat area and progressed along this area to reach the patterned area. After that, the growth direction of the SWNT changed and the SWNT was aligned in the direction parallel to the groove-and-terrace structures. Therefore, these results indicate that patterned substrates are useful to control the growth direction of SWNTs. Some SWNTs on the patterned substrates grew astride a few groove-and-terrace structures, as shown in Fig. 10.2b. The growth direction of the SWNTs, however, was parallel to the groove-and-terrace structures. As shown in Fig. 10.2c, other SWNTs were oriented in a straight line along one groove-and-terrace structure.

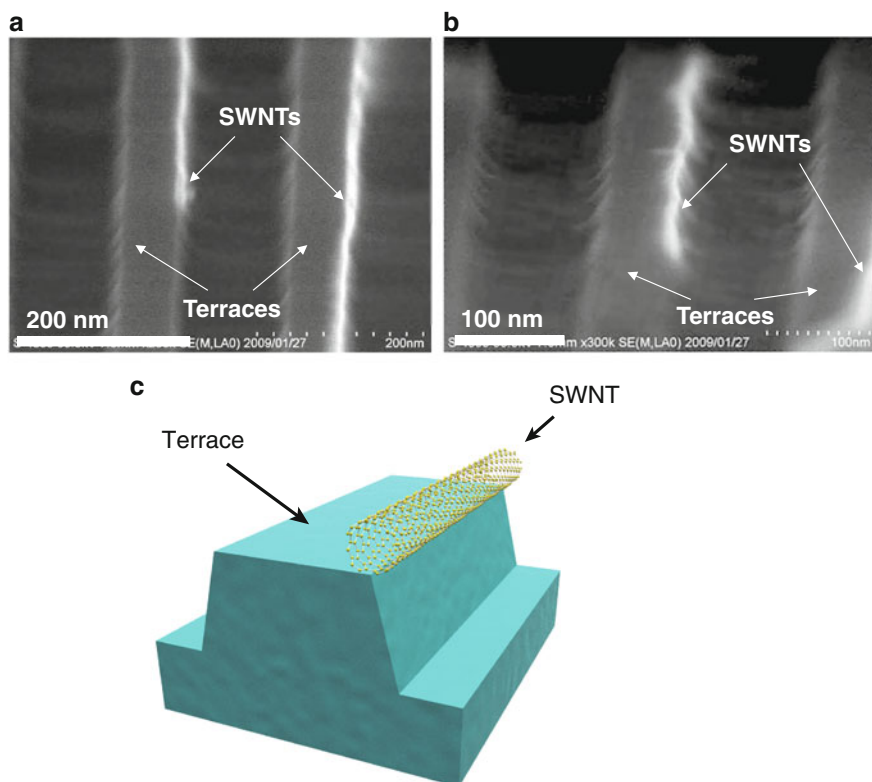


Fig. 10.3 (a) and (b) SEM images of SWNTs on the patterned SiO₂/Si substrate with groove-and-terrace structures. (c) Schematic illustration of SWNTs on the patterned SiO₂/Si substrate with groove-and-terrace structures

Figure 10.3a shows an enlarged SEM image to investigate the exact position of the SWNTs on patterned SiO₂/Si substrates with groove-and-terrace structures. It is found that the SWNTs grew parallel to the groove-and-terrace structures. Next, the sample was tilted, and then in almost the same position as that in Fig. 10.3a, it was observed as shown in Fig. 10.3b. The SEM image reveals that the SWNTs adhered onto the edge of the terraces, as shown in a schematic image of Fig. 10.3c. For this reason, the growth direction of the SWNTs is parallel to the groove-and-terrace structures.

Figure 10.4a shows an SEM image of SWNTs on the patterned SiO₂/Si substrates with half-cylinder structures, as shown in Fig. 10.1b, d. The SWNTs were also aligned on the patterned SiO₂/Si substrate with half-cylinder structures. A magnified SEM image in Fig. 10.4b reveals that the majority of SWNTs adhered onto the sidewalls of the half-cylinder structures. As a result, the growth direction of the SWNTs is parallel to the half-cylinder structures, as shown in Fig. 10.4a.

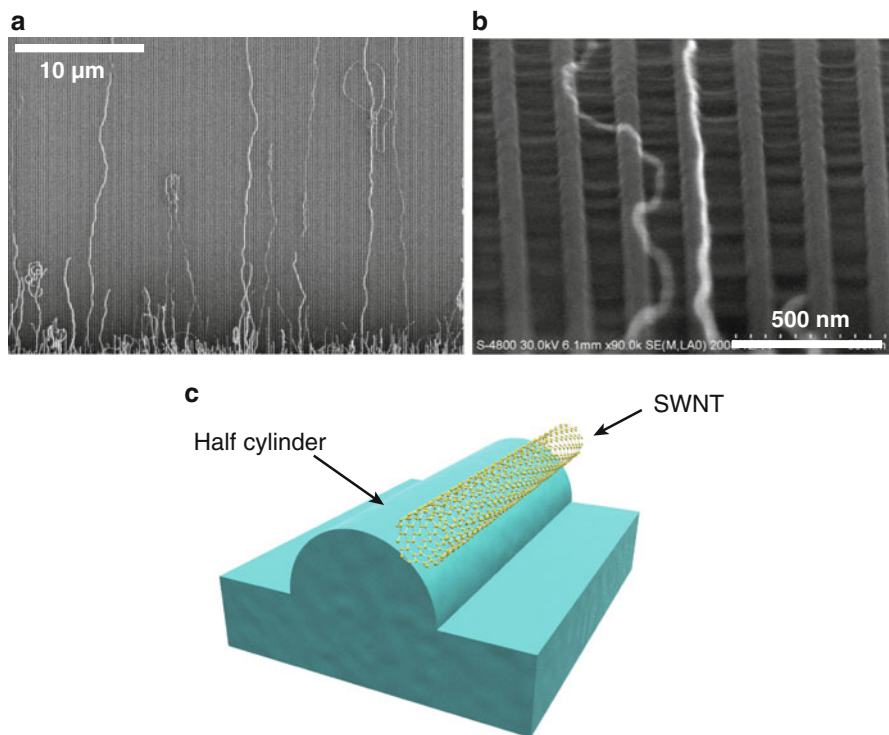


Fig. 10.4 (a) SEM image of SWNTs on the SiO₂/Si patterned substrate with half-cylinder structures. (b) Magnified SEM image of SWNTs. (c) Schematic illustration of SWNTs on the patterned SiO₂/Si substrate with half-cylinder structures

Two dielectric materials such as the SWNTs and Si substrate are attracted to each other by the Casimir–Polder interaction [8, 9]. The potential energy of a small portion of SWNTs located near the infinite flat substrate is proportional to $\sim -1/d^4$, where d is the distance from the substrate surface. Such forces work during and after growth and perhaps determine the configuration of SWNTs. Figure 10.5a, b shows the contour plots of the Casimir–Polder potential E and the force lines calculated for the patterned substrates with groove-and-terrace and half-cylinder structures, respectively. The position 0 on the horizontal axis corresponds to the center of the terrace or half cylinder, and the position 0 on the vertical axis corresponds to the surface of the grooves. The calculations reveal that the Casimir–Polder potential decreased as the SWNTs approached the patterned substrates. The force lines are drawn at regular intervals in the upper part of the figures where the potential contour is almost flat since the effect of the patterned structures becomes negligible with distance from the surface. In contrast, near the substrate surface, the potential contour and force lines are more affected by the patterned structures. In particular, the force lines are concentrated at a certain region near the surface, as

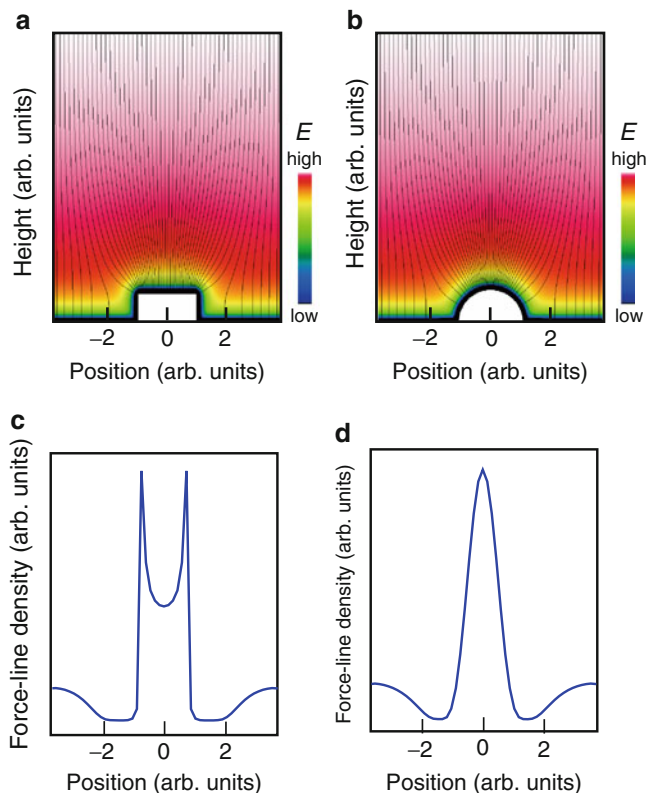
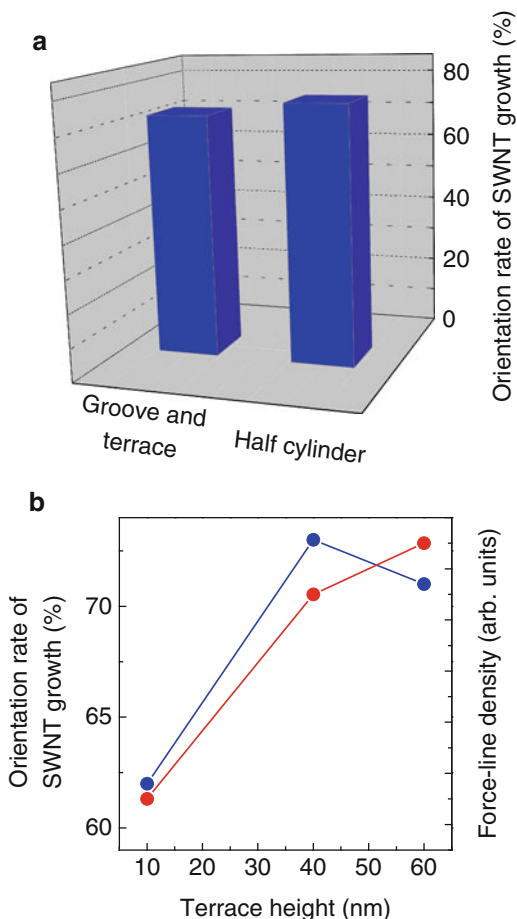


Fig. 10.5 Contour plots of the Casimir–Polder potential E and the force lines for the SiO₂/Si patterned substrates with the groove-and-terrace (a) and half-cylinder (b) structures. Density of the force lines on the surfaces of the patterned substrates with the groove-and-terrace (c) and half-cylinder (d) structures

shown in Fig. 10.5a, b. Thus, we define the density of the force lines as the inverse of the force-line interval. For groove-and-terrace structures, the direction of the force lines is concentrated on the edge of the terraces, as shown in Fig. 10.5a. Figure 10.5c shows the density of the force lines on the surface of the patterned substrate with groove-and-terrace structures. As a result, the density of the force lines on the edges of the terraces becomes much higher than that on the edge of the grooves, as shown in Fig. 10.5c. Therefore, the SWNTs were preferentially grown along the edge of the terraces. This result was consistent with the SEM image, as shown in Fig. 10.3b. For half-cylinder structures, the density of the force lines at the sidewalls of the half-cylinder structures became higher than that at groove regions and the density at the center of the sidewalls was highest, as shown in Fig. 10.5d. Although the majority of SWNTs adhered onto the sidewalls of the half-cylinder structures, some of the SWNTs did not grow along the center of the sidewalls. The results are considered to be due to the effects of contaminations and distortion of the half-cylinder structures.

Fig. 10.6 (a) Orientation rate of SWNT growth on the patterned SiO_2/Si substrates with the groove-and-terrace and half-cylinder structures. (b) Orientation rate of SWNT growth and density of the force lines on the patterned SiO_2/Si substrate with groove-and terraces as a function of the terrace height



The orientation rate of SWNT growth on the patterned substrates was estimated from the SEM images, where the orientation rate of SWNT growth in percentage was defined as the length of SWNTs on the edges of the terraces or the sidewalls of the half-cylinder structures with respect to the total length of the SWNTs on the patterned substrates. Figure 10.6a shows the orientation rates of SWNT growth on the patterned substrates with the groove-and-terrace and half-cylinder structures, which were estimated to be 72 and 77 %, respectively. The results indicate that the patterned structures are useful to control the direction of SWNT growth. The orientation rate of SWNT growth on the patterned SiO_2/Si substrates with the groove-and-terrace structures was investigated as a function of the height of the terraces from the SEM images, as shown in Fig. 10.6b. Although there is no large difference between the orientation rates of SWNT growth for the terraces with heights of 40 and 60 nm, these orientation rates became much larger than

that for the height of 10 nm. We suggest that terrace heights of 40 and 60 nm are sufficient for the alignment of SWNT growth because these are much larger than the diameter of the SWNTs. The density of the Casimir–Polder force lines on the patterned substrates with groove-and-terrace structures was also calculated for the terrace heights of 10, 40, and 60 nm, as shown in Fig. 10.6b. The results reveal that the density of the force lines increased with increasing terrace height, indicating that the difference in the density of the force lines between the edge of the terrace and the groove became larger with increasing terrace height. Consequently, the calculated results are consistent with the terrace height dependence of the orientation rate of SWNT growth, as shown in Fig. 10.6b. Therefore, the terrace heights of 40 and 60 nm are effective to control the direction of SWNT growth.

However, the density of SWNTs on the patterned SiO₂/Si substrates was lower than that on single-crystal quartz substrates [10, 11]. As shown in SEM images of Fig. 10.2a, the growth of many SWNTs stopped, which is considered to be due to the roughness and contamination of resist. If the technique of EB lithography and RIE process is improved, the density of SWNTs on the patterned SiO₂/Si substrates can be increased. Moreover, when the width of terraces and grooves is changed, the density of SWNTs can be controlled.

Figure 10.7 shows typical Raman spectra of the SWNTs at low- and high-frequency regions, respectively, which were synthesized on the patterned SiO₂/Si substrates. Radial breathing modes that are specific to SWNTs were clearly observed, as shown in Fig. 10.7. In addition, a strong G-band peak was observed, and the D-band peak, which is related to structural disorder, was quite weak, as shown in Fig. 10.3. These results indicate that high-purity, high-quality SWNTs were formed on the patterned SiO₂/Si substrates.

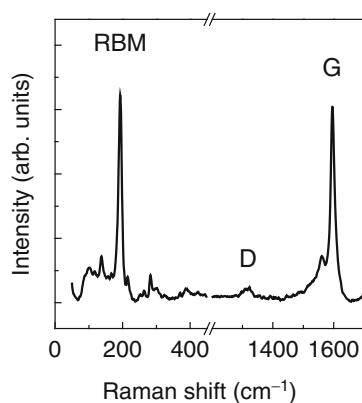
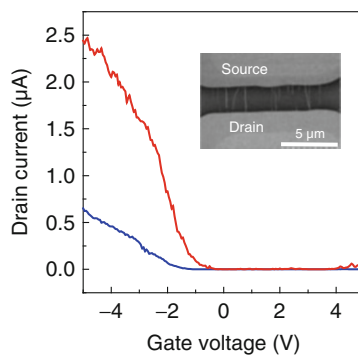


Fig. 10.7 Raman spectra of SWNTs synthesized on patterned SiO₂/Si substrates

10.3.2 Fabrication of FETs

Finally, CNT-FETs were fabricated on the patterned SiO_2/Si substrates with groove-and-terrace structures. The horizontally aligned SWNTs were used as the channels of the CNT-FETs. The inset of Fig. 10.8 shows an SEM image of a CNT-FET fabricated on the patterned SiO_2/Si substrate. Ti/Pd was used for source and drain electrodes. The distance between the source and drain electrodes was estimated to be approximately $3\ \mu\text{m}$. The SEM image reveals that several SWNTs bridged between the source and drain electrodes. Figure 10.5a shows the drain current in the CNT-FET on the patterned SiO_2/Si substrates with groove-and-terrace structures at room temperature as a function of back-gate voltage. The back-gate voltage was swept from -5 to 5 V. The source-drain current increased with decreasing back-gate voltage in the positive direction, indicating that the device had *p*-type characteristics. A good pinch-off characteristic with a threshold voltage of 0.5 V and an on/off ratio of 10^4 were obtained. The transconductance was estimated to be $1.7\ \mu\text{S}$. It is noted that no leakage current between the source and back-gate electrodes was measured. For comparison, transfer characteristics of a CNT-FET fabricated on a flat surface are shown in Fig. 10.8. The device was formed under the same conditions as that on the patterned SiO_2/Si substrates. Similar transfer characteristics to those in the previous report were obtained. These results indicate that the CNT-FET fabricated on the patterned SiO_2/Si substrates had five times higher transconductance and four times larger on-current than that built on the flat surface. For the CNT-FET on the flat surface, one SWNT was bridged between the source and drain electrodes. In contrast, several SWNTs were bridged between the source and drain electrodes for the CNT-FET on the patterned SiO_2/Si substrates. As a result, a higher-performing CNT-FET was obtained. We expect to synthesize more aligned SWNTs with high density using the described method, optimizing the formation condition of the patterned substrate and the growth conditions of the SWNTs.

Fig. 10.8 Transfer characteristics in CNT-FETs fabricated on (a) patterned and (b) flat SiO_2/Si substrates. The *inset* shows an SEM image of the CNT-FET fabricated on the patterned SiO_2/Si substrate



10.4 Conclusion

We fabricated horizontally aligned SWNTs on patterned SiO₂/Si substrates with groove-and-terrace or half-cylinder structures by EB lithography and RIE. SEM reveals that the SWNTs preferentially grew along the edges of terraces or along the sidewalls of the half cylinders. We calculated the Casimir–Polder potential on the surfaces of the patterned substrates to clarify the SEM observations. As a result, it was found that the density of the force lines on the edges of terraces or the sidewalls of the half cylinders became much higher than that on the flat areas. The orientation rate of SWNT growth on the patterned SiO₂/Si substrates with the groove-and-terrace structures was also shown to be a function of the height of the terraces. CNT-FETs with multichannels were fabricated on the patterned SiO₂/Si substrates. This method will be promising to control the direction of SWNTs on SiO₂/Si substrates for the fabrication of high-performance CNT-FETs with high-current outputs.

References

1. Han S, Liu X, Zhou C (2005) Template-free directional growth of single-walled carbon nanotubes on a- and r-plane sapphire. *J Am Chem Soc* 127:5294–5295
2. Kocabas C, Hur S, Gaur A, Meitl M, Shim M, Rogers J (2005) Guided growth of large-scale, horizontally aligned arrays of single-walled carbon nanotubes and their use in thin-film transistors. *Small* 1:1110–1116
3. Kang S, Kocabas C, Ozel T, Shim M, Pimparkar N, Alam M, Rotkin S, Rogers J (2007) High-performance electronics using dense, perfectly aligned arrays of single-walled carbon nanotubes. *Nat Nanotechnol* 2:230–236
4. Shulaker MM, Hills G, Patil N, Wei H, Chen H-Y, Wong H-SP, Mitra S (2013) Carbon nanotube computer. *Nature* 501:526–530
5. Liu X, Han S, Zhou C (2006) Novel Nanotube-on-Insulator (NOI) approach toward single-walled carbon nanotube devices. *Nano Lett* 6:34–39
6. Cao Q, Kim H, Pimparkar N, Kulkarni J, Wang C, Shim M, Roy K, Alam M, Rogers J (2008) Medium-scale carbon nanotube thin-film integrated circuits on flexible plastic substrates. *Nature* 454:495–500
7. Huang S, Cai X, Liu J (2003) Growth of millimeter-long and horizontally aligned single-walled carbon nanotubes on flat substrates. *J Am Chem Soc* 125:5636–5637
8. Casimir H, Polder D (1948) The influence of retardation on the London-van der Waals Forces. *Phys Rev* 73:360–372
9. Milton K, Parashar P, Wagner J (2008) Exact results for casimir interactions between dielectric bodies: the weak-coupling or van der Waals limit. *Phys Rev Lett* 101:160402
10. Cao Q, Rogers J (2009) Ultrathin films of single-walled carbon nanotubes for electronics and sensors: a review of fundamental and applied aspects. *Adv Mater* 21:29–53
11. McNicholas T, Ding L, Yuan D, Liu J (2009) Density enhancement of aligned single-walled carbon nanotube thin films on quartz substrates by sulfur-assisted synthesis. *Nano Lett* 9:3646–3650

Chapter 11

Plasma Doping Processes for CNT Devices

Rikizo Hatakeyama, Toshiaki Kato, Yongfeng Li, and Toshiro Kaneko

Abstract A variety of plasmas including positive and negative ions are prepared in gaseous, liquid, and gas–liquid interfacial phases in order to functionalize carbon nanotubes (CNTs) with properties corresponding to electronic and biomedical device applications. In the case of internal doping, alkali metal, alkaline-earth metal, halogen, iron atoms, fullerene, azafullerene, and DNA molecules are encapsulated inside single-walled carbon nanotubes (SWNTs) and double-walled carbon nanotubes (DWNTs) with hollow inner spaces using the plasma-ion irradiation method. The electrical, magnetic, and optical properties of the encapsulated SWNTs and DWNTs are found to be greatly changed compared with those of pristine ones. As a result, a number of significant and nanodevice-applicable transport phenomena are observed, in which air-stable carrier-type control, embedded formation of p – n junction, quantum dot formation, distinct negative differential resistance, magnetic semiconducting behavior, photoinduced electron transfer, and photoelectric conversion are highlighted here. Furthermore, the combination of internal and surface doping processes leads to the creation of Au nanoparticle–DNA–SWNT conjugates toward a nano-biomedical device application.

Keywords Plasma doping • Encapsulation • Functionalization • CNT devices

Carbon nanotubes (CNTs), such as single-walled CNTs (SWNTs) formed by rolled graphene sheets, have become a subject of intensive investigation. In addition to their remarkable intrinsic properties, new functional CNT-based materials are expected to be created by incorporating foreign materials, enlarging application scopes in nanodevices and nano-bio fusion devices with novel electrical, magnetic, and optical properties. Here, an original approach of ion irradiation to CNTs using various kinds of plasmas is introduced for the purpose of tailoring physical, chemical, and biological properties of pristine CNTs. Concretely, a variety of atoms, molecules including DNA, and their combinations can selectively be encapsulated inside CNTs during plasma processing in either gaseous or liquid phase, while

R. Hatakeyama (✉) • T. Kato • Y. Li • T. Kaneko
Department of Electronic Engineering, Tohoku University, Sendai 980-8579, Japan
e-mail: hatake@ecei.tohoku.ac.jp

CNTs are conjugated with nanoparticles using plasma–liquid interfaces from the viewpoint of CNT surface modification. Next, electrical and magnetic properties of these doped CNTs are experimentally clarified, which constitute fundamentals of nanodevice applications such as air-stable conductance, carrier-type, and magnetism control. The following is the potential for making electro-optic fusion devices including photoinduced switching and solar cell devices using the doped CNTs. Finally, the future challenge related to a nano-biomedical electronic system emerges, where the encapsulation of DNA–nanoparticle conjugates inside CNTs is tried using gas–liquid interfacial plasmas.

11.1 Internal and Surface Doping of CNTs Using Various Kinds of Plasmas

Modification of SWNTs with other foreign materials is recognized to be attractive for the purpose of controlling their properties through the interaction with electron donors or acceptors. A plasma-ion irradiation method is found to be efficient for the insertion of various kinds of atoms or molecules into CNTs, where different polarity ions can selectively be accelerated toward a substrate coated with pristine CNTs by adjusting its bias voltages ϕ_{ap} [1–3]. Figure 11.1a shows a schematic of the generation of alkali–fullerene plasmas ($A^+ - C_{60}^-$, $A = \text{Li}^+, \text{Na}^+, \text{K}^+, \text{Cs}^+$) with a very small fraction of the electron density. At one machine end, the plasma is produced through surface–contact ionization of alkali metals on a hot tungsten plate ($A^+ - e^-$), the density and electron temperature of which are $1 \times 10^8 \sim 10^{10} \text{ cm}^{-3}$ and 0.2 eV (\geq positive ion temperature). On the way of flowing downstream, electron attachment to sublimated C_{60} molecules takes place in the middle part of the plasma column, and C_{60} negative ions are formed ($C_{60} + e^- \rightarrow C_{60}^-$), resulting in the generation of alkali–fullerene plasmas. The controllable ion irradiation to the CNTs can be realized when largely positive or negative biases are applied to the substrate: $\phi_{\text{ap}} \gg 0$ for C_{60}^- , $\phi_{\text{ap}} \ll 0$ for A^+ . In addition, a plasma source consisting of alkali positive ions and halogen negative ions is developed with a DC magnetron discharge under a uniform magnetic (B) field, as schematically shown in Fig. 11.1b. Thermal electrons drift in the azimuthal ($E \times B$) direction, and the electrons collide with alkali salt, dissociating and ionizing it. As a result of this process, alkali positive ions, halogen negative ions, and electrons are produced. The electrons can be removed from the processing region by a magnetic filter effect. Furthermore, in order to exploit a unique electrical property of some fullerene, i.e., $C_{59}\text{N}$ (azafullerene), one carbon atom of which is displaced by atomic nitrogen, a quasipair fullerene-ion plasma is generated as depicted in Fig. 11.1c. In this case, both the massive $C_{59}\text{N}^+$ and C_{60}^- ions preferentially diffuse across strong axial B field lines, forming the quasipair ion plasma with slightly different masses outside a core region of the plasma column.

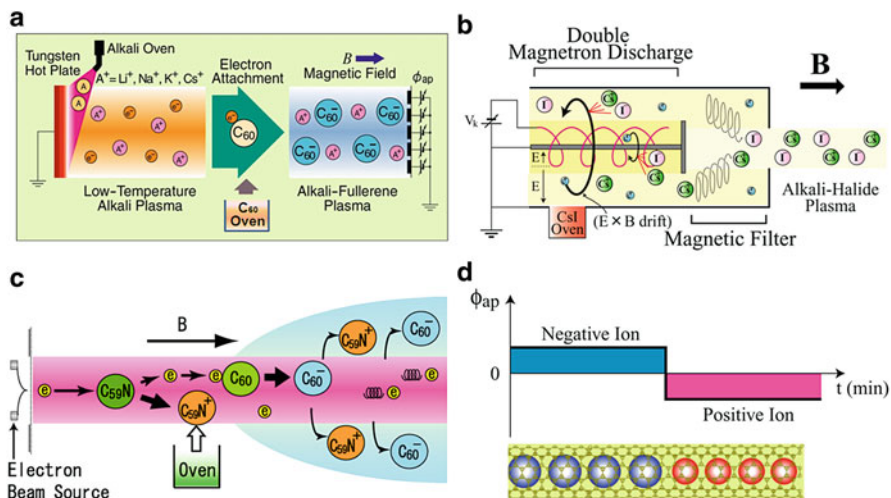


Fig. 11.1 Schematics of alkali–fullerene plasma (a), alkali–halogen plasma (b), quasipair fullerene-ion plasma (c) sources. Time sequence of bias-voltage application with instantaneous polarity change (d)

Figure 11.2a, d is typical transmission electron microscope (TEM) images of SWNTs which are processed by C_{60}^- and Cs^+ irradiation for 1 h in the $Cs^+ - C_{60}^-$ plasma, respectively. C_{60} molecules and Cs atoms are linearly and spirally encapsulated in SWNTs, respectively ($C_{60}@SWNTs$, $Cs@SWNTs$). Similarly, the azafullerene $C_{59}N$ molecules are confirmed to be encapsulated in SWNTs ($C_{59}N@SWNTs$) using the quasipair fullerene-ion plasma (Fig. 11.2b). I atoms are observed to be encapsulated (I@SWNTs) by the I^- irradiation experiment with the $Cs^+ - I^-$ plasma, as shown in Fig. 11.2c, and Fe atoms are encapsulated in a dotted fashion with a diameter less than 1 nm as seen in Fig. 11.2e (Fe@SWNTs). On the basis of these results, we have performed an experiment on the bias application with instantaneous polarity change between positive and negative values (see Fig. 11.1d) in the $Cs^+ - C_{60}^-$ plasma, namely, C_{60}^- are irradiated onto SWNTs for 30 min with substrate bias ϕ_{ap} of 20 V and Cs^+ are consecutively irradiated onto the same SWNTs for 30 min with ϕ_{ap} of -100 V. As a result, a junction structure in nanotubes, where Cs atoms are encapsulated on the left-hand side and C_{60} molecules are encapsulated on the right-hand side ($Cs/C_{60}@SWNT$), is found to be formed as given in Fig. 11.2f. Because Cs atoms and C_{60} molecules are an electron donor and an electron acceptor, respectively, it is conjectured that the junction structure displays the rectifying behavior, similar to a $p-n$ diode made of Si. The same result is also obtained in the case of using the $Cs^+ - I^-$ plasma, where the junction structure consisting of electron donor Cs atoms on one side and acceptor I atoms on the other is formed inside SWNTs ($Cs/I@SWNT$).

From the viewpoint of nano-bio fusion devices, DNA is also one of the candidates for materials to be encapsulated into SWNTs to modify the electronic properties

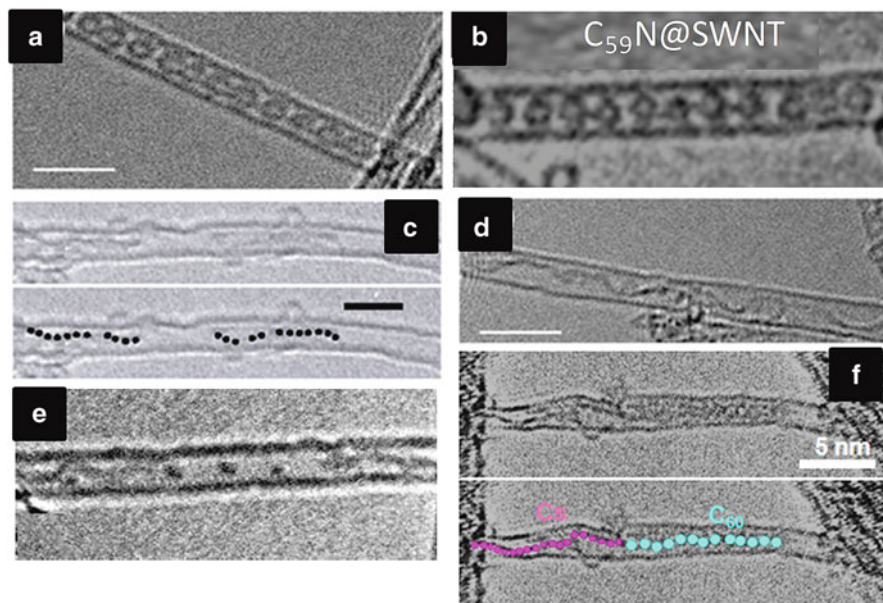


Fig. 11.2 Typical TEM images of SWNTs encapsulating C₆₀ (a), C₅₉N (b), I (c), Cs (d), Fe (e), and Cs/C₆₀ junction structure (f) inside. The *bottom* images in (c) and (f) show the related schematic illustration. Scale bars without notation indicate 2 nm

of them. Because DNA easily forms negative ions in a solution, we apply the ion irradiation method to electrolyte solutions with DNA, which mainly consist of negative (DNA⁻) and positive (H⁺) ions and neutral particles (H₂O) and consequently can be regarded as “electrolyte plasmas.” Figure 11.3a presents a schematic of an experimental apparatus for the DNA negative ion irradiation in the DNA electrolyte plasma [4], where the single-stranded DNA molecule is dissolved into pure water. Direct current voltage (V_{DC}) and/or radio frequency voltage (V_{RF}) can independently be supplied to aluminum (Al) electrodes (anode and cathode) immersed in the electrolyte plasma. The conformation of the DNA molecule takes on a random-coiled shape by the Brownian motion in the solution as shown in Fig. 11.3b, where its apparent size (diameter of gyrations) becomes larger than that of SWNT as the number of the DNA bases (n of A_n) increases. Here, the bases of adenine, thymine, guanine, and cytosine are represented by A, T, G, and C, respectively. In the case that both V_{DC} and V_{RF} are applied simultaneously, in other words, stretched DNA is irradiated to CNTs, TEM observation of encapsulated DNA (A₁₅) inside SWNT and double-walled carbon nanotube (DWNT) is presented in Fig. 11.4. These results reveal that the encapsulation yield of DNA into CNTs is considerably enhanced when both the DC and RF electric fields are superimposed.

On the other hand, CNTs functionalized by metal nanoparticles (MNPs) have recently attracted much attention due to their versatile applications. Since the MNPs attached on the outside of SWNTs are unstable in the conformation and quality,

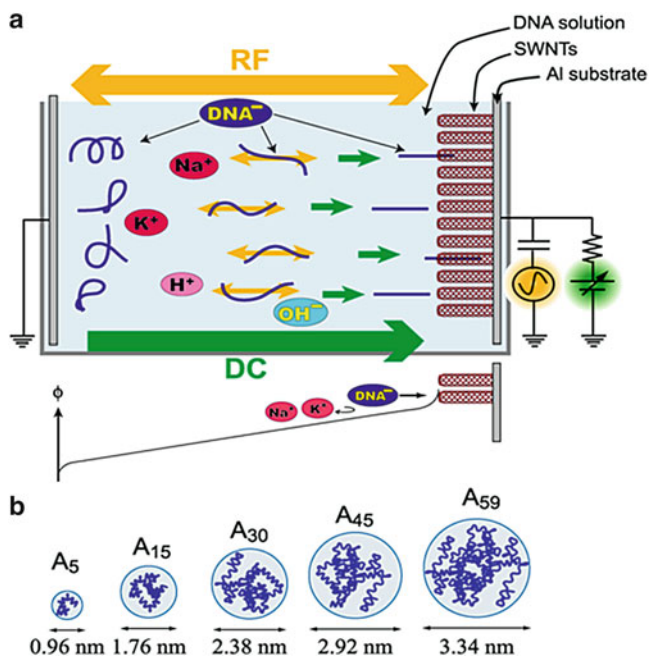
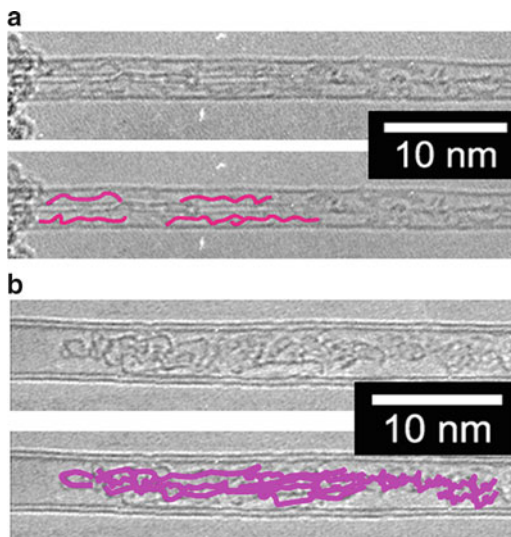


Fig. 11.3 (a) Process schematic of substrate bias method with electrolyte plasma in DNA solution, and (b) random-coiled single-stranded DNA (adenine: A) showing relation between number of bases (e.g., A₃₀) and effective diameter

Fig. 11.4 TEM images demonstrating: (a) adenine DNA (A₁₅) encapsulated SWNT and (b) cytosine DNA (C₃₀) encapsulated DWNT. The encapsulation is outlined schematically by red lines. $V_{DC} = 10$ V and $V_{RF} = 20$ V



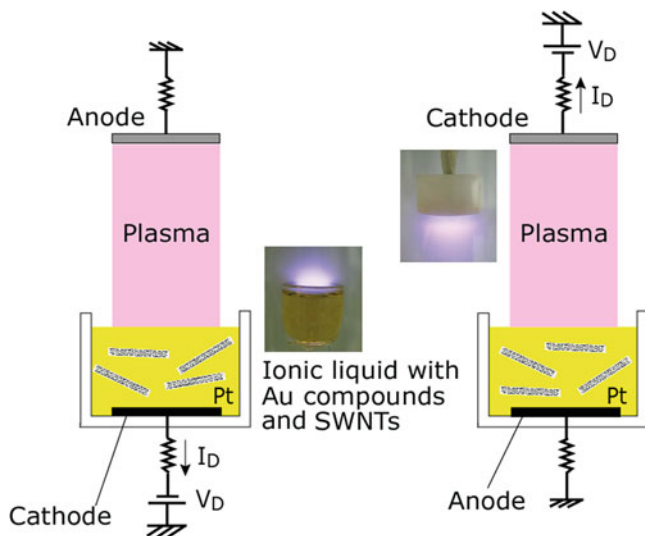


Fig. 11.5 Schematic diagrams of the DC discharge experimental setup for synthesizing SWNTs functionalized by Au nanoparticles, where the cathode is an IL (*left hand*) and a gas plasma region (*right hand*). Photos show discharges ($V_D = -400 \sim -500$ V, $I_D \approx 1$ mA) near the cathode areas at a pressure of 60 Pa

the synthesis approach which can keep SWNTs stably functionalized by MNPs is required. A novel method using gas–liquid interfacial plasmas (GLIPs) is developed to synthesize SWNTs functionalized by MNPs as shown in Fig. 11.5, in which the particle size and interparticle distance can also be controlled. In this process, an ionic liquid (IL) is introduced for the formation of a stable gas–liquid interface. The DC voltage V_{DC} (current: I_D) is applied to a “cathode electrode” located in the IL (or gas phase), causing a DC discharge between the cathode electrode and an “anode electrode” located in the Ar gas phase at low pressures (or IL) and being accompanied by high-energy ion irradiation (low-energy electron injection) toward the IL [5]. The SWNTs are dispersed in the IL of 2-hydroxyethylammonium formate which consists of carboxyl groups, and the IL is irradiated by the plasma. High-energy ions dissociate the IL, and the dissociated carboxyl groups bond to the surface of the SWNTs. When the Au chloride (HAuCl_4) is dissolved in the IL with the bonded SWNTs, the Au chloride is reduced by the IL, and the Au nanoparticles (AuNPs) are selectively synthesized on the carboxyl groups at the surface of the SWNTs. Figure 11.6a–c presents TEM images of the AuNPs synthesized on the bonded SWNTs without plasma irradiation (a) and by plasma irradiation for $t = 1$ min (b) and $t = 10$ min (c). Monodispersed AuNPs are found to be synthesized on the bonded SWNTs by plasma irradiation, and the distance between the AuNPs decreases with increasing irradiation time. In the light of size-controlled MNP synthesis, meanwhile, the interstitial nanospaces between bundled SWNT layers (Fig. 11.6d) are expected to form the synthesis field with a uniform size. Then, the

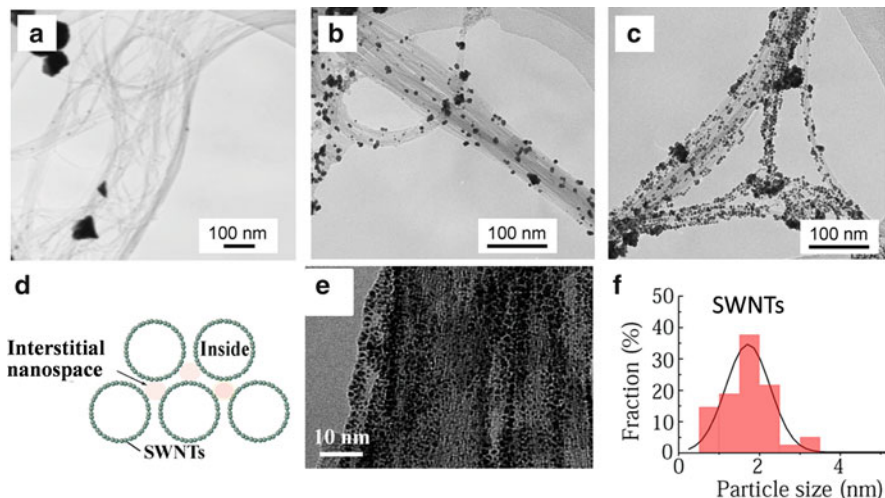


Fig. 11.6 TEM images of AuNPs synthesized on bonded SWNTs: (a) no plasma treatment, (b) plasma treatment for 1 min, (c) plasma treatment for 10 min. (d) Cross-sectional diagram of AuNP synthesis sites in bundled SWNTs. (e) TEM image showing SWNTs intercalating dense AuNPs. (f) Particle size distribution of AuNPs estimated by TEM image in (e)

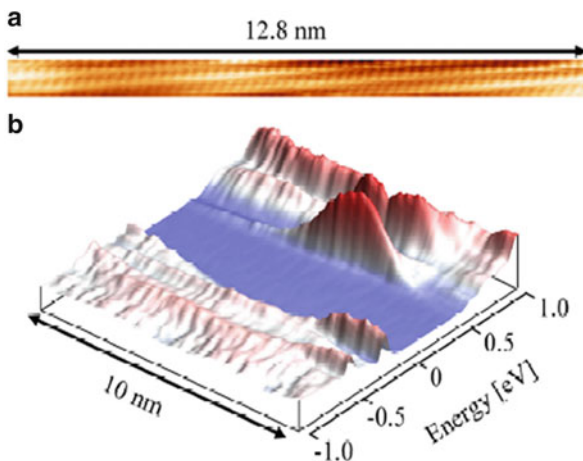
bundled SWNTs are impregnated with HAuCl_4 dissolved in the IL ($[\text{C}_8\text{H}_{15}\text{N}_2]^+$ $[\text{BF}_4]^-$) and exposed to the plasma. The AuNPs in the neighborhood of 2 nm diameter are observed at high density between the SWNT layers (Fig. 11.6e, f).

11.2 Device-Applicable Properties of Doped CNTs

For semiconducting device applications of atoms or molecules encapsulated SWNTs, it is necessary to beforehand confirm the existence of electronic interaction between the encapsulated one and SWNT wall. Then, details of the local electronic structure of the Cs partially encapsulated SWNT are measured using scanning tunneling microscopy (STM) and scanning tunneling spectroscopy (STS) in low-temperature ultrahigh vacuum [6]. Figure 11.7a is an STM topographic image, where a bright area shows a Cs-filled state in a gray scale image. Local variations in the electron density can be observed in Fig. 11.7b, where the conduction and valence are shifted downward and new localized gap states strikingly appear near the conduction band. Thus, electrons are verified to be transferred from Cs to SWNT.

The electronic transport properties of various nanotube samples are investigated by fabricating them as channels of field-effect transistor (FET) devices with transport parameters of V_G (back-gate bias), V_{DS} (source–drain voltage), and I_{DS} (source–drain current). Our results reveal that the electronic transport properties of

Fig. 11.7 (a) A typical STM topographic image, (b) 3D plot of SR-STs maps measured along the tube axis of a Cs partially encapsulated SWNT



SWNTs are significantly changed after encapsulating different atoms or molecules. In the case of pristine SWNTs, I_{DS} starts to increase for negative V_G , indicating the well-known p -type transport characteristic (see Fig. 11.8a). When the C_{60}^- irradiation time is increased enough, $C_{60}@SWNTs$ enhance this p -type characteristic of pristine SWNTs [7], i.e., the threshold gate-voltage shift takes place to some extent (Fig. 11.8a). Similarly, this threshold voltage tends to shift from -20 V to about 60 V in the case of $I@SWNTs$, i.e., the p -type characteristic is more strongly enhanced, as shown in Fig. 11.8b [8]. In contrast to $C_{60}@SWNTs$, on the other hand, $C_{59}N@SWNTs$ are found to display a complete n -type behavior (Fig. 11.8a) [9]. $Cs@SWNTs$ [10] and $Ca@SWNTs$ [11] also behave as n -type semiconductors, which is attributed to the occurrence of electron transfer from Cs and Ca atoms to SWNTs, as given in Fig. 11.8c, d. These results indicate that the alkali and alkaline-earth metal atoms, some kinds of fullerenes, and halogen atoms display the roles of strong electron donor, electron acceptor, and strong acceptor, respectively. Since the shell of nanotubes can protect well the encapsulated atoms and molecules against oxidation in air, air-stable p - and n -type characteristics are confirmed to be obtained, as verified in the case of $Ca@SWNTs$ (Fig. 11.8d). In addition, various base sequences of encapsulated DNA are demonstrated to have different effects on the transport properties of DNA@CNTs [12, 13] as shown in Fig. 11.9, where pristine DWNTs with ambipolar characteristics are exemplified. DWNTs encapsulating $C_{30}DNA$, $T_{30}DNA$, $A_{30}DNA$, and $G_{30}DNA$ change to the pure p -type, p -dominant ambipolar, n -dominant ambipolar, and pure n -type semiconductors, respectively. According to work function measurements by ultraviolet photoelectron spectroscopy (UPS), the work function of pristine DWNTs is 0.16 eV larger than that of $G_{30}DNA$ but 0.05 eV smaller than that of $C_{30}DNA$, clearly identifying the direction of charge transfer between the DWNTs and base sequences of encapsulated DNA and giving direct evidence for the observed conductance types.

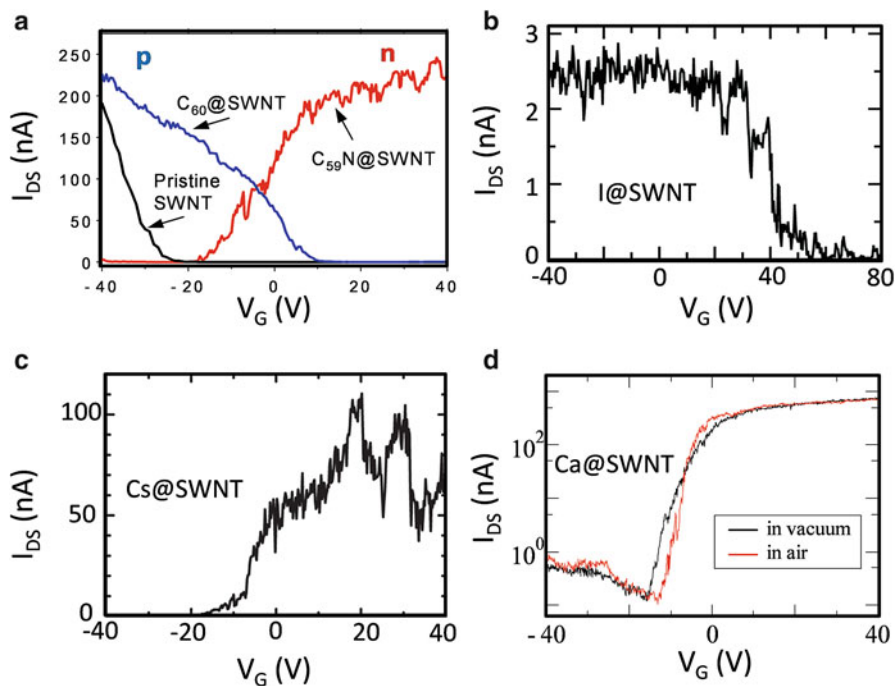


Fig. 11.8 A series of I_{DS} - V_G characteristics measured at room temperature in vacuum for (a) pristine SWNTs at $V_{DS} = 0.5$ V, C_{60} @SWNTs at $V_{DS} = 1$ V, C_{59} @SWNTs at $V_{DS} = 1$ V, (b) I@SWNTs at $V_{DS} = 0.1$ V, (c) Cs@SWNTs at $V_{DS} = 1$ V, (d) Ca@SWNTs at $V_{DS} = 1$ V (I_{DS} - V_G in air is also shown)

To get further insight into the transport properties of encapsulated nanotubes, low-temperature measurements are performed by lowering from 300 K to 10 K [7]. In comparison with the transport properties of pristine SWNTs, Coulomb oscillation peaks with fairly regular intervals are strikingly found on C_{60} @SWNT and $C_{59}N$ @SWNT devices at 10 K, as described in Fig. 11.10a, b, and such a phenomenon has never been found in the pristine SWNT-FET device. This result suggests that tunneling barriers are possibly formed due to the fullerene- or azafullerene-induced modulation of the electronic band of the nanotube, and a single-electron transistor could be realized by foreign molecule encapsulation of individual SWNT. More controlled encapsulation processes by the plasma method, for example, via precisely controlled amount of dopants, should open the possibility to tune the electronic properties of the quantum dot.

In order to reveal the effects of heterodoping inside SWNTs on the electronic states of nanotubes, the electrical features are investigated for Cs/I@SWNTs and Cs/ C_{60} @SWNTs based on an FET configuration [14]. Figure 11.11a gives a typical I_{DS} - V_G characteristic of Cs/I@SWNTs measured at room temperature in the case where Cs and I ion dosages are almost the same. The fairly unique hump current

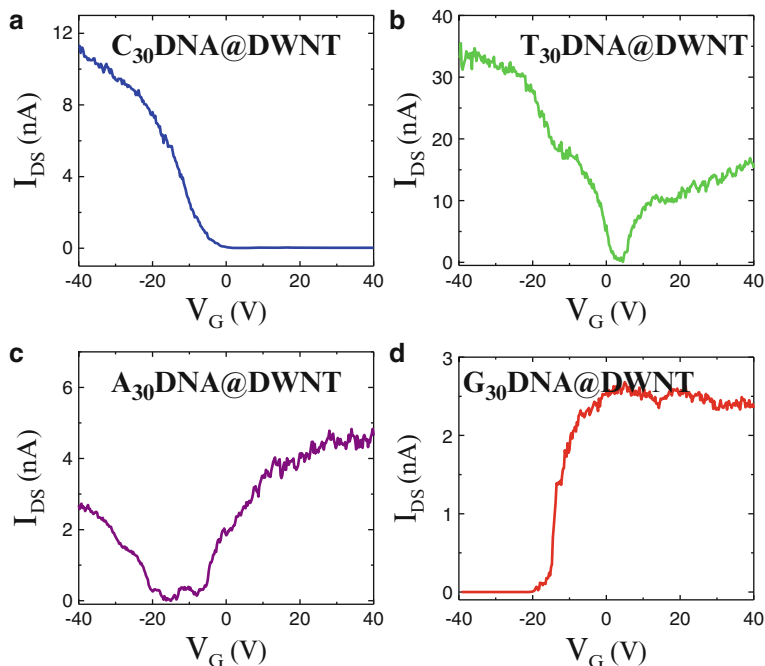


Fig. 11.9 I_{DS} - V_G characteristics measured at room temperature in vacuum for DWNTs encapsulating (a) $C_{30}DNA$, (b) $T_{30}DNA$, (c) $A_{30}DNA$, and (d) $G_{30}DNA$ ($V_{DS} = 0.1$ V)

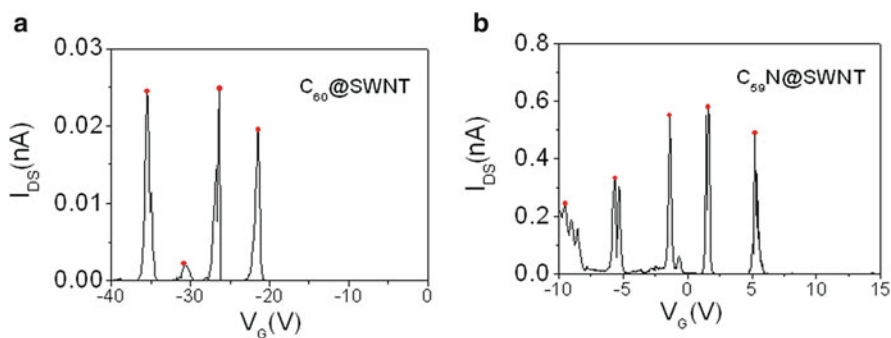


Fig. 11.10 Coulomb oscillation peaks measured at $V_{DS} = 10$ mV and 10 K for (a) $C_{60}@SWNT$ s and (b) $C_{59}N@SWNT$ s

feature is found, which is known as a unique characteristic for a p - n junction. Figure 11.11b shows the current rectification ratio as a function of Cs^+ irradiation time (prior to this, the I^- irradiation was performed for 2 h), which is defined as the absolute value of maximum to minimum current ratio ($|I_{DSmax}/I_{DSmin}|$) in an I_{DS} - V_{DS} characteristic for a fixed V_G . It is found that clear current-rectifying features with

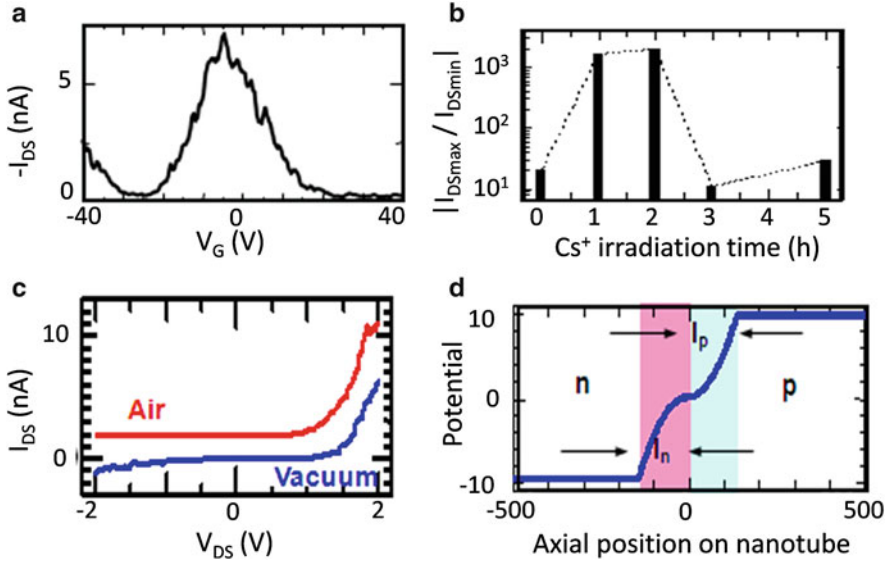


Fig. 11.11 (a) I_{DS} - V_G characteristic of Cs/I@SWNTs ($V_{DS} = 2$ V) at 2 h of Cs^+ irradiation (I^+ irradiation at 2 h). (b) Variation of the absolute value of I_{DSmax}/I_{DSmin} with Cs^+ irradiation time. (c) I_{DS} - V_{DS} characteristics of Cs/I@SWNTs measured under the vacuum (blue) and air (red) conditions ($V_G = 40$ V), where the datum in air is offset for the visual help. (d) Calculated potential profile around the p - n junction area ($N_D = N_A$)

a maximum ratio between 10^3 and 10^4 are realized only when almost the same amount of Cs and I is irradiated, which is consistent with the I_{DS} - V_G characteristic in Fig. 11.11a. It is worthwhile to emphasize that this rectifying structure is stable even under air condition (Fig. 11.11c). These indicate that the p - n junction is formed inside the nanotubes. To achieve more detailed understanding of heterojunction inside SWNTs, potential structure calculations are carried out along the tube axes (diameter = 1.4 nm and length = 1 μ m), where the doping carrier densities of Cs, I, and C_{60} can be estimated to be -1.5 , 1.1 , and 0.14 e/nm, respectively. As a result, the potential at the depletion layer is found to be symmetric in the case of Cs/I@SWNT as seen in Fig. 11.11d because the doping densities are equal (electron donor density: N_D = electron acceptor density: N_A) in the n and p regions. On the other hand, the depletion layer in the p region (I_p) becomes much wider than in the n region (I_n) in the case of Cs/ C_{60} @SWNT because of $N_D = 10N_A$, i.e., the carrier density difference causes the significant effect on depletion layer structures.

When ferromagnetic elements such as Fe, Co, or Ni are encapsulated into semiconducting SWNTs, both charge and spin of electrons in SWNTs are thought to be exploited like magnetic semiconductors. Our measurements demonstrate that high-performance unipolar n -type characteristics with a very high on-off ratio around 10^6 are observed for Fe@SWNTs [15]. Figure 11.12 presents magnetization vs. applied magnetic field for pristine SWNTs and Fe@SWNTs measured at 5 K,

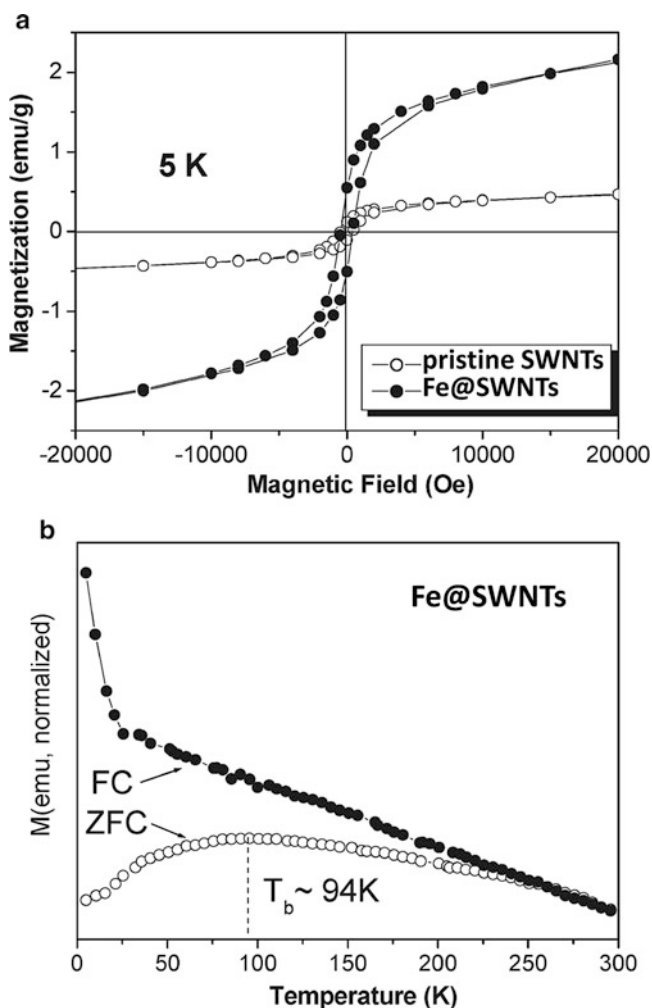
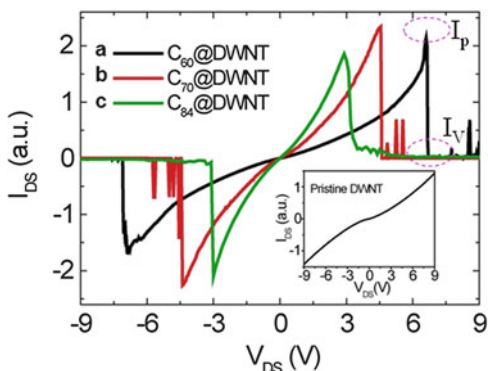


Fig. 11.12 (a) Magnetization curves of pristine SWNTs and Fe@SWNTs at 5 K. (b) Temperature dependence of ZFC and FC measurements recorded at a magnetic field of 100 Oe for Fe@SWNTs

respectively [16]. Fe@SWNTs with magnetization much larger than that of pristine SWNTs exhibit a ferromagnetic characteristic with a hysteresis loop, while the magnetization of pristine SWNTs results from residual catalysts. Zero-field-cooled (ZFC) and field-cooled (FC) magnetization measurements are performed from 5 to 300 K, as shown in Fig. 11.12b for the case of Fe@SWNTs [16]. A strikingly sharp decrease can clearly be observed in the FC curve at about 25 K, corresponding to the existence of small magnetic particles inside SWNTs in the superparamagnetic state. Besides a blocking temperature (T_b : transition temperature from ferromagnetic to superparamagnetic property), peak for the Fe@SWNTs can be observed in the ZFC curve at about 94 K much lower than room temperature of pristine SWNTs. These

Fig. 11.13 $I_{DS}-V_{DS}$ curves ($V_G = 0$) for (a) $C_{60}@DWNT$, (b) $C_{70}@DWNT$, and (c) $C_{84}@DWNT$ devices measured at room temperature. The characteristic for an empty metallic DWNT is shown in the inset



features of Fe@SWNTs are greatly different from the behavior of pristine SWNTs, which are expected to give rise to many interesting and new physical phenomena applicable to spintronic devices.

Concerning metallic CNTs instead of semiconducting ones treated so far, a high-performance negative differential resistance (NDR) characteristic is found at room temperature in fullerene encapsulated DWNTs with large diameter [17]. In the case of $I_{DS}-V_{DS}$ characteristic for a pristine metallic DWNT, the measured current gives rise to a linear increase under different gate voltages ($V_G = -20, 0,$ and 20 V), which displays a typical metallic behavior (see the inset in Fig. 11.13). By comparison, for a $C_{60}@DWNT$ device, the measured curves exhibit unique NDR characteristics at high bias values of both ~ 6 V and -6 V, namely, an initial rise of the current is followed by a sharp decrease instead of the linear increase expected from Ohm's law when the voltage is progressively increased. A high peak-to-valley current ratio ($PVCR = I_p/I_v$) about 1,300 is surprisingly observed, which is much higher than that reported previously for NDR devices fabricated using other nanomaterials. It is also interesting to mention that the peak positions of NDR move toward lower voltages with increasing diameter of the encapsulated fullerenes ($C_{60}@DWNT$, $C_{70}@DWNT$, and $C_{84}@DWNT$), as indicated in Fig. 11.13. Since numerous fullerene molecules with diameters of 0.7–0.9 nm are encapsulated in one-dimensional space of DWNTs, one can easily conceive the construction of ideal superlattice structure inside DWNTs. When electrons tunnel through the potential barriers in series separated by fullerene molecules, the coherent nature of ballistic electron propagation can generate constructive interference, resulting in the occurrence of unusual physical phenomena.

11.3 Electro-optic Fusion Devices Using Doped CNTs

Many works have recently been devoted to constructing optoelectronic devices such as photoabsorber, emitter, and sensors using modified SWNTs because light may provide a convenient way to control the conductivity of SWNTs. It is found that photoinduced electrical transport properties of SWNTs are very sensitive

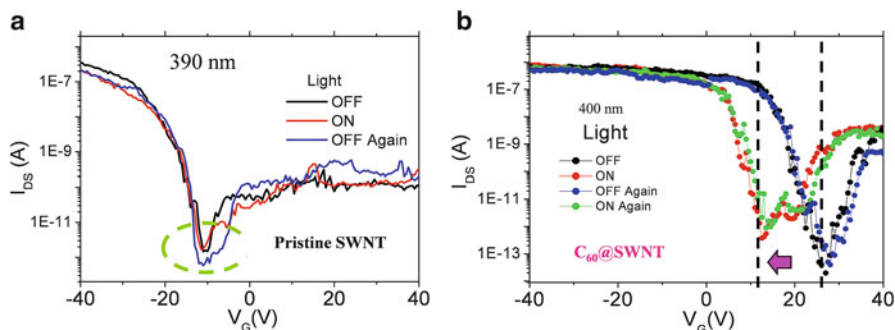


Fig. 11.14 (a) I_{DS} - V_G characteristics of a pristine SWNT-FET device without and with light illumination for 5 s. (b) I_{DS} - V_G curves of a C_{60} @SWNT-FET device before and after 390 nm light illumination, showing a good recovery. As indicated by an arrow, about 14 V shift of threshold voltage is observed

to the encapsulated molecules such as fullerenes and azafullerenes. Under light illumination, both C_{60} @SWNTs with the p -type property and $C_{59}N$ @SWNTs with the n -type property show interesting photoinduced transport behaviors, which is different from the case of pristine SWNTs. The response of the transport properties of pristine SWNTs to light is first shown in Fig. 11.14a, where an FET device of their channel is measured before and after exposure to the 390 nm UV light. There is no apparent shift in the threshold voltage under light illumination. By comparison, a clear photoswitching effect is observed in the transport characteristics of C_{60} @SWNT [7]. Figure 11.14b depicts transfer curves of an FET device of C_{60} @SWNTs, which are recorded without light and upon light illumination and again measured without light and under light illumination. Obviously, the response of the device to light is the shift of threshold voltage toward negative voltages, with a recoverable photoresponse. The explanation for this phenomenon is the occurrence of photoinduced electron transfer (PET) process in the nanosystem of C_{60} @SWNT. Electrons are transferred from SWNTs to the ground state of C_{60} in the absence of light, during which C_{60} behaves as a good electron acceptor. On the other hand, under light illumination, C_{60} in the excited state displays the electron donor behavior, giving back electrons to SWNTs. In other words, the electron-withdrawing ability of C_{60} in the excited state becomes weaker as compared with that of C_{60} in the ground state. As a result, the PET process may at least cause a partial recovery of these transferred electrons, that is, upon excitation of the C_{60} molecules, some of the electrons that have been transferred to C_{60} in the ground state from the SWNT are now transferred back to the SWNT when C_{60} is in the excited state.

Compared with the case of C_{60} peapod, the photoresponse of $C_{59}N$ @SWNTs exhibits a different photosensitive behavior [18]. When an I_{DS} - V_G curve of $C_{59}N$ @SWNT-FET device is measured at room temperature by sweeping the gate voltage from the negative to positive voltage direction, a drastic decrease of current by over 95 % is observed under instantaneous (1 s) UV light exposure. As the gate

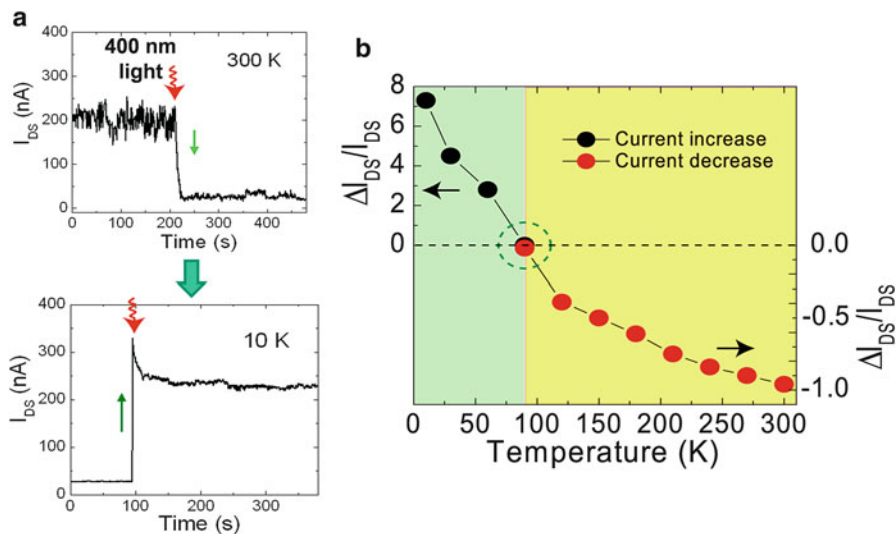


Fig. 11.15 (a) I_{DS} characteristics measured as a function of time at 300 K and 10 K under exposure of a light pulse (400 nm) for $C_{59}N@SWNT$ -FET devices with $V_G = 20$ V and $V_{DS} = 0.5$ V. (b) Variation of photoinduced current ($\Delta I_{DS}/I_{DS}$) measured with temperature under exposure of the light pulse

voltage is continually swept, the current is restored gradually to its initial current during scanning to high positive gate voltages, indicating the recovery can be made by sweeping the gate voltage. Moreover, when the devices are exposed to stationary light illumination, the n -type conductance is greatly reduced. These phenomena are recognized at a glance in the upper part of Fig. 11.15a, where I_{DS} is measured as a function of time at room temperature. A sharp decrease in current is immediately observed at 200 s upon the UV (400 nm) light pulse. The photoresponse is also found to gradually become less pronounced with increasing the wavelength of light. This finding demonstrates evidently that the light energy exerts an important effect on the conductance of $C_{59}N@SWNT$ s. Since the photoresponse of $C_{59}N@SWNT$ s is obviously different from that observed for $C_{60}@SWNT$ s, a different photoinduced charge transfer mechanism is considered to exist between them. The specific electronic structure of $C_{59}N$ seems to be responsible for its difference. It is well known that the $C_{59}N$ radical is very active and can easily lose or gain electrons by binding other atoms or molecules. Under light illumination, such a bond will break by a high photoenergy.

At low temperatures such as 10 K, on the other hand, a different photoresponse phenomenon is observed in the transport property of $C_{59}N@SWNT$ -FET device under light illumination, and the source-drain current displays a several times increase under stationary light illumination, which is exactly the opposite phenomenon to that observed at 300 K [19]. The I_{DS} measured as a function of time at 10 K under exposure of a light pulse for the $C_{59}N@SWNT$ -FET device

is shown at the bottom of Fig. 11.15a, indicating strong evidence for the great increase in current under the light pulse. Interestingly, this current increase is found to depend inversely on the temperature and becomes gradually negligible when the temperature is increased from 10 to 90 K. As the temperature is further increased, a negative photocurrent, i.e., a decrease in current starts to be observed, and the current significantly decreases up to 300 K upon pulsed light illumination, just in agreement with the result in the upper part of Fig. 11.15a. Figure 11.15b presents the ratio of the changed current (ΔI_{DS}) caused by instantaneous light illumination to the original current ($\Delta I_{DS}/I_{DS}$) as a function of temperature in the range of 10–300 K. A variation of photoinduced current vs. temperature indicates that when the temperature is decreased and increased from 90 K in the range of 10–300 K, the positive and negative photocurrents rise, respectively. Concerning the mechanism of current increase at low temperatures, it is mentioned that the thermal effect is reduced in the low-temperature environment; as a result, the weak bonding between $C_{59}N$ and SWNT may remain linked under light illumination. This experimental finding reveals that it is possible to read the temperature by monitoring the optoelectronic signal of $C_{59}N@SWNTs$, making them an attractive candidate as a component of nanothermometers covering a wide temperature range. In particular, sensing low temperature would become more convenient and easy by giving a simple signal.

On the other hand, SWNTs have narrow absorption bandgaps which make them promising in constructing infrared solar cells, namely, it is of crucial importance to harvest the infrared solar spectrum by using SWNTs, due to their outstanding infrared properties. The present study indicates that it is possible to make infrared solar cells based on heterojunctions fabricated using an *n*-type silicon and *p*-type pristine SWNTs or enhanced *p*-type SWNTs, i.e., $C_{60}@SWNTs$ that can serve as an energy conversion material [20]. Here, the solar cells are fabricated by spin coating a nanotube film onto the *n*-type silicon, as schematically shown in Fig. 11.16a. Figure 11.16b describes the characterization of the $C_{60}@SWNT$ film by atomic force microscopy. UV–Vis–NIR absorption spectra confirm that SWNTs have the narrow bandgap energy of 0.66 eV. Peaks in the ranges $\sim 1,500$ – $2,100$ nm and ~ 900 – $1,100$ nm are assigned as the first (E_{11}) and second (E_{22}) van Hove transitions in the semiconducting nanotubes, respectively. In the solar cells constructed with Si, the main contribution of power conversion is strictly dependent on the wavelengths of light, that is, Si mainly contributes to the conversion efficiency in the wavelength range less than 1,100 nm. A comparative experiment is performed between the solar cells based on pristine SWNTs/Si and $C_{60}@SWNTs/Si$ under 1,550 nm light emission diode (LED) illumination. Solar cell characteristics are definitely observed in both devices, i.e., a clear open-circuit voltage (V_{oc}) and a short-circuit current (I_{sc}) are observed. Moreover, the solar cell device based on the $C_{60}@SWNT$ film shows much better performance in the open-circuit voltage, where the V_{oc} substantially rises up to 100 mV, as disclosed in Fig. 11.16c, much higher than 57 mV of pristine SWNTs/Si, as a result of C_{60} encapsulation. The increase of the V_{oc} in the case of $C_{60}@SWNT/Si$ solar cell might be explained by the charge transfer effect between C_{60} and SWNT, which enhances the *p*-type transport characteristic [7].

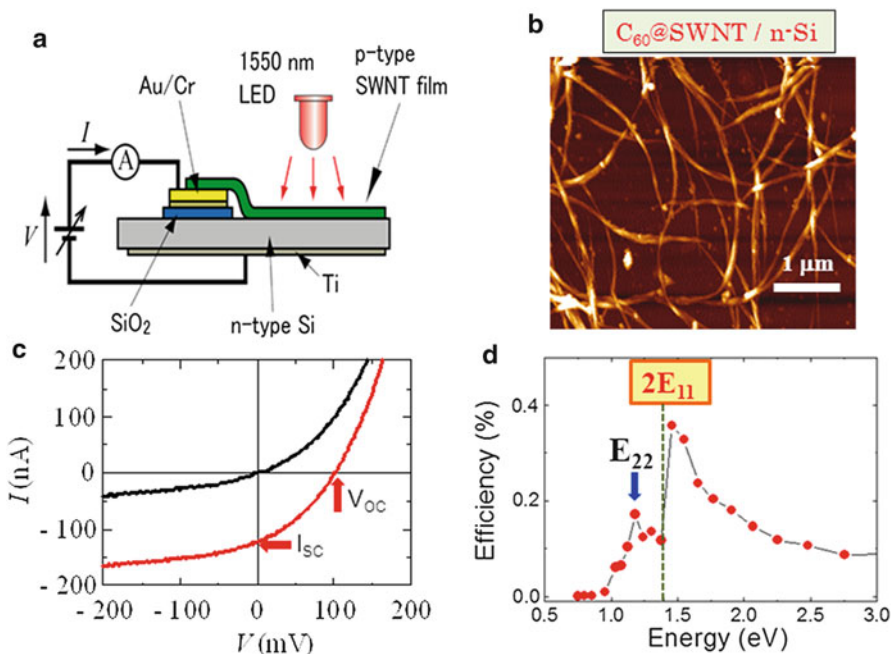


Fig. 11.16 (a) Schematic illustration of infrared solar cell incorporating *n*-Si and *p*-type pristine SWNTs or C_{60} @SWNTs, (b) an AFM image of C_{60} @SWNT network on the Si substrate. (c) Current–voltage (I – V) characteristics of solar cell based on C_{60} @SWNT/Si measured in the dark (black) and under 1,550 nm LED illumination (red). (d) Power conversion efficiency measured as a function of light (photon) energy for the C_{60} @SWNT solar cell

In conventional solar cells, one charge carrier is typically created upon absorption of a single photon. Although a multiple exciton generation (MEG) mechanism has recently been discussed [21], the MEG effect is not well understood in the SWNT solar cell. In order to detect MEG, the energy conversion efficiency is measured under illumination of different wavelength light, where the MEG threshold energy in SWNTs can be close to the limit of 2 times the absorption energy gap ($2E_{11}$). Figure 11.16d presents the power conversion efficiency for the C_{60} @SWNT/Si solar cell with varying the light in the range 400–1,650 nm corresponding to the illumination energy from 0.75 to 3.0 eV. The efficiency suddenly increases when the light energy is higher than two times the bandgap of nanotubes (just above $2E_{11}$), suggesting the possibility for the occurrence of MEG in the C_{60} @SWNT-based solar cell [22]. Because the C_{60} @SWNTs used in the present experiments contain mainly semiconducting and partially metallic SWNTs, it is expected that the performance of SWNT/Si-based solar cells will be further improved by constructing solar cells with purely semiconducting SWNTs. Furthermore, surface doping of AuNPs on SWNTs by using GLIPs could be available for the solar cell efficiency enhancement [23].

11.4 Toward Emerging CNT Nano-biomedical Electronic System

MNP–DNA conjugate encapsulated SWNTs [(MNP–DNA)@SWNTs] have the potential for emerging nano-biomedical applications such as high-sensitivity biosensing using surface plasmon resonance and optically manipulatable drug delivery system (DDS) with intracellular nanoelectronic engineering. For that purpose, the three stages have to be overcome. The first stage on DNA@SWNTs was already demonstrated in 11.1 As a basis of DDS using DNA@CNTs, however, the encapsulated DNA molecules have to be verified to be efficiently released from CNTs first by any kind of methods. One method is to utilize DC electric fields with the polarity opposite to those for inserting DNA into CNTs in the electrolyte plasma as already explained in Fig. 11.3. Figure 11.17 gives the UV–Vis absorption spectra of pristine DWNTs, C_{30} DNA@DWNTs, and three kinds of C_{30} DNA@DWNTs from which DNA is tried to be released by applying an opposite-polarity voltage of -10 V to the Al electrodes in Fig. 11.3a for 10, 30, and 60 min, respectively [24]. In contrast to the case of pristine DWNTs, the absorption spectrum peak at about 275 nm for DNA@DWNTs is attributed to the encapsulation of C_{30} DNA molecules and shows a relative decrease after 10 min

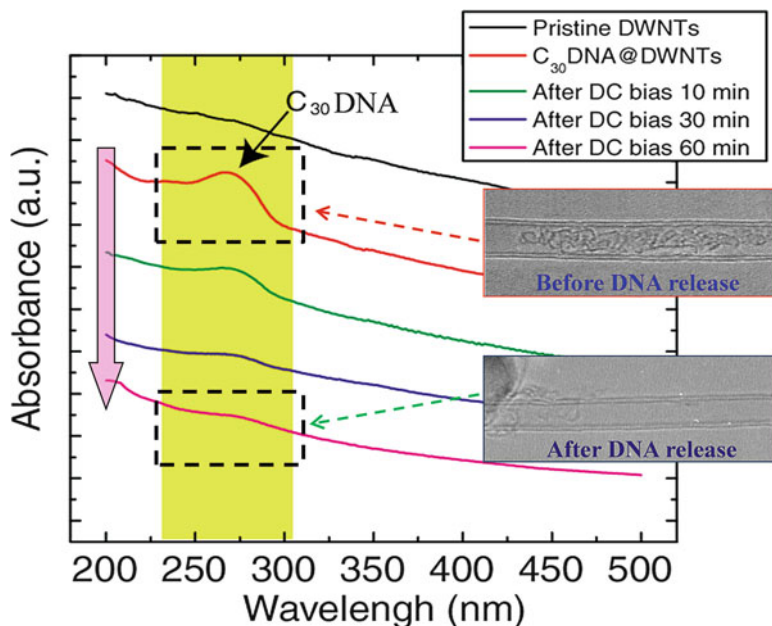


Fig. 11.17 Absorbance spectra of pristine DWNTs, C_{30} @DWNTs before application of negative DC bias, after its application for 10, 30, and 60 min. TEM images before and after DAN release are also shown

extraction by the electric field. With increasing time up to 60 min, the absorption spectrum of $C_{30}DNA@DWNTs$ is similar to that of pristine DWNTs, implying that DNA molecules are indeed removed from the inside of DWNTs as confirmed by the TEM images. In order to understand how electrical properties of DWNTs are affected by the release of DNA molecules, a series of experiments are performed to measure the transport properties of DWNTs after releasing $C_{30}DNA$ under the FET configuration. The average threshold voltage (V_{th}) for p -type $C_{30}@DWNT$ is found to shift to more negative voltages with increasing the applied DC bias time, which is the opposite direction compared with the encapsulation case. Since the carrier (hole) concentration on DWNT-FET is proportional to the value of V_{th} , this phenomenon signifies that the amount of the released DNA molecules has an effect on the transport properties of DWNTs. Therefore, taking into account the changes of the electrical transport properties and UV absorption spectra, it is evident that the release of DNA molecules from the inner space of DWNTs is successfully controlled by utilizing DC electric fields with the different polarity.

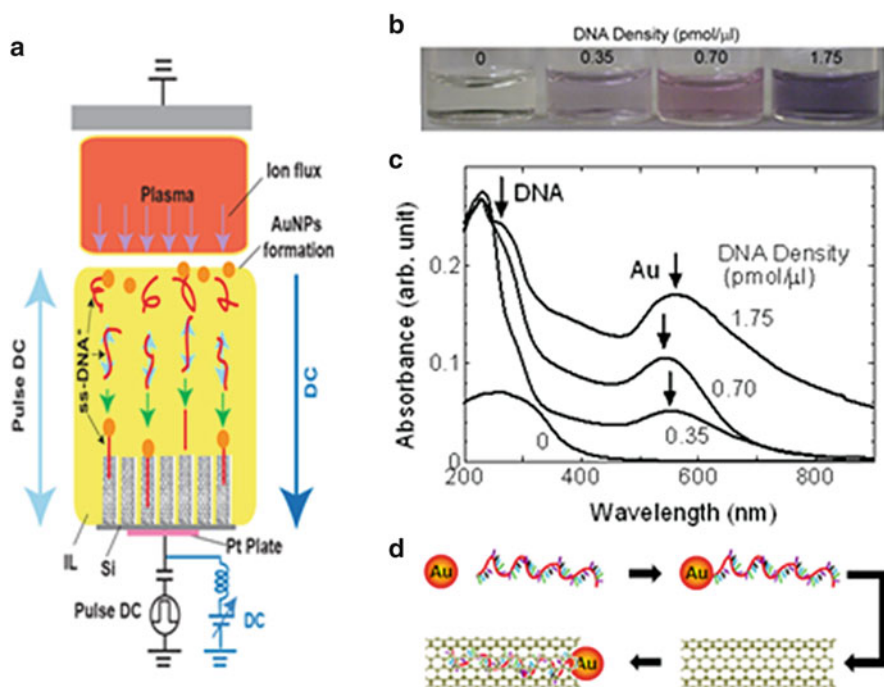


Fig. 11.18 (a) Schematic of gas-liquid interfacial plasma experiment for AuNP-DNA-SWNT conjugate creation. (b) Photograph of the aqueous solution of AuNPs synthesized with plasma irradiation at a pressure of 40 kPa, (c) dependence of UV-Vis light absorbance characteristics on DNA concentration, and (d) procedure schematic of AuNP-DNA conjugate encapsulation inside DNA

Returning to the subject on the creation of (MNP–DNA)@SWNTs, the second stage is the synthesis of MNP–DNA conjugates. Then, a pulse DC discharge inducing the ion irradiation is driven at high pressures in the case of using a solution of aqueous single-stranded DNA and gold compound $\text{HAuCl}_4 \cdot 3\text{H}_2\text{O}$, a gas–liquid interfacial situation of which is partially shown in Fig. 11.18a. When the DNA concentration is increased, the aqueous solution turns into a deep purplish red (see Fig. 11.18b). Since both the peaks of AuNP and DNA are detected in UV–Vis absorbance spectra as shown in Fig. 11.18c, the soluble AuNP–DNA conjugate is confirmed to be successfully synthesized [25]. The final (third) stage on the creation of (AuNP–DNA)@SWNTs described schematically in Fig. 11.18d is performed under the discharge configuration with a cathode coated with open-ended SWNTs, to which positive DC biases V_{DC} are superimposed upon pulse DC voltages in order to transport the negatively charged AuNP–DNA conjugate toward SWNTs, as depicted in Fig. 11.18a. With the application of highly positive V_{DC} , large quantities of (AuNP–DNA)@SWNTs are observed for the first time [26]. Based on the successful achievement of the DNA release by the DC electric field, the further remaining step for its application in advanced DDS is the development and establishment of a method for sustained release by optical manipulation of the Au nanoparticles in (AuNP–DNA)@SWNTs such as using lasers to withdraw the encapsulated DNA from the SWNT interior.

11.5 Conclusions

The ion irradiation method as internal doping using novel plasmas including positive and negative ions in gaseous and liquid phases enables various kinds of atoms and molecules with electron acceptor, electron donor, and magnetic characteristics to be efficiently encapsulated inside SWNTs and DWNTs. The encapsulated CNTs display unique transport properties applicable to air-stable carrier-type controlled, built-in p – n junction, quantum dot origin, negative differential resistance, magnetic semiconducting, temperature-sensitive photoinduced switching, and infrared solar cell devices. The gas–liquid interfacial plasma makes the combination of internal and surface doping processes possible, creating SWNTs encapsulating the soluble AuNP–DNA conjugate, which is expected to contribute to the construction of emerging nano-biomedical electronic system.

Acknowledgments We are grateful to Prof. K. Tohji and Mr. K. Motomiya for their help with the TEM observations.

References

1. Hatakeyama R et al (2008) Novel-structured carbon nanotubes creation by nanoscopic plasma control. *Plasma Sources Sci Technol* 17:024009-1-11
2. Hatakeyama R et al (2011) Plasma-synthesized single-walled carbon nanotubes and their applications. *J Phys D Appl Phys* 44:174004-1-21

3. Hatakeyama R, Kaneko T (2011) Nano-bio fusion science opened and created with plasmas. *Plasma Fusion Res* 6:1106011-1-12
4. Kaneko T et al (2007) DNA encapsulation inside carbon nanotubes using micro electrolyte plasmas. *Contrib Plasma Phys* 47:57–63
5. Kaneko T et al (2009) Novel gas-liquid interfacial plasmas for synthesis of metal nanoparticles. *Plasma Process Polym* 6:713–718
6. Kim SH et al (2007) Cesium-filled single wall carbon nanotubes as conducting nanowire: scanning tunneling spectroscopy study. *Phys Rev Lett* 99:256407-1-4
7. Li YF et al (2008) Photoinduced electron transfer in C₆₀ encapsulated single-walled carbon nanotube. *Appl Phys Lett* 92:183115-1-3
8. Shishido J et al (2008) Modification of electrical transport properties of single-walled carbon nanotubes realized by negative-ion irradiation with electron-free pure alkali-halogen plasma. *Jpn J Appl Phys* 47:2044–2047
9. Kaneko T et al (2008) Azafullerene encapsulated single-walled carbon nanotubes with n-type electrical transport property. *J Am Chem Soc* 130:2714–2715
10. Izumida T et al (2006) Electronic transport properties of cs-encapsulated single-walled carbon nanotubes created by plasma ion irradiation. *Appl Phys Lett* 89:093121-1-3
11. Shimizu T et al (2010) Electrical transport properties of calcium encapsulated single-walled carbon nanotubes realized using calcium plasma. *Jpn J Appl Phys* 49:02BD05-13
12. Kaneko T, Hatakeyama R (2009) Versatile control of carbon nanotube semiconducting properties by DNA encapsulation using electrolyte plasmas. *Appl Phys Express* 2:127001-1-3
13. Li YF et al (2010) Tailoring electronic structure of double-walled carbon nanotubes by encapsulating single-stranded DNA. *Small* 6:729–732
14. Kato T et al (2009) P-N junction with donor and acceptor encapsulated single-walled carbon nanotubes. *Appl Phys Lett* 95:083109-1-3
15. Li YF et al (2006) Electrical properties of ferromagnetic semiconducting single-walled carbon nanotubes. *Appl Phys Lett* 89:083117-1-3
16. Li YF et al (2007) Magnetic characterization of fe-nanoparticles encapsulated single-walled carbon nanotubes. *Chem Commun*: 254–256
17. Li YF et al (2007) Negative differential resistance in tunneling transport through C₆₀ encapsulated double-walled carbon nanotubes. *Appl Phys Lett* 90:073106-1-3
18. Li YF et al (2009) Photoswitching in azafullerene encapsulated single-walled carbon nanotube FET devices. *J Am Chem Soc* 131:3412–3413
19. Li YF et al (2013) C₅₉N peapods sensing the temperature. *Sensors* 13:966–974
20. Hatakeyama R et al (2010) Infrared photovoltaic solar cells based on C₆₀ fullerene encapsulated single-walled carbon nanotubes. *Appl Phys Lett* 97:013104-1-3
21. Wang S et al (2010) Multiple exciton generation in single-walled carbon nanotubes. *Nano Lett* 10:2381–2386
22. Li YF et al (2011) Harvesting infrared solar energy by semiconducting-single-walled carbon nanotubes. *Appl Phys Express* 4:065101-1-3
23. Li YF et al (2012) Performance enhancement of solar cells based on single-walled carbon nanotubes by au nanoparticles. *Appl Phys Lett* 101:083901-1-4
24. Li YF et al (2011) Electrically moving single-stranded DNA into and out of double-walled carbon nanotubes. *Chem Commun* 47:2309–2311
25. Chen Q et al (2012) Rapid synthesis of water-soluble gold nanoparticles with control of size and assembly using gas-liquid interfacial discharge plasma. *Chem Phys Lett* 521:113–117
26. Chen Q et al (2011) Characterization of pulse-driven gas-liquid interfacial discharge plasmas and application to synthesis of gold nanoparticle-DNA encapsulated carbon nanotubes. *Curr Appl Phys* 11:S63–S66

Chapter 12

Stochastic Resonance Effect on Carbon Nanotube Field-Effect Transistors

Yasuhide Ohno, Kenzo Maehashi, and Kazuhiko Matsumoto

Abstract Stochastic resonance (SR) in carbon nanotube field-effect transistors (CNT-FETs) was investigated to enhance their weak-signal response. When weak pulse trains were applied to the gate of a CNT-FET operating in a subthreshold region, the correlation between the input and output voltages increased upon addition of noise with optimized intensity. Virtual CNT-FET summing networks of N units were demonstrated to improve SR. When no noise was applied for $N = 1$, the correlation coefficient was nearly 0, while the correlation coefficient at the peak intensity for $N = 8$ was estimated to be 0.58, indicating that significant enhancement of the correlation was observed in the summing network of the CNT-FETs. Then, a solution-gated CNT-FET based on SR was investigated. When noise of optimal intensity was introduced at the reference electrode in a nonlinear CNT-FET, the electric double layer in the solution was modulated, resulting in SR behavior. Moreover, when the CNT-FET was used as a pH sensor, high sensitivity was achieved, which enabled the detection of small differences in pH. The best results were obtained in a noisy environment; therefore, a solution-gated SR-based CNT-FET operated in the subthreshold regime is a promising high-sensitivity sensor.

Keywords Stochastic resonance • Enhance weak signal • Noise • Correlation coefficient

12.1 Introduction

Carbon nanotubes (CNTs) are currently one of the most attractive materials for nanodevice fabrication, owing to their many excellent properties. In particular, CNT field-effect transistors (CNT-FETs) are expected to have a high sensitivity for

Y. Ohno (✉) • K. Matsumoto

Institute of Scientific and Industrial Research, Osaka University, Mihogaoka 8-1, Ibaraki, Osaka 567-0047, Japan

e-mail: ohno@sanken.osaka-u.ac.jp; k-matsumoto@sanken.osaka-u.ac.jp

K. Maehashi

Tokyo University of Agriculture and Technology, Tokyo, Japan

e-mail: maehashi@sanken.osaka-u.ac.jp

biomolecule detection, which has recently attracted considerable attention in many fields, for example, practical pharmacy, genomics, clinical diagnosis for health care, and life sciences [1,2]. This high sensitivity is because biomolecules are much larger than the diameter of CNT channels (1–2 nm). Many CNT-FET-based biosensors have been reported [3–5]. However, a large amount of unintentional noise around CNT channels exists in a solution of biosensors, and surrounding noise easily affects the electrical properties of CNT-FETs. Thus, one promising approach for improving the sensitivity of CNT-FETs is noise reduction [6]. However, noise plays important roles in biological systems [7]. Biological systems with molecular-scale architecture can operate robustly even with fluctuations in a noisy environment. Stochastic resonance (SR) has been hypothesized to explain this mechanism [8,9], and SR-based techniques have been developed as a technique for improving signal detection in a wide variety of systems [10–12].

In this chapter, SR in CNT-FETs to enhance their weak-signal response by adding noise was investigated. CNT-FETs have nonlinear electrical properties; thus, when noise with optimized intensity is introduced into CNT-FETs, the noise allows weak signals to reach the threshold in these devices. As a result, signal response is enhanced. Moreover, multichannel CNT-FETs, in which many CNTs are bridged between the source and drain electrodes, are suitable to form physical network structures [13]. And, virtual CNT-FET summing networks were also demonstrated to improve SR. In addition, the use of SR in a solution-gated CNT-FET in conjunction with external noise in order to enhance the detection of small signals was described. When noise was applied to an Ag/AgCl reference electrode, the electric double layer in the solution was modulated, resulting in SR behavior. Although CNT-FET-based pH sensors have already been investigated, in this chapter, we demonstrate an increase in sensitivity that allows the detection of small differences in pH using SR in a solution-gated CNT-FET operated in the subthreshold regime.

12.2 Experimental Procedure

12.2.1 Device Fabrication

CNT-FETs were fabricated using position-controlled growth. First, a patterned Co chemical catalyst was formed by conventional photolithography and lift-off process technology on heavily doped p^+ -Si substrates capped with a 100 nm-thick SiO_2 layer. CNTs were grown by ethanol thermal chemical vapor deposition. Source and drain contacts were formed on the patterned chemical catalyst after CNT growth, and the Si substrate was used as a back gate. The spacing between the source and drain electrodes was approximately 3 μm . The gate transfer characteristics of the back-gated CNT-FET are shown in Fig. 12.1 at a source–drain voltage of 1.0 V. Good pinch-off characteristics with V_{th} of 5.5 V were obtained. Transconductance (g_m) was estimated to be 0.2 μS .

Fig. 12.1 Transfer characteristics of a CNT-FET against back-gate voltage in air

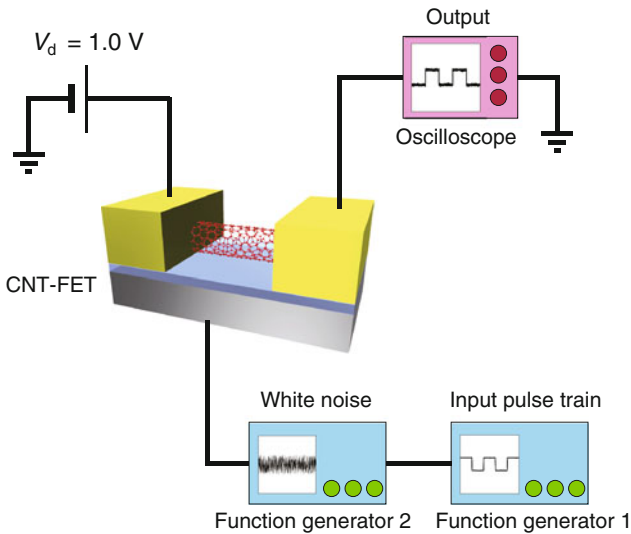
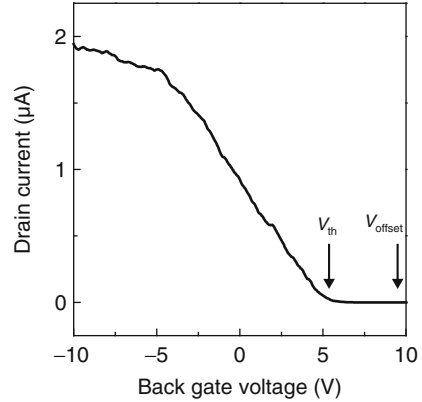


Fig. 12.2 Schematic of measurement setup for the back-gate operation

12.2.2 Back-Gate Operation

Figure 12.2 shows a schematic illustration of the measurement setup for the back-gate operation. A common voltage pulse train was applied to the back gates of the CNT-FETs as an input signal. The source–drain current was monitored as output through a circuit. Noise was added to the gate input. Here, a gate voltage less than the threshold voltage (V_{th}) was applied so that the CNT-FETs operated in the subthreshold region. The pulse train and voltage noise were generated by conventional digital signal synthesizers, as shown in Fig. 12.2. A Gaussian white

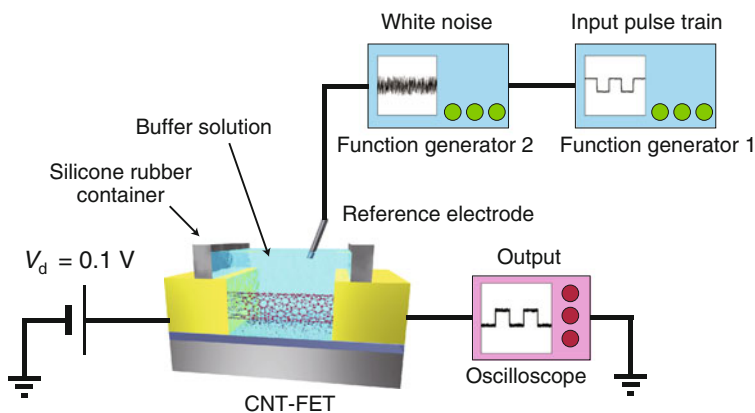


Fig. 12.3 Schematic of measurement setup for the solution-gate operation

noise with a bandwidth of 26 MHz was used as the generated noise. The output waveforms were measured using a digital oscilloscope. In this study, an N -parallel network with an uncorrelated noise was virtually reproduced by dividing a sample waveform from a single CNT-FET into N pieces and summing them up. All the measurements were carried out at room temperature.

12.2.3 Solution-Gate Operation

For solution-gated system, a silicone rubber container was put on the substrates (Fig. 12.3). A common voltage pulse train with a frequency of 0.1 Hz was applied to the Ag/AgCl electrode as the input for modulating the electric double layer in the solution. The pulse trains were also synchronized with Gaussian white noise with a bandwidth of 26 MHz. Aqueous solutions were buffered at pH 6.86 using a 10 mM phosphate buffer. The threshold voltage (V_T) of the device was set at -30 mV .

12.2.4 Correlation Coefficient

There are several methods for quantifying the correlation between input and output signals such as the output power spectral density method, the use of correlation functions, and entropy calculations [10, 14–16]. In this study, the correlation between the pulse train and the output waveforms was calculated using the correlation coefficient C given by

$$C = \frac{\langle V_{in} \times I_{out} \rangle - \langle V_{in} \rangle \langle I_{out} \rangle}{\sqrt{\langle V_{in}^2 \rangle - \langle V_{in} \rangle^2} \sqrt{\langle I_{out}^2 \rangle - \langle I_{out} \rangle^2}}, \tag{12.1}$$

where $\langle V_{in} \rangle$ denotes the ensemble average of the pulse train, $V_{in}(t)$. In this work, CNT-FETs have p -type characteristics; thus, the absolute values of the calculated correlation coefficients were used.

Theoretical analysis was carried out to fit the theoretical results with experimental results in Fig. 12.4c using a physical model of carrier motion in the subthreshold region of FETs [17]. The Langevin equation was deduced from the drift motion of carriers in the semiconductor. Thus, the Kramers rate k_0 [10], which is the rate of carriers transitioning from electrodes, was obtained using Eq. (12.3). The expected current $\langle I_{out} \rangle$ was estimated from the Fokker–Planck equation. Then, the theoretical

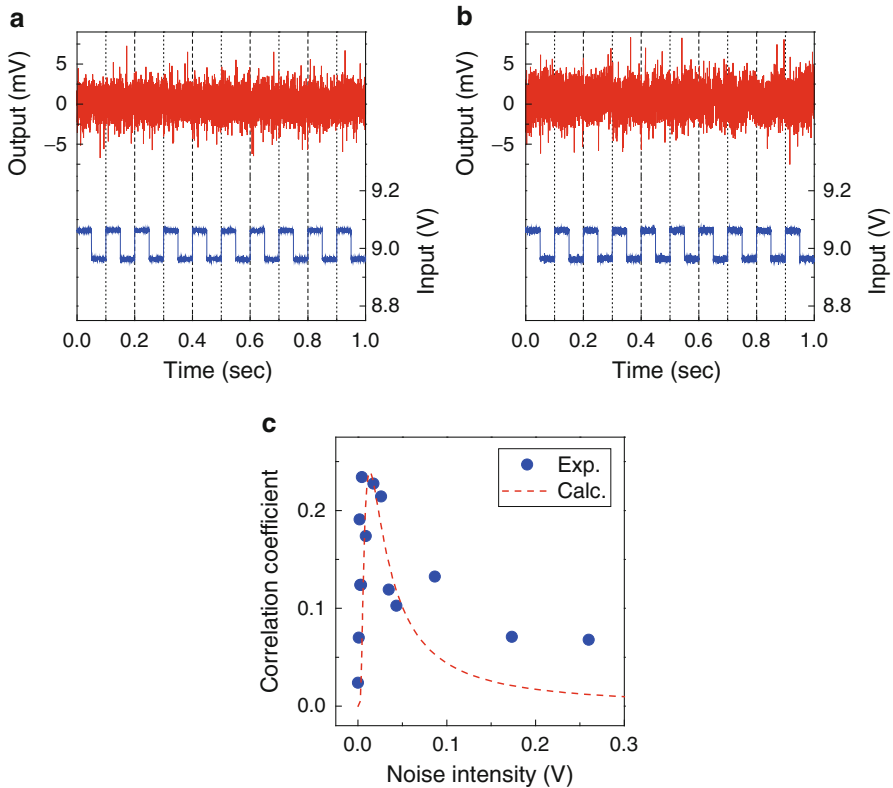


Fig. 12.4 Input pulse train and output-drain characteristics after adding noise at $V_{noise} = 0$ V (a) and 0.004 V (b). (c) Correlation coefficient C plotted against noise intensity

correlation coefficient C_1 was calculated by inputting the expected current into Eq. (12.1) as

$$C_1 = \frac{\cos \phi}{\sqrt{1 + \frac{1}{N} \left(\frac{V_{\text{noise}}}{\gamma \Delta V_{\text{in}}} \right)^2 (2k_0 \beta \eta + 2\beta^2) \frac{V_{\text{noise}}}{k_0^2} \left\{ 1 + \left(\frac{\Omega}{2k_0} \right)^2 \right\}}}, \quad (12.2)$$

$$k_0 = \frac{4\mu_e k_B T \ln(10) \Delta V_G}{L_G^2} \exp\left(-\frac{2\Delta V_G}{V_{\text{noise}}}\right), \quad (12.3)$$

where β is an empirical parameter coming from the time-dependent fluctuation in Kramers rate due to noise in the input pulse train [14]. In Eqs. (12.2) and (12.3), μ_e , T , η , ΔV_G , and $\tan \phi$ are the carrier mobility, temperature, G^2 , $V_{\text{offset}} - V_{\text{th}}$, and $\Omega/2k_0$, respectively.

12.3 Results and Discussion

12.3.1 Back-Gate Operation and Summing Network Effect

Figure 12.4a, b shows the characteristics of the input and output waveforms in the CNT-FET after adding noise, respectively. Pulse trains were applied to the back-gated voltage at an offset voltage (V_{offset}) of 9 V in the CNT-FET, where the height (ΔV_{in}), duty ratio (γ), and frequency (Ω) of the pulse train were 0.1 V, 50 %, and 10 Hz, respectively. The V_{th} and V_{offset} are exhibited in Fig. 12.1. The upper and lower panels of Fig. 12.4a, b correspond to the output and input pulse train voltages, respectively. The pulse trains were also synchronized with Gaussian white noise, as shown in Fig. 12.2. Noise intensity (V_{noise}) was defined as the root mean square of the generated noise voltage. The waveforms in Fig. 12.4a, b were measured after adding noise at V_{noise} of 0 and 0.004 V, respectively. When noise of 0 V was added to the pulse train, no response correlating with the pulse train was obtained, as shown in Fig. 12.4a. This is because the input pulse train never reached V_{th} . In contrast, after adding a noise of 0.004 V, as shown in Fig. 12.4b, the output in the CNT-FET exhibited a response that correlated with the pulse train.

A plot of the calculated correlation coefficient as a function of noise intensity is shown in Fig. 12.4c. When no noise was applied, the correlation coefficient became nearly 0. With increasing noise intensity, the correlation coefficient significantly increased. However, the correlation coefficient rapidly decreased and gradually saturated with the addition of stronger noise intensity, as shown in Fig. 12.4c. The results reveal that when appropriate noise intensity is applied, signals are enhanced. Therefore, characteristic signatures of the SR system behavior were clearly observed in the CNT-FETs. The curve in Fig. 12.4c shows the theoretical correlation coefficient C_1 obtained using Eq. (12.2). It reveals that the curve fitted

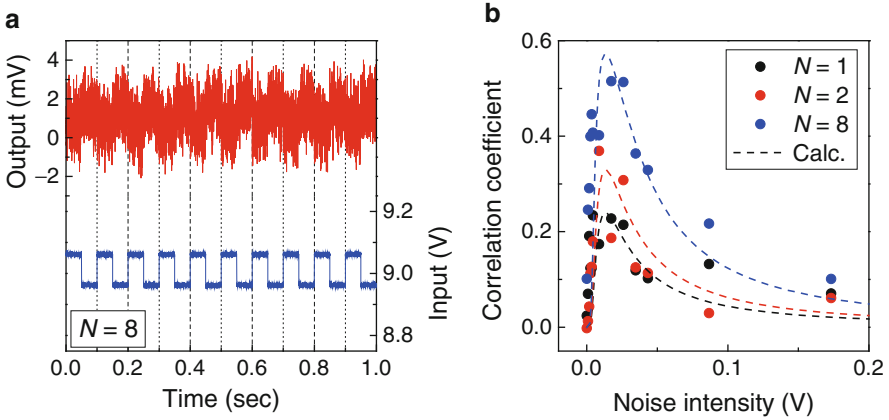
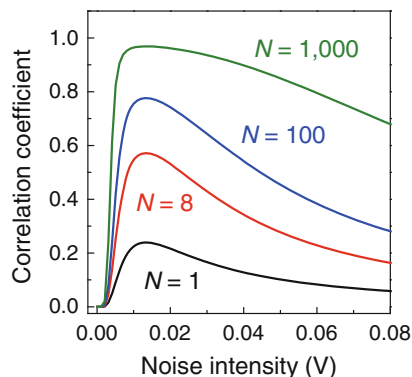


Fig. 12.5 (a) Input pulse train and output-drain characteristics after adding noise at $V_{\text{noise}} = 0.017$ V for $N = 8$ and (b) correlation coefficient vs noise intensity for various N values

the experimental results well and had a maximum of 0.24 at V_{noise} of 0.01 V. These results indicate that the experimental behaviors observed can be explained using the physical model of carrier motion in the subthreshold region of FETs.

Next, a virtual CNT-FET summing network of N units was demonstrated to improve SR. Figure 12.5a shows the characteristics of the input and output waveforms in the CNT-FET after adding noise at V_{noise} of 0.017 V for $N = 8$. The result revealed that the output in the CNT-FET exhibited a clearer response, which correlated with the pulse train, than those for $N = 1$ in Fig. 12.4b. Figure 12.5b shows the calculated correlation coefficients as functions of noise intensity for $N = 1, 2,$ and 8 . The theoretical correlation coefficients obtained using Eq. (12.2) were fitted with the experimental results. It is found that every correlation coefficient for $N = 1, 2,$ and 8 had one peak as a function of noise intensity, indicating that the virtual CNT-FET summing networks exhibited the SR system behavior. With an increasing number of units in the network, peak intensity increased, as shown in Fig. 12.5b. The peak intensity for $N = 8$ was estimated to be 0.58, which was more than twice larger than that for $N = 1$, indicating that significant enhancement of the correlation was obtained in the summing network of the CNT-FETs. Figure 12.6 shows the theoretical correlation coefficients obtained using Eq. (12.2) as functions of noise intensity for $N = 1, 8, 100,$ and $1,000$. As N increased, the correlation coefficient was close to 1.0 for a range of noise intensity. For single-unit CNT-FET, optimized noise is needed to be added to enhance weak-signal response. In contrast, a relatively large summing network had a plateau in the correlation coefficient near 1.0, indicating that CNT-FET summing networks are more robust against noise than single-unit CNT-FETs. This finding is similar to the behavior observed in the summing networks of sensory neurons reported by Collins et al. [13]. Therefore, the virtual CNT-FET summing networks are useful for enhancing the weak signals and moreover can work well even in a

Fig. 12.6 Theoretical correlation coefficients obtained using Eq. (12.2) as functions of noise intensity for $N = 1, 8, 100,$ and $1,000$



solution with large ionic strength, which has a large amount of unintentional noise. Recently, CNTs were aligned in a specific crystallographic direction on single-crystal or patterned substrates [18, 19]. As a result, CNT-FETs with multichannels were fabricated. Multichannel CNT-FETs can be applied in CNT-FET summing networks.

12.3.2 Solution-Gate Operation and Faint pH Detection

Figure 12.7a, b shows the drain current (I_d) and the input for a CNT-FET with an offset voltage of 150 mV after adding a noise intensity (V_{noise}) of 0.1 and 27 mV, respectively. The upper and lower panels of Fig. 12.7a, b correspond to I_d and the input, respectively. V_{noise} was defined as the root mean square (rms) of the generated noise voltage. Including the system noise, the minimum V_{noise} was found to be 0.1 mV. When the pulse train with the minimum V_{noise} was added, a large amount of I_d fluctuations in the CNT-FET was observed (Fig. 12.7a), resulting from the characteristics of CNTs to be easily affected by surrounding conditions. Moreover, no response correlated with the input was obtained. This is because the top gate in the CNT-FET was modulated in the subthreshold regime and the CNT-FET's electrical properties remained in the off state. However, after adding V_{noise} of 27 mV, I_d exhibited a clear response that correlated with the input, even though the CNT-FET operated in the subthreshold regime (Fig. 12.7b). Since external noise modulated the electric double layer in the solution, the top-gated voltage showed a decrease in the statistical average, which I_d then followed. Consequently, the noise allows small signals in the subthreshold regime to reach the device threshold. These results indicate that the external noise induces small-signal detection in a solution-gated CNT-FET operated in the subthreshold regime.

The correlation between the input trigger signal and I_d was calculated using the correlation coefficient (C). A plot of C as a function of V_{noise} is shown in Fig. 12.7c. When no noise was applied, C was small. As V_{noise} was increased, C

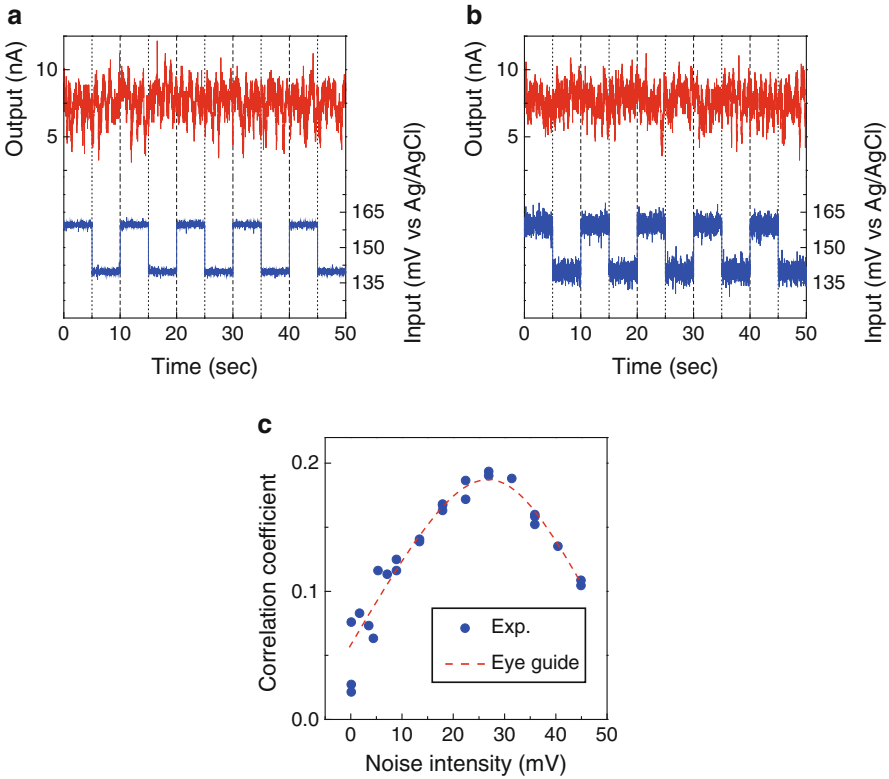


Fig. 12.7 SR in a solution-gated CNT-FET. I_d and input characteristics after adding external noise with $V_{\text{noise}} = 0.1$ (a) and 27 mV (b). (c) C plotted against V_{noise} . The dashed line is an eye guide

increased rapidly, reached a maximum, and then decreased due to the frequency of random transitions. These results show that a bell-shaped curve is observed for the solution-gated CNT-FET, which is consistent with the behavior in air-based SR experiments [20, 21]. Therefore, SR characteristics were demonstrated in the solution-gated CNT-FET.

Figure 12.8a shows the gate transfer curves of a solution-gated CNT-FET at pH 4.01 and 4.11. First, the CNT-FET was incubated in 200 μL of a 10 mM phthalate buffer at pH 4.01 (Fig. 12.3). Subsequently, 10 μL of a 10 mM phosphate buffer was added to raise the pH to 4.11. Because there was little difference in the gate transfer curves between pH 4.01 and 4.11, external noise was introduced to the Ag/AgCl solution-gated CNT-FET in the subthreshold regime in order to monitor the pH change. Figure 12.8b, c shows the time dependence of I_d in the solution-gated CNT-FET after V_{noise} of 0.1 and 5.3 mV was added, respectively. After 50 s, a 10 mM phosphate buffer was introduced to change the pH. In Fig. 12.8b, c, the white dashed and solid lines show the average of I_d before and after the introduction of the phosphate buffer, respectively. When V_{noise} of 0.1 mV was

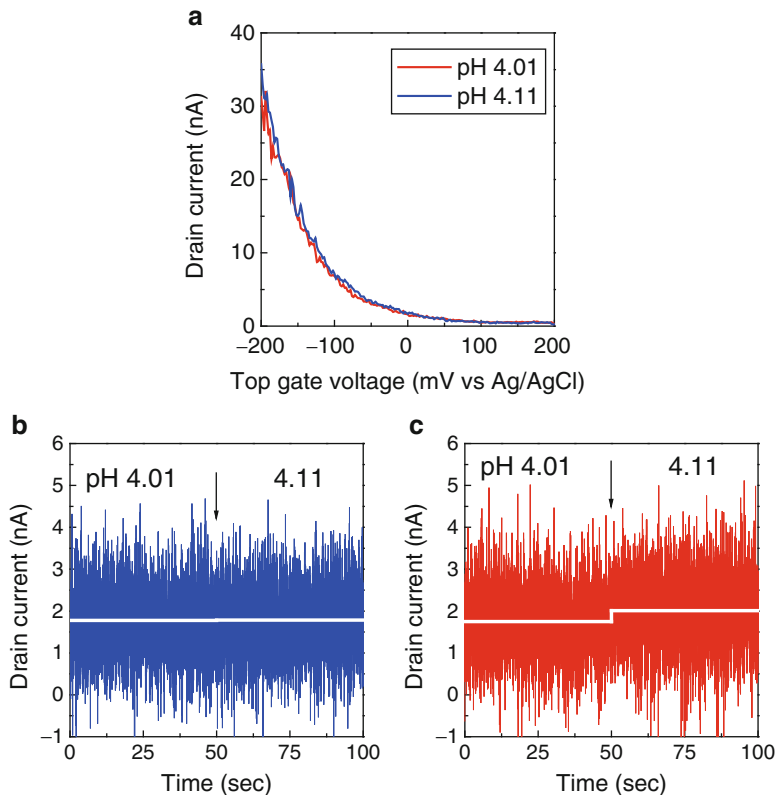
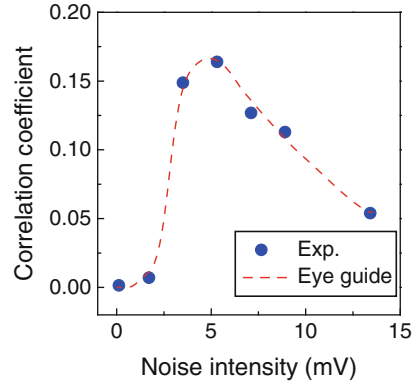


Fig. 12.8 Solution pH sensor based on SR in solution-gated CNT-FET. (a) Transfer characteristics recorded for a solution-gated CNT-FET at pH 4.01 and 4.11. Real-time current response to a step change in the pH from 4.01 to 4.11, with $V_{\text{noise}} = 0.1$ (b) and 5.3 mV (c)

introduced as the top-gate bias, no response was obtained after adding the phosphate buffer (Fig. 12.8b), which is consistent with the results shown in Fig. 12.8a. This is because the signals were too small to detect by I_d in a noisy environment, although sensing experiments are best performed in the subthreshold regime for optimal SNR [22, 23]. In contrast, when V_{noise} of 5.3 mV was added, I_d rose after the phosphate buffer was introduced, showing a clear response (Fig. 12.8c). The results indicate that SR occurred in the CNT-FET-based pH sensor and that the signal, which was hardly recognized (Fig. 12.8b), was clearly obtained by adding external noise.

From the results shown in Fig. 12.8b, c, fluctuations in I_d (I_{rms}) and the SNR (ΔI , defined as (solid – dashed lines of I_d)/ I_{rms}) were calculated after supplying external noise to the Ag/AgCl electrode. After adding V_{noise} of 0.1 mV, I_{rms} and the SNR were estimated to be 1.9 nA and 0.0034, respectively (Fig. 12.8b). However, after V_{noise} of 5.3 mV was added, I_{rms} and the SNR were estimated to be 2.1 nA and

Fig. 12.9 SR in pH sensor based on solution-gated CNT-FET showing the bell-shaped curve for C as a function of V_{noise} . The dashed line is an eye guide



0.12, respectively (Fig. 12.8c), indicating that the SNR increased by almost 2 orders of magnitude despite the increase in I_{rms} . CNT-FET-based pH sensors have already been reported for which stepwise increases in I_d were observed from pH 4.04 to 8.29 and for which I_d at each pH maintained a constant value when the CNT-FET was operated at maximum transconductance. The SNR was estimated to be 0.038 for a difference in pH of 0.1. In comparison with the value, the SNR in Fig. 12.8b was improved by almost 1 order of magnitude using SR. These results demonstrate that solution-gated CNT-FET sensing experiments carried out in the subthreshold regime are best performed in a noisy environment.

The correlation coefficient between I_d and a step function for the difference in pH was calculated and was plotted as a function of V_{noise} (Fig. 12.9). When minimal V_{noise} was applied in the subthreshold regime of the solution-gated CNT-FET, C was nearly 0, showing that the CNT-FET in the subthreshold regime had reached its limit of detection. C increased significantly with V_{noise} and peaked at 0.16 when $V_{\text{noise}} = 5.3$ mV, indicating that the detection limit of the CNT-FET-based sensor had been greatly improved. C in SR mode was more than 100-fold larger than its value when V_{noise} was at the minimum. These results show a bell-shaped curve for C as a function of V_{noise} for the solution-gated CNT-FET-based pH sensor as a result of SR. Therefore, a solution-gated sensor based on SR can be useful for enhancing sensitivity.

12.4 Conclusion

SR in CNT-FETs to enhance their weak-signal response by adding noise was described. With increasing noise intensity, the correlation coefficients significantly increased and exhibited a peak, indicating the SR behavior in CNT-FETs. Moreover, virtual CNT-FET summing networks were found to improve SR. The measurements revealed that with an increasing number of the units in the network, peak intensity increased and the network became robust against the noise.

Then, SR using a solution-gated CNT-FET operated in the subthreshold regime was investigated. It was found that the correlation between the input and I_d increased when external noise was applied to the CNT-FET reference electrode and that SR characteristics were obtained in solution. Furthermore, a pH sensor based on SR in the solution-gated CNT-FET was demonstrated, revealing that the small signals that were drowned out by I_{rms} were detected in a noisy environment. C for the optimal V_{noise} was highest when added noise led to an increase of up to 2 orders of magnitude in the SNR. These results indicate that solution-gated CNT-FETs operated in the subthreshold regime based on SR can be useful for enhancing the sensitivity limit of chemical and biological sensors.

References

1. Brekkan E, Lundqvist A, Lundahl P (1996) Immobilized membrane vesicle or proteoliposome affinity chromatography. Frontal analysis of interactions of cytochalasin B and d-Glucose with the human red cell glucose transporter. *Biochemistry* 35:12141–12145
2. Lyon LA, Musick MD, Natan MJ (1998) Colloidal Au-enhanced surface plasmon resonance immunosensing. *Anal Chem* 70:5177–5183
3. Chen RJ, Bangsaruntip S, Drouvalakis KA, Kam NWS, Shim M, Li Y, Kim W, Utz PJ, Dai H (2003) Noncovalent functionalization of carbon nanotubes for highly specific electronic biosensors. *Proc Natl Acad Sci USA* 100:4984–4989
4. Besteman K, Lee JO, Wiertz FGM, Heering HA, Dekker C (2003) Enzyme-coated carbon nanotubes as single-molecule biosensors. *Nano Lett* 3:727–730
5. Maehashi K, Katsura T, Kerman K, Takamura Y, Matsumoto K, Tamiya E (2007) Label-free protein biosensor based on aptamer-modified carbon nanotube field-effect transistors. *Anal Chem* 79:782–787
6. Yamamoto Y, Ohno Y, Maehashi K, Matsumoto K (2009) Noise reduction of carbon nanotube field-effect transistor biosensors by alternating current measurement. *Jpn J Appl Phys* 48:06FJ01
7. Moss F, Ward LM, Sannita WG (2004) Stochastic resonance and sensory information processing: a tutorial and review of application. *Clin Neurophysiol* 115:267–281
8. Douglass JK, Wilkens L, Pantazelou E, Moss F (1993) Noise enhancement of information transfer in crayfish mechanoreceptors by stochastic resonance. *Nature* 365:337–340
9. Russell DF, Wilkens LA, Moss F (1999) Use of behavioural stochastic resonance by paddle fish for feeding. *Nature* 402:291–294
10. Gammaitoni L, Hänggi P, Jung P, Marchesoni F (1998) Stochastic resonance. *Rev Mod Phys* 70:223–287
11. Benzi R, Sutera A, Vulpiani A (1981) The mechanism of stochastic resonance. *J Phys A* 14:L453
12. Lee I, Liu X, Kosko B, Zhou C (2003) Nanosignal processing: stochastic resonance in carbon nanotubes that detect subthreshold signals. *Nano Lett* 3:1683–1686
13. Collins JJ, Chow CC, Imhoff TT (1995) Stochastic resonance without tuning. *Nature* 376:236–238
14. Collins JJ, Chow CC, Imhoff TT (1995) Aperiodic stochastic resonance in excitable systems. *Phys Rev E* 52:R3321
15. Wehrl A (1991) The many facets of entropy. *Rep Math Phys* 30:119–129
16. Neiman A, Shulgina B, Anishchenko V, Ebeling W, Schimansky-Geier L, Freund J (1996) Dynamical entropies applied to stochastic resonance. *Phys Rev Lett* 76:4299–4302

17. Kasai S, Asai T (2008) Stochastic resonance in schottky wrap gate-controlled GaAs nanowire field-effect transistors and their networks. *Appl Phys Express* 1:083001
18. Kocabas C, Hur S-H, Gaur A, Meitl MA, Shim M, Rogers JA (2005) Guided growth of large-scale, horizontally aligned arrays of single-walled carbon nanotubes and their use in thin-film transistors. *Small* 1:1110–1116
19. Maehashi K, Iwasaki S, Ohno Y, Kishimoto T, Inoue K, Matsumoto K (2010) Improvement in performance of carbon nanotube field-effect transistors on patterned SiO₂/Si substrates. *J Electron Mater* 39:376–380
20. Hakamata Y, Ohno Y, Maehashi K, Kasai S, Inoue K, Matsumoto K (2010) Enhancement of weak-signal response based on stochastic resonance in carbon nanotube field-effect transistors. *J Appl Phys* 108:104313
21. Kanki T, Hotta Y, Asakawa N, Kawai T, Tanaka H (2010) Noise-driven signal transmission using nonlinearity of VO₂ thin films. *Appl Phys Lett* 96:242108
22. Heller I, Mannik J, Lemay SG, Dekker C (2009) Optimizing the signal-to-noise ratio for biosensing with carbon nanotube transistors. *Nano Lett* 9:377–382
23. Gao XPA, Zheng G, Lieber CM (2010) Subthreshold regime has the optimal sensitivity for nanowire FET biosensors. *Nano Lett* 10:547–552

Chapter 13

Electrochemical Biological Sensors Based on Directly Synthesized Carbon Nanotube Electrodes

Kenzo Maehashi, Kazuhiko Matsumoto, Yuzuru Takamura,
and Eiichi Tamiya

Abstract We have fabricated electrochemical biological sensors based on directly synthesized carbon nanotube (CNT) electrodes. Since CNTs have a large specific surface area, the direct synthesis of CNTs on electrodes in amperometric biosensors is expected to significantly enhance electroactive surface area. Moreover, in electrochemical detections, CNT electrodes promote electron-transfer reactions on CNT surfaces. In this section, we have investigated the technology and performance of the electrochemical biosensors based on CNT electrodes and described microfluidic chips with multibiosensors based on CNT electrodes for commercialization.

Keywords Electrochemical biosensors • Carbon nanotube electrodes • Immunosensors • Microfluidic chips • Pneumatic micropumps

13.1 Introduction

In recent years, biological sensors for detections of biomolecules such as DNA, proteins, etc., have attracted great attention in clinical diagnosis for health care [1–4]. In particular, label-free electrochemical detections of biorecognition events provide a promising platform, which are simpler, less expensive, and require less

K. Maehashi (✉)

Tokyo University of Agriculture and Technology, Tokyo, Japan
e-mail: maehashi@cc.tuat.ac.jp

K. Matsumoto

Institute of Scientific and Industrial Research, Osaka University,
Mihogaoka 8-1, Ibaraki, Osaka 567-0047, Japan
e-mail: k-matsumoto@sanken.osaka-u.ac.jp

Y. Takamura

Japan Advanced Institute of Science and Technology, Ishikawa, Japan
e-mail: takamura@jaist.ac.jp

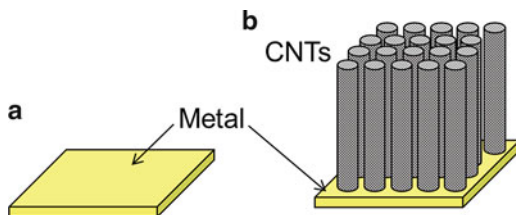
E. Tamiya

Osaka University, Osaka, Japan
e-mail: tamiya@ap.eng.osaka-u.ac.jp

© Springer Japan 2015

K. Matsumoto (ed.), *Frontiers of Graphene and Carbon Nanotubes*,
DOI 10.1007/978-4-431-55372-4_13

Fig. 13.1 Schematic illustrations of working electrodes in electrochemical detection: (a) conventional metal and (b) CNT electrodes



energy. Moreover, they are very suitable for minimization of biosensors [5]. In the electrochemical amperometric sensing, in general, three types of electrode are arranged: working, reference, and counter electrodes. Electroactive biomolecules are oxidized or reduced on the working electrode surfaces, and then electron-transfer reactions occur. Thus, choosing appropriate materials of the working electrodes is crucial for sensitivity of electrochemical detections. Gold, platinum, and glassy carbon have been utilized as working electrodes.

Carbon nanotubes (CNTs) are one of the most promising materials owing to their unique electric and mechanical properties and nanoscale size [6–8]. Then, CNTs are utilized as a channel of CNT field-effect transistors for label-free potentiometric biosensors [9–12]. In the electrochemical amperometric sensing, it was reported that CNTs have a higher ability to promote electron-transfer reactions than conventional metal electrodes for electrochemical measurements [13]. Since CNTs have a high aspect ratio, the total surface area of working electrodes becomes larger when CNTs are modified on the surface of electrodes. As a result, highly sensitive detection of biomolecules is expected using CNT-modified electrodes for electrochemical analysis. In recent years, CNT-modified electrodes were fabricated by scattering CNTs on the metal surfaces [14–16]. However, they are considered to have high contact resistance between CNTs and metal electrodes.

In this section, we have fabricated electrochemical amperometric biosensors based on CNT-modified electrodes. When dense CNTs are directly synthesized on the surface of bare metal electrodes, the total surface area of working electrodes is estimated to be more than a thousand times larger than that of the bare metal electrode at the same site, as shown in Fig. 13.1. As a result, the sensitivity in detection of biomolecules will be enhanced and the CNT working electrodes can be integrated into micro total analysis systems. In this section, we performed the detection of amino acids and a protein cancer marker, prostate-specific antigen (PSA), using microelectrodes modified with CNTs. Moreover, microfluidic and label-free multi-immunosensors based on CNT microelectrodes and pneumatic micropumps were fabricated and detections of glucose and two kinds of cancer markers were demonstrated.

13.2 Biosensors Based on CNT Electrodes

CNT-arrayed electrodes were directly synthesized on Pt surfaces by thermal chemical vapor deposition [17] and were also arrayed on a chip [18], as shown in Fig. 13.2a. Figure 13.2b shows a schematic image of a three-electrode system

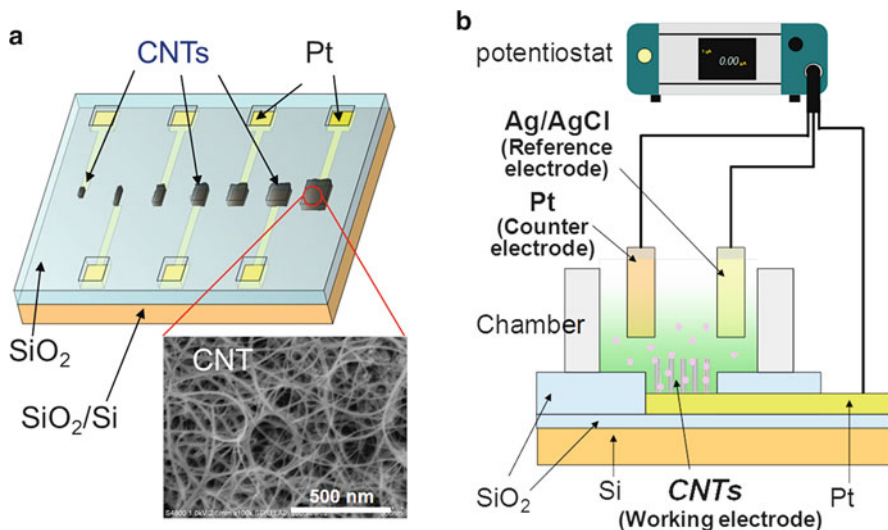


Fig. 13.2 (a) Schematic illustration of electrochemical biosensor based on CNT-arrayed electrodes. A scanning electron microscopy image of a CNT electrode is shown in the inset. (b) Schematic image of experimental setup of electrochemical biosensor based on CNT-arrayed electrodes

that was applied in electrochemical measurements. CNT-arrayed electrodes, a Pt wire, and Ag/AgCl were utilized as the working, counter, and reference electrodes, respectively. The working electrodes were surrounded by a silicone chamber attached to the substrate, as shown in Fig. 13.2b. The electrochemical characteristics of the devices were investigated using $K_3[Fe(CN)_6]$ and electroactive amino acids: L-tyrosine, L-cysteine, and L-tryptophan. The lower oxidation potential for the amino acids was obtained compared with Pt disk electrodes [19]. The electrochemical measurements of $K_3[Fe(CN)_6]$ and amino acids revealed that the peak current intensities using the CNT-arrayed electrodes were more than 100-fold higher than those using bare Pt electrodes. The results indicated that the biosensors based on CNT-arrayed electrodes showed a high sensitivity to detect biomolecules.

A cancer marker, prostate-specific antigen (PSA), was selectively detected using the CNT electrodes. Monoclonal antibodies against prostate-specific antigen (PSA-mAb) were covalently anchored onto the CNTs using 1-pyrenebutanoic acid succinimidyl ester (linker), as shown in Fig. 13.3a. Electrochemical signals of CNT-modified electrodes were measured using differential pulse voltammetry (DPV) [20]. The peak current signal was obtained at +0.5 V from only PSA-mAb, as shown in Fig. 13.3b. After the introduction of 1 ng/mL PSA on the PSA-mAb-modified CNT electrodes, the electrochemical current signal significantly increased, as shown in Fig. 13.3c, indicating that the antigen-antibody complex was formed. The selectivity of the biosensor was also observed in a study using bovine serum albumin as the nontarget protein, as shown in Fig. 13.3d. PSA in the range of

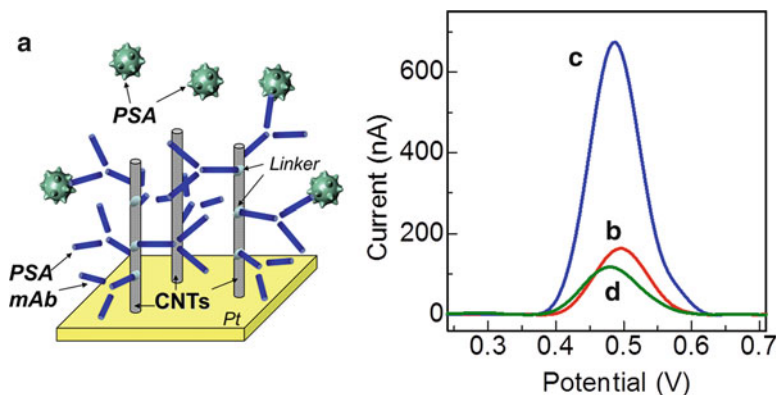


Fig. 13.3 (a) Schematic illustration of label-free electrochemical immunosensor. PSA-mAb was covalently immobilized on the CNTs using linkers. Electrochemical signals of (b) PSA-mAb, after introduction of (c) 1 ng/mL PSA and (d) bovine serum albumin as the nontarget protein

0.25–1 ng/mL was effectively detected using the CNT electrodes. Since the cutoff limit of PSA for distinguishing between prostate hyperplasia and cancer is 4 ng/mL, the performance of the label-free electrochemical immunosensor is promising for further clinical applications. Furthermore, the nanoscale features by semiconductor processing made it possible to fabricate arrays with extremely high density and compatibility for further integration.

13.3 Microfluidic Chips with Multibiosensors Based on CNT Electrodes

A micro total analysis system (μ TAS) has attracted attention worldwide [21–23]. In this system, the units of measurements are integrated using semiconducting fine processes, and all analytical processes are automatically carried out on one chip. It has dual benefits of consumption of only a very small amount of reagents for analysis and of a markedly reduced analysis time. Significant research and development efforts have been devoted to producing microfluidic chips for the realization of μ TAS. Our group fabricated microfluidic chips using the combination of amperometric biosensors based on CNT-arrayed electrodes and microchannels with pneumatic micropumps.

Figure 13.4a, b show schematic and optical images of microfluidic chips based on CNT-arrayed electrodes, respectively [24]. Four liquid inlets, six pneumatic micropumps, one liquid outlet, and three channels were integrated in the chip. Twelve CNT working electrodes, three Pt counter electrodes, and three Ag/AgCl reference electrodes were also arrayed on the substrate. The pneumatic micropumps were composed of three poly(dimethylsiloxane) (PDMS) layers: an air layer,

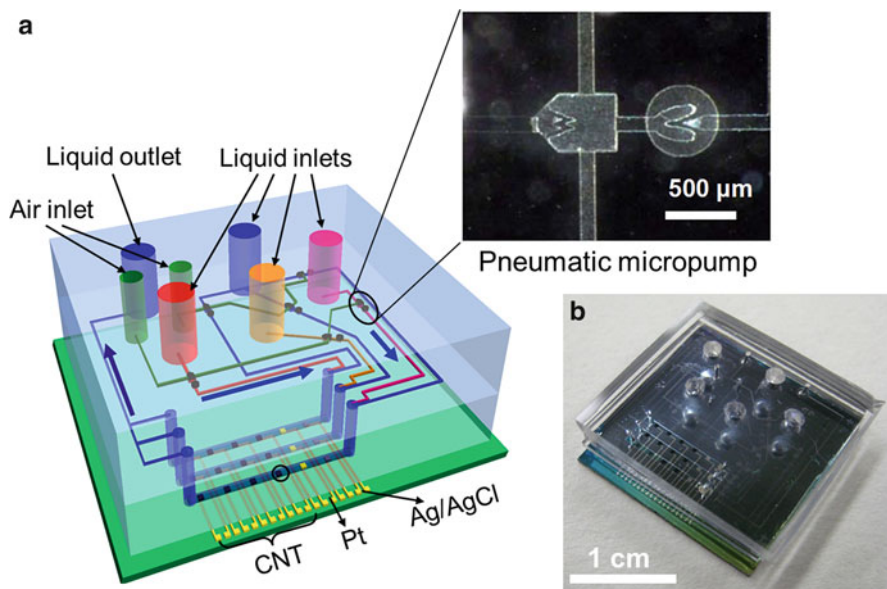


Fig. 13.4 (a) Schematic illustration of a microfluidic chip based on CNT electrodes. An optical image of a pneumatic micropump is shown in the inset. (b) Optical image of the microfluidic chip, which included twelve CNT, three Pt, and three Ag/AgCl electrodes

an intermediate membrane, and a liquid layer. The air layers of the pneumatic micropumps were connected to the air pressure control. By pulling the air layers of the drive section, the reagents were sucked from inlets to the valve. Subsequently, by pushing them, the reagents were pushed out to the electrodes. By repeatedly pulling and pushing them, the reagents were constantly introduced to microchannels. The check valves prevented unexpected reverse flow and diffusion. In the microfluidic systems, four types of reagents can be transported from each liquid inlet to arrayed microelectrodes using integrated pumps without an unexpected reverse flow and diffusion.

In the chip, phosphate buffer solution (PBS) and $K_3[Fe(CN)_6]$ were introduced into the CNT electrodes using pneumatic micropumps. Electrochemical measurements indicated that the chips can automatically exchange reagents on the CNT electrodes and clearly detect molecules. Moreover, by modifying the CNT electrodes with enzyme glucose oxidase, as shown in Fig. 13.5a, glucose molecules were detected by chronoamperometry (CA). Figure 13.5b shows the time dependence of electrochemical signals by CA at an applied potential of 450 mV vs Ag/AgCl [25]. Glucose samples at three concentrations and PBS were alternately introduced into CNT electrodes from different inlets using the pumps. In Fig. 13.5b, the amperometric response to glucose at each concentration was clearly observed. In addition, after PBS was introduced, the signals of glucose disappeared, indicating that PBS can rinse glucose out of the surfaces of the CNT electrodes. This result

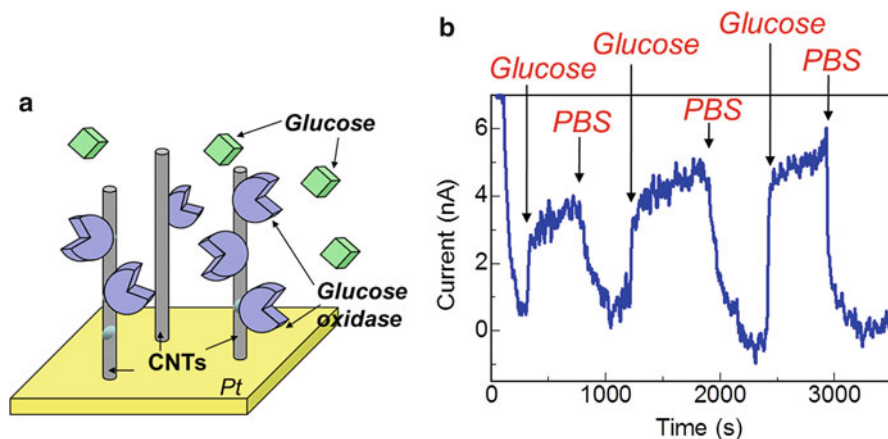


Fig. 13.5 (a) Schematic illustration of detection of glucose molecules. Glucose oxidase was covalently immobilized on the CNTs using linkers. (b) Time dependence of electrochemical signals by CA at an applied potential of 450 mV vs Ag/AgCl. Glucose samples at 5, 10, and 20 mg/mL in PBS and PBS were alternately introduced into CNT electrodes from different inlets using two pumps

clearly revealed that a linear response to glucose concentration within the range from 5 to 20 mg/mL was obtained. These results indicate that glucose can be quantified using the CNT electrodes modified with glucose oxidase, and PBS washes the glucose out of the CNT electrodes in the system.

Furthermore, simultaneous detection of two types of cancer marker, PSA and human chorionic gonadotropin (hCG), using the chip was reported [24]. First, two types of antibody, PSA-mAb and hCG antibody, were automatically immobilized onto different CNT electrodes using the microfluidic systems. Next, PSA and hCG were injected into corresponding CNT electrodes. Finally, after rising all electrodes with blank PBS, PSA and hCG were simultaneously detected by DPV.

13.4 Conclusions

In this section, we provide an introduction to electrochemical amperometric biosensors based on CNT electrodes, which were directly synthesized on the metal surfaces. The electrochemical measurements indicated that the CNT electrodes have a much higher sensitivity than conventional electrodes. Moreover, PSA in the range of 0.25–1 ng/mL can be effectively detected using the CNT electrodes, indicating that the label-free electrochemical biosensors are useful for the clinical diagnosis of prostate cancer. Microfluidic chips based on the CNT electrodes were also reviewed. The chip consisted of amperometric biosensors based on CNT-arrayed electrodes and microchannels with pneumatic micropumps. The reagents were introduced

to arrayed electrodes without unexpected reverse flow and diffusion and were automatically exchanged on the CNT electrodes. In this system, two types of cancer marker, PSA and hCG, were simultaneously detected by DPV. It is concluded that microfluidic chips with CNT-arrayed electrodes are promising candidates for the development of handheld electrochemical multiplex biosensors.

References

1. Leiner MJP (1991) Luminescence chemical sensors for biomedical applications: scope and limitations. *Anal Chim Acta* 255:209
2. Muller KM, Arndt KM, Bauer K, Pluckthun A (1998) Tandem immobilized metal-ion affinity chromatography/immunoaffinity purification of His-tagged proteins—evaluation of two anti-His-tag monoclonal antibodies. *Anal Biochem* 259:54
3. Lyon LA, Musick MD, Natan MJ (1998) Colloidal Au-enhanced surface plasmon resonance immunosensing. *Anal Chem* 70:5177
4. Drummond T, Hill M, Barton J (2003) Electrochemical DNA sensors. *Nat Biotechnol* 21:1192
5. Stradiotto NR, Yamanaka H, Valnice M, Zanoni B (2003) Electrochemical sensors: a powerful tool in analytical chemistry. *J Braz Chem Soc* 14:159
6. Bockrath M, Cobden DH, McEuen PL, Chopra NG, Zettl A, Thess A, Smalley RE (1997) Single-electron transport in ropes of carbon nanotubes. *Science* 275:1922
7. Tans S, Verschueren A, Dekker C (1998) Room-temperature transistor based on a single carbon nanotube. *Nature* 393:49
8. Star A, Gabriel J, Bradley K, Gruner G (2003) Electronic detection of specific protein binding using nanotube FET devices. *Nano Lett* 3:459
9. Besteman K, Lee J, Wiertz F, Heering H, Dekker C (2003) Enzyme-coated carbon nanotubes as single-molecule biosensors. *Nano Lett* 3:727
10. Maehashi K, Katsura T, Karman K, Matsumoto K, Tamiya E (2007) Label-free protein biosensor based on aptamer-modified carbon nanotube field-effect transistors. *Anal Chem* 79:782
11. Katsura T, Yamamoto Y, Maehashi K, Ohno Y, Matsumoto K (2008) High-performance carbon nanotube field-effect transistors with local electrolyte gates. *Jpn J Appl Phys* 47:2060
12. Maehashi K, Matsumoto K, Takamura Y, Tamiya E (2009) Aptamer-based label-free immunosensors using carbon nanotube field-effect transistors. *Electroanalysis* 21:1285
13. Wang J (2004) Carbon-nanotube based electrochemical biosensors. *Electroanalysis* 17:7
14. Liu G, Riechers SL, Mellen MC, Lin Y (2005) Sensitive electrochemical detection of enzymatically generated thiocholine at carbon nanotube modified glassy carbon electrode. *Electrochem Commun* 7:1163
15. Fei S, Chen J, Yao S, Deng G, He D, Kuang Y (2005) Electrochemical behavior of L-cysteine and its detection at carbon nanotube electrode modified with platinum. *Anal Biochem* 339:29
16. Lawrence NS, Wang J (2006) Chemical adsorption of phenothiazine dyes onto carbon nanotubes: Toward the low potential detection of NADH. *Electrochem Commun* 8:71
17. Maehashi K, Ohno Y, Inoue K, Matsumoto K (2004) Chirality selection of single-walled carbon nanotubes by laser resonance chirality selection method. *Appl Phys Lett* 85:858
18. Okuno J, Maehashi K, Matsumoto K, Kerman K, Takamura Y, Tamiya E (2007) Single-walled carbon nanotube-arrayed microelectrode chip for electrochemical analysis. *Electrochem Commun* 9:13
19. Moreno L, Merkoci A, Alegret S, Cassou SH, Saurina J (2004) Analysis of amino acids in complex samples by using voltammetry and multivariate calibration methods Laura Moreno. *Anal Chim Acta* 507:247

20. Okuno J, Maehashi K, Kerman K, Matsumoto K, Takamura Y, Tamiya E (2007) Label-free immunosensor for prostate-specific antigen based on single-walled carbon nanotube array-modified microelectrodes. *Biosens Bioelectron* 22:2377
21. Manz A, Graber N, Widmer HM (1990) Miniaturized total chemical analysis systems: a novel concept for chemical sensing. *Sens Actuators B1*:244
22. Harrison DJ, Fluri K, Seiler K, Fan Z, Effenhauser CS, Manz A (1993) Micromachining a miniaturized capillary electrophoresis-based chemical analysis system on a chip. *Science* 261:895
23. Reyes DR, Iossifidis D, Auroux P, Manz A (2002) Micro total analysis systems. 1. introduction, theory, and technology. *Anal Chem* 74:2623
24. Tsujita Y, Maehashi K, Matsumoto K, Chikae M, Takamura Y, Tamiya E (2009) Microfluidic and label-free multi-immunosensors based on carbon nanotube microelectrodes. *Jpn J Appl Phys* 48:06FJ02
25. Tsujita Y, Maehashi K, Matsumoto K, Chikae M, Torai S, Takamura Y, Tamiya E (2008) Carbon nanotube amperometric chips with pneumatic micropumps. *Jpn J Appl Phys* 47:2064

Chapter 14

Nanomechanical Application of CNT

Seiji Akita

Abstract Carbon nanotubes (CNT) are appropriate for nanoscale mechanical system such as nano-switches and nanomechanical resonators for mass sensor application because of their lightweight, high aspect ratio, and extraordinary mechanical properties. The resonator miniaturization is crucial in bringing highly sensitive force and mass detection into practice, so that the CNTs are appropriate for the force and mass sensing. Here, we focus on highly sensitive mass and force detections using CNT mechanical resonators as nanomechanical application of CNTs. Loss factors of the multiwall-CNT resonators, which determine the sensitivity of the resonator, are strongly correlated to the CNT diameter due to the van der Waals interaction between layers. Down-mixing method for detecting the resonance frequencies of CNT mechanical resonators is one of key techniques to achieve the extremely high sensitivity. The doubly clamped CNT resonators consisting of single-wall CNTs achieved the sensitivity with ~ 10 zN Hz^{-1/2} at 1.2 K in ultrahigh vacuum. For the ambient condition, which is preferable for the biological samples, optical detection using opt-mechanical heterodyne technique was proposed and achieved high mass sensitivity with ~ 100 zg under the atmospheric conditions. We believe that this extraordinarily high sensitivity offers new possibilities for the investigation of a wide range of materials, especially nanoscale materials.

Keywords Nanoscale mechanical system • Nanomechanical resonators • Force and mass sensing • Down-mixing method • Opt-mechanical heterodyne technique

Carbon nanotubes (CNT) are appropriate for nanoscale mechanical system such as nano-switches [1–9] and nanomechanical resonators for mass sensor application [10–14] because of their lightweight, high aspect ratio, and extraordinary mechanical properties [15–17]. A force sensing using a resonant-frequency shift of a mechanical resonator is expected to provide a high sensitivity. The highly sensitive force sensor is expected in a wide variety of applications to sense all of

S. Akita (✉)

Department of Physics and Electronics, Osaka Prefecture University, 1-1Gakuen-cho, Naka-ku, Sakai 599-8531, Japan

e-mail: akita@pe.osakafu-u.ac.jp

the interaction forces induced in nanoscale such as single-electron phenomena. The resonator miniaturization is crucial in bringing highly sensitive detection into practice. Therefore, nanoscale mechanical resonators consisting from CNTs are widely studied as highly sensitive mass and force sensors. In this section, we will focus on the mass or force sensing application of CNTs due to limited number of pages.

14.1 Suspended Resonators

For the mass sensor application of CNTs, we have to detect the mechanical motion of resonating CNTs. The electron beam in the electron microscope has been used to detect the mechanical motion of CNT resonators [10–13, 18]. In this case, only the envelope of the vibrating CNTs was measured to extract the frequency response of the vibration amplitude. The phase difference between the actuation signal and the CNT vibration is very crucial for understanding the vibrating system.

CNT resonators with doubly suspended geometries have been also widely characterized electrically by detecting the drain current through CNT channels based on field effect transistors (FETs) as shown in Fig. 14.1 [19–22]. This detection method has a strong advantage to detect the vibration of CNTs with high frequency because of electrical down-mixing method, which enables us to detect the vibration and the phase difference of CNTs at arbitrary frequency with high accuracy. The vibration of a CNT-FET channel results in the change in gate capacitance δC_g between a gate and the CNT channel, leading to the change in drain current through a CNT channel, which can be measured by a lock-in amplifier. To actuate the suspended CNT, the gate bias $V_g(f) = (V_g^{\text{DC}} + \delta V_g \cos 2\pi f t)$ modulated with a frequency f is applied, while the source–drain bias $V_d(f) = \delta V_d \cos 2\pi (f + \Delta f) t$ is also modulated with small amplitude with a frequency $f + \Delta f$, which is slightly different from the actuation frequency. For simplicity, we assumed that the change in the gate capacitance also follows only the gate voltage change as expressed by

$$C_g(f) = (C_g^{\text{DC}} + \delta C_g \cos 2\pi f t). \quad (14.1)$$

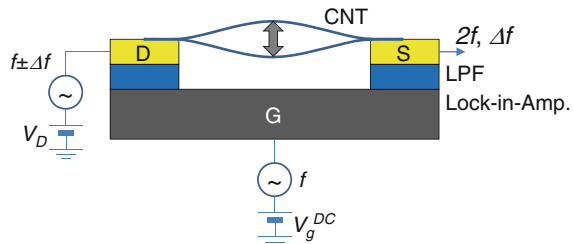


Fig. 14.1 Schematic illustration of doubly suspended CNT resonator with the down-mixing readout

Since the drain current I_d is proportional to the product of $C_g V_g V_d$, we have a relation expressed as

$$I_d \propto C_g^{\text{DC}} V_g^{\text{DC}} \delta V_d \cos 2\pi (f + \delta f) t + \delta V_d \left(C_g^{\text{DC}} \delta V_g + \delta C_g V_g^{\text{DC}} \right) (\cos 4\pi f t + \cos 2\pi \Delta f t), \quad (14.2)$$

where the highest order of $\delta C_g \delta V_g \delta V_d$ was omitted. The 2nd term corresponds to the mixed-frequency term consisting of $2f$ and Δf and includes the δC_g dependence. It should be noted that the δC_g is only induced by the vibration of the suspended CNT. Thus, the magnitude of the Δf component of the drain current corresponds to the vibration amplitude of the suspended CNT. Using the lock-in amplifier, only the Δf component of the drain current can be extracted. Thus, we can measure the frequency response of the CNT vibration including the phase difference through the down-mixed drain current with the arbitrarily frequency Δf . This technique is now widely used for detecting the nanoscale mechanical resonator including graphene resonators.

The tension of the suspended CNT channel can be modified electrostatically by changing the DC component of V_g^{DC} . Figure 14.2 shows 3D map of the down-mixed drain current taken under the sweep of V_g^{DC} and f [19]. As shown in Fig. 14.2, the resonant frequency of the suspended CNT increases with V_g^{DC} as a result of the increase of the tension. For the mass measurement, the mass of the mechanical spring is one of the important factors to determine the mass resolution related to

$$m \approx m_{\text{CNT}} \delta f / f_0, \quad (14.3)$$

where m , m_{CNT} , and δf are an attached mass, mass of CNT, and the frequency shift induced by the attachment of the added mass. For instance, the mass CNT for 1.3 nm

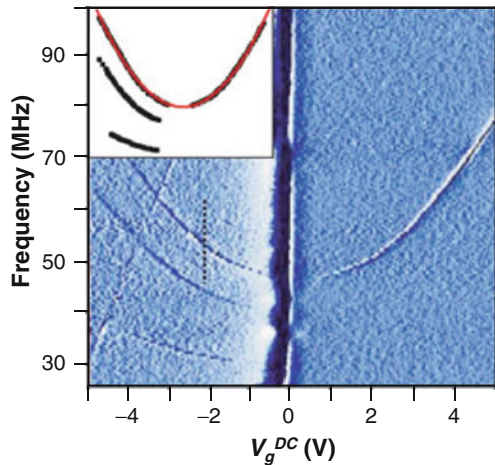


Fig. 14.2 3D map of the down-mixed signal corresponding to the amplitude of a doubly clamped CNT resonator taken under the sweep of actuation frequency f and DC component of gate voltage V_g^{DC} (Adopted from Sazonova et al. [19] with permission)

diameter and 500 nm long is only about 1.6 ag, so that the extreme mass and force sensitivity corresponding to the single atom can be achieved by using single-wall CNT resonators. This high sensitivity is also applicable to detect the very weak force interaction such as electrostatic force induced by single-electron tunneling [23, 24]. Recently, it has reported that the highly sensitive detection which can measure the thermal vibration of CNT resonators down to cryogenic temperatures has been realized by using cross-correlated electrical noise measurements [25]. In this case, the detectable force has reached to $10 \text{ zN Hz}^{-1/2}$ at 1.2 K.

14.2 Cantilever Resonator

As mentioned in previous subsection, the signal readout of the suspended resonator is electrical readout, so that this kind of device can only work in vacuum or air. The extraordinary sensitivity was achieved only in the condition under a cryogenic temperature and ultrahigh vacuum [25, 26]. In air, the collision of gas molecules to the CNT resonator which is very lightweight may perturb the stable operation. Furthermore, the mass measurements for biomolecules are preferable in liquid condition. To overcome this problem, the other technique to detect the CNT motion should be required such as an optical detection method. The scattered light from tiny objects with the size less than optical diffraction limits can be detected, so that the motion of the object can be detected by the fluctuation of the scattered light. In this case, however, conventional optical detection method is hard to apply to single-wall CNTs because of their size limitation. Recently, we have measured successfully the resonant properties of multiwall CNTs (10–70 nm in diameter) in air [27, 28] or liquid [29] by using an optical detection method toward the biological applications. In this subsection, we focus on the cantilever resonators consisting of multiwall CNTs.

Multiwall CNTs examined in this study were synthesized by chemical vapor deposition (CVD) with post-annealing treatment at temperatures higher than $1,500 \text{ }^\circ\text{C}$. The G/D ratio of the Raman spectrum after the post-annealing treatment is greater than 10. Therefore, the CNTs synthesized by CVD after the post-annealing treatment have a highly graphitized structure and a less amorphous carbon layer. The CNTs were aligned on the edge of a Si chip by an AC electrophoresis technique [30] to produce a CNT cantilever array. Note that the edge of the Si chip was inversely tapered to eliminate the background signal.

First, we have evaluated the resonant property of multiwall CNTs in vacuum by using a scanning electron microscope (SEM) in order to clarify the energy loss mechanism of multiwall CNTs. It should be noted that the Q factor obtained from the resonant property indicates the sharpness of the resonant and corresponds to the inverse of the internal mechanical loss of the resonating system. The Q factors for several arc-produced CNTs measured in a scanning electron microscope (SEM) were varied in the range of 300–2000 with a center of $\sim 1,000$. The Q factors and Young's moduli for the CVD-synthesized nanotubes are respectively lower than

Fig. 14.3 CNT diameter dependence of Q^{-1} corresponding to the mechanical loss factor of the resonating system

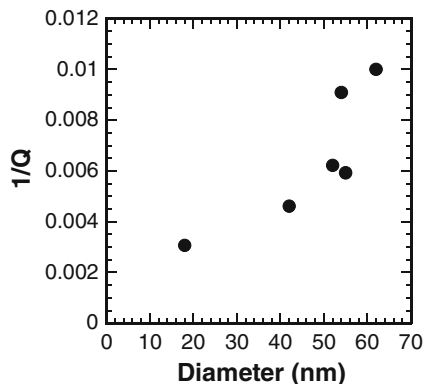
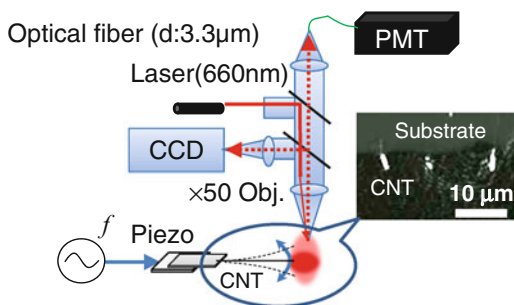


Fig. 14.4 Schematic diagram of simple optical detection for CNT cantilever



200 and lower than 0.3 TPa, which are smaller than those for the arc-produced nanotubes. We have found that the Q factor strongly correlated to the CNT diameter as shown in Fig. 14.3, although the nanotube maintains high mechanical strength around 0.5 TPa [18]. This fact implies that the vibration energy is dissipated mainly not by defects but by van der Waals interactions between walls in multiwall CNT. Although the thinner CNTs show higher Q factors, the lower scattering cross section of the light for thinner CNTs results in a lower signal-to-noise (S/N) ratio in the optical detection. In present, CNTs with diameters around 50 nm give a highest sensitivity in our experimental setup.

Figure 14.4 shows the schematic diagram of the experimental setup for the optical detection [27, 28]. The CNT cantilever array was set on a piezo oscillator and then oscillated mechanically by applying an AC voltage to the piezo oscillator. Individually protruded CNTs are clearly observed under the dark-field illumination mode as shown in an inset of Fig. 14.4. In this image, the shortest protrusion of the nanotube is 2 μm in length. A laser with a wavelength of 660 nm was irradiated to probe the vibration of CNTs, where the laser (spot size $< 2 \mu\text{m}$) power is limited less than 30 μW to eliminate the thermal effect. Scattered light from a certain CNT cantilever was collected by an objective lens ($\times 50$, numerical aperture = 0.7) to a CCD or a single-mode optical fiber with a core diameter of 3.3 μm , which acts as an optical aperture, as schematically shown in Fig. 14.4. Figure 14.5a shows

Fig. 14.5 Typical nanotube cantilever: (a) intensity profile across the CNT cantilever shown in (b), (b) optical microscope image at non-resonant, and (c) SEM image

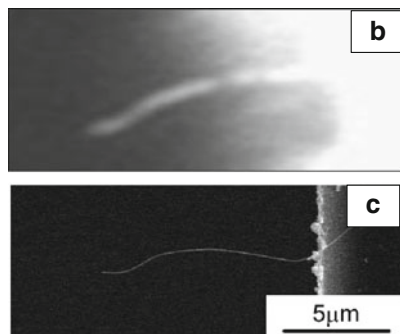
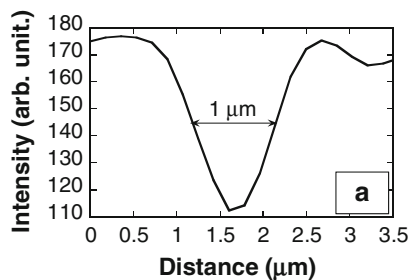
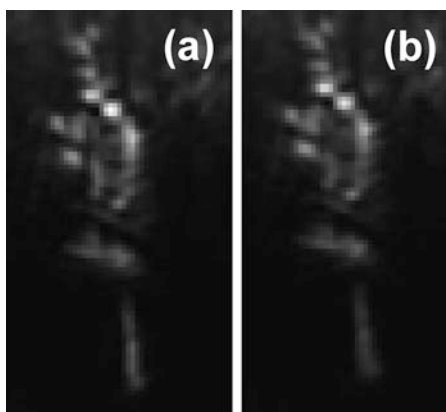


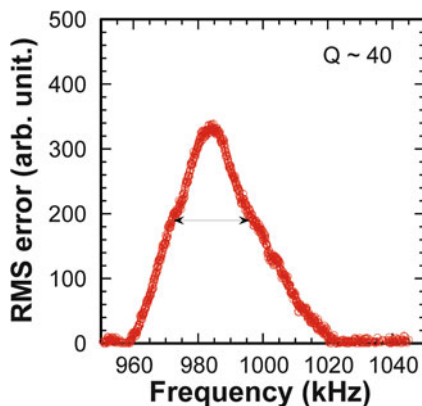
Fig. 14.6 Optical microscope images of (a) a CNT cantilever in off-resonant and (b) in-resonant states in air



an intensity profile across the CNT cantilever shown in Figs. 14.5b, c. Full width at half maximum (FWHM) is $\sim 1 \mu\text{m}$ for the CNT cantilever, which corresponds to the width of $50 \mu\text{m}$ estimated from the magnification of the objective lens at the focal plane on the CCD. Since the effective pixel size of the CCD camera is $\sim 10 \mu\text{m}$, the fluctuation of the scattered light from the CNT is sufficiently detected with sub-micrometer order.

Figure 14.6a, b shows a CNT cantilever in off-resonant and in-resonant states in air, respectively. The width of the tip of the nanotube in the resonant is slightly wider than that in off resonant. Thus, we have succeeded the optical detection of the vibrating CNTs in air. In order to extract the frequency dependence of vibrating

Fig. 14.7 Resonant curve taken in air for the CNT resonator shown in Fig. 14.6

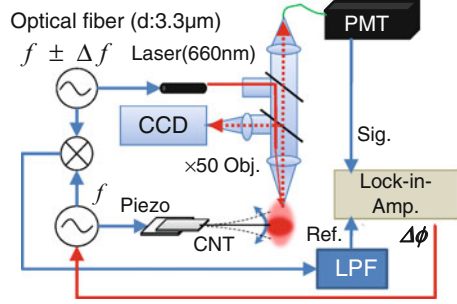


amplitude from the image, an image processing procedure was performed for each excitation frequency as follows. The square of the difference of each pixel brightness between the off resonant and the vibrating image at a certain excitation frequency was summed up for certain area in the optical images, which corresponds to the difference of the area between the areas for the vibrating CNT and the off-resonant CNT. The difference of the areas is roughly proportional to the product of the length and the vibrating amplitude of the nanotube. As a result, the square root of the sum is roughly proportional to the vibrating amplitude for each excitation frequency under the condition of small vibrating amplitude. Figure 14.7 shows the resonant curve for the nanotube resonator shown in Fig. 14.6 obtained by the previous procedure. The resonant frequency and the Q factor for the nanotube resonator are 985 KHz and 40, respectively. From the thermal noise analysis for mechanical resonators, the theoretical limit for the mass sensing using the nanotube resonator becomes sub atto-gram estimated from the resonant frequency and Q factor. Thus, the nanotube resonator acts as highly sensitive mass sensors even in the air. It should be noted that the shorter and thinner nanotube shows higher sensitivity because of lighter weight of resonators.

Instead of image analysis, we have measured the scattered light intensity through the single-mode optical fiber as a pinhole [27]. As shown in Fig. 14.5a, the scattered light intensity depends on the measured position with a certain slope. Initially, the position of the optical fiber entrance was adjusted at the highest slope of the scattered light profile. If the position of the CNT fluctuates, the signal intensity should drastically change because of the tiny core diameter ($\sim 3.3 \mu\text{m}$) of the optical fiber used as an aperture. Thus, we can measure the vibration of the CNT cantilever by measuring the scattered light intensity through the optical fiber.

To improve the S/N ratio, we have developed the so-called opto-mechanical heterodyne technique, which is similar to the electromechanical down-mixing method mentioned before [31]. As shown in Fig. 14.8, the intensity of the laser is modulated with a frequency $f \pm \Delta f$, where Δf is the frequency difference between the oscillation frequency of the CNT and the modulation frequency of the laser light. The intensity of the laser is modulated with a frequency $f \pm \Delta f$, where Δf

Fig. 14.8 Schematic of the experiment setup for *opt-mechanical heterodyne system with phase-locked loop*



is the frequency difference between the oscillation frequency of the CNT and the modulation frequency of the laser light. The time-dependent displacement $x(t)$ of the harmonically oscillating CNT and the modulated laser intensity is, respectively, expressed by

$$x(t) = x_0 \cos(2\pi f t), \quad (14.4)$$

and

$$I(t) = I_0 \cos(2\pi(f \pm \Delta f)t), \quad (14.5)$$

where x_0 is the oscillation amplitude and I_0 the modulation amplitude of the laser. For the certain position x of the tip of the oscillating CNT, the corresponding time t satisfies the condition of

$$2\pi f t = 2\pi n + \delta, \quad (14.6)$$

where n is the integer and δ the phase corresponding to the position x . To obtain the temporal dependence of the scattered light intensity at x , Eq. (14.6) is substituted into Eq. (14.5), and then we have a solution for the temporal dependence as

$$\begin{aligned} I(t) &= I_0 \cos(2\pi n + \delta \pm 2\pi \Delta f t) \\ &= I_0 \cos(\pm 2\pi \Delta f t + \delta). \end{aligned} \quad (14.7)$$

Consequently, the scattered light intensity from the CNT cantilever oscillating with a frequency f can be observed at a frequency of Δf , which is much lower than the resonant frequency of the CNT cantilever. This enables us to utilize measurement devices for low-frequency signals with high S/N ratio such as conventional lock-in amplifiers (LIA). In the case of $\Delta f = 0$, we can observe a “snap shot,” which is very similar to “the stroboscopic photography,” at a certain phase by changing the phase δ as shown in Fig. 14.9.

In order to measure the frequency response, we maintain the frequency difference Δf during the frequency scan. It is noted that we used the lock-in technique to

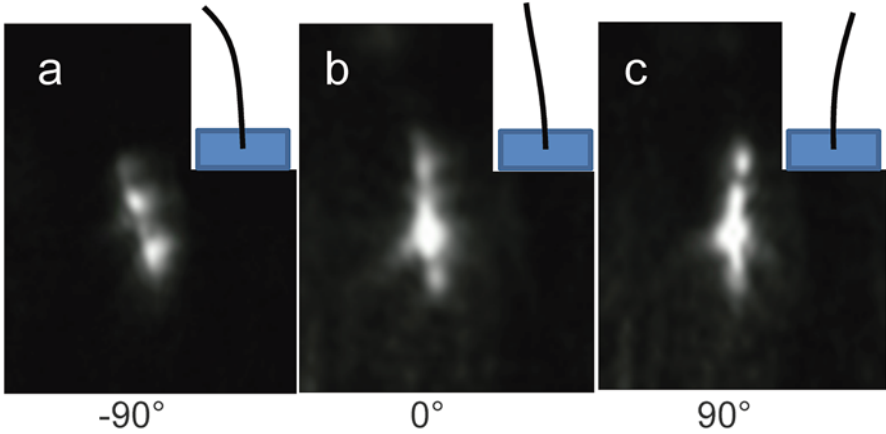
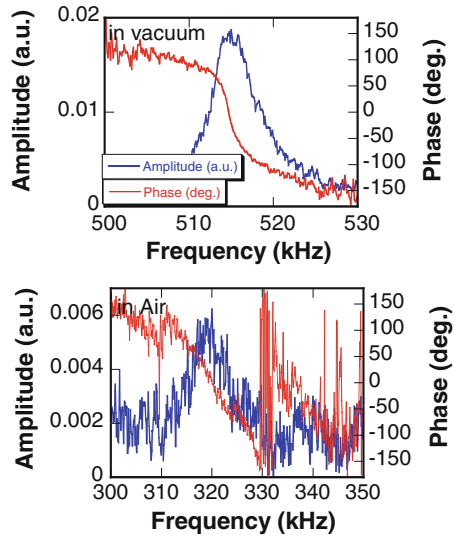


Fig. 14.9 Snap shots of vibrating CNT cantilever: (a) $\delta = -90^\circ$, (b) 0° , and (c) $+90^\circ$

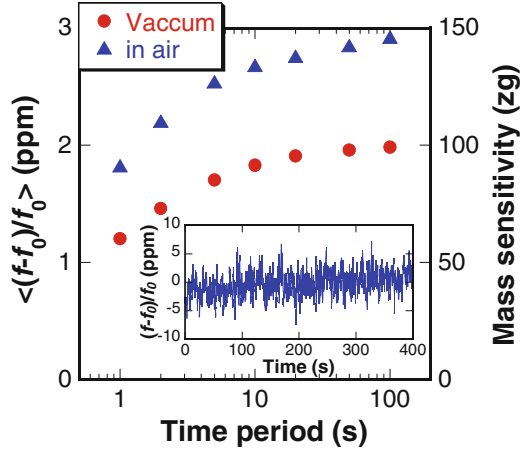
Fig. 14.10 Frequency response curve measured by the *opt-mechanical heterodyne* method: (a) in vacuum around 10^{-3} Pa and (b) in air



improve the signal-to-noise ratio, where the reference signal Δf was taken from the frequency difference between two signal generators as shown in Fig. 14.8. In this setup, we can measure not only the amplitude of the vibration but also the phase change between the vibrating CNT and the applying AC voltage to vibrate the piezo-oscillator. The detected phase difference was entered to a voltage-controlled oscillator (VCO) to obtain the sustained oscillation of the CNT cantilever by the PLL. In this experiment, the Δf and time constant were typically set to be 1 kHz and 300 ms, respectively.

Figures 14.10a, b show the frequency responses of amplitude and phase measured by the heterodyne detection system in vacuum and air, respectively. When the

Fig. 14.11 Time period dependence of the standard deviation of resonant frequency fluctuations $\langle (f - f_0) / f_0 \rangle$ for both conditions of vacuum and air. Inset shows the fluctuation of resonant frequency measured by PLL in vacuum



oscillator is driven through resonance, a sharp change occurs in both the amplitude and the phase. The fundamental resonances in vacuum ($\sim 10^{-3}$ Pa) and in air are respectively observed at ~ 515 and ~ 320 kHz, and the corresponding Q factors for each condition are 130 and 32, respectively. Thus, we have successfully measured both of the amplitude and the phase using the *opto-mechanical heterodyne technique* even in air.

To utilize the CNT oscillator for the mass measurement, the mass resolution should be considered based on the frequency fluctuation. Figure 14.11 shows the time period dependence of the standard deviation of resonant frequency fluctuations $\langle (f - f_0) / f_0 \rangle$ for vacuum and air. The relation between the frequency shift, δf , and an added mass, m , at the tip of the CNT cantilever is given by $m \cong m_0 \delta f / 2f_0$ under an assumption of $m \ll m_0$ which is also plotted, where m_0 is the mass of the CNT cantilever itself. The expected minimal mass resolution estimated from the frequency fluctuation for the CNT cantilever with $m_0 = 10^{-13}$ g is also plotted in Fig. 14.11. The mass sensitivity less than 100 zg is easily achieved in vacuum for long-term (~ 100 s) deviation and even in air for short-term (~ 1 s) deviation.

The minimum detectable force gradient, dF/dx , is crucial for the force-sensing application, where F is the force acting on the CNT cantilever at position x . In the case of the frequency shift detection method, dF/dx is approximately determined by $dF/dx \cong 2k\delta f/f$, where k is the spring constant of the CNT cantilever and δf the frequency shift induced by dF/dx [32]. As mentioned above, the noise limit of the detectable $\delta f/f$ for our experimental setup is around $1 \sim 2$ ppm, so that the minimum detectable force gradient is estimated to be $\sim 10^{-10}$ N/m. It is noted that the minimum detectable force gradient of the conventional atomic force microscopy is typically on the order of $10^{-4} \sim 10^{-5}$ N/m at room temperature [33]. Thus, the CNT cantilever with the PLL detection is successfully achieved with very high sensitivity.

Although there are several origins to limit the detectable sensitivity, thermal vibration of the cantilever limits the minimum detectable sensitivity, dF/dx , determined as

$$dF/dx|_{\min} = \sqrt{4kk_B TB/2\pi fQ \langle x_0^2 \rangle}, \quad (14.8)$$

where k_B is the Boltzmann constant, T the temperature, B the band width of the system, and Q the quality factor of the cantilever [34]. To improve the sensitivity, lower k and higher f are appropriate corresponding to high aspect ratio and lightweight. Thus, the CNT is appropriate for the application of the force detection. The force sensitivity limited by the thermal vibration is estimated to be $\sim 10^{-10}$ N/m, where $k \sim 10^{-4}$ N/m, $f \sim 500$ kHz, $Q \sim 150$, $B \sim 3$ Hz, and $x_0 \sim 100$ nm were used. Thus, the detectable force gradient estimated from the fluctuation is comparable to the thermal noise limit.

This highly sensitive mechanical resonator is applicable to the highly sensitive calorimeter if the different kind of material is deposited on the CNT cantilever, namely, bi-material system. In this system, thermal expansion coefficients for each material are different, so that the thermal stress should be induced on the mechanical resonator resulting in the frequency shift of the resonator. It should be noted that the size of the resonator consisting of the CNTs is very small, so that the heat capacity of this system is also very small. This small heat capacity enables us to measure the minute heat in the order of 100 aJ/K [35].

14.3 Summary

In this subsection, highly sensitive mass and force detections using CNT mechanical resonators have been described as one of applications of CNT nano-electromechanical devices. The down-mixing method for detecting the resonant frequencies of CNT mechanical resonators is one of key techniques to achieve the extremely high sensitivity. The doubly clamped CNT resonators consisting of single-wall CNTs achieved the sensitivity with ~ 10 zN Hz^{-1/2} at 1.2 K in ultrahigh vacuum by the combination of the single-electron tunneling detection and cross-correlated electrical noise measurements. For atmospheric conditions, the optical detection method with the opt-mechanical heterodyne offers high mass sensitivity with ~ 100 zg. Furthermore, the optical detection was applicable for the measurement in viscous fluid such as water. We believe that this extraordinarily high sensitivity offers new possibilities for the investigation of a wide range of materials, especially nanoscale materials.

References

1. Kim P, Lieber CM (1999) Nanotube nanotweezers. *Science* 286:2148–2150
2. Akita S, Nakayama Y, Mizooka S, Takano Y, Okawa T, Miyatake Y, Yamanaka S, Tsuji M, Nosaka T (2001) Nanotweezers consisting of carbon nanotubes operating in an atomic force microscope. *Appl Phys Lett* 79:1691–1693

3. Cha SN, Jang JE, Choi Y, Amaratunga GAJ, Kang DJ, Hasko DG, Jung JE, Kim JM (2005) Fabrication of a nanoelectromechanical switch using a suspended carbon nanotube. *Appl Phys Lett* 86:083105
4. Jang JE, Cha SN, Choi Y, Amaratunga GAJ, Kang DJ, Hasko DG, Jung JE, Kim JM (2005) Nanoelectromechanical switches with vertically aligned carbon nanotubes. *Appl Phys Lett* 87:163114
5. Jang JE, Cha SN, Choi YJ, Kang DJ, Butler TP, Hasko DG, Jung JE, Kim JM, Amaratunga GA (2008) Nanoscale memory cell based on a nanoelectromechanical switched capacitor. *Nat Nanotechnol* 3:26–30
6. Kaul AB, Wong EW, Epp L, Hunt BD (2006) Electromechanical carbon nanotube switches for high-frequency applications. *Nano Lett* 6:942–947
7. Kinaret JM, Nord T, Viefers S (2003) A carbon-nanotube-based nanorelay. *Appl Phys Lett* 82:1287–1289
8. Lee SW, Lee DS, Morjan RE, Jhang SH, Sveningsson M, Nerushev OA, Park YW, Campbell EEB (2004) A three-terminal carbon nanorelay. *Nano Lett* 4:2027–2030
9. Loh OY, Espinosa HD (2012) Nanoelectromechanical contact switches. *Nat Nanotechnol* 7:283–295
10. Poncharal P, Wang ZL, Ugarte D, de Heer WA (1999) Electrostatic deflections and electromechanical resonances of carbon nanotubes. *Science* 283:1513–1516
11. Nishio M, Sawaya S, Akita S, Nakayama Y (2005) Carbon nanotube oscillators toward zeptogram detection. *Appl Phys Lett* 86:133111
12. Nishio M, Sawaya S, Akita S, Nakayama Y (2005) Density of electron-beam-induced amorphous carbon deposits. *J Vac Sci Technol B* 23:1975–1979
13. Sawaya S, Akita S, Nakayama Y (2006) In situ mass measurement of electron-beam-induced nanometer-sized W-related deposits using a carbon nanotube cantilever. *Appl Phys Lett* 89:193115
14. Jensen K, Kim K, Zettl A (2008) An atomic-resolution nanomechanical mass sensor. *Nat Nanotechnol* 3:533–537
15. Treacy MMJ, Ebbesen TW, Gibson JM (1996) Exceptionally high Young's modulus observed for individual carbon nanotubes. *Nature* 381:678–680
16. Wong EW, Sheehan PE, Lieber CM (1997) Nanobeam mechanics: Elasticity, strength, and toughness of nanorods and nanotubes. *Science* 277:1971–1975
17. Akita S, Nishijima H, Nakayama Y, Tokumasu F, Takeyasu K (1999) Carbon nanotube tips for a scanning probe microscope: their fabrication and properties. *J Phys D Appl Phys* 32:1044–1048
18. Sawaya S, Arie T, Akita S (2011) Diameter-dependent dissipation of vibration energy of cantilevered multiwall carbon nanotubes. *Nanotechnology* 22:165702
19. Sazonova V, Yaish Y, Ustunel H, Roundy D, Arias TA, McEuen PL (2004) A tunable carbon nanotube electromechanical oscillator. *Nature* 431:284–287
20. Peng HB, Chang CW, Aloni S, Yuzvinsky TD, Zettl A (2006) Ultrahigh frequency nanotube resonators. *Phys Rev Lett* 97:087203
21. Witkamp B, Poot M, Pathangi H, Huttel AK, van der Zant HSJ (2008) Self-detecting gate-tunable nanotube paddle resonators. *Appl Phys Lett* 93:111909
22. Wu CC, Zhong ZH (2011) Capacitive spring softening in single-walled carbon nanotube nanoelectromechanical resonators. *Nano Lett* 11:1448–1451
23. Steele GA, Huttel AK, Witkamp B, Poot M, Meerwaldt HB, Kouwenhoven LP, van der Zant HSJ (2009) Strong coupling between single-electron tunneling and nanomechanical motion. *Science* 325:1103–1107
24. Lassagne B, Tarakanov Y, Kinaret J, Garcia-Sanchez D, Bachtold A (2009) Coupling mechanics to charge transport in carbon nanotube mechanical resonators. *Science* 325:1107–1110
25. Moser J, Guttinger J, Eichler A, Esplandi MJ, Liu DE, Dykman MI, Bachtold A (2013) Ultra-sensitive force detection with a nanotube mechanical resonator. *Nat Nanotechnol* 8:493–496
26. Chaste J, Eichler A, Moser J, Ceballos G, Rurali R, Bachtold A (2012) A nanomechanical mass sensor with yoctogram resolution. *Nat Nanotechnol* 7:300–303

27. Fukami S, Arie T, Akita S (2009) Effect of gaseous dissipation of oscillating cantilevered carbon nanotubes. *Jpn J Appl Phys* 48:06FG04
28. Akita S, Arie T (2009) Carbon nanotube mechanical resonators for mass sensing. *Sensor Mater* 21:339–349
29. Sawano S, Arie T, Akita S (2010) Carbon nanotube resonator in liquid. *Nano Lett* 10:3395–3398
30. Yamamoto K, Akita S, Nakayama Y (1998) Orientation and purification of carbon nanotubes using ac electrophoresis. *J Phys D Appl Phys* 31:L34–L36
31. Yoshinaka A, Arie T, Akita S (2011) Sustained mechanical self-oscillation of carbon nanotube cantilever by phase locked loop with optomechanical heterodyne. *Appl Phys Lett* 98:133103
32. Garcia R, Perez R (2002) Dynamic atomic force microscopy methods. *Surf Sci Rep* 47:197–301
33. Wiesendanger R (1994) *Scanning probe microscopy and spectroscopy*. Cambridge University Press, Cambridge
34. Albrecht TR, Grutter P, Home D, Rugar D (1991) Frequency-modulation detection using high-Q cantilevers for enhanced force microscope sensitivity. *J Appl Phys* 69:668–673
35. Hiroshima S, Yoshinaka A, Arie T, Akita S (2013) Photothermal actuation of cantilevered multiwall carbon nanotubes with bimaterial configuration toward calorimeter. *Jpn J Appl Phys* 52:06GH02

Chapter 15

Carbon Nanotube Quantum Nanomemory

Takafumi Kamimura, Yasuhide Ohno, Kenzo Maehashi,
and Kazuhiko Matsumoto

Abstract Single-charge memory operated at room temperature was fabricated with single-walled carbon nanotube (SWNT) transistor surrounded by $\text{SiN}_x/\text{Al}_2\text{O}_3$ double-gate insulator layers, which demonstrates discrete hysteresis characteristics by single-hole transfers. The present memory has the short top gate length of 10 nm fabricated by a self-assemble process which contributes to the room temperature operation. Owing to the strong concentrated electric field due to the top gate electrode which surrounds the SWNT channel with small diameter of 1 nm, Fowler-Nordheim tunneling becomes easy to occur, and the device achieved writing voltage of as small as 0.16 V, which is more than 100 times smaller than the present conventional planer-type flash memory.

Keywords Single charge • Multilevel • Quantum dot • Hysteresis

15.1 Single-Charge Memory Operated at Room Temperature

15.1.1 Introduction

Flash memory has been the leading player in the nonvolatile memories in recent 10 years because of a small cell size and a high scalability. A gate length of a

T. Kamimura (✉)

Institute of Scientific and Industrial Research, Osaka University, Mihogaoka 8-1,
Ibaraki, Osaka 567-0047, Japan

Advanced ICT Research Institute, National Institute of Information and Communications
Technology, 4-2-1 Nukui-Kitamachi, Koganei, Tokyo 184-8795, Japan

e-mail: Kamimura@nict.go.jp

Y. Ohno • K. Matsumoto

Institute of Scientific and Industrial Research, Osaka University, Mihogaoka 8-1,
Ibaraki, Osaka 567-0047, Japan

e-mail: ohno@sanken.osaka-u.ac.jp; k-matsumoto@sanken.osaka-u.ac.jp

K. Maehashi

Tokyo University of Agriculture and Technology, Tokyo, Japan

e-mail: maehashi@cc.tuat.ac.jp

flash memory has reached to 20 nm. A number of charges also have been getting smaller, e.g., a several hundred in the 20 nm device. However, a flash memory needs high operating voltage for short write time. The high operating voltage causes low durability, and also a signal crossing due to the capacitance coupling between neighbor cells becomes larger with further miniaturization [1]. Therefore, lower operating voltage and stronger capacitive coupling between a gate electrode and a charge storage compared to neighbor cells are desired.

A single-walled carbon nanotube (SWNT) is a cylindrical structure with a diameter of about 1 nm. An SWNT with a semiconductor property is very sensitive to the charge sit around the SWNT, because whole SWNT channel can be easily modulated by the surrounded charge because of the small diameter of an SWNT. This high sensitivity can sense even a single charge [2, 3]. Therefore, many sensor applications of SWNT have been reported, e.g., biosensors and gas sensors [4–8]. Moreover, a cylindrical-type memory can achieve higher electric field concentration compared to a planer-type memory because of higher capacitive coupling between charge storage and a gate electrode. Therefore, the signal noise attributed to the parasitic capacitances between neighbor cells can be reduced by this higher capacitive coupling. In this paper, single-charge memory operated at room temperature was fabricated with an SWNT channel surrounded by $\text{SiN}_x/\text{Al}_2\text{O}_3$ double-gate insulator layers, demonstrating multilevel memory state.

15.1.2 Sample Preparations

The fabrication process of the single-charge memory is shown in Fig. 15.1. An SWNT was grown by the chemical vapor deposition process on the SiO_2 substrate, and the source and drain electrodes were formed on the SWNT, where a distance between the electrodes was 70 nm. The SiO_2 under the SWNT was etched off by chemical wet process, and the SWNT bridge was formed between source and drain electrodes as shown in Fig. 15.1a. Then, the SWNT was surrounded by double layers of SiN_x of 27 nm over Al_2O_3 of 3 nm using atomic layer deposition (ALD) process (FlexAL, Oxford Inst.) using tris(dimethylamino)silane for SiN_x and trimethylaluminum for Al_2O_3 as a precursor as shown in Fig. 15.1b. Figure 15.1c–g shows scanning electron microscope (SEM) images of a device after an ALD process. Owing to thin insulator layers and high acceleration energy of SEM, the insulator layers can be seen through and the difference of the materials are recognized because of the difference of the contrast as shown in Fig. 15.1c–g. Figure 15.1c, d shows the top view and bird's-eye view of the device near the gap. The gap of 10 nm length is realized between the source and drain electrode. Figure 15.1e shows the cross-sectional view around the drain electrode indicated by dashed rectangle in Fig. 15.1b. The drain electrode is fully covered by the insulator layers, and the space under the channel can be seen. Figure 15.1f–g shows the side view and cross-sectional view of the SWNT surrounded by the insulator layer of 30 nm thick in which the SWNT is seen as a light-gray line at the center of the

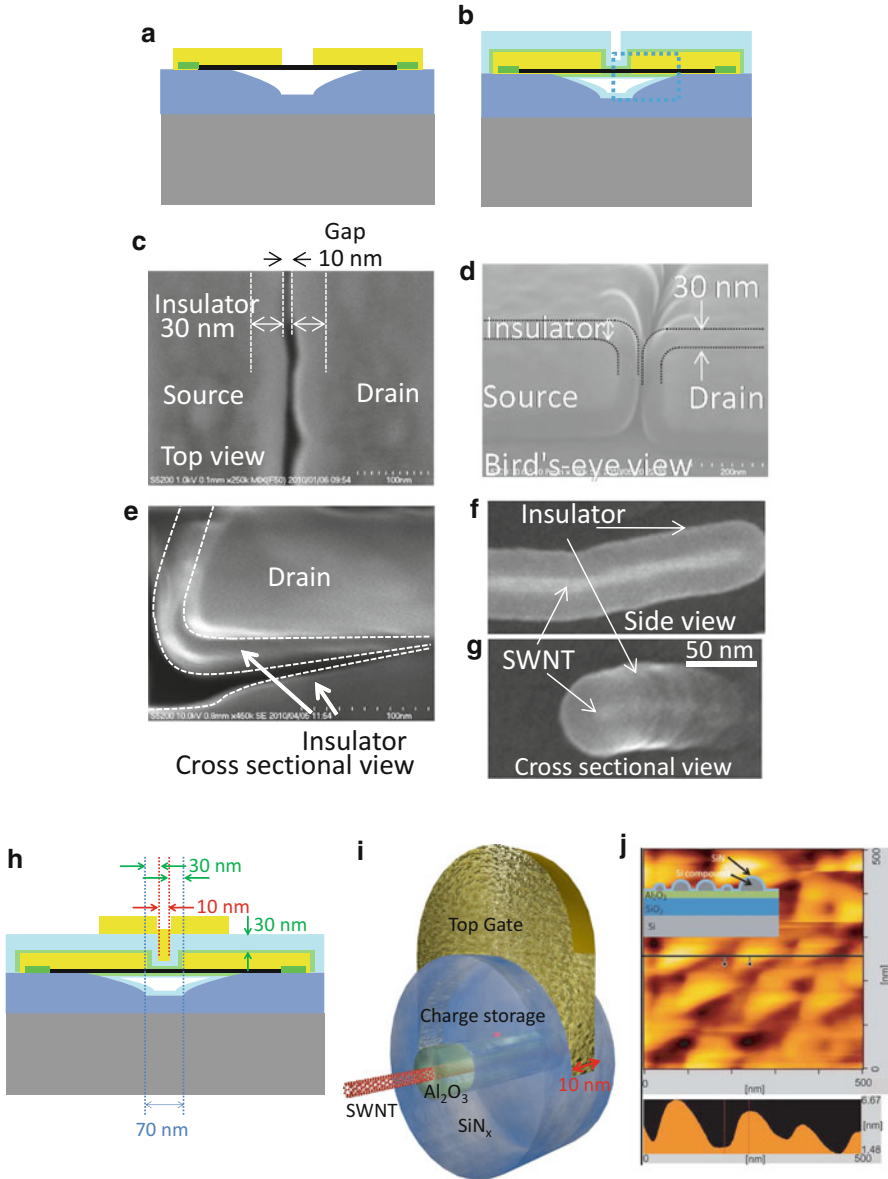


Fig. 15.1 The device fabrication process. (a) Schematic of the device after the SiO_2 etching, which is the cross-sectional view along with the SWNT. (b) Schematic of the device after the ALD process, which is the cross-sectional view along with the SWNT. Scanning electron microscope images of (c) top view, (d) bird's-eye view, and (e) cross-sectional view around the drain electrode. (f) Side view and (g) cross-sectional view of the SWNT surrounded by the insulator layer. (h) Schematic of the device after the top gate electrode fabrication, which is the cross-sectional view along with the SWNT. (i) Three-dimensional schematic around the top gate electrode. (j) AFM image of the charge storage dot formed on the planer substrate

insulator. Figure 15.1h is the schematic cross-sectional view of the device after the formation of the top gate electrode.

Using an isotropic deposition of the ALD process, the 10 nm length of top gate electrode is realized self-assembly as shown in Fig. 15.1h. The 30 nm thick insulator layer was deposited from the source and drain electrode which narrowed a gap between the electrodes from 70 to 10 nm by the isotropic ALD deposition. Ti and Au were deposited through this gap to form a top gate electrode. Thus, the 10 nm long top gate electrode was self-assembly formed at a center of the source and drain electrode which is covered by the ALD insulator layers. The three-dimensional schematic structure around the top gate electrode is shown in Fig. 15.1i, where the source electrode, drain electrode, and substrate are omitted for easy viewing.

The SiN_x deposition by ALD enables to form the composite of nanoparticles of Si, N, and C at the beginning of the deposition because of the low uniformity and the incomplete reaction. The composite of nanoparticles acts as a dot for the charge storage. The dots formed on the planar 3 nm Al₂O₃ layer measured by atomic force microscope (AFM) are shown in Fig. 15.1j as a reference. The upper inset is schematic of the cross section of the sample, and lower inset is cross-sectional profile of the transverse line in AFM image. The heights of the dots are several nanometers as shown in Fig. 15.1j. The size in a transverse direction seems several tens of nanometers. This is much larger than the height because of the limit of the AFM resolution for neighboring same-size dot.

The density of the charge storage dots D between the Al₂O₃ layer and the SiN_x layer was estimated to be $D = 1 \times 10^{12} \text{ cm}^{-2}$ from conventional capacitance-voltage measurement. The area just under the top gate electrode was 91.4 nm² from πrL , where r is the thickness of the Al₂O₃ layer of 3 nm and L is the length of a top gate electrode of 10 nm. Then the estimated number of charge storage dots can be calculated using $D\pi rL$ and is 0.914. This estimation means almost one charge storage dot exists in the area just under a top gate electrode as shown in Fig. 15.1i.

15.1.3 Experimental Results and Discussions

Figure 15.2a–c shows the electric field intensity simulated by the finite element method and corresponding device structures. Figure 15.2a shows the distribution of the electric field along with the carbon nanotube channel between source and drain electrode which is indicated by dashed square in the schematic structure. The gate bias of 1 V and the drain and source biases of –25 mV and +25 mV were applied. From this figure, the top gate bias is found to affect locally only around the SWNT channel and the insulator just under the top gate electrode. Figure 15.2b is the strength of the electric field along the cross section of A–A' line just under the top gate electrode which is indicated in the schematic structure of Fig. 15.2a. The simulated electric field reaches as high as 0.92 MV/cm near the SWNT channel which is high enough for charge to tunnel through the barrier by Fowler-Nordheim tunneling. Figure 15.2c shows the electric field distribution at the cross section of

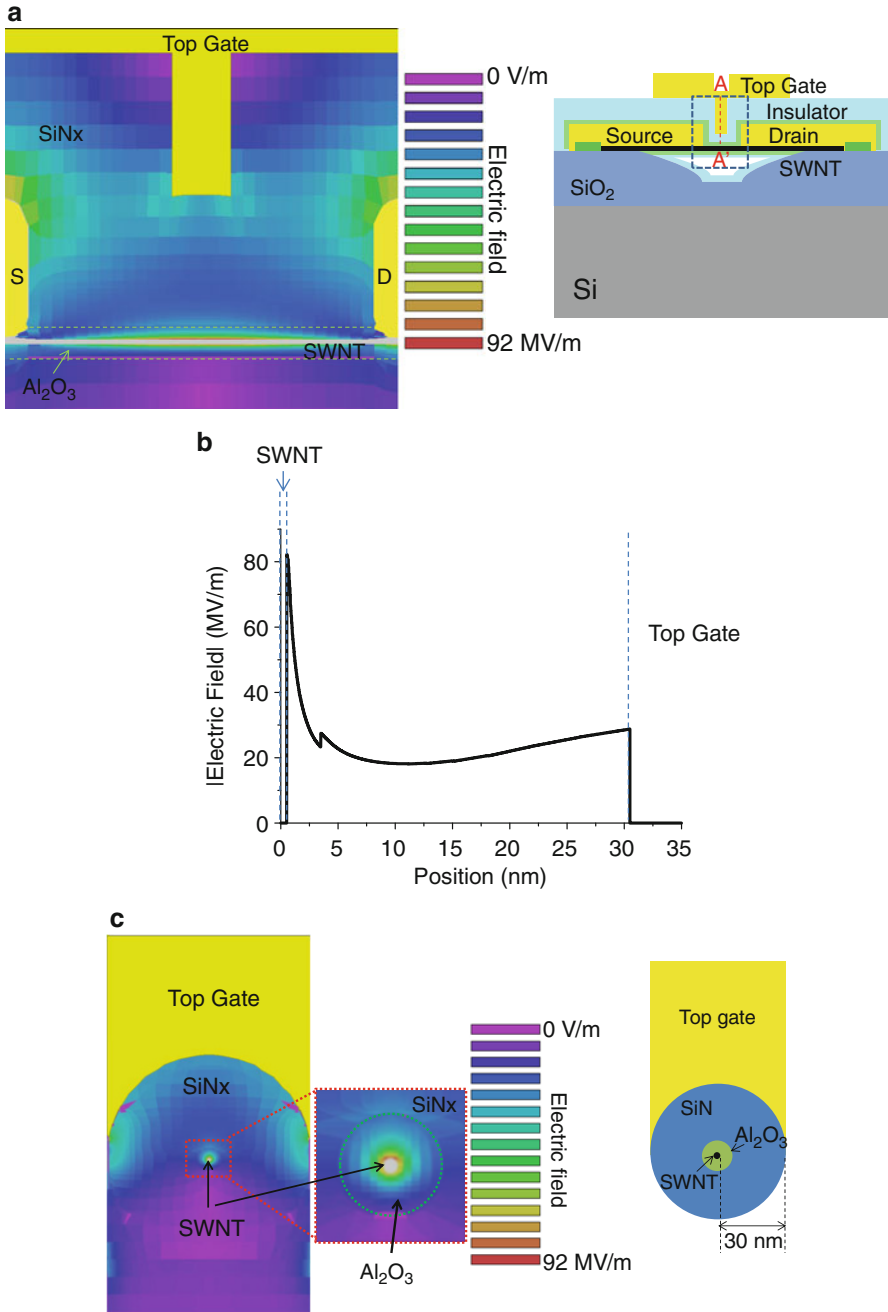


Fig. 15.2 (a) Calculated electric field by finite element method with corresponding cross-sectional view of the device in y - z plane. (b) Calculated electric field by finite element method with corresponding cross-sectional view of the device in x - z plane. (c) Calculated cross-sectional electric field plot at A-A' line in (a)

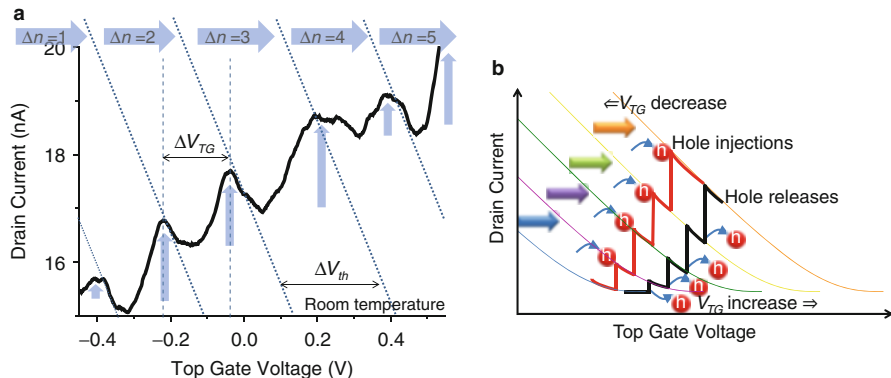


Fig. 15.3 (a) Drain current characteristic as a function of applied top gate voltage at room temperature. (b) Schematic of the drain current characteristics as a function of hole gate voltage

A–A' line in Fig. 15.2a. In the figure, the SWNT is surrounded by the concentric layers of the Al_2O_3 and the SiN_x . Though the top gate electrode covered only the upper half of the concentric insulator layers as shown in the schematic structure of Fig. 15.2c, the electric field intensity reaches high enough all around the SWNT as shown in the enlarged figure of Fig. 15.2c indicated by dashed square. This is because the ratio between the perimeter of the top gate electrode and the SWNT is as large as 60:1. Owing to this high electric field concentration effect at all around SWNT, the charge in the SWNT can be easily injected to the $\text{Al}_2\text{O}_3/\text{SiN}_x$ interface even at the low applied gate bias, which stays there and works as the memory effect.

Figure 15.3a shows drain current characteristic as a function of the applied top gate voltage at room temperature. The source and drain voltage were set at -25 mV and 25 mV, respectively. The drain current showed the repeated threshold voltage shift characteristic indicated by right arrows. The drain current increased drastically indicated by up arrows and decreases gradually following the tangential dashed lines, repeatedly with the increase of the applied top gate voltage. The threshold voltage shift ΔV_{th} was $\Delta V_{th} = 0.256$ V. The holes had been accumulated in the charge storage dot by the negative gate voltage. At the beginning of the measurement and the period of the threshold shifts, ΔV_{TG} was $\Delta V_{TG} = 0.177$ V. By increasing the applied top gate voltage in the positive direction, the hole started to transfer from the charge storage dot to the SWNT channel. At this moment, the potential of the charge storage dot decreased and blocked the transfer of other holes, i.e., Coulomb blockade effect. Therefore, the hole could transfer one by one, where each transfer was separated by Coulomb blockade effect. The potential decrease of the charge storage dot also impacted the potential of SWNT channel, and the drain current drastically increased because of p-type channel. Therefore, the drastic increases of the drain current in Fig. 15.3a are attributed to a single-hole transfer from the charge storage dot to the SWNT channel. The gradual decreases of the drain current are attributed to the channel modulation by the applied top gate voltage as well as a conventional FET device.

Figure 15.3b shows schematic of the drain current characteristics as a function of gate voltage where the characteristics shift to the right direction with the same intervals as indicated by arrows. The shifts of the drain current represent the threshold voltage shifts caused by the transfer of single holes between the charge storage dot and the SWNT channel. The black bold line represents the trace of the drain current with increase of the gate voltage, i.e., the forward sweep. This is the case observed in Fig. 15.3a. The red bold line represents the case with the decrease of the gate voltage, i.e., the backward sweep. At the gate voltage of single-hole transfer, the drain current drastically increased in forward sweep and decreased in backward sweep. The present SWNT transistor shows p-type property with Ti source and drain electrode [9]. Usually, p-type channel transistor shows the decrease of the drain current with increase of applied gate voltage. In the present device, however, the drain current increases with increase of the applied top gate voltage as shown in Fig. 15.3a even though the SWNT channel is p type. This is because the drain current modulations by the threshold shifts are larger than that by the applied top gate voltage. Therefore, the drain current increases though the applied top gate voltage increases even in p-type channel as shown in Fig. 15.3a, b.

The ΔV_{TG} in Fig. 15.3a is given by $\Delta V_{TG} = e/C_{TG-Dot}$, where e is elementary charge and C_{TG-Dot} is capacitance between the top gate electrode and the charge storage dot [10, 11]. Therefore, C_{TG-Dot} was estimated to be $C_{TG-Dot} = 905$ zF. The radius of the charge storage dot can be roughly estimated by the capacitance between concentric spheres of the gate metal and the charge storage dot, which is $C_{TG-Dot} \approx 4\epsilon_r\epsilon_0 / (1/r_{Dot} + 1/t_{SiNx})$, where r_{Dot} is radius of the charge storage dot and t_{SiNx} is thickness of the SiN_x layer. r_{Dot} is estimated to be 3.9 nm, which was a reasonable value as radius of a nanoparticle. The C_{TG-Dot} was estimated to be 901 zF from the simulation by the finite element method in which the dot of $r_{Dot} = 3.99$ nm was assumed on the 3 nm thick Al_2O_3 . The C_{TG-Dot} obtained from the measurement is in good agreement with the C_{TG-Dot} obtained from the simulation.

Moreover, the discrete threshold shifts in Fig. 15.3a are not a result from the interfacial traps, because the threshold shifts due to the traps must not be equally spaced as the charge will be trapped at the various different locations of the channel [12, 13].

Figure 15.4a, b shows the hysteresis characteristics of the drain current as a function of top gate voltage V_{TG} at room temperature. The round-trip top gate voltage was applied symmetrically around $V_{TG} = 0$ V. The sweep started from negative voltage to positive voltage and after that returned to negative voltage again. The top gate voltage was swept between $V_{TG} = -0.1$ V and $V_{TG} = 0.1$ V in Fig. 15.4a and between $V_{TG} = -0.3$ V and $V_{TG} = 0.3$ V in Fig. 15.4b, respectively. In the forward sweep of Fig. 15.4a, b, as well as in Fig. 15.3a, the threshold voltage shift characteristic could be seen. The threshold shifts occurred one time in Fig. 15.4a and two times in Fig. 15.4b. The number of threshold voltage shifts directly corresponds to the number of transfer holes Δn . Therefore, the number of transfer hole was $\Delta n = 1$ in Fig. 15.4a and $\Delta n = 2$ in Fig. 15.4b. In the backward sweep of Fig. 15.4a, b, the drain current decreased and the threshold voltage shifted to the opposite direction to that of the forward sweep. However, the top

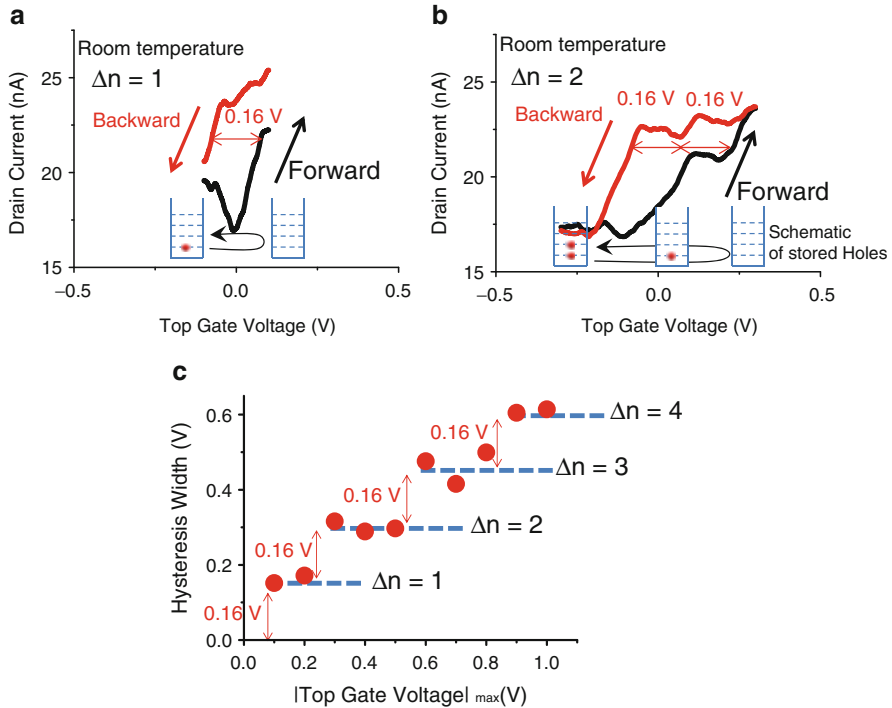


Fig. 15.4 Drain current hysteresis characteristic as a function of round-triply applied top gate voltage in the range of (a) $V_{TG} = |0.1 \text{ V}|$, (b) $V_{TG} = |0.3 \text{ V}|$, at room temperature. Source and drain voltage are set at -25 mV and $+25 \text{ mV}$. (c) Hysteresis width as a function of maximum of round-triply applied top gate voltage

gate voltages which caused the threshold voltage shifts were different between the forward sweep and the backward sweep because of the stored charge both in Fig. 15.4a, b [12]. Therefore, in both plots, the drain current shows hysteresis characteristic. The hysteresis widths ΔV_{TG-hys} were $\Delta V_{TG-hys} = 0.16 \text{ V}$ in Fig. 15.4a and $\Delta V_{TG-hys} = 0.32 \text{ V}$ in Fig. 15.4b, which were also determined by the number of the transferred holes. Therefore, the hysteresis width $\Delta V_{TG-hys} = 0.16 \text{ V}$ and 0.32 V corresponded to $\Delta n = 1$ and $\Delta n = 2$, respectively. In Fig. 15.4a, b, the direction of the hysteresis loops was anticlockwise. This is one of the evidences of the p-type property of the SWNT channel. If the channel property is n type, the hysteresis loop must be clockwise. The jump of the drain current between the forward sweep and backward sweep at the top gate bias of $V_G \sim 0.1 \text{ V}$ in Fig. 15.4a may attribute to the noise in the measurement.

Figure 15.4c shows the hysteresis width characteristic as a function of the maximum value of the applied round-trip top gate voltage at room temperature. The hysteresis width increased discretely with the increase of the maximum value of the applied round-trip top gate voltage. In the plot, the four steps of hysteresis

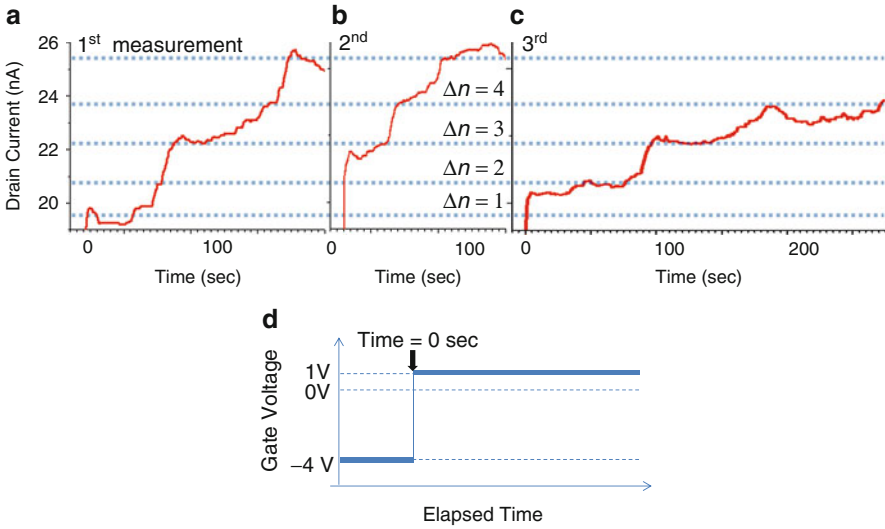


Fig. 15.5 (a)–(c). The time-dependent characteristics of the drain current at room temperature. The top gate voltage of $\Delta V_{\text{TG}} = -4$ V had been applied before the measurements, and $\Delta V_{\text{TG}} = 1$ V was applied in the measurements. Same measurements were repeated three times and plotted in (a)–(c). (d) Schematic of applied top gate voltage as a function of elapsed time

widths were observed in which each discrete increment of the hysteresis width was about $\Delta V_{\text{TG-hys}} = 0.16$ V. This increment of $\Delta V_{\text{TG-hys}} = 0.16$ V was caused by the single-hole transfer. Therefore, the four steps in the hysteresis width attributed to the variation of the number of the transferred single holes. The sweep speed of the top gate voltage for the hysteresis measurement was about 5.5 mV/min. Tunneling probability was low because the thick tunneling barrier consists of Al_2O_3 of 3 nm. Therefore, the slow sweep allowed individual single-hole transfer between the storage dot and the SWNT channel at low applied gate voltage.

Figure 15.5a–c shows the time t dependence of the drain current characteristics at top gate voltage of $V_{\text{TG}} = 1$ V at room temperature in which $V_{\text{TG}} = -4$ V had been applied before $t = 0$ s as shown in Fig. 15.5d. The source and drain voltages were set at 25 mV and -25 mV in the measurement. The measurement was carried out three times, and each measurement was plotted in Fig. 15.5a–c, respectively. The drain currents were plotted in the same time scale; however, time lengths of the measurement were different. The drain current increased with elapsed time and also showed five steps indicated by dotted lines as shown in Fig. 15.5a–c. The increases of the drain current at each step were the same among Fig. 15.5a–c. However, the time width of each steps showed the variety even if the steps were at the same drain current levels in Fig. 15.5a–c. From these plots, the average of the drain current width was $t_{\text{ave}} = 68.82$ s. By applying $V_{\text{TG}} = -4$ V before the measurement, holes had been accumulated in the storage dot. After the top gate voltage was turned to the positive bias of 1 V at $t = 0$ s, the accumulated holes started to release from

storage dot to the SWNT channel one by one. The SWNT channel was modulated by the transferred single hole and showed discrete drain current levels, i.e., the current steps as shown in Fig. 15.5a–c. In other words, discrete changes of the drain current directly corresponded to the variation of single-hole Δn in the storage dot. Therefore, the transfer of single hole could be directly counted as the discrete modulation of the drain current at room temperature in real time [14]. Moreover, each transfer of single hole took several tens of seconds because of thick tunneling barrier of Al_2O_3 of 3 nm. The variety of time widths of each step attributed to the stochastic transfers of single hole. These stochastic characteristics also indicate the evidence of the single-hole transfer in the device.

15.1.4 Summary

In conclusion, single-charge memory operated at room temperature was fabricated with SWNT channel surrounded by $\text{SiN}_x/\text{Al}_2\text{O}_3$ double-gate insulator layers. To obtain the narrow top gate electrode of 10 nm, the isotropic deposition by ALD process for the insulators formation was used. At the same time, the concentric circle structure of insulators was formed around the SWNT channel which was on the center. Because of the narrow top gate electrode, only single dot was just under the top gate electrode which stored single hole one by one. The top gate electrode surrounding the SWNT channel realized the high electric field concentration and caused Fowler-Nordheim tunneling even at low applied voltage. The drain current affected by the stored single charge showed the threshold voltage shift at room temperature. The device also showed hysteresis characteristics. The hysteresis width changed discretely by the applied top gate voltage, which is attributed to the one by one transfer of single holes in the dot. The transfer of four single holes was observed, which can be applied to the single-charge memory. The time dependence of the drain current showed the step-like characteristics. The time widths of the steps corresponded to the interval of stochastic transfer of single holes, and the number of the steps corresponded to the variation of single holes in the dot. By observing the steps, the individual transfers of single holes could be counted in real time at room temperature.

References

1. Kitamura T, Kawata M, Honma I, Yamamoto I, Nishimoto S, Oyama K (1998) A low voltage operating flash memory cell with high coupling ratio using horned floating gate with fine HSG. Symp VLSI Tech Dig 104–105
2. Peng HB, Hughes ME, Golovchenkoa J (2006) Room-temperature single charge sensitivity in carbon nanotube field-effect transistors. Appl Phys Lett 89:243502
3. Kamimura T, Ohono Y, Matsumoto K (2009) Carbon nanotube Fabry-Pert device for detection of multiple single charge transitions. Jpn J Appl Phys 48:025001

4. Kojima A, Hyon CK, Kamimura T, Maeda M, Matsumoto K (2005) Protein sensor using carbon nanotube field effect transistor. *Jpn J Appl Phys* 44:1596–1598
5. Okuda S, Okamoto S, Ohno Y, Maehashi K, Inoue K, Matsumoto K (2012) Horizontally aligned carbon nanotubes on a quartz substrate for chemical and biological sensing. *J Phys Chem C* 116:19490–19495
6. Abe M, Ohno Y, Matsumoto K (2012) Schottky barrier control gate-type carbon nanotube field-effect transistor biosensors. *J Appl Phys* 111:034506
7. Yeo S, Choi C, Jang CW, Lee S, Jhon YM (2013) Sensitivity enhancement of carbon nanotube based ammonium ion sensors through surface modification by using oxygen plasma treatment. *Appl Phys Lett* 102:073108
8. Hu ZL, Martensson G, Murugesan M, Fu Y, Guo X, Liu J (2012) Detecting single molecules inside a carbon nanotube to control molecular sequences using inertia trapping phenomenon. *Appl Phys Lett* 101:133105
9. Heinze S, Tersoff J, Martel R, Derycke V, Appenzeller J, Avouris P (2002) Carbon nanotubes as Schottky barrier transistors. *Phys Rev Lett* 89:106801
10. Gruneis A, Esplandiu MJ, Garcia-Sanchez J, Bachtold A (2007) Counting and manipulating electrons using a carbon nanotube transistor. *Nano Lett* 7:3766–3769
11. Ohori T, Ohno Y, Maehashi K, Inoue K, Hayashi Y, Matsumoto K (2011) Quantized characteristics in carbon nanotube-based single-hole memory with a floating nanodot gate. *Appl Phys Lett* 98:223101
12. Guo L, Leobandung E, Chou SY (1997) A silicon single-electron transistor memory operating at room temperature. *Science* 275:649
13. Davis JR (1980) *Instabilities in MOS devices*. Gordon and Breach, New York
14. Yano K, Ishii T, Hashimoto T, Kobayashi T, Murai F (1994) Room-temperature single-electron memory. *IEEE Trans Electron Devices* 41:1628–1638

Chapter 16

Control of Particle Nature and Wave Nature of Electron in CNT

Takafumi Kamimura and Kazuhiko Matsumoto

Abstract A resonant tunneling transistor (RTT) which shows the Fabry–Perot interference characteristics is a device that uses the wave nature of holes. A single-hole transistor (SHT) which shows Coulomb blockade characteristics uses the particle nature of the holes in the SWNT. Both devices need tunneling barriers at both sides of the quantum island. The RTT needs strong coupling, while the SHT weak coupling between the quantum island and the source and drain electrodes. In the single-walled carbon nanotube (SWNT) device, the Schottky barriers act as the tunneling barriers. Therefore, the thickness of the tunneling barriers and the coupling strength between the SWNT and source and drain electrodes can be controlled by the applied control-gate voltage. Therefore, both characteristics of RTT and SHT can be observed in the same device only by changing the applied gate bias. The coupling energy of the electron–electron correlation via spin between the electron in the CNT and those in the electrodes (this energy is referred to as the Kondo temperature) can be also tuned by modifying the tunneling barrier thickness.

Keywords Carbon nanotube • Resonant tunneling transistor • Single-electron transistor • Single-hole transistor • Kondo effect • Spin

16.1 Introductions

Various electrode materials for single-walled carbon nanotube (SWNT) transistors were investigated. Pd electrodes have been used for Ohmic contacts [1]. Ti electrodes have been used for Schottky contacts for hole conduction [2–4], and Mg

T. Kamimura (✉)

Institute of Scientific and Industrial Research, Osaka University, Mihogaoka 8-1, Ibaraki, Osaka 567-0047, Japan

Advanced ICT Research Institute, National Institute of Information and Communications Technology, 4-2-1 Nukui-Kitamachi, Koganei, Tokyo 184-8795, Japan
e-mail: Kamimura@nict.go.jp

K. Matsumoto

Institute of Scientific and Industrial Research, Osaka University, Mihogaoka 8-1, Ibaraki, Osaka 567-0047, Japan
e-mail: k-matsumoto@sanken.osaka-u.ac.jp

and Ca electrodes for electron conduction [5]. Moreover, in the case of sub- μm -order channel lengths at low temperatures, SWNT transistors with Ohmic contacts have shown a resonant tunneling transistor (RTT) characteristics [6, 7], which are also called as a Fabry–Perot characteristics, and SWNT transistors with Schottky contacts have shown a single-hole transistor (SHT) characteristics [8–11], in which the Schottky barriers act as tunneling barriers. Therefore, electrodes materials should be chosen to obtain the desired characteristics.

An RTT which shows the Fabry–Perot interference characteristics is a device that uses the wave nature of holes. An SHT which shows Coulomb blockade characteristics uses the particle nature of the holes in the SWNT. Both devices need tunneling barriers at both sides of the quantum island. The RTT needs strong coupling, while the SHT weak coupling between the quantum island and the source and drain electrodes. Usually, tunneling barriers fabricated in a quantum dot are made from thin oxide layers or different composition material such as AlGaAs for GaAs, etc. Therefore, the thickness of the tunneling barriers and the coupling strength cannot normally be controlled in a given device. In the present device, however, the Schottky barriers act as the tunneling barriers. Therefore, the thickness of the tunneling barriers and the coupling strength between the SWNT and source and drain electrodes can be controlled by the applied control-gate voltage. Therefore, both characteristics of RTT and SHT can be observed in the same device only by changing the applied gate bias. The SHT shows the periodic current suppressed region which is called Coulomb diamond characteristic. Additionally, the quantum levels are observed near the Coulomb diamond characteristic [8, 9, 11]. The SHT requires thick tunneling barriers at the both sides of the quantum island and has high impedance [8, 9, 11]. Therefore, the SHT is not suitable for high-speed application. However, the SHT can store hole one by one and has high sensitivity to even the single charge [14–16]. Therefore, the SHT is suitable for the single-charge memory application. On the other hand, the RTT is the low-impedance device and can be operate in the high-speed applications because of the thin tunneling barriers. The present device which can be converted between the SHT and RTT can be applied for both the programmable high-speed circuit and single-charge memory.

The Kondo effect, which describes the scattering of conduction electrons in a metal due to the presence of magnetic impurities, has been studied extensively in quantum dot devices composed of various materials [1–5]. The binding energy of the spins of conduction electrons subject to the Kondo effect has been modulated by the applied gate voltage for devices composed of compound semiconductor materials [2]. Single-walled carbon nanotubes (CNTs) with semiconducting properties [5, 7–9] have been also investigated for quantum effect characteristics such as Coulomb blockade phenomena, Fabry–Perot oscillation [17–26], and the Kondo effect [5, 6, 10, 11–16, 27–31].

The coupling energy of the electron–electron correlation via spin between the electron in the CNT and those in the electrodes (this energy is referred to as the Kondo temperature) can be tuned by modifying the tunneling barrier thickness. For this tuning to occur, the Kondo temperature should be sufficiently high when compared with the ambient temperature; moreover, the isolated spin must be

localized in the CNT quantum well to realize the Kondo state. In realizing these conditions, control of the barrier thickness by means of the applied gate voltage plays an important role.

16.2 The Transistor That Is Compatible with the Resonant Tunneling Transistor and the Single-Hole Transistor

A multifunctional quantum transistor using the particle nature and wave nature of holes in SWNT is described here. This transistor can operate as the RTT and also as an SHT.

16.2.1 Sample Preparations

A schematic of the sample structure is shown in Fig. 16.1. SWNT was prepared as follows. An n^+ -Si wafer with a thermally grown 300 nm thick oxide was used as a substrate. Layered Fe/Mo/Si (2 nm/20 nm/40 nm) catalysts were evaporated using an electron-beam evaporator under a vacuum of 10^{-6} Pa. These layered catalysts were patterned on the substrate using the conventional photolithography process. An SWNT was grown by thermal chemical vapor deposition (CVD) using the mixed gases of a hydrogen and an argon-bubbled ethanol. After the growth of the SWNT, it was purified by burning out the amorphous carbon around the SWNT in an air atmosphere at a temperature of several hundred degrees Celsius [12]. Ti (30 nm)

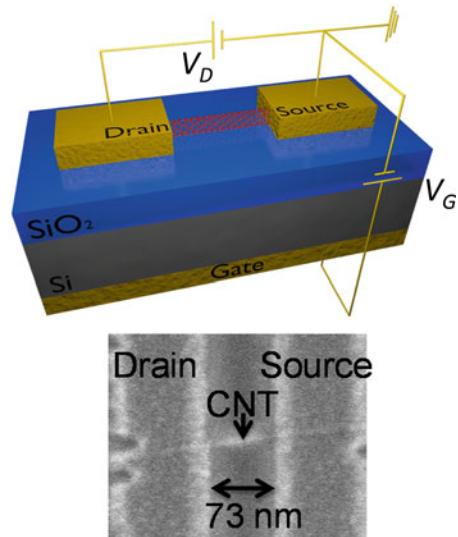


Fig. 16.1 Schematic sample structure and SEM image around channel. The channel length is 73 nm. The electrode material is Ti

electrodes were deposited on the patterned catalysts as the source and drain, and on the back side of the n^+ -Si substrate for the gate, using the electron-beam evaporator under a vacuum of 10^{-6} Pa. The distance (L) between the source and drain was 73 nm. Thus, a back-gate-type multifunctional transistor with an SWNT channel was fabricated that had the functions of the RTT and the SHT.

16.2.2 Experimental Results and Discussions

Figure 16.2a shows the differential conductance dI_D/dV_D characteristic as a function of the V_G at 7.3 K, where the drain voltage was set at 8 mV. An oscillation characteristic with two oscillation periods was also observed in Fig. 16.2a. A large oscillation period of $\Delta V_G = 1.1$ V was at $V_G \geq -16$ V, and a small oscillation period of $\Delta V_G = 0.65$ V was at $V_G \leq -16$ V. Figure 16.2b shows the dI_D/dV_D peak on a linear scale at $V_G \geq -16$ V and $V_G \leq -16$ V. A clear difference in the oscillation period is observed as follows. The peaks of dI_D/dV_D at $V_G \geq -16$ V are well fitted by the differential Fermi function, i.e., $G = (2e^2/h) (T_L T_R / \Gamma) (1/4kT) \cosh^{-1} [(\varepsilon_F - \varepsilon_0/2kT)]$ [13], and at $V_G \leq -16$ V by the Lorentzian, i.e., $G = (2e^2/h) \{4T_L T_R / [(\varepsilon_F - \varepsilon_0) + \Gamma^2]\}$ [13], as shown in Fig. 16.2c and d, respectively, where e is the elementary charge, h is the plank constant, T_L and T_R are the tunneling probabilities at the left and right tunneling barriers, Γ is the full width at half maximum, k is the Boltzmann constant, T is the temperature, ε_F is the Fermi level, and ε_0 is the quantum level. The shape of the Coulomb oscillation peaks must be differential Fermi function, which is attributed to thermal broadening, while the resonant tunneling current peaks must be Lorentzian, which is attributed to energy uncertainty [13]. Therefore, the dI_D/dV_D oscillation at $V_G \geq -16$ V in Fig. 16.2a should be Coulomb oscillation peaks, and at $V_G \leq -16$ V in Fig. 16.2a, they should be resonant tunneling current peaks [14]. In other words, the device operates in particle nature mode at $V_G \geq -16$ V, and in wave nature mode at $V_G \leq -16$ V. The conductance value of resonant current peaks shown in Fig. 16.2a is about one-fifth of $4e^2/h$. The height of Schottky barriers at the contact between SWNT and metal electrode is affected by the absorbed molecules such as oxygen and/or water, etc. [15]. Moreover, the transmission coefficient T in resonant tunneling regime in double-barrier structure with asymmetric potential profiles do not reach to $T = 1$ [16, 27, 28]. In the case of large asymmetric potential barrier profiles, T becomes one hundred times worse compared to $T = 1$ of symmetric barrier profiles. Therefore, the low conductance of resonant tunneling current peaks shown in Fig. 16.2a may be attributed to the asymmetric Schottky barriers between SWNT and metal electrodes.

Figure 16.3 shows the dI_D/dV_D characteristic as a function of the drain voltage V_D at 7.3 K and $V_G = -12.795$ V. The dI_D/dV_D peak spacing of 26 mV is observed in the plot, which corresponds to the quantum energy level separation in the SWNT quantum island. The separation of the quantum energy levels is indicated by

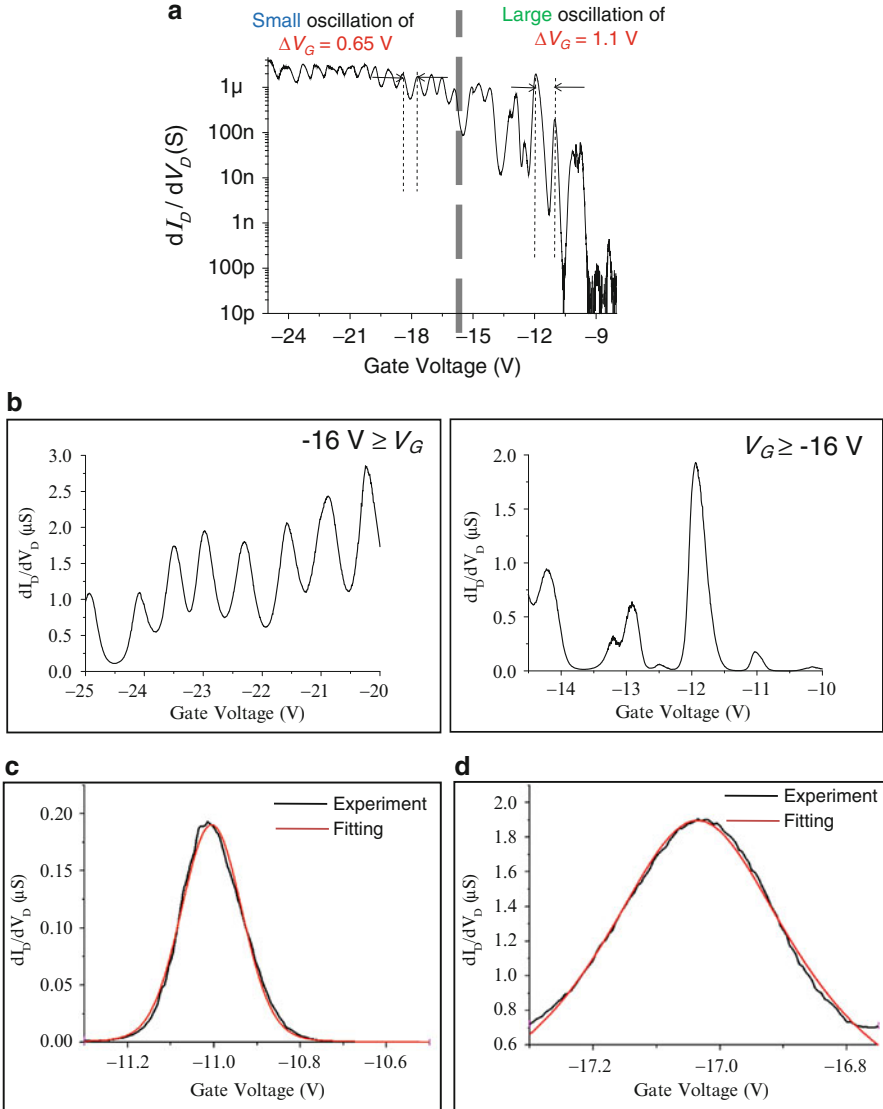
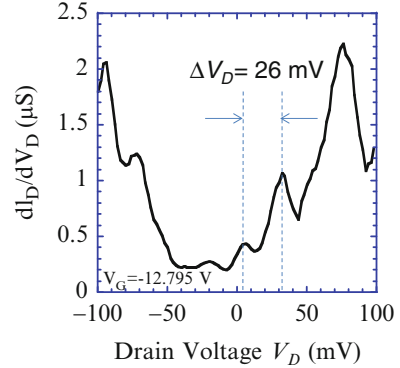


Fig. 16.2 (a) Differential conductance dI_D/dV_D characteristic as a function of V_G at 7.3 K. Two frequencies of oscillation were observed, which were $\Delta V_G = 1.1$ V and 0.65 V. (b) dI_D/dV_D peak in linear scale at low and high V_G . (c) dI_D/dV_D peak at $V_G = -11$ V (black) and Gaussian fitting line (red). The peak is well fitted by the Gaussian function, which means the shape of the peak can be attributed to thermal broadening. Therefore, the peak must be a Coulomb oscillation peak. (d) dI_D/dV_D peak at $V_G = -17$ V (black) and Lorentzian fitting line (red). The peak is well fitted by the Lorentzian function, which means the shape of the peak can be attributed to energy uncertainty broadening. Therefore, the peak must be a resonant tunneling current peak

Fig. 16.3 dI_D/dV_D characteristic as a function of drain voltage V_D at $V_G = -12.795$ V and 7.3 K. The peaks are attributed to quantum energy levels in the SWNT. The estimated energy separation in 73 nm SWNT was 24 meV, which is in good agreement with the peak spacing of 26 mV in the plot



$$\Delta E_Q = \left(\frac{h\nu_F}{2L} \right) \left[1 + \left(\frac{2L}{3rn} \right)^2 \right]^{-1/2} \quad (16.1)$$

where r is the radius of the SWNT, L is the length of the SWNT, and ν_F is the Fermi velocity [29]. When n becomes large, the equation becomes

$$\Delta E_Q = \frac{h\nu_F}{2L} \quad (16.2)$$

and shows a constant value independent of n . The energy separation ΔE_Q of the quantum levels for an SWNT length of 73 nm is calculated to be 24 mV from Eq. (16.2). Because this estimated value of energy separation of 24 mV is in good agreement with the dI_D/dV_D peak spacing of 26 mV in Fig. 16.3, it can be concluded that the entire SWNT channel acts as a single quantum island [18, 19, 23–25, 35, 39, 40].

Figure 16.4 shows a contour plot of the dI_D/dV_D characteristic as a function of V_G and V_D at 7.3 K. The characteristic can also be divided into two modes, the particle nature mode and wave nature mode. At $V_G \geq -16$ V, as shown in Fig. 16.4a, b, the plot clearly shows the Coulomb diamond structures, which are getting smaller with negatively increasing V_G . Additionally, line-shaped quantum levels are observed outside of these Coulomb diamond structures. Therefore, at $V_G \geq -16$ V, the device operated in the particle nature mode. As shown in Fig. 16.4b, at $-16 \geq V_G \geq -20$ V, the Coulomb blockade was lifted, and the Coulomb diamond structures disappeared at around $V_G = -16$ V. The quantum levels still remain, and the so-called Fabry–Perot quantum interference pattern is observed at this region. Finally, at $V_G \leq -20$ V, the quantum levels are getting blurred with negatively increasing V_G , as shown in Fig. 16.4c. Figure 16.4d shows gray-scale image of d^2I_D/dV_D^2 , showing the presence of Fabry–Perot quantum interference pattern at $V_G \leq -20$ V, in which dot lines are corresponding to the quantum energy levels of the SWNT. At the cross points of the dot lines, high conductance is appeared. Therefore, at -16 V $\geq V_G$, the device operated in the wave nature mode [20–23].

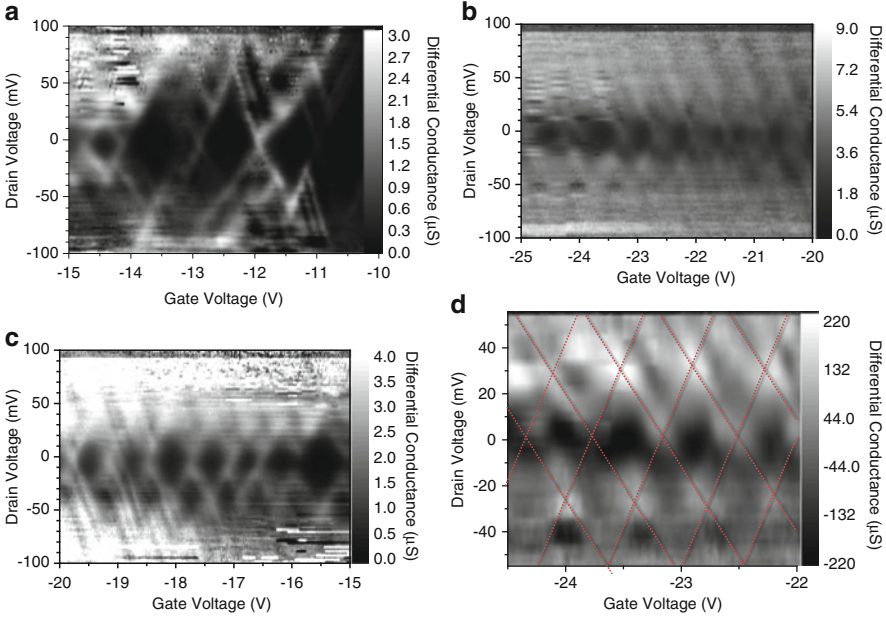


Fig. 16.4 Contour plot of dI_D/dV_D characteristic as a function of V_G and V_D at 7.3 K. **(a)** At $V_G \geq -16$ V, Coulomb diamond structures and line-shaped quantum levels outside of the Coulomb diamond structures are observed. Moreover, the Coulomb diamonds become smaller with a negatively increasing V_G . **(b)** At $-16 \text{ V} \geq V_G \geq -20$ V, the Coulomb blockade is lifted, and the Coulomb diamonds disappear. And the quantum levels become blurred with the negatively increasing V_G . The so-called Fabry-Perot quantum interference pattern is observed. **(c)** At $-20 \text{ V} \geq V_G$, the blurred quantum levels still remain. **(d)** Gray-scale image of $d^2 I_D/dV_D^2$, showing the presence of Fabry-Perot quantum interference pattern at $V_G \leq -20$ V, in which *dot lines* are corresponding to the quantum energy levels of the SWNT

Figure 16.5a shows the Coulomb charging energy E_C as a function of V_G , in which the line is guided to the eyes. E_C is obtained by $E_C = \Delta E - E_Q$ [30], where ΔE is estimated from the size of the Coulomb diamond. E_C drastically decreases with a negatively increasing V_G , almost reaching zero at $V_G \geq -16$ V. Therefore, the Coulomb diamonds disappear at $-16 \text{ V} \geq V_G$. The tunneling capacitance C_t and the gate capacitance C_G as a function of V_G are shown in Fig. 16.5b. The C_t and the C_G are obtained from the equations of $C_t = e/2E_C - C_G$ and $C_G = e/\Delta V_G$ [30], respectively. The C_t depends on the thickness of the tunneling barrier, and the C_G depends on the gate structure. The C_t drastically increases with a negatively increasing the V_G , while the C_G is almost constant, independent of the changing V_G . The drastic increase in the C_t is attributed to the decrease in the thickness of the Schottky barriers at the contacts between the SWNT quantum island and the electrodes [1]. When the Schottky barriers become thin with negatively increasing V_G , as shown in the inset of Fig. 16.5b, the C_t drastically increases, and the coupling strength of the wave function between the outside and the inside of the Schottky

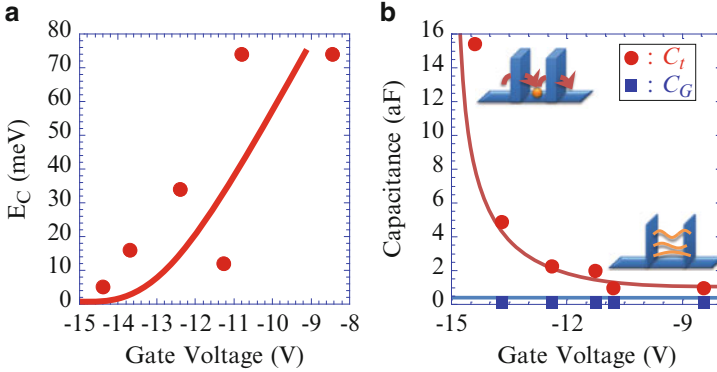


Fig. 16.5 (a) Coulomb charging energy E_C as a function of V_G . E_C drastically decreases at $V_G \geq -16$ V and reaches zero at around $V_G = -16$ V. Therefore, the Coulomb diamonds disappear at the mid- V_G region. (b) Tunneling capacitance C_t and gate capacitance C_G characteristics as functions of V_G . C_t drastically increases at $V_G \geq -16$ V. On the other hand, C_G is almost constant, independent of the changing V_G . The drastic increase of C_t is attributed to the change in the thickness of the Schottky barriers at the contact between the SWNT channel and electrodes

barrier becomes stronger. Therefore, the Coulomb blockade is lifted, and the E_C becomes zero at $-16 \text{ V} \geq V_G$.

The dependence of the full width at half maximum (FWHM) of the resonant tunneling current peak characteristic on the V_G is shown in Fig. 16.6a, in which the line is guided to the eye. The FWHM is estimated from an I_D - V_G plot using the Voigt function, which is a convolution of the Gaussian and the Lorentzian functions, and can be used to divide the FWHM into the FWHM of the Gaussian w_G and that of the Lorentzian w_L , where the differential Fermi function is approximated by the Gaussian profile to simplify the calculations. Figure 16.6b–d shows several curves fitted by the Voigt function, where the black line is the experimental data, the blue lines are the fitting curves, the red line is the cumulative fitting curves, and each alphabetic marker for peaks A–F corresponds to a marker in the plot of Fig. 16.6a. In the particle nature mode of $V_G \geq -16$ V, w_L is negligibly small, and the w_G of about 0.2 V is independent of V_G because the FWHM of the Coulomb oscillation mainly depends on the thermal broadening of Fermi dispersion [13]. On the other hand, in the wave nature mode of $-16 \text{ V} \geq V_G$, w_G becomes negligibly small, and w_L increases linearly with the negatively increasing V_G . w_L is proportional to the tunneling probability as follows: $\alpha w_L = Thv_F/2L$, where α is the ratio of the modulated energy to applied V_G and T is the tunneling probability [29]. Therefore, the increase in w_L seen in Fig. 16.6 represents an increase in the tunneling probability, which is attributed to the decrease in the thickness of the Schottky barriers with a negatively increasing V_G .

The logarithmic dependence of the drain current I_D on the inverse of the temperature is shown in Fig. 16.7. At $V_G = -38$ V of the wave nature mode, I_D is almost constant which is independent of the temperature. In the wave nature mode, the Schottky barrier is so thin that the tunneling current becomes dominant.

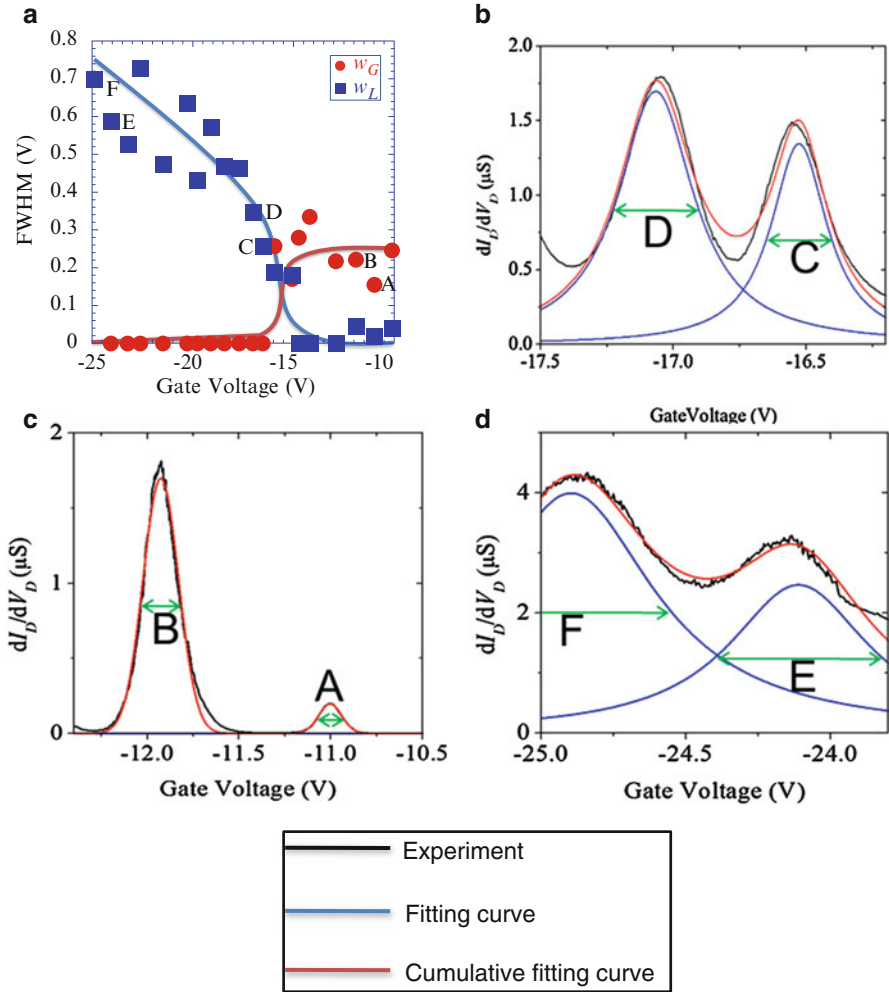


Fig. 16.6 (a) FWHM of the dI_D/dV_D peak characteristics as a function of V_G . w_G is almost constant, independent of V_G , and w_L is negligibly small at $V_G \geq -16$ V. w_G becomes vanishingly small and w_L increases linearly with a negatively increasing V_G at $-16 \text{ V} \geq V_G$. (b)–(d) FWHMs: the experimental data are indicated by the *black line*, the fitting curves are indicated by the *blue lines*, the cumulative fitting curves are indicated by *red line*, and each alphabetic marker for a peak corresponds to a marker in the plot of (a)

In contrast, at $V_G = -10$ V of the particle nature mode, I_D drastically increases at the high-temperature region, and the Schottky barrier height $\Delta\phi$, as estimated from the slope, is $\Delta\phi = 50$ mV. In the particle nature mode, the Schottky barriers are so thick that the thermal emission current becomes dominant at the high-temperature region. These results indicate that the tunneling probabilities at the Schottky barriers can

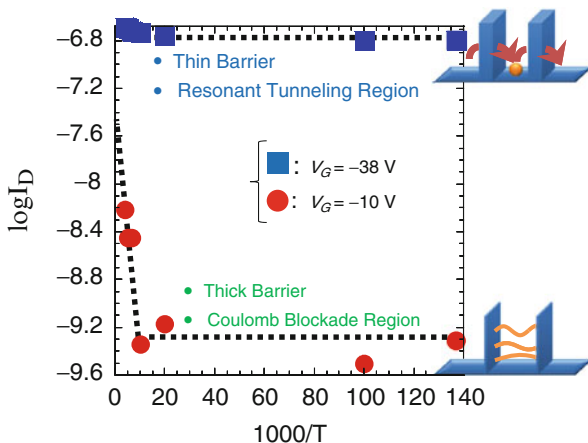
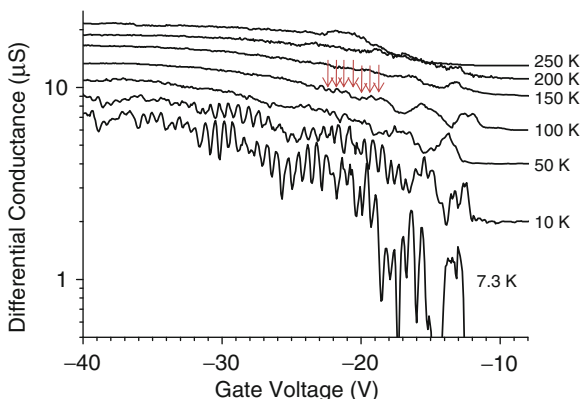


Fig. 16.7 The logarithmic dependence of the drain current I_D on the inverse of the temperature. At $V_G = -38$ V of the wave nature mode, I_D is almost constant, independent of the temperature. In the wave nature mode, the Schottky barrier is so thin that the tunneling current becomes dominant. In contrast, at $V_G = -10$ V of the particle nature mode, I_D drastically increases at the high-temperature region, and the Schottky barrier height estimated from the slope is $\Delta\phi = 50$ mV

Fig. 16.8 Temperature dependence of differential conductance on V_G . Each plot is shifted by $3 \mu\text{S}$ to make it easier to see. The quantum level peaks are becoming blurred with increasing temperature. However, even at $T = 100$ K, the quantum levels remain, as indicated by the arrows



be modulated by the applied V_G and that the coupling between the SWNT quantum island and electrodes is strong in the wave nature mode and weak in the particle nature mode.

Figure 16.8 shows the temperature dependence of differential conductance as a function of the gate voltage. The quantum level peaks became blurred with increasing temperature. However, even at $T = 100$ K, the quantum levels still remained, as indicated by arrows.

Figure 16.9 shows the device structure for the measurement of the channel length dependence. The four electrodes are fabricated on the one SWNT. Therefore, three transistors share the common SWNT. The distances between the electrodes, which are the channel lengths, are $L = 69.4$ nm, 90.3 nm, and 119 nm, respectively.

Fig. 16.9 Device structure for the measurement of the channel length dependence. One SWNT is shared by three devices which have different channel length, respectively. The fabricated channel lengths are $L = 69.4$, 90.3 , and 119 nm from the SEM images

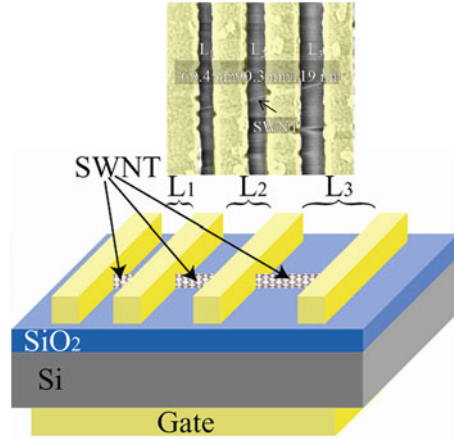


Figure 16.10a, b shows the characteristics of the $L = 69.4$ nm device, and Fig. 16.10c, d shows the characteristics of the $L = 119$ nm device. These devices also show Coulomb diamond characteristics at $0 \text{ V} \geq V_G \geq -5 \text{ V}$ as shown in Fig. 16.10b, d. Moreover, these devices also show Fabry–Perot quantum interference pattern at $-15 \text{ V} \geq V_G \geq -20 \text{ V}$ in the case of $L = 69.4$ nm device and at $-10 \text{ V} \geq V_G \geq -15 \text{ V}$ in the case of $L = 119$ nm device as shown in Fig. 16.10a, c. The difference of the V_G showing Fabry–Perot quantum interference pattern is corresponding to the difference of the threshold voltage, which is attributed to the contact condition between the electrodes and SWNT, e.g., absorbed molecules [4]. The periods of the Coulomb diamond characteristic and Fabry–Perot quantum interference pattern of the $L = 69.4$ nm device are larger than that of the $L = 119$ nm device, which are $\Delta V_G = 0.64 \text{ mV}$ and $\Delta E_Q = 19.3 \text{ mV}$ at $L = 69.4$ nm device and $\Delta V_G = 0.44 \text{ mV}$ and $\Delta E_Q = 9.05 \text{ mV}$ at $L = 119$ nm device.

Figure 16.11a shows the channel length dependence of the separation of the quantum energy levels. ΔE_Q is linearly depending on the $1/L$, which is corresponding to the Eq. (16.2). Figure 16.11b shows the channel length dependence of the gate capacitance. C_G is linearly depending on the L , which is corresponding to the $C_G \approx C_g L$ [31], where C_g is the gate capacitance per unit length.

16.2.3 Summary

In summary, a multifunctional quantum transistor using the particle nature and wave nature of holes in SWNT is fabricated and demonstrated here. This transistor can operate in the wave nature mode as an RTT and in the particle nature mode as an SHT. The principle of the characteristic conversion from an SHT to an RTT is also revealed, which is the modulation of the coupling strength between the SWNT quantum island and the electrodes by the applied V_G [22, 23].

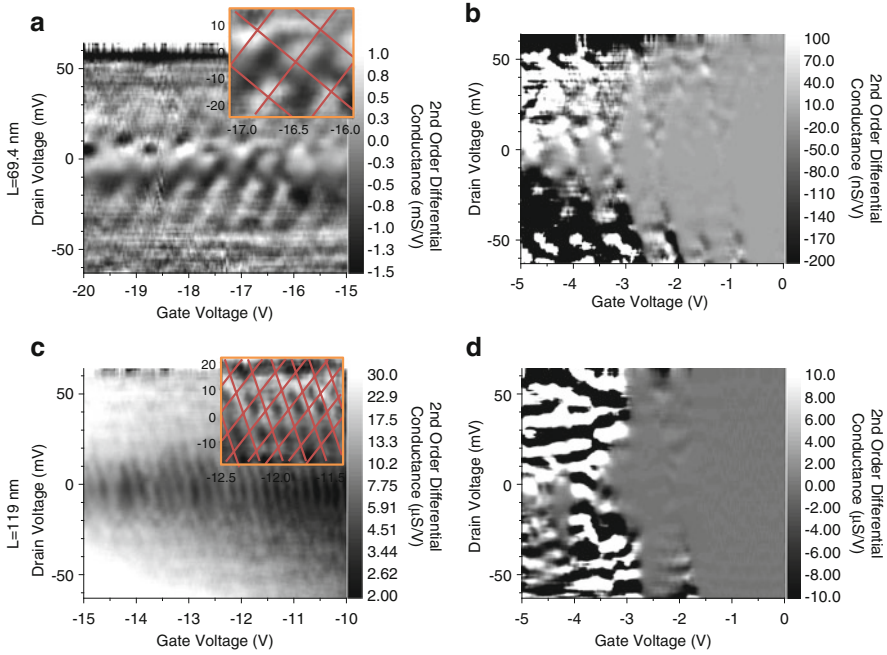


Fig. 16.10 (a) Fabry-Perot quantum interference pattern of the shortest channel length of 69.4 nm. *Inset* is the enlargement plot and the *dot lines* showing the corresponding quantum levels. At the cross points of the *dot lines*, high conductance is appeared. (b) Coulomb diamond characteristic of the shortest channel length of 69.4 nm. (c) Fabry-Perot quantum interference pattern of the longest channel length of 119 nm. *Inset* is the enlargement plot and the *dot lines* showing the corresponding quantum levels. At the cross points of the *dot lines*, high conductance is also appeared. (d) Coulomb diamond characteristic of the shortest channel length of 119 nm

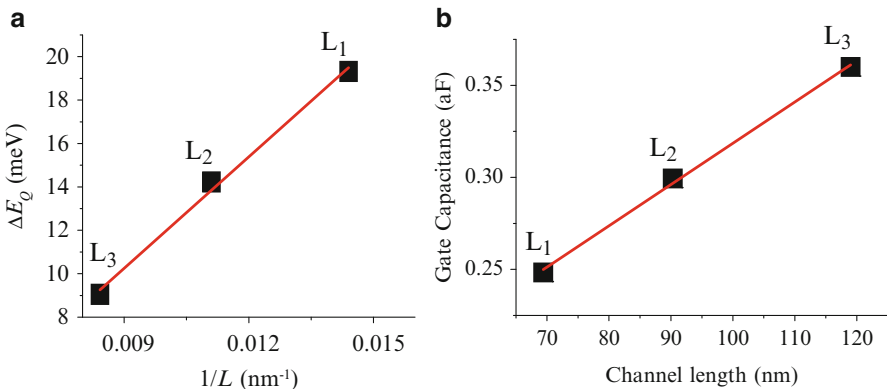


Fig. 16.11 (a) The channel length dependence of the separation of the quantum energy levels. (b) The channel length dependence of the gate capacitance

16.3 The Double-Gated Operation of the Multifunctional Quantum Transistor

The double-gated SWNT quantum transistor which operates as an RTT and also as an SHT was fabricated. The double-gated structure was fabricated to shift the high threshold voltage of the compatible transistor. The two behaviors of the RTT and the SHT were controlled by the control gate and observed by the sweep gate.

16.3.1 Sample Preparations

A schematic sample structure is shown in Fig. 16.12. The three electrodes, source, drain, and control gate, are fabricated on the one SWNT. The distances between the source and drain electrodes and between the drain and control-gate electrodes are $L_1 = 69.4$ nm and $L_2 = 90.3$ nm, respectively. Large voltage up to 6 V is applied

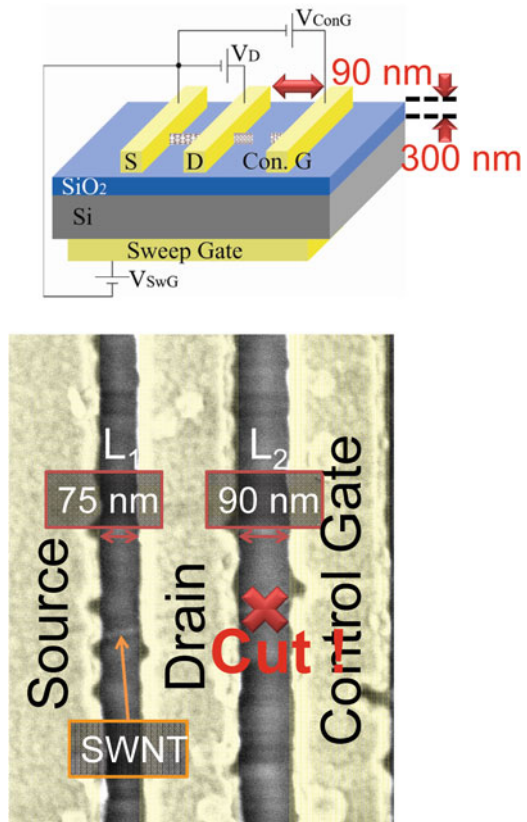


Fig. 16.12 Schematic sample structure and SEM image around channel

between drain and control gate, and SWNT is cut. Thus, the channel of the SWNT transistor with side-gate electrode, i.e., the control gate, is formed. The SWNT transistor also has back-gate electrode at the back side of the substrate. The control gate and the back gate are used for applying the control-gate voltage, V_{conG} , and sweep-gate voltage, V_{swG} , respectively. The device is measured at 6.3 K using cryogenic probing station.

16.3.2 Experimental and Discussions

Figure 16.13a–d shows the d^2I_D/dV_D^2 mappings as a function of the drain voltage and the sweep-gate voltage. When control-gate bias of $V_{\text{conG}} = 0$ V is applied, the device shows Fabry–Perot quantum interference pattern between $V_{\text{swG}} = -20$ V and -17.5 V surrounded by dashed line and Coulomb diamond characteristic between $V_{\text{swG}} = -17$ V and -10 V as shown in Fig. 16.13a, b. Thus, the crossovers between Fabry–Perot interference characteristics and Coulomb blockade characteristics are observed. When the Schottky barriers are thick enough to confine hole in the SWNT channel, the device operates as an SHT. When the Schottky barriers are too thin to confine hole in the SWNT channel, the device operates as an RTT. In the case of the thin tunneling barrier, the overlap of the hole wave functions of pre-tunneling and post-tunneling is very large and the inhibition of tunneling does not occur. Therefore, the condition of $R_t \gg h/4e^2 \equiv R_Q$, where R_t is the tunnel resistance and R_Q is the quantum resistance, is required to observe the Coulomb blockade phenomena [28–30]. The detail analysis of the Fabry–Perot interference pattern surrounded by dashed line will be shown in Fig. 16.13e, f as described later. When $V_{\text{conG}} = -25$ V is applied, all characteristics of Fig. 16.13a, b shift 5.26 V to the positive sweep-gate bias direction and become Fig. 16.13c, d. The device shows Fabry–Perot interference pattern between $V_{\text{swG}} = -15$ V and -12.5 V and Coulomb diamond characteristic $V_{\text{swG}} = -12$ V and -5 V as shown in Fig. 16.13c, d. From the $C_{\text{conG}}/C_{\text{swG}} = 0.21$, the impact of applying $V_{\text{conG}} = -25$ V is projected to be the shift of -5.26 V in V_{swG} scale. The characteristics of Fig. 16.13b, c in the sweep-gate bias region between $V_{\text{swG}} = -12.5$ V and -15 V are compared as follows, which is surrounded by dot–dash line. When the control gate is $V_{\text{conG}} = 0$ V (Fig. 16.13b), clear Coulomb diamond characteristics are observed, which means the hole shows the particle nature. When the control-gate bias $V_{\text{conG}} = -25$ V is applied (Fig. 16.13c), Coulomb diamond characteristics disappeared, and Fabry–Perot interference patterns emerged instead, though in the same sweep-gate bias region as in Fig 16.13b. This means the hole shows the wave nature. Therefore, the particle nature and wave nature of hole can be controlled at our will only by adjusting the value of the control-gate bias.

Figure 16.13e, f is the enlarged characteristics of the square regions indicated by dotted line and dashed line in Fig. 16.13a and c, respectively. In the figures, each dashed lines are corresponding to the quantum energy levels in the SWNT. At the

cross-point of the two dashed lines, d^2I_D/dV_D^2 show high-value patterns, which are called Fabry–Perot interference pattern. The periods of the Fabry–Perot interference pattern on the sweep-gate bias are $\Delta V_{\text{swG}} = 0.82$ V and $\Delta V_{\text{swG}} = 0.89$ V at $V_{\text{conG}} = 0$ V and $V_{\text{conG}} = -25$ V, respectively, which are almost the same period, while the periods of the Fabry–Perot interference pattern on the drain bias are $\Delta V_D = 15.7$ mV and $\Delta V_D = 37.4$ mV at $V_{\text{conG}} = 0$ V and $V_{\text{conG}} = -25$ V, respectively. The difference of ΔV_D is more than two times, which is attributed to the asymmetric distribution of electric field by the applied V_{conG} . The control gate has the asymmetric structure as shown schematically in Fig. 16.12. When the large V_{conG} is applied, the modulation of the energy band in SWNT by V_D becomes inefficient because the energy band in SWNT near the drain electrode is almost pinned by the large V_{conG} . Therefore, the Fabry–Perot interference pattern becomes large on the V_D axis.

Figure 16.13g shows differential conductance as a function of V_D at $V_{\text{swG}} = -6.06$ V and $V_{\text{conG}} = -25$ V (red solid line), related to Fig. 16.13d, and at $V_{\text{swG}} = -11.38$ V and $V_{\text{conG}} = 0$ V (black dashed line), related to Fig. 16.13b. From the $C_{\text{conG}}/C_{\text{swG}} = 0.21$, the impact of applying $V_{\text{conG}} = -25$ V is projected to be -5.26 V in V_{swG} scale. And, the Coulomb diamond around $V_{\text{swG}} = -11.38$ V as shown in Fig. 16.13b is shifted to around $V_{\text{swG}} = -6.12$ V in Fig. 16.13d by applied $V_{\text{conG}} = -25$ V. Therefore, the Coulomb diamond around $V_{\text{swG}} = -11.38$ V in Fig. 16.13b and that around $V_{\text{swG}} = -6.06$ V in Fig. 16.13d are the Coulomb diamond having the same number of confined hole. However, the Coulomb gaps E_C are different values of $E_C = 77$ mV for $V_{\text{conG}} = -25$ V and $E_C = 49$ mV for $V_{\text{conG}} = 0$ V as shown in Fig. 16.13g, though the periods of Coulomb oscillations are almost the same. This difference of the Coulomb gaps might be the same reason with the case of the difference of Fabry–Perot interference patterns in Fig. 16.13e, f.

Figure 16.14a shows drain current I_D characteristic as a function of sweep-gate voltage V_{swG} with constant drain voltage V_D of 1 mV and control-gate voltage V_{conG} of 0 V. The Coulomb oscillation characteristic is clearly observed. The period of Coulomb oscillation peaks is $\Delta V_{\text{swG}} = 1.05$ V. Figure 16.14b shows drain current I_D characteristic as a function of V_{conG} with constant drain voltage V_D of 1 mV and V_{swG} of 0 V. The Coulomb oscillation characteristic is also clearly observed. The period of Coulomb oscillation peaks of which is $\Delta V_{\text{swG}} = 5.00$ V. In this case, the SHT operations are achieved using the SWNT as quantum well and the Schottky barriers at the contact between the SWNT and source and drain electrodes as tunneling barriers [8]. The Coulomb oscillation characteristics in Fig. 16.14a, b have the difference of the applied gate voltage range, and the difference of the drain current values. The difference of applied gate voltage range is attributed to the difference of the gate capacitances. The difference of the drain currents value is attributed to the asymmetry of the potential energy distribution of SWNT as described below [31, 41, 42]. The sweep-gate capacitance C_{swG} and the control-gate capacitance C_{conG} are estimated to be $C_{\text{swG}} = e/\Delta V_{\text{swG}} = 0.154$ aF and $C_{\text{conG}} = e/\Delta V_{\text{conG}} = 0.0324$ aF, where e is elementary charge. The ratio between C_{swG} and C_{conG} is $C_{\text{conG}}/C_{\text{swG}} = 0.21$, which also represents the ratio between the

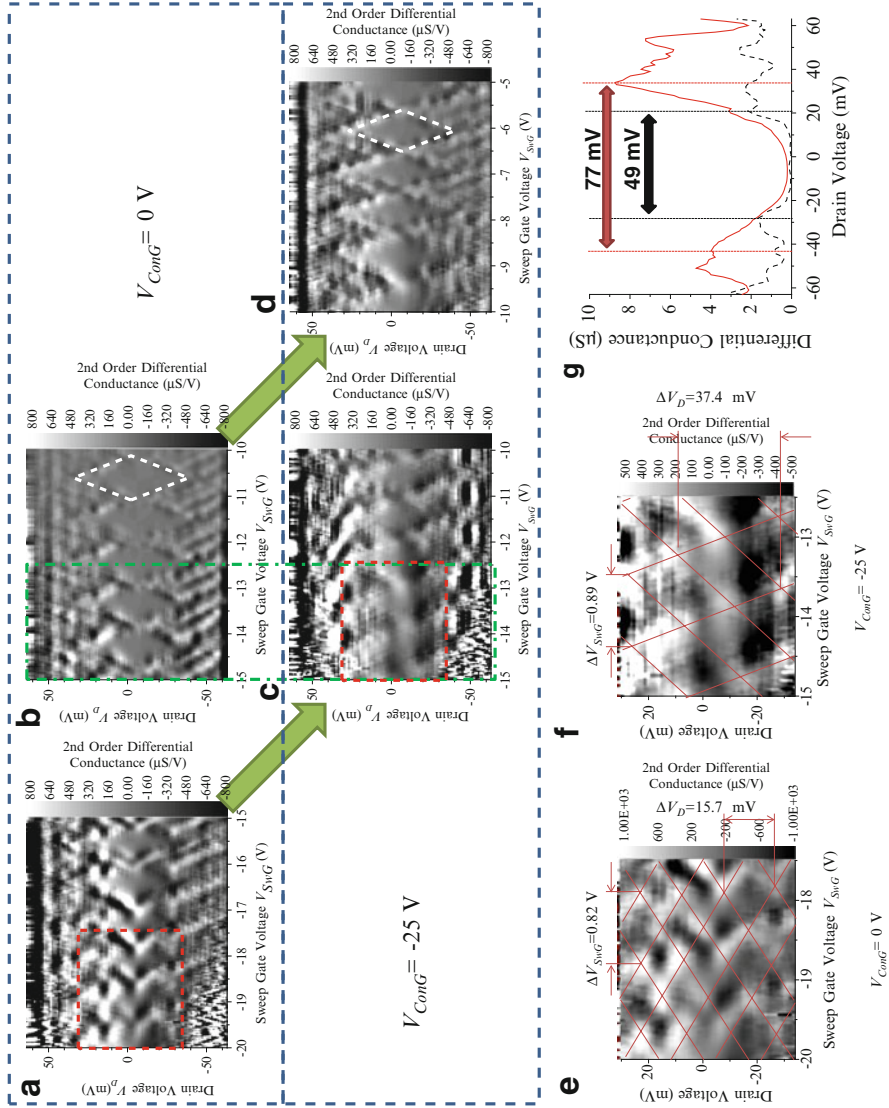


Fig. 16.13 d^2I_D/dV_D^2 mappings as a function of drain voltage and sweep voltage, where the applied drain voltage ranges from -63 to 64 mV. **(a, b)** d^2I_D/dV_D^2 mapping plot as a function of V_D and V_{swG} with constant “ $V_{conG} = 0$ V.” **(c, d)** d^2I_D/dV_D^2 mapping plot as a function of V_D and V_{swG} with constant “ $V_{conG} = -25$ V.” **(e, f)** Enlargement characteristics of the *square region* indicated by the *dashed line* in **(a)** and **(c)**, respectively, which show Fabry–Perot interference characteristics. **(g)** Comparison of Coulomb gaps at $V_{swG} = -11.38$ V with $V_{conG} = 0$ V (*dashed line*) and $V_{swG} = -6.06$ V with $V_{conG} = -25$ V (*solid line*)

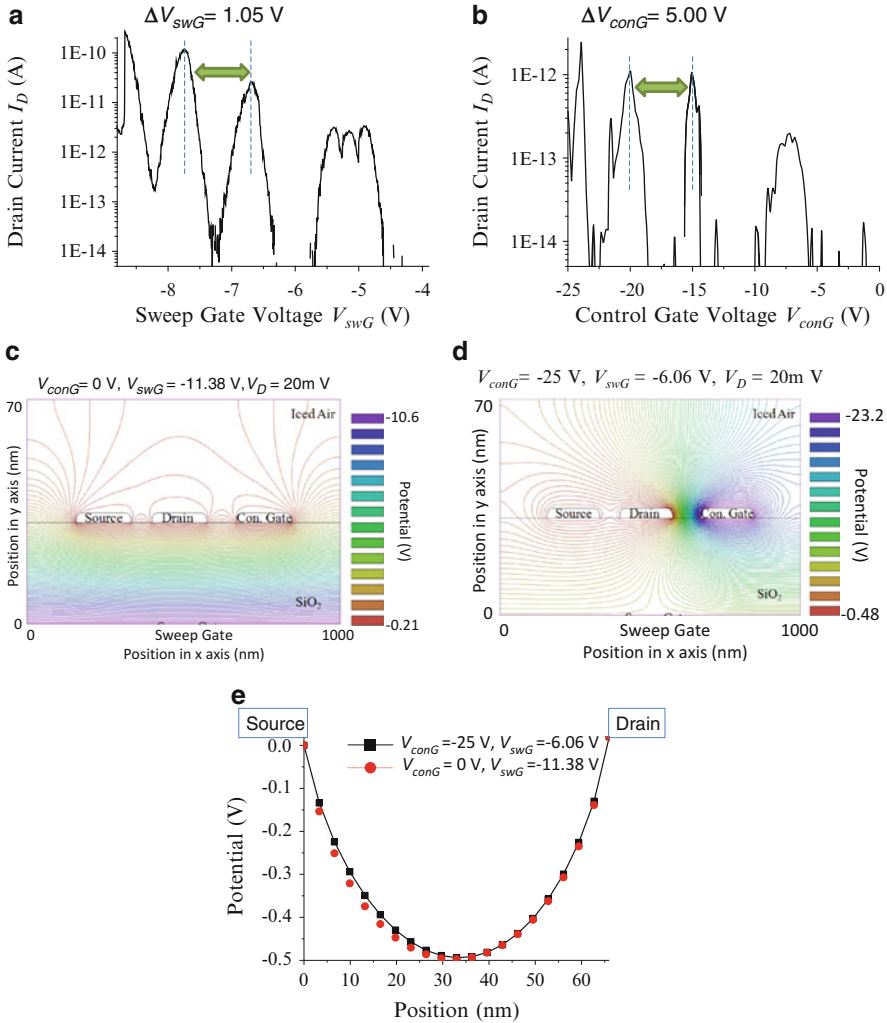


Fig. 16.14 (a) Coulomb oscillation characteristic as a function of sweep-gate voltage. (b) Coulomb oscillation characteristic as a function of control-gate voltage. (c, d) Calculated potentials at the condition of $V_{conG} = 0$ V and $V_{swG} = -11.38$ V and at $V_{conG} = -25$ V and $V_{swG} = -6.06$ V, respectively. (e) Cross-sectional potential at a point 1 nm above the SiO₂ surface between the source and drain electrodes for the condition of $V_{conG} = 0$ V and $V_{swG} = -11.38$ V (dotted line) and at $V_{conG} = -25$ V and $V_{swG} = -6.06$ V (solid line)

modulations of the potential energies in the SWNT channel by each gate voltage. The applied V_{swG} can modulate whole channel symmetrically including the Schottky barriers. On the other hand, the applied V_{conG} modulates the channel asymmetrically because of the location of the control-gate electrode. By applying V_{conG} , the widths of the Schottky barriers which act as the tunneling barriers at the each side become

different and tunneling coefficients become low [31, 41, 42]. Therefore, the value of the drain currents as shown in Fig. 16.14a, b are different in the log scale.

The large difference of drain current value between Fig. 16.14a and b is attributed to the asymmetry of the tunneling barriers. In order to ensure this asymmetry, the potential distributions around the channel at the applied voltage of V_{conG} and V_{swG} are calculated. Figure 16.14c is the calculated potential distributions for the voltage condition at $V_{\text{D}} = 20$ mV, $V_{\text{conG}} = 0$ V, and $V_{\text{swG}} = -11.38$ V, and (d) is at $V_{\text{D}} = 20$ mV, $V_{\text{conG}} = -25$ V, and $V_{\text{swG}} = -6.06$ V using ESTAT 6.5 (Advanced Science Laboratory, Inc.), in which SWNT is left out for the simplicity. In both calculations, the dielectric constant of the surface layer is used as a parameter because the sample surface is covered by the ice of air. The persisting air molecules are absorbed on the sample surface at low temperature and become ice. Therefore, the dielectric constant of the surface layer is unknown and must be a parameter in the calculation. In these calculations, we used the dielectric constant of the iced air of 4.06. The difference of potential distributions between Fig. 16.14c and d is large. Figure 16.14e is the cross-sectional potential 1 nm upper point from SiO_2 surface between source and drain electrodes. The x axis expresses the distance from source electrode edge. Dotted line (red) is the potential for the voltage condition of $V_{\text{conG}} = 0$ V and $V_{\text{swG}} = -11.38$ V, and solid line (black), $V_{\text{conG}} = -25$ V and $V_{\text{swG}} = -6.06$ V. The difference of the potential distribution came out near the source edge at the position between 5 and 30 nm, in which the potential becomes higher when the control-gate bias of $V_{\text{conG}} = -25$ V is applied (solid line) than the potential with the control-gate bias of $V_{\text{conG}} = 0$ V (dotted line) and $V_{\text{swG}} = -11.38$ V. Therefore, tunneling barrier near the source electrode edge becomes wider when the control gate is applied. Then, the tunneling barrier becomes asymmetric between at the source and drain electrodes. Therefore, the drain current becomes lower at the applied control-gate voltage because the tunneling probabilities strongly depend on the symmetry of the tunneling barriers [31, 41, 42]. These results of calculation can explain qualitatively the measure results as shown in Fig. 16.14a, b.

16.3.3 Summary

The wave nature and the particle nature of hole in an SWNT transistor though at the same drain and sweep-gate bias condition were observed only by adjusting the control-gate bias. The wave nature of hole corresponds to Fabry–Perot interference characteristics and the particle nature Coulomb blockade characteristics. Therefore, the wave nature and the particle nature of hole can be controlled at our will only by modulating the control-gate bias.

16.4 The Kondo Effect in the Transition Region Between the Resonant Tunneling Transistor Operation and the Single-Electron Transistor Operation

The Kondo temperature changing from 105 to 170 K was demonstrated in the gate-induced crossover region between the resonant tunneling and single-electron transistor regions for a CNT-channel Schottky barrier transistor.

16.4.1 Sample Preparations

The schematic structure and scanning electron microscopy (SEM) image of the sample CNT-channel Schottky transistor are shown in Fig. 16.15a. The CNT-channel transistor has tunable tunneling barriers of Schottky barriers at the source and drain contacts, where the distance between source and drain contacts is 73 nm. Under a low applied gate voltage, the Schottky barrier forms thick depletion layers at the source and drain electrodes; the depletion layers cause the formation of quantum well as schematically shown in Fig. 16.15b. When a high gate voltage is applied, the quantum well with thin tunnel barriers is formed, as shown in Fig. 16.15c. This device can be operated as both a single-electron transistor and resonant tunneling transistor by tuning the thickness of the tunneling barriers by means of the applied gate voltage [22, 23, 29–31].

16.4.2 Experimental and Discussions

Figure 16.16a–d shows the differential conductance as a function of the gate and drain voltages. The gate bias was changed from 0 to 33 V. In the low-gate-voltage region, shown in Fig. 16.16a, a series of the rhombus-shaped patterns surrounded by high-conductance lines (indicated by light gray lines) are clearly observed. The high-conductance lines and the rhombus patterns are attributed to the quantum energy levels in the CNT channel and the Coulomb diamond characteristic, respectively. In addition, the Coulomb diamonds show a regularity of the fourfold shell filling, in which every fourth Coulomb diamond (marked by open circles) is larger than the other three Coulomb diamonds (marked by closed circles) [42]. The single-electron transistor characteristics observed in the low applied gate voltage region, shown in Fig. 16.16a–c, transit to the resonant tunneling transistor characteristics in the high applied gate voltage region because of thinning of the tunneling barriers, as shown in Fig. 16.16d [22, 23, 29–31].

Of significance in Fig. 16.16c are the high-conductance regions (marked by dotted circles) in the small Coulomb diamond characteristic observed at around zero drain bias; further, at around $V_D = -25$ mV and $+25$ mV, high-conductance regions

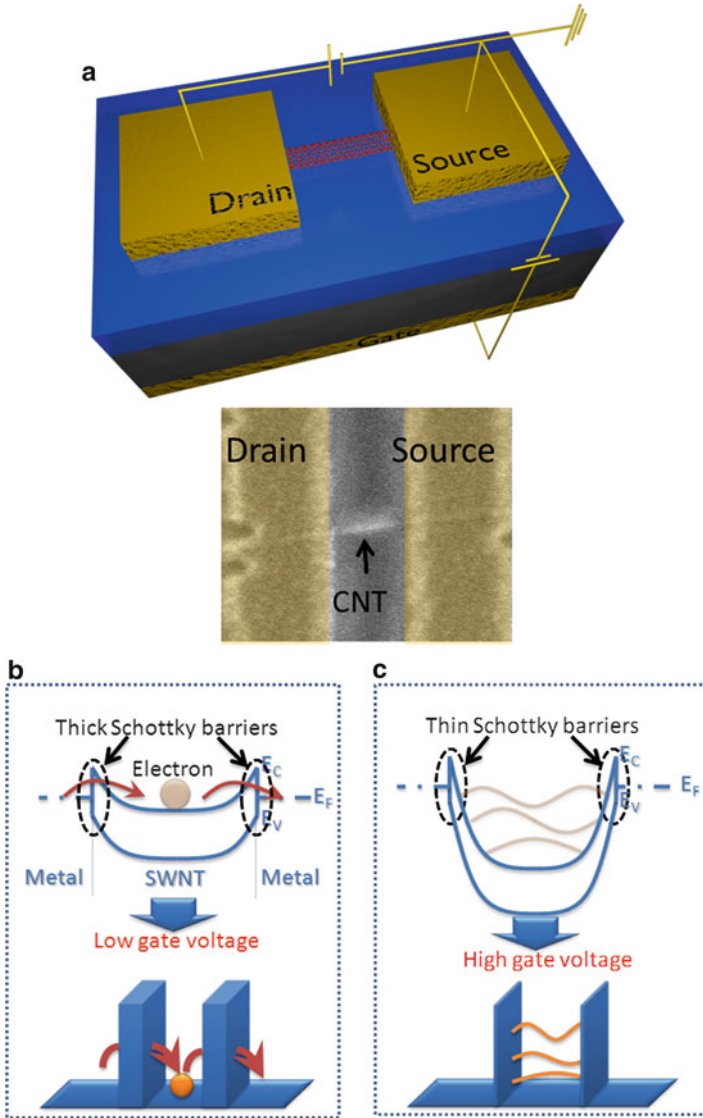


Fig. 16.15 (a) Schematic structure of carbon nanotube (CNT) Schottky transistor with bird's-eye of the device by scanning electron microscopy (SEM). (b). Schematic of band diagram with image of thick tunneling barriers under single-electron transistor characteristic conditions due to low applied gate voltage. (c). Schematic of band diagram with image of thin tunneling barriers under resonant tunneling transistor characteristic conditions due to high applied gate voltage

(marked by dashed circles) were observed in the large Coulomb diamond characteristics for gate voltages ranging from $V_G = 10$ V to 28 V. These high-conductance regions are attributed to the Kondo resonance effect. In the four-electron-shell filling system, the Kondo resonance effect appears at spin quantum numbers $S = 1/2$ and

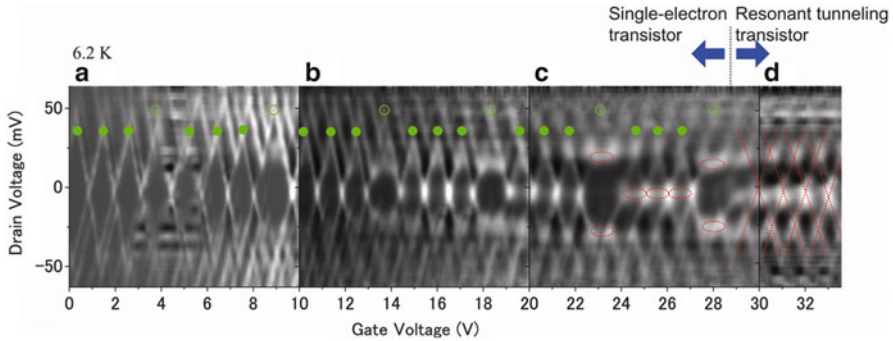


Fig. 16.16 (a)–(d) Differential conductance of the device as a function of the gate and drain voltages. The drain voltage V_D is applied in the range of $V_D = -63$ mV to $+63$ mV. The gate voltage V_G is applied separately over four ranges of $V_G = 0$ –10 V, $V_G = 10$ –20 V, $V_G = 20$ –30 V, and $V_G = 30$ V–33.5 V. The small Coulomb diamonds are marked by close circles, and the large Coulomb diamonds are marked by *open circles*

1 [32–38]. In the sequence of three small Coulomb diamonds marked by the three dotted circles, i.e., from $V_G = 24$ V to $V_G = 27$ V, the spin quantum number changes to $S = 1/2$, 1, and $1/2$ in that sequence. In the large Coulomb diamonds marked by dashed circles, i.e., $V_G = 23$ V and 28 V, the spin number becomes $S = 0$ at zero drain bias. However, the spin quantum number shifts to $S = 1$ at $V_D = -25$ mV and $+25$ mV in order to lower the energy in the quantum well, and Kondo resonance appears not at zero drain bias but at $V_D = -25$ mV and $+25$ mV, as indicated by the dashed circles in Fig. 16.16c [43]. This is the first reported demonstration of Kondo resonance observed only at the transition from the Coulomb-blockaded region to the resonant tunneling region in CNT.

The enlarged plot of the Kondo peaks obtained at the gate voltage ranges of $V_G = 14$ V to 18 V and $V_G = 23.7$ V to 27.7 V in Fig. 16.16 are shown in Figs. 16.17 and 16.18 with the contour lines, respectively. Figures 16.17a and 16.18a show the cross-sectional plots at the B–B' line (solid line) at around zero drain bias and the C–C' line (dotted line) at a finite drain bias in Figs. 16.17b and 16.18b. Figures 16.17c and 16.18c show the cross-sectional plots at the A–A' line shown in Figs. 16.17b and 16.18b. In Fig. 16.17b, c, the Kondo peaks are observed at around zero drain bias and gate bias voltages of $V_G = 15$ V, 16 V, and 17 V. In Fig. 16.18b, c, the Kondo peaks are observed at around zero drain bias and $V_G = 24.5$ V, 25.5 V, and 26.5 V. In Figs. 16.17a and 16.18a, the differential conductance becomes higher at the Coulomb oscillation valleys for the B–B' lines when compared with those for the C–C' lines. This indicates that the conductance at zero drain bias is higher than that at finite drain bias, though this conductance is in the Coulomb-blockaded region, i.e., this conductance value is the Kondo peak. Upon comparing Figs. 16.17a–c and 16.18a–c, it is observed that the Kondo peaks become larger and wider along the drain voltage axis with increasing gate bias. The full width at half maximum (FWHM) of the Kondo peak is 8.2 mV at $V_G = 16$ V in Fig. 16.17c, and it is 10.9 mV at $V_G = 26.5$ V in Fig. 16.18c.

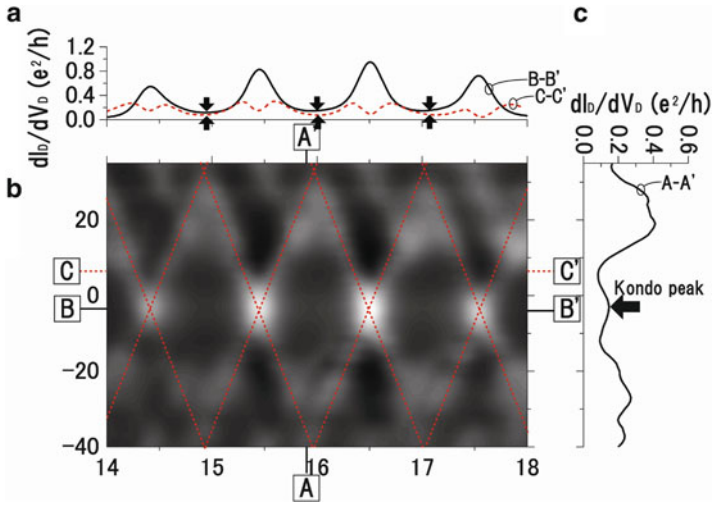


Fig. 16.17 (a) Cross-sectional plots at the B–B' line (solid line) at around zero drain bias and C–C' line (dotted line) at finite drain bias in (b). (b) Enlarged plot of Fig. 16.16b with contour lines at $V_D = -40$ mV to $+35$ mV and $V_G = 14$ – 18 V. (c) Cross-sectional plot at the A–A' line in (b)

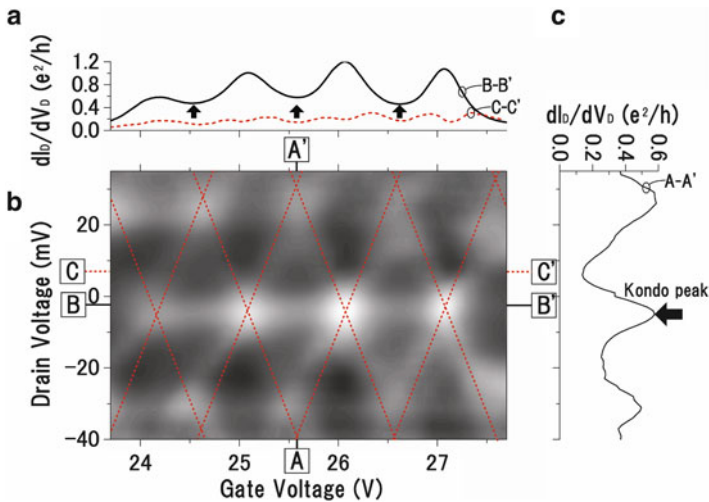


Fig. 16.18 (a) Cross-sectional plots at the B–B' line (solid line) at around zero drain bias and C–C' line (dotted line) at finite drain bias in (b). (b) Enlarged plot of Fig. 16.16c with contour lines at $V_D = -40$ mV to $+35$ mV and $V_G = 23.7$ – 27.7 V. (c) Cross-sectional plot at the A–A' line in (b)

The Kondo temperature T_K corresponds to the binding energy between the isolated electron in the CNT and the electrons in the electrodes via spin [2, 44]. The Kondo temperature can be roughly estimated from the FWHM of the Kondo resonance peak, i.e., the FWHM can be set as equal to $k_B T_K/e$, where k_B represents

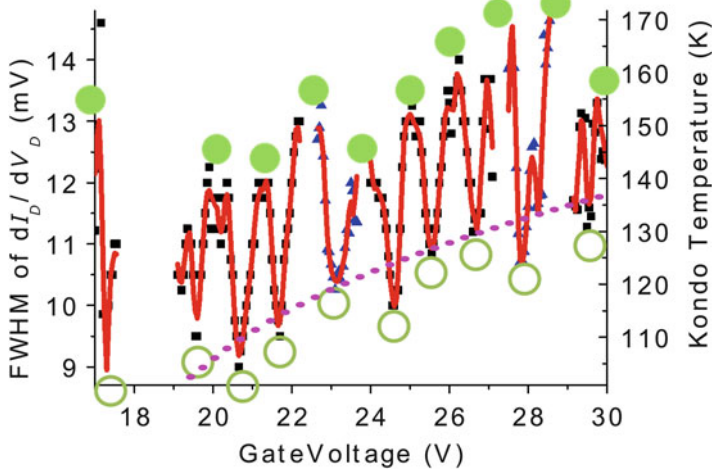


Fig. 16.19 Full width at half maximum of Kondo peaks (*left axis*) and estimated Kondo temperature (*right axis*) as function of applied gate voltage. The *blue triangles* represent the plot due to the triplet state. The peaks marked by *closed circles* indicate the Coulomb oscillation peaks. The valleys marked by *open circles* indicate the midpoint of the Coulomb oscillation peaks. The *pink dot line* is the calculated Kondo temperature, where the Fermi level was set at the center of quantum energy levels

the Boltzmann's constant and e denotes the elementary charge; the dephasing effect is ignored in this calculation [2, 44]. Figure 16.19 shows the FWHM (left axis) and the estimated Kondo temperature (right axis) as a function of the applied gate voltage. Here, the triangle-shaped plots represent the triplet state of the large Coulomb characteristics at $V_D = 25$ mV. The Kondo temperature shows a large dependence on the applied gate voltage [2, 45]. Figure 16.19 shows two important features. The first feature is the oscillation characteristic. The Kondo temperature shows a local maximum value at the edge of the Coulomb diamond (marked by closed circles) and a local minimum at the midpoint of the Coulomb diamond (as marked by open circles) [2, 45]. This is because the distance between the Fermi level and the quantum energy levels is one of the factors that determine the Kondo temperature. When this distance reaches a maximum, the Fermi level is at the center between the upper and lower quantum energy levels, i.e., at the midpoint of the Coulomb diamond, and the Kondo temperature reaches the local minimum value [2, 45]. When the Fermi level is close to the quantum energy levels, i.e., at the edge of the Coulomb diamond, the Kondo temperature reaches the local maximum value. Thus, the oscillation characteristics of the Kondo temperature could be observed along with variation in the gate bias, as shown in Fig. 16.19. In Fig. 16.19, the pink dot line is the calculated Kondo temperature, where the Fermi level was set at the center of quantum energy levels [46]. The calculated Kondo temperature is well fitted to the experimentally obtained Kondo temperature at the local minimum.

The second point of discussion in the figure is that the local minimum values of the Kondo temperature (marked by the open circles) increase with increasing gate voltage. The tunneling probabilities of the barriers are also a factor that determines the Kondo temperature [45]. When the depletion layers formed by the Schottky barriers at the source and drain contacts become thinner with increasing applied gate voltage, the tunneling probabilities increase, and consequently, the spin correlation between the isolated electron in the CNT and the electrons in the electrodes grows stronger. Therefore, the local minimum of the Kondo temperature increases with increasing gate voltage [2, 45]. Therefore, Fig. 16.19 also reveals that the increase in Kondo temperature can be attributed to not only the energy distance between the Fermi level and quantum energy levels but also to the tunneling probabilities that confine the electron. This is the first reported demonstration of the Kondo temperature being modulated by variation of the barrier thickness. In our study, a large Kondo temperature range from $T_K = 105$ K to 170 K was realized by modulating the applied gate voltage at 6.2 K; this corresponds to an increase of 162 % in the Kondo temperature.

In order to realize the Kondo state, there must be sufficient correlation of the electrons in the CNT and those in the electrodes in terms of spin, and the electron in the CNT must also be sufficiently isolated from the many electrons in the electrode [2, 43–45]. In our fabricated device, the isolation of the electron in the CNT is achieved by the presence of Schottky barriers at the source and drain contacts. Because of low carrier density in the CNT, potential energy modulation becomes possible over a wide range via modulation of the gate bias. When the applied gate voltage is low, the Schottky barriers are thick (as schematically shown in Fig. 16.15b), and the electron in the CNT is completely isolated and has poor correlation with the electrons in the electrode in terms of spin. Therefore, the Kondo peaks cannot be observed at gate voltages less than $V_G = 10$ V, as observed in Fig. 16.16a. When the Schottky barriers become thinner with increasing gate voltage, the isolated electron in the CNT has sufficient correlation with the electrons in the electrodes to attain the Kondo state. Consequently, Kondo peaks are observed at the gate voltage range between $V_G = 10$ V and $V_G = 28$ V, as shown in Fig. 16.17b, c. When the Schottky barriers become too thin (Fig. 16.1c), thereby corresponding to gate voltages larger than $V_G = 28$ V (Fig. 16.17d), the electron in the CNT cannot be sufficiently isolated from the electrons in the electrode, and the Kondo state cannot be realized.

16.4.3 Summary

In summary, our study is the first to demonstrate that the Kondo temperature can be modulated by the varying the barrier thickness. Our study is also the first to demonstrate that Kondo resonance phenomena can be observed only at the transition region between the Coulomb blockade characteristic and the resonant tunneling characteristic regions in a CNT-channel Schottky barrier transistor. The transition

of the characteristics was realized via control of the tunneling barrier thickness by varying the applied gate voltage. The Kondo temperature was tuned by varying two factors. One factor is the distance between the Kondo resonance energy level and the quantum energy levels; however, this distance can be modulated only in the range of the quantum energy separation, i.e., several tens of millivolts. This limits the range of the Kondo temperature tuning. On the other hand, modification of the tunneling barrier thicknesses can tune the Kondo temperature over a wide range from $T_K = 105$ K to 170 K; this range corresponds an increase of 162 %.

16.5 Summary of the Chapter

The durability of the electron in the CNT has been used for the device operation as described above. The tunneling barriers consist of the Schottky barriers easily modulated by the applied gate voltage. Therefore, the tunability of the tunneling probabilities, i.e., the localization of the wave function of the electron confined in the CNT quantum dot, has been easily realized in the CNT quantum device as shown above. This feature is originated in the dilution of numbers on charges in the CNT. This is one of most important features in the one-dimensional semiconductor materials, even as other features, e.g., the Von Hove singularity and the suppression of the back scatterings.

References

1. Javey A, Guo J, Wang Q, Lundstrom M, Dai H (2003) Ballistic carbon nanotube field-effect transistors. *Nature* 424:654
2. Heinze S, Tersoff SJ, Martel R, Derycke V, Appenzeller J, Avouris P (2002) Carbon nanotubes as Schottky barrier transistors. *Phys Rev Lett* 89:106801
3. Martel R, Derycke V, Lavoie C, Appenzeller J, Chan KK, Tersoff J, Avouris P (2001) Ambipolar electrical transport in semiconducting single-wall carbon nanotubes. *Phys Rev Lett* 87:256805
4. Kamimura T, Matsumoto K (2005) Room-temperature single-hole transistors made using semiconductor carbon nanotube with artificial defects near carrier depletion region. *Jpn J Appl Phys* 44:1603
5. Noshio Y, Ohno Y, Kishimoto S, Mizutani T (2006) Relation between conduction property and work function of contact metal in carbon nanotube field-effect transistors. *Nanotechnology* 17:3412
6. Liang W, Bockrath M, Bozovic D, Hafner JH, Tinkham M, Park H (2001) Quantum interference in nanotubes. *Nature* 411:665
7. Kong J, Yenilmez E, Tomblor TW, Kim W, Dai H (2001) Quantum interference and ballistic transmission in nanotube electron waveguides. *Phys Rev Lett* 87:106801
8. Suzuki M, Ishibashi K, Ida T, Tsuya D, Toratani K, Aoyagi Y (2001) Fabrication of single and coupled quantum dots in single-wall carbon nanotubes. *J Vac Sci Technol B* 19:2770
9. Kamimura T, Ohno Y, Matsumoto K (2009) Transition between particle nature and wave nature in single-walled carbon nanotube device. *Jpn J Appl Phys* 48:15005

10. Kamimura T, Ohno Y, Matsumoto K (2009) Carbon nanotube Fabry–Perot device for detection of multiple single charge transitions. *Jpn J Appl Phys* 48:025001
11. Postma HWC, Teepen T, Yao Z, Grifoni M, Dekker C (2001) Carbon nanotube single-electron transistors at room temperature. *Science* 293:76–79
12. Kamimura T, Ohno Y, Matsumoto K (2004) Reduction of hysteresis characteristics in carbon nanotube field-effect transistors by refining process. *IEICE Trans Electron* E87-C:1795
13. Foxman EB, McEuen PL, Meirav U, Wingreen NS, Meir Y, Belk PA, Wind SJ (1993) Effects of quantum levels on transport through a Coulomb island. *Phys Rev B* 47:10020
14. Tsu R, Esaki L (1973) Tunneling in a finite superlattice. *Appl Phys Lett* 22:562
15. Kamimura T, Matsumoto K (2005) Electrical heating process for p-type to n-type conversion of carbon nanotube field effect transistors. *Jpn J Appl Phys* 44:1603
16. Allen SS, Richardson SL (1994) Theoretical investigations of resonant tunneling in asymmetric multibarrier semiconductor heterostructures in an applied constant electric field. *Phys Rev B* 50:11693
17. Tans SJ, Devoret MH, Groeneveld RJA, Dekker C (1998) Electron–electron correlations in carbon nanotubes. *Nature* 394:761–764
18. Jarillo-Herrero P, Sapmaz S, Dekker C, Kouwenhoven LP, van der Zant HSJ (2004) Electron–hole symmetry in a semiconducting carbon nanotube quantum dot. *Nature* 429:389–392
19. Maki H, Ishiwata Y, Suzuki M, Ishibashi K (2005) Electronic transport of a carbon nanotube quantum dot in different coupling regimes. *Jpn J Appl Phys* 44:4269–4271
20. Jorgensen HI, Grove-Rasmussen K, Novotny T, Flensberg K, Lindelof PE (2006) Electron transport in single-wall carbon nanotube weak links in the Fabry–Perot regime. *Phys Rev Lett* 96:207003
21. Cao J, Wang Q, Dai H (2005) Electron transport in very clean, as-grown suspended carbon nanotubes. *Nat Mater* 4:745–749
22. Grove-Rasmussen K, Jorgensen HI, Lindelof PE (2007) Fabry–Perot interference, Kondo effect and Coulomb blockade in carbon nanotubes. *Phys E* 40:92–98
23. Kamimura T, Matsumoto K (2009) Gate induced crossover between Fabry–Pérot and quantum dot behavior in a single walled carbon nanotube hole transistor. *J Appl Phys* 106:113718–113724
24. Moriyama S, Fuse T, Suzuki M, Aoyagi Y, Ishibashi K (2005) Four-electron shell structures and an interacting two-electron system in carbon-nanotube quantum dots. *Phys Rev Lett* 94:186806
25. Liang W, Bockrath M, Park H (2002) Shell filling and exchange coupling in metallic single-walled carbon nanotubes. *Phys Rev Lett* 88:126801
26. Ng TK, Lee PA (1988) On-site Coulomb repulsion and resonant tunneling. *Phys Rev Lett* 61:1768–1771
27. Racec ER, Wulf U (2001) Resonant quantum transport in semiconductor nanostructures. *Phys Rev B* 64:115318
28. Orellana P, Claro F, Anda E, Makler S (1996) Self-consistent calculation of resonant tunneling in asymmetric double barriers in a magnetic field. *Phys Rev B* 53:12967
29. Kamimura T, Matsumoto K (2006) Coherent transport of hole and Coulomb blockade phenomenon in long p-type semiconductor carbon nanotube. *Jpn J Appl Phys* 45:338
30. Kamimura T, Maeda M, Sakamoto K, Matsumoto K (2005) Room-temperature single-hole transistors made using semiconductor carbon nanotube with artificial defects near carrier depletion region. *Jpn J Appl Phys* 44:461
31. Kim W, Javey A, Vermesh O, Wang Q, Li Y, Dai H (2003) Hysteresis caused by water molecules in carbon nanotube field-effect transistors. *Nano Lett* 3:193
32. Cronenwett SM, Oosterkamp TH, Kouwenhoven LP (1998) A tunable Kondo effect in quantum dots. *Science* 281:540–544
33. Simmel F, Blick RH, Kotthaus JP, Wegscheider W, Bichler M (1999) Anomalous Kondo effect in a quantum dot at Nonzero bias. *Phys Rev Lett* 83:804–807
34. Park J, Pasupathy AN, Goldsmith JJ, Chang C, Yaish Y, Petta JR, Rinkski M, Sethna JP, Abruna HD, McEuen PL, Ralph DC (2002) Coulomb blockade and the Kondo effect in single-atom transistors. *Nature* 417:722–725

35. Makarovski A, Liu J, Finkelstein G (2007) Evolution of transport regimes in carbon nanotube quantum dots. *Phys Rev Lett* 99:066801
36. Nygard J, Cobden DH, Lindelof PE (2000) Kondo physics in carbon nanotubes. *Nature* 408:342–346
37. van der Wiel WG, De Franceschi S, Fujisawa T, Elzerman JM, Tarucha S, Kouwenhoven LP (2000) The Kondo effect in the Unitary Limit. *Science* 289:2105–2108
38. Ralph DC, Buhrman RA (1994) Kondo-assisted and resonant tunneling via a single charge trap: a realization of the Anderson model out of equilibrium. *Phys Rev Lett* 72:3401–3404
39. Wang X (1997) Quantum conductance of the single-electron transistor. *Phys Rev B* 55:12868
40. Schmid J, Weis J, Eberl K, Klitzing KV (1998) A quantum dot in the limit of strong coupling to reservoirs. *Phys B* 256:182–185
41. Visscher EH, Verbrugh SM, Lindeman J, Hadley P, Mooij JE (1995) Fabrication of multilayer single-electron tunneling devices. *Appl Phys Lett* 66:305
42. Saitoh M, Hiramoto T (2004) Extension of Coulomb blockade region by quantum confinement in the ultrasmall silicon dot in a single-hole transistor at room temperature. *Appl Phys Lett* 84:3172
43. Ono Y, Takahashi Y (2003) Electron pump by a combined single-electron/field-effect-transistor structure. *Appl Phys Lett* 82:1221
44. Andresen SES, Wu F, Danneau R, Gunnarsson D, Hakonen PJ (2008) Highly sensitive and broadband carbon nanotube radio-frequency single-electron transistor. *J Appl Phys* 104:033715
45. Biercuk MJ, Reilly DJ, Buehler TM, Chan VC, Chow JM, Clark RG, Marcus CM (2006) Charge sensing in carbon-nanotube quantum dots on microsecond timescales. *Phys Rev B* 73:201402
46. Aassime A, Delsing P, Claeson T (2001) A sensitive and fast radio frequency single-electron transistor. *Nanotechnology* 12:96

Chapter 17

Quantum-Dot Devices with Carbon Nanotubes

Koji Ishibashi

Abstract Carbon nanotubes (CNTs) are attractive building blocks for quantum dots because of their extremely small diameters. In this chapter, typical behaviors of the carbon nanotube quantum dots and their artificial atom features are discussed. Then, some applications to the quantum-dot devices are presented. Some challenges on the necessary technologies toward integrated quantum-dot devices are also described.

Keywords Quantum dot • Single-electron device • Coulomb blockade • Artificial atom

17.1 Introduction

A quantum dot is a structure where electrons are confined in three dimensions and has been studied for functional device applications as well as for exploring interesting physics in nanoscale. The spacing between confined discrete energy levels (ΔE) is an important energy scale associated with the quantum dot, which becomes large as the size of the quantum dot becomes small. In the surface-gated quantum dots formed at an interface between the GaAs/AlGaAs heterostructures, which have been widely used to study transport physics [1], a size of the dot is in a range of submicron. This is limited by the resolution of electron beam lithography, and the corresponding level spacing is of the order of ~ 0.1 meV. Another important energy scale associated with the quantum dot is a charging energy of single electrons ($E_c = e^2/C_\Sigma$: e is an elementary charge and C_Σ is a self-capacitance of the dot). It is of the order of ~ 1 meV for the lithographically defined quantum dots. With those energy scales, quantum confinement effects and single-electron effects are usually observable below 1 K. Therefore, it is natural to use carbon nanotubes as building blocks of the extremely small quantum dot to realize larger quantum effects and higher temperature operation of quantum-dot devices.

K. Ishibashi (✉)

Advanced Device Laboratory, and Center for Emergent Matter Science (CEMS), RIKEN, 2-1, Hirosawa, Wako, Saitama 351-0198, Japan
e-mail: kishiba@riken.jp

Besides the interesting electronic properties and device applications, which are described in this chapter, the carbon nanotubes may have interesting optical properties as well because of the expected large exciton energy that arises from the one-dimensional nature of single-walled carbon nanotubes (SWCNTs) [2, 3]. Excitons in the quantum dot could have larger oscillator strength, compared with bulk excitons, which can be applied for their coherent manipulation [4, 5] and a single photon source [6], as have been intensively studied in self-assembled semiconductor quantum dots. The bandgap of the semiconducting nanotubes lies in the optical communication wavelength [7], which is of practical importance for light emission sources.

The quantum dot could be applied for various functional devices [8]. It has been already applied for lasers with self-assembled semiconductor quantum dots, but there are many other possible applications. The Coulomb blockade in the quantum dot can be used for single-electron devices, which include a current standard with a turnstile [9] and a pump [10], single-electron logic [11] and memory devices [12], and logic devices with new architectures such as the quantum-dot cellular automata [13]. These single-electron devices only need the Coulomb blockade effect, so the smaller structures produce better performance. The operation of those devices has been demonstrated at low temperatures, typically below 1 K, with the surface-gated GaAs/AlGaAs quantum dots and the metallic dots (Al/AlOx). The techniques used are flexible to fabricate the device structures by using electron beam lithography, but the size of the structures is limited and, correspondingly, the possible operation temperature is limited. With a SWCNT quantum dot, a room temperature operation has been demonstrated with artificially formed tunnel barriers [14].

Another possible application of the quantum dot would be the quantum computing devices that require the quantum coherence as well [15]. To use electron spins as quantum media for computation (spin qubit) would be advantageous because of the long coherence time. The spin qubit has already been demonstrated with the surface-gated GaAs/AlGaAs [16], but it has been found that the nuclear spins of the host atoms (Ga, As) could be a major decoherence source [17]. In this regard, quantum dots with group IV materials are preferred because of the natural abundance of the zero-nuclear spin atoms [18, 19]. Carbon nanotubes could also be a good candidate for this, but a spin-orbit interaction (SOI) would be an issue to be made clear, which can cause decoherence source. The atomic SOI is known to be small in carbon atoms, but the SOI in the carbon nanotube is predicted in relation to the curvature effects [20, 21] and was experimentally demonstrated in the ultraclean SWCNTs [22, 23].

Despite the expected advantages of the carbon nanotubes for the quantum-dot devices, the experimental demonstration has been limited, mainly because the device fabrication processes suitable for the nanotubes have not been developed yet. In most cases, the quantum dot is formed simply by depositing metallic contact on top of individual carbon nanotubes. This method is not flexible to fabricate integrated quantum-dot devices and circuits. Another issue is low reproducibility or yield to realize designed structures and behaviors as quantum dots. The problems would be a quality of the grown nanotubes and its degradation during the device fabrication processes. Besides, technologies, such as a separation or selected growth

of the metallic or semiconducting nanotubes, aligned growth on a substrate, and the reliable tunnel barrier formation, have to be developed. Various attempts and techniques have been tested, but still further study is needed.

In this chapter, we start with the basic transport properties of the quantum dots with discrimination between “classical” and “quantum” dots which are usually used without clear definition. Then, unique features of the SWCNT quantum dot as an artificial atom are described for the metallic SWCNT, and electron–hole symmetries observed in the semiconducting SWCNT are described. Some efforts toward quantum-dot-based integrated devices and circuits are described, which includes a local tunnel barrier formation technique and an aligned nanotube formation technique. Quantum-dot-based devices, such as double-quantum dots, single-electron logic devices, and quantum THz detection, demonstrated with carbon nanotubes, are described. Finally, conclusions are made with future challenges and perspectives.

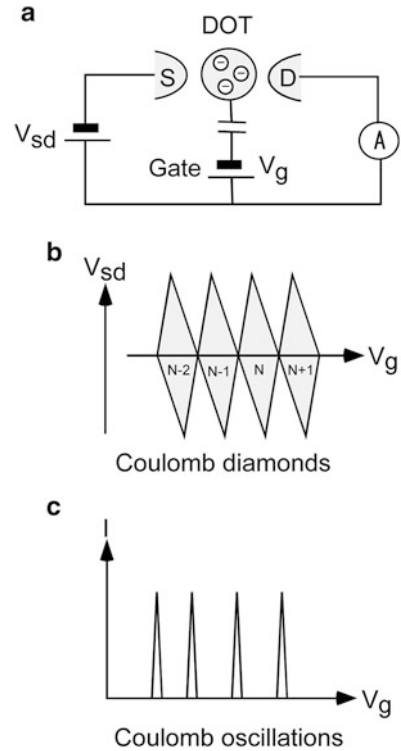
17.2 Quantum Dot and Artificial Atom

17.2.1 Coulomb Blockade and Single-Electron Transistor

The Coulomb blockade effect plays an essential role in the transport through the quantum dot [24]. In the simplest case, the Coulomb blockade appears in the current-biased single tunnel junction. Electron tunneling is blocked when the voltage of the junction is smaller than $e/2C$ and is allowed when it is larger than that, where e is an elementary charge and C the capacitance of the junction. To suppress thermal fluctuations of charges on the capacitor, the charging energy ($E_c = e^2/C$) should be much larger than $k_B T$, where k_B is the Boltzmann’s constant, and to suppress quantum fluctuations, the tunnel resistance of the junction should be much larger than the quantum resistance ($R_q \sim h/e^2$, where h is the Planck’s constant). In the current-biased single junction, the voltage of the junction should oscillate in time. But it is experimentally very difficult to observe because the junction is easily voltage biased in many experimental situations, which hinders the effect.

The two tunnel junctions connected in series, a single-electron transistor (SET) configuration where the dot is connected with a gate voltage (Fig. 17.1a), can make use of the Coulomb blockade effects even when the junctions are voltage biased. The charge fluctuations in each capacitor are possible as far as the sum of voltages at each capacitor is equal to the applied source–drain voltage (V_{sd}). The operation of the single-electron transistor is characterized by the charge stability diagram, commonly called Coulomb diamonds, which shows the conductance as functions of the gate voltage (V_g) and source–drain voltage, V_{sd} (Fig. 17.1b). It is obtained based on the classical electrostatic energy arguments, so this does not include any quantum effect of discrete energy levels. The simple model is a good approximation for the classical dot, where $\Delta E \ll k_B T$. For the quantum dot, where $\Delta E \gg k_B T$, the diagram

Fig. 17.1 (a) Equivalent model of the single-electron transistor. (b) Current or conductance as functions of the source–drain voltage (V_{sd}) and the gate voltage (V_g). In the diamond-shaped shaded regions, a current is blocked (Coulomb blockade). The plot is called Coulomb diamonds. (c) Current as a function of the gate voltage for the small V_{sd} . The oscillations are called Coulomb oscillations



and Coulomb oscillations are modified, as described in the next section. The dots fabricated with the carbon nanotubes usually behave as the quantum dot. In the diamond-like regions which lie periodically along the gate voltage, the conductance is zero, meaning the current is blocked (Coulomb blockade). So, the number of electrons is fixed. An important feature of the SET is that the number of electrons in the adjacent diamonds differs exactly by one. In a linear response regime, where V_{sd} is small, the current flows at gate voltages where two adjacent diamonds meet, as shown in Fig. 17.1c, and the current flows periodically as a function of the gate voltage (Coulomb oscillations).

Figure 17.2 shows (a) the Coulomb diamonds and (b) the Coulomb oscillations of the classical SET fabricated with a Si nanowire (NW) [25]. The Si-NW dots tend to be classical because of the relatively large diameter for the present NW (~ 70 nm) and a heavier effective mass compared with those of GaAs and InAs. The periodic and similarly sized diamonds lie along the gate voltage, a typical behavior of the classical dot. Another characteristic behavior of the classical dot is a similar height of each Coulomb oscillation peak. This is because a lot of energy levels come into the bias window set by V_{sd} and the couplings between each level and the source–drain electrode are averaged out, independent of the number of electrons in the dot. This leads to the similar current peak height of each Coulomb oscillation.

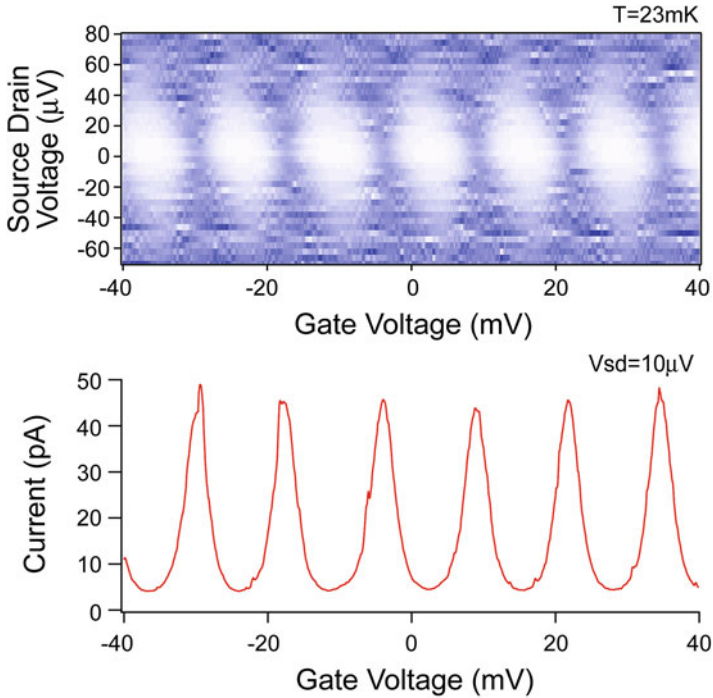


Fig. 17.2 Coulomb diamonds (*upper*) and Coulomb oscillations (*lower*) for the Si nanowire SET [25]

This behavior should be contrasted with the quantum dot, where the peak height of each Coulomb oscillation varies very much, depending on the number of electrons in the dot. This is because one or few levels come into the bias window to flow current.

17.2.2 Quantum Dot and Artificial Atom (Metallic Tubes)

The arguments in the previous section are for the classical dots. In the quantum dots where the level spacing due to confinement cannot be ignored, the SET behaviors need to be modified [26]. In this case, the Coulomb oscillations are no longer periodic and should be $E_c + \Delta E$. In the simplest case, only with a twofold spin degeneracy in the confined levels, the Coulomb oscillations have a two-electron periodicity, as shown in Fig. 17.3, where the larger diamond or the larger period is indicated by the circle [27].

This effect is called the even–odd effect. When the number of electrons in the dot is odd, the next electron sits on the topmost level of the confined states with the opposite spin direction to the other electron. In this case, the addition energy is E_c .

Fig. 17.3 Coulomb diamonds (*upper*) and Coulomb oscillations in the two-electron periodicity regime. The *circles* show the larger diamonds [27]

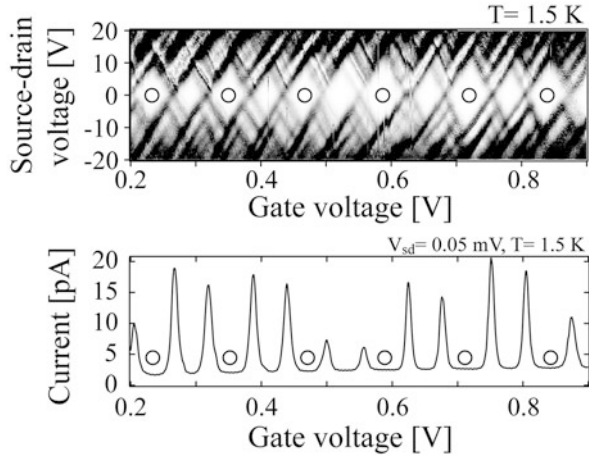
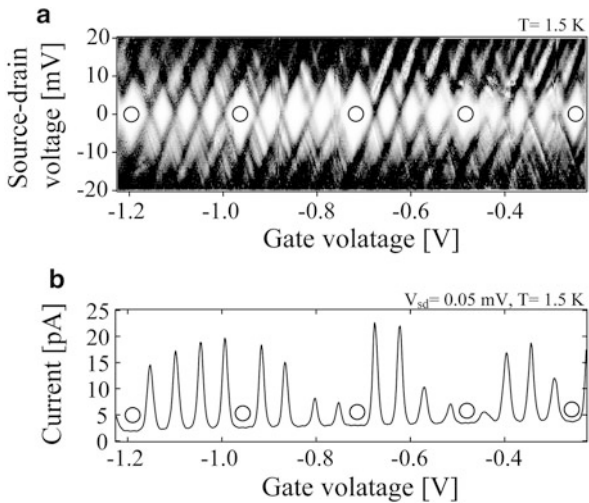


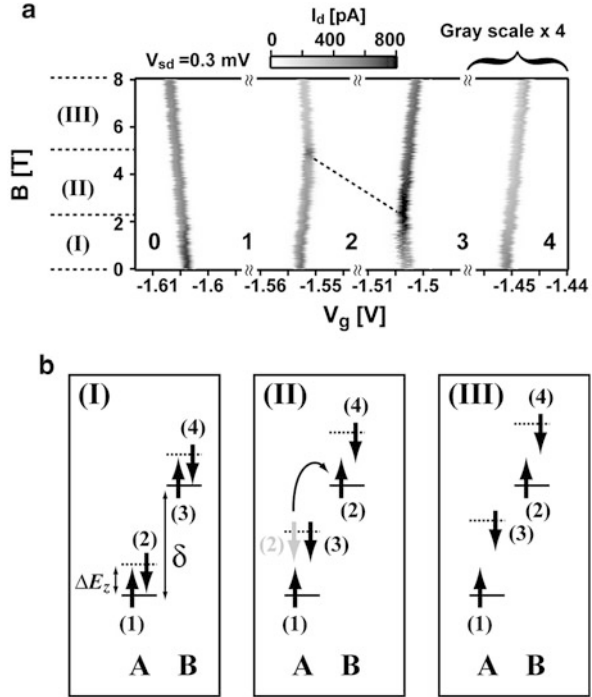
Fig. 17.4 Coulomb diamonds (*upper*) and Coulomb oscillations in the four-electron periodicity regime. The *circles* show the larger diamonds [27]



When the number of electrons is even, the next electron sits on the upper level by ΔE from the occupied topmost level. In this case, the addition energy is $E_c + \Delta E$. For this simple shell filling to occur and to be observable, (1) each level has to have only twofold spin degeneracy without other degeneracies; (2) ΔE should be larger than other energy scales associated with electron–electron interactions, the on-site Coulomb interaction energy (U), and the exchange interaction energy (J); and (3) $E_c \sim \Delta E$. In the present sample, $E_c \sim 9$ meV and $\Delta E \sim 3$ meV. In practice, the effect has been observed in very small quantum dots as well as the SWCNT quantum dots [28, 29].

In the ideal cases, the Coulomb oscillations should show a four-electron periodicity for the SWCNT quantum dot because there is a twofold degeneracy of the orbital states in addition to the twofold spin degeneracy [30]. Figure 17.4

Fig. 17.5 Shell filling in magnetic fields at 40 mK. (a) Evolution of Coulomb peak. (b) Shell filling scheme in (I) low, (II) intermediate, and (III) high magnetic fields. ΔE_z is the Zeeman energy and δ is the energy mismatch in the A and B bands. (1)–(4) indicate the order of electrons filling in the dot [32]

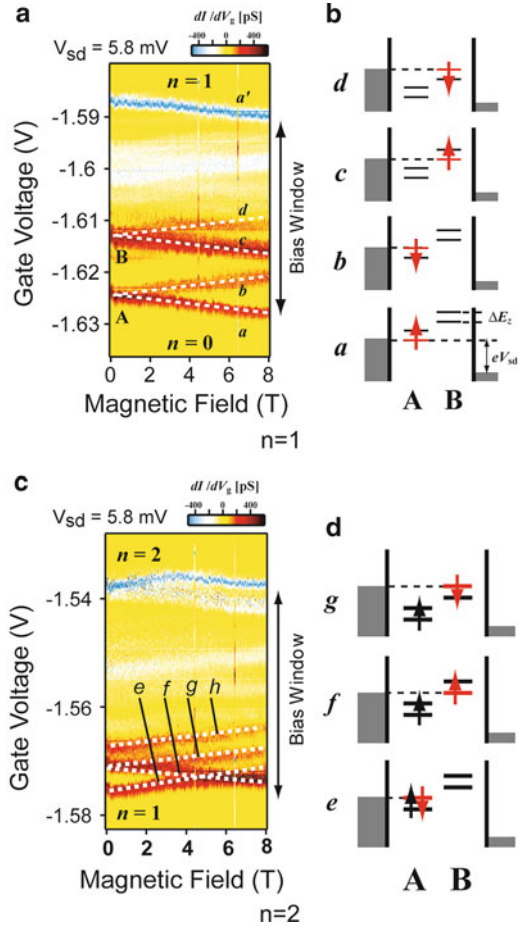


shows Coulomb diamonds and Coulomb oscillations that show the four-electron periodicity. In every four electron, there appears the larger diamonds and the larger peak distance between the adjacent peaks, as indicated by the circle. In general, the twofold degeneracy of the orbital states is easily lifted by various imperfections of the nanotube. Even in the sample shown in Fig. 17.4, the two states that should be degenerated may have a small energy difference (δ). When $\delta \sim \Delta E$, the two-electron periodicity should be observed rather than the four-electron periodicity [31].

The four-electron shell filling scheme can be understood by investigating an evolution of each Coulomb peak position as a function of magnetic fields [32]. Figure 17.5a shows the result of the peak evolution in the four-electron periodicity regime. The magnetic field range can be divided into three regions that have a different shell filling. Basically, a direction the peak moves in determines the spin direction, from which the shell filling is evaluated. There is an energy level mismatch due to the lifted degeneracy of the orbital states, which is denoted by δ , and each level is Zeeman-split in the magnetic field (ΔE_z). The shell filling scheme is indicated in Fig. 17.5b in the three magnetic field ranges. In the region (II), a spin-flip of the second electron occurs during the gate sweep. This is because each level is shifting at a different rate with the gate voltage sweep [33], and Hund's rule is playing a central role to determine the shell filling [34].

An energy spectrum of the quantum dot or artificial atom can be investigated by measuring a Coulomb peak with a large bias voltage ($V_{sd} > \Delta E$) [32]. Whenever

Fig. 17.6 Energy spectrum in magnetic fields for (a) one electron and (c) two electrons in the dot. $T = 40\text{mK}$ (b) and (d) show the process that produces each line for one electron and two electrons in the dot, respectively. Each line appears when the electron indicated by the red arrow (this indicates the spin direction) enters the dot [32]



a new level comes in or out of the bias window during a gate sweep, a current changes in a Coulomb peak and they are made clearer by differentiating the current with respect to the gate voltage. Figure 17.6 shows such plots as a function of the magnetic field for the peaks that occur when the number of electrons in a shell changes between 0 and 1 (a and b) and between 1 and 2 (c and d). The energy spectrum in the former case is simple (Fig. 17.6a). There are two confined states that split into two due to the Zeeman effect with increasing magnetic field. Lines indicated by a, b, c, and d correspond to the situations shown in Fig. 17.6b. The latter is a bit complicated because quantum states in this situation are those of a two-electron system, where the singlet and triplet states are the possible two-electron states. The lines f and g correspond to the triplet states, while the line h corresponds to the singlet state, and there exists an energy difference at $B=0$ between the triplet states (lines f and g) and the singlet state, which corresponds to the exchange interaction energy (J).

The single-walled carbon nanotubes provide a simple model of an artificial atom with a one-dimensional hard-wall potential. This is an advantage over quantum dots with complicated shell structures and quantum dots without the shell structures in terms of determination of the spin configurations, which is good for the spin qubit. For example, in the even–odd regime, the spin qubit is realized when the number of electrons is odd. The electron–electron interaction effects are relatively small for the shell filling in the SWCNT quantum dot because ΔE is larger than other energy scales associated with the effects [32].

17.2.3 Quantum Dots with Semiconducting Tubes

An interesting characteristic of the semiconducting carbon nanotubes would be the ambipolar behaviors. In the semiconducting SWCNTs, as shown in Fig. 17.7a, the current decreases and stays constant and increases again as a gate voltage is increased from a large negative value [35]. The region where a current decreases with the gate voltage corresponds to a p-type carrier transport regime, and the region where it increases corresponds to an n-type carrier transport regime. In between

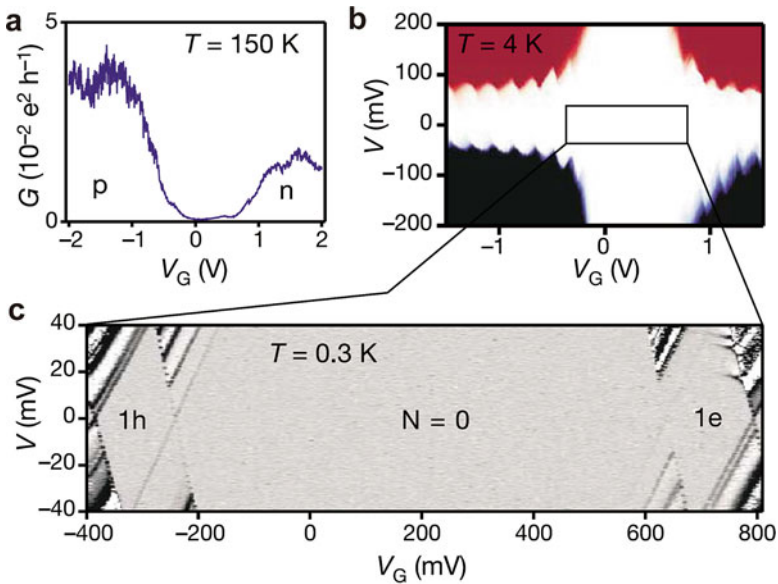


Fig. 17.7 Symmetric transport characteristics of an individual semiconducting SWCNT. (a) Ambipolar characteristic of the current as a function of a gate voltage. (b) Conductance as a function of V_{sd} and V_g the Coulomb diamonds. (c) Enlarged diamonds around zero electrons. The right diamond corresponds to one electron (1e) in the dot, while the left diamond corresponds to one hole (1h) in the dot (Figures taken from [35])

the two regions, the current does not flow because the Fermi level in the nanotube locates in a bandgap [36]. The Coulomb diamonds for the ambipolar quantum dots show symmetric diamonds in the electron and hole transport regimes (Fig. 17.7b,c). This is because of the symmetric energy dispersion for holes and electrons in the carbon nanotube, which should be contrasted with semiconductors where the dispersion for electrons in a conduction band and holes in a valence band is different.

In the semiconducting nanotubes with metallic contacts, carriers are injected from the contact through the Schottky barriers formed between the nanotube and the contact. The carrier type should be determined by the work function difference between the metal and the nanotube [36]. In practice, however, p-type behaviors are widely observed when the samples are fabricated and measured in air mainly because of absorbed molecules at the junction such as water or oxygen. Figure 17.8 shows the single-electron transport behaviors of the p-type semiconductor quantum dot [37]. An important feature here is that the single-dot behaviors with periodic Coulomb oscillations are observed when the gate voltage is small (~ 2 V) (Fig. 17.8b,c), but the multi-dot behaviors with irregular peak spacings (stochastic Coulomb blockade [38, 39]) are observed as the gate voltage is further increased, and finally, the current becomes totally zero, meaning that

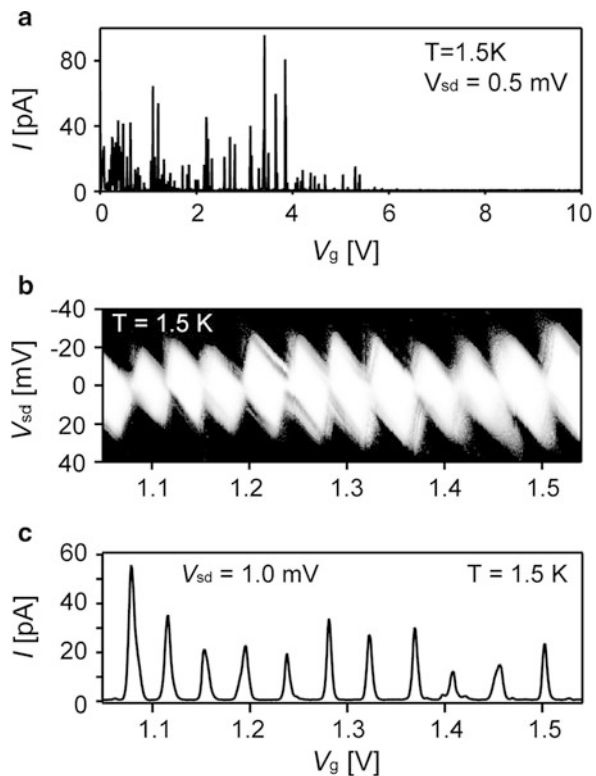


Fig. 17.8 Quantum-dot behaviors in the p-type semiconducting SWCNT. (a) Coulomb oscillations in a small gate voltage range (~ 1 V), (b) Coulomb diamonds, and (c) Coulomb oscillations. In this range, the sample behaves as a single-quantum dot [37]

holes are completely depleted (Fig. 17.8a). The multi-dot behaviors observed before the carriers are depleted occurs because of the multi-tunnel barrier formation due to possible potential fluctuations. The multi-dot behaviors appear to be observed more frequently in the semiconducting nanotubes rather than in the metallic nanotubes, possibly because the semiconducting nanotubes are much more sensitive to disorders coming from impurities and defects, etc. [40, 41].

17.3 Fabrication Process

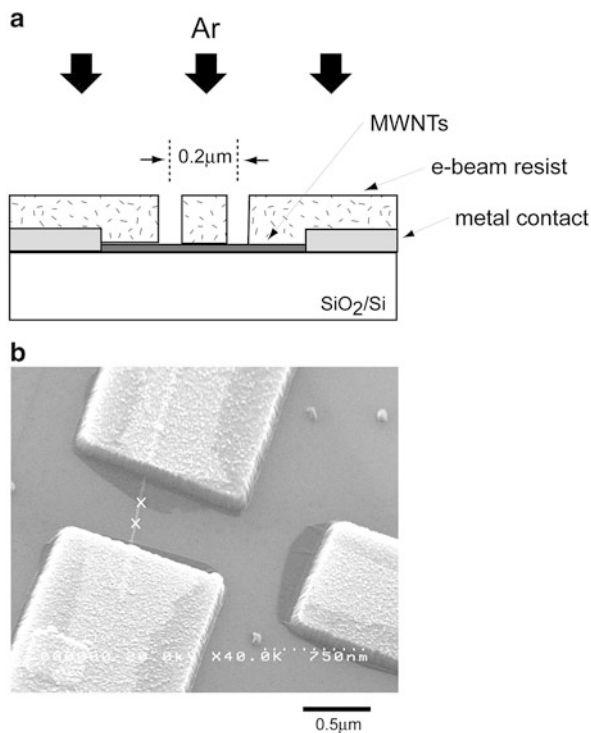
In an early stage to study the transport properties of individual carbon nanotubes, nanotubes were first randomly dispersed on a substrate and electrical contacts to flow a current and gates were formed to the specific nanotubes dispersed on the substrate by using a standard mark alignment technique in electron beam lithography [42]. The quantum dots are formed simply by depositing metallic contacts on top of the nanotube. Or nanotubes were dispersed on a substrate on which electrical contacts were preformed [43]. The Schottky barriers formed at an interface between the SWCNT and a metal worked as tunnel barriers for the SET. To fabricate integrated SET circuits with many SETs, it is necessary to develop a technique to form the tunnel barrier at desired positions. Another important technique to develop is to align nanotubes in a controlled manner, instead of the random distribution on the substrate. To meet these requirements, we have developed (1) a technique to form the tunnel barriers by local Ar ion beam irradiation and (2) a technique to grow aligned nanotubes and subsequent transfer to a suitable substrate for device fabrication.

17.3.1 Tunnel Barrier Formation

Figure 17.9a shows the fabrication process of the SET in a multi-walled carbon nanotube (MWCNT), and a SEM image of the fabricated SET is shown in Fig. 17.9b where the crosses indicate the irradiated region [44]. An advantage to use MWCNTs would be that the ohmic contacts are easily formed because of the larger diameter of the nanotube. In typical conditions to form the tunnel barrier, an acceleration voltage of 300 V and a dose of 10 mC/cm² were used. The mechanism of the tunnel barrier formation due to the ion bombardment is the sputtering of host carbon atoms, which was confirmed by the height measurements of the irradiated MWCNTs with an atomic force microscope (AFM) [44].

Figure 17.10 shows (a) the Coulomb oscillations and the (b) Coulomb diamonds of a fabricated sample. The data appear to show the single-dot behaviors with an indication of the excited states. The charging energy of the dot is about 17 meV (~ 200 K). Correspondingly, the Coulomb oscillations are clearly observable up to ~ 50 K. But the sample showed multi-dot behaviors in the mK temperatures,

Fig. 17.9 (a) Schematic picture of the local ion beam irradiation technique to fabricate the SET. (b) SEM image of the fabricated SET in a MWCNT. The cross (x) mark shows an approximate position where the tunnel barrier should be formed by the ion beam irradiation [44]



suggesting that unwanted tunnel barriers were also formed, which became important only at low temperatures and not at higher temperatures possibly due to a small barrier height.

This technique can be applied also for the SWCNTs with reduced acceleration energy and dose [45]. Figure 17.11 shows Coulomb oscillations of one of the SETs fabricated with the method: (a) in low temperatures (below 20 K) and (b) in high temperatures (above 80 K). The acceleration voltage and the dose used were 100 V and $100\mu\text{C}/\text{cm}^2$, respectively, to form the tunnel barriers. When the similar conditions for the MWCNT were used, the SWCNT disappeared completely by sputtering. The quantum-dot behaviors are similar with those of the MWCNT except the temperature range. At low temperatures (Fig. 17.11a), the Coulomb oscillations are aperiodic, suggesting the formation of multi-dots (unwanted tunnel barriers), while they are periodic at high temperatures (Fig. 17.11b). The energy scale for the tunnel barriers is several tens of Kelvin in the SWCNT and is compared with ~ 1 K for the MWCNT, which makes the difference in temperature-dependent behaviors between the SWCNT and MWCNT quantum dots. We have to admit the technique applied for the SWCNT is less reproducible and less reliable than for the MWCNT.

Fig. 17.10 SET behaviors of the fabricated SET in a MWCNT with the local ion beam irradiation technique. (a) Coulomb oscillations at various temperatures and (b) Coulomb diamonds at the lowest temperature (10 K) [44]

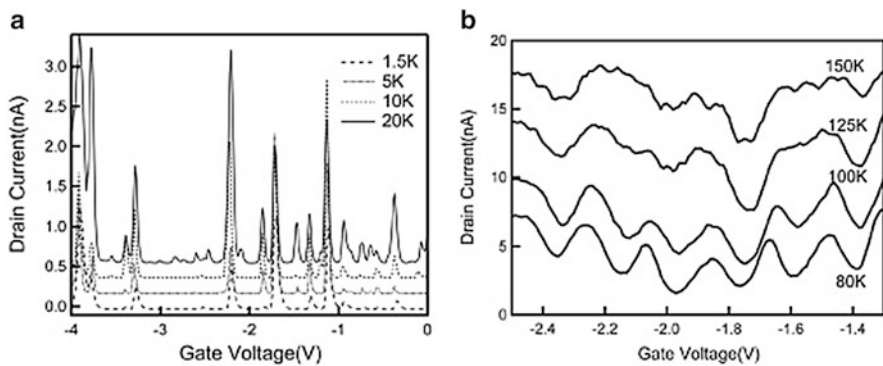
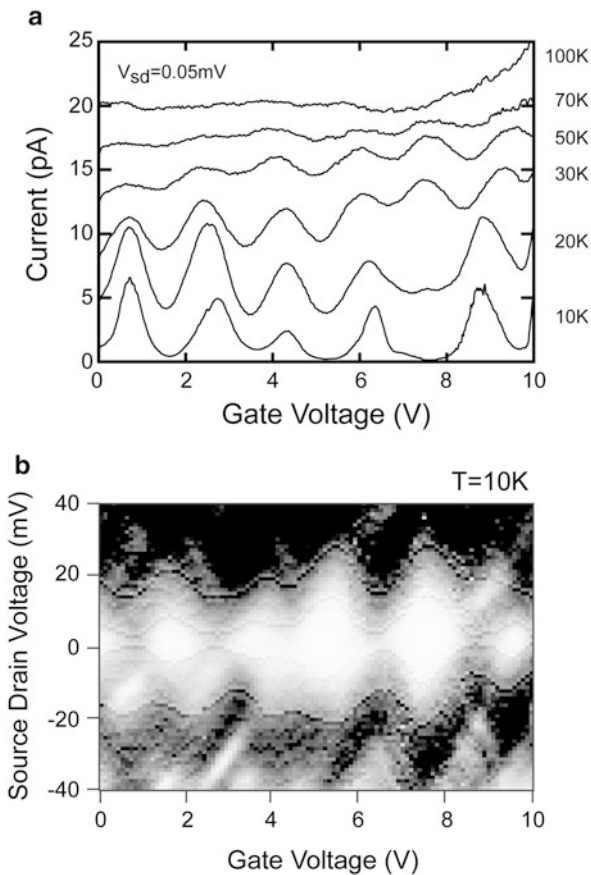


Fig. 17.11 SET behaviors of the fabricated SET in a SWCNT with the local ion beam irradiation technique. Coulomb oscillations (a) at low temperatures and (b) at high temperatures [45]

17.3.2 Aligned Nanotubes

To align nanotubes on a substrate is important to fabricate nanotube-based integrated circuits. One of the promising techniques is a combination of the aligned SWCNT growth on a single crystalline substrate and a subsequent transfer to another substrate suitable for device fabrication [46, 47]. In our process [48], first, aligned SWCNTs were grown on the quartz substrate by a standard chemical vapor deposition (CVD) technique with CH_4 and ferritin particles as catalysts which were patterned. The quartz substrate was cut from a single-crystal ST-cut wafer. With appropriate growth conditions, aligned SWCNTs were grown with a suitable density for device fabrication. The aligned SWCNTs on the quartz substrate were transferred to the SiO_2/Si substrate, as shown in Fig. 17.12a–d. The capacitively coupled quantum dots described in the following section were fabricated by following the process to form electrical contacts and gates to two adjacent SWCNTs (Fig. 17.12e–g).

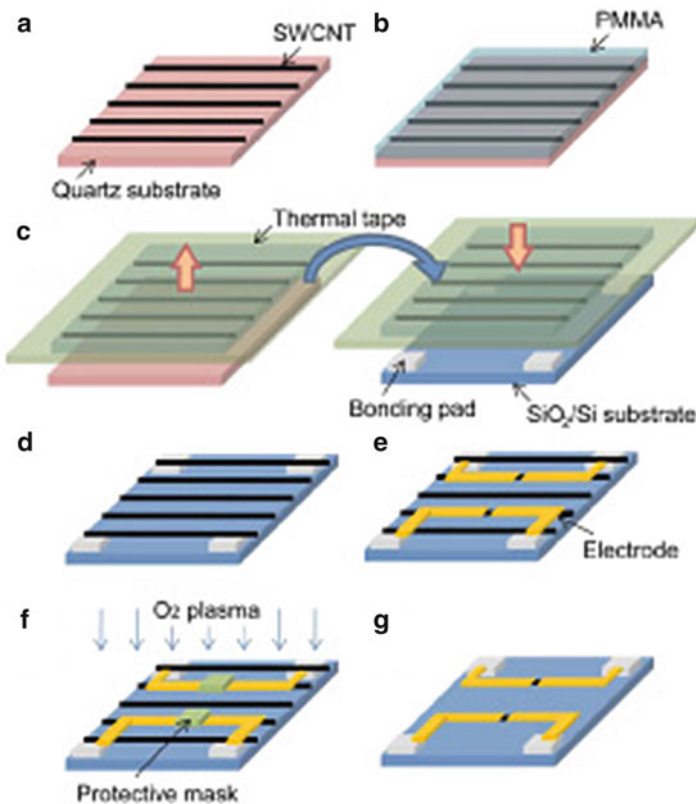


Fig. 17.12 Transfer printing technique sequence (a–g) to fabricate two SETs in the aligned SWCNTs [48]

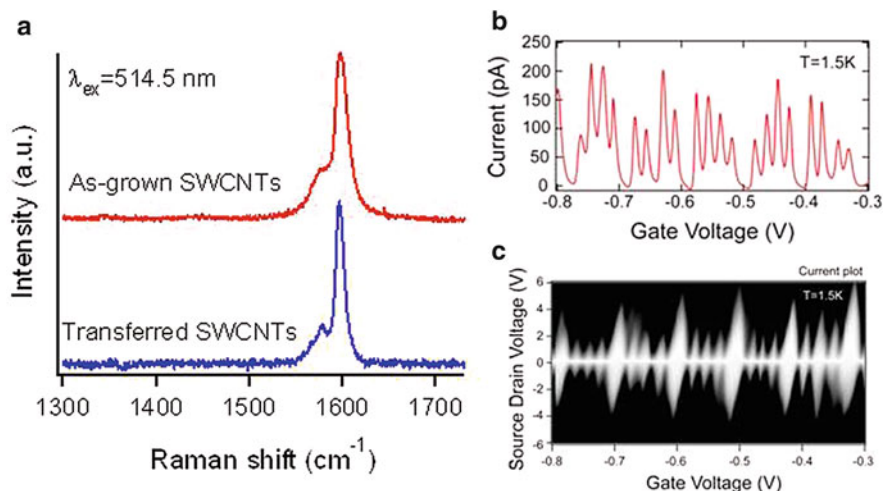


Fig. 17.13 (a) Raman spectrum of the SWCNTs before and after the transfer process. (b) Coulomb oscillations with a 4-electron periodicity for the SET fabricated by the transferred SWCNT. (c) Coulomb diamonds (Current is plotted instead of conductance)

The above transfer technique uses mechanical process to push the grown nanotubes to another substrate, which may induce damages in the grown SWCNTs. But we have not found any indication of serious damages. Figure 17.13a shows a Raman spectrum of the grown SWCNTs before (as grown) and after the transfer process. They are almost similar. Besides, we could observe the Coulomb oscillations with the four-electron periodicity, as shown in Fig. 17.13b, c.

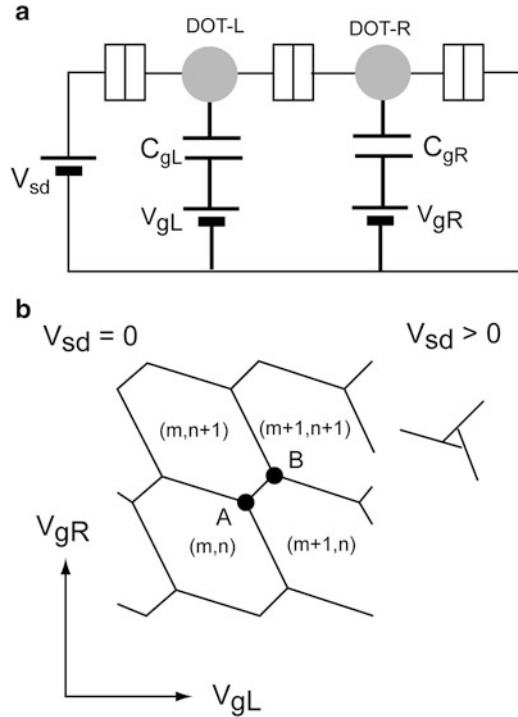
17.4 Quantum-Dot Devices

17.4.1 Double-Quantum Dots

Double-quantum dots are a simple extension of the single-quantum dot but can be applied for various functional devices. The two dots are coupled with a tunnel barrier and the potential of each dot can be controlled by the gates attached to each dot (Fig. 17.14a). Figure 17.14b shows a charge stability diagram of the double-quantum dots [10], which corresponds to the Coulomb diamonds in Fig. 17.1b for the single-quantum dot. The states of the double-quantum dot are defined by excess charges in the left and right dots, like (m, n) , while the states of the single-quantum dot are defined by an excess charge in the dot, like (m) . A current flows at the triple points indicated by A and B, where three different charge states are degenerated.

In an early attempt to realize the double-quantum dot with a SWCNT, a narrow SiO₂ layer ($\sim 100 \text{ nm}$) was deposited on the SWCNT between the source and drain

Fig. 17.14 (a) Equivalent circuit of the double (coupled) quantum dots. (b) Charge stability diagram of the double dots for the small V_{sd} . The diagram shows the characteristic honeycomb patterns for double dots



contacts (S and D) to divide the SWCNT into two dots (Fig. 17.15a, b) [49]. The two gates, indicated by G, are placed near each dot hoping that each gate would control a potential in each dot independently (but it failed as described later). The bottom panels in Fig. 17.15 show the current–voltage curves with one of the two gates changed with a small step and with the other grounded. Before the SiO_2 layer was deposited, the sample showed the single-dot behaviors with the periodic Coulomb diamonds as the gate voltage was changed (Fig. 17.15 left). The formation of the double-quantum dot can be suggested in Fig. 17.15 (right) by the irregular Coulomb diamonds due to the stochastic Coulomb blockade [38] and the negative differential conductance (NDC) observed around $V \sim -10$ mV. The NDC does not occur in the single-quantum dot with the metallic contacts at the source and drain and is a strong evidence for the formation of the double-quantum dot. The stochastic Coulomb blockade occurs in the multi-dots with one gate changed and produces the irregular diamonds in which a current is suppressed around $V_{sd} \sim 0$ for all the gate voltage ranges changed [39].

In the structure in Fig. 17.15 (SEM), we could not observe the characteristic honeycomb patterns in the charge stability diagram that suggested the formation of the double-quantum dots. This was because each gate did not change the potential of each dot independently. Looking at the arrangement of the gates and the SWCNT double dots in Fig. 17.15, we think a gate changes potential in both dots, and each

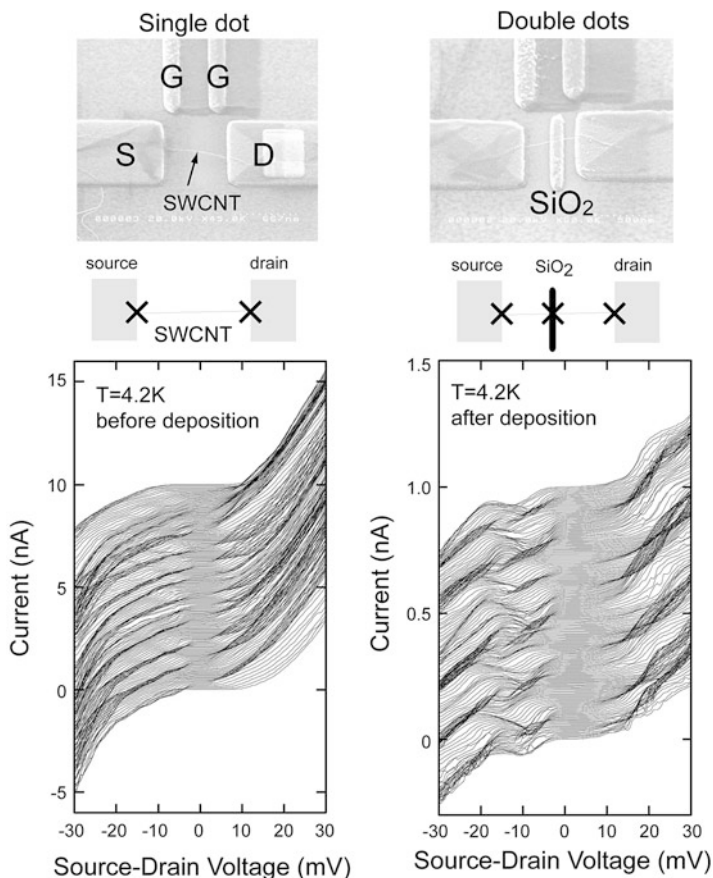
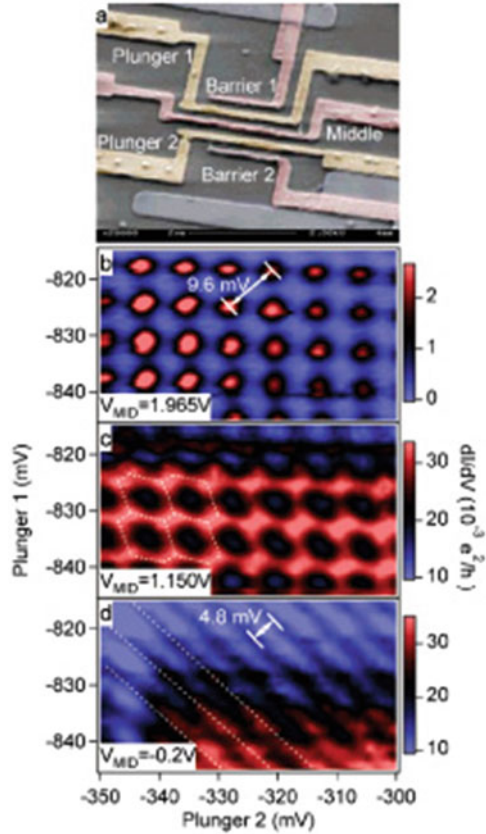


Fig. 17.15 SWCNT with contacts before (*left*) and after (*right*) a narrow SiO₂ layer is deposited. The same sample was processed and measured. The data shows the current–voltage characteristics with one gate changed by a small step and with the other gate grounded [49]

gate does not work independently to change the potential in each dot. In more sophisticated structures shown in Fig. 17.16a, the double dots were defined by the local top gates and the potential in each dot was also changed by the gate defined on top of the SWCNT [50]. In the double dots, the coupling strength can be controlled by tuning the center gate that separates the two dots from the isolated two dots (top), intermediately coupled double dots (center), and the one dot formed by merging the two dots into one (bottom), as shown in Fig. 17.16b–d.

One of the important applications of the double dots would be to use the spin blockade effect to detect the spin state in one dot [51]. This technique is widely used

Fig. 17.16 Gate-defined double dots in a semiconducting SWCNT. (a) SEM image of the device structures. The tunnel barriers are formed by the “barrier and middle” gates and a potential in each dot is changed by the “plunger” gates. (b)–(d): charge stability diagram of the dot when the middle gate voltage is changed. The SWCNT is changed from (b) the isolated double dots to (c) coupled double dots and (d) a merged single dot (Figures taken from [50])



for the readout method of the spin qubit in the quantum dot [52]. The capacitively coupled double dots without tunneling between them can be used to detect a single charge [53]. In this case, the double dots can be separated with a distance but can be coupled by a metal gate that capacitively couples the two dots [53, 54]. In the device shown in Fig. 17.17a, the two dots separated with a distance of $\sim 2 \mu\text{m}$ are capacitively coupled through the coupling metal that is formed on top of the dots with a thin HfO_x layer between the SWCNTs and the metal. The idea in the device is to detect a single electron in one dot with the other dot used as a single-electron electrometer. Figure 17.17b shows the operation of the device. The dot current (I_{d1}) and the electrometer current (I_{d2}) were measured simultaneously as a function of the gate voltage to the dot. As seen in the Fig. 17.17b, small current changes in I_{d2} are observed at the gate voltages where the Coulomb oscillations in the dot current show the peaks, meaning that the electrometer responds to the change in the number of electrons in the dot.

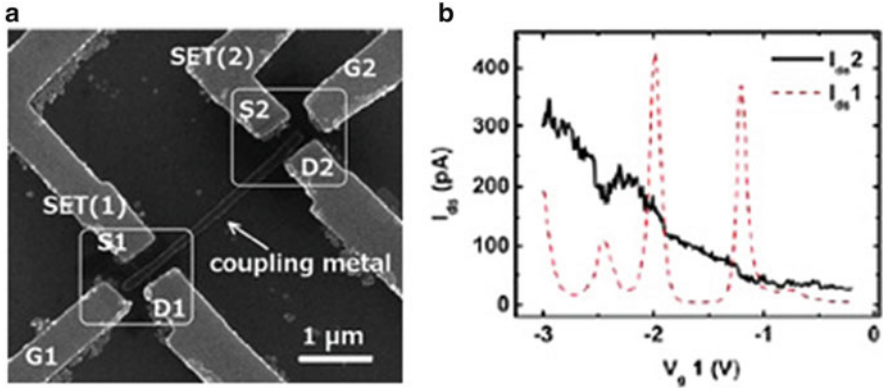


Fig. 17.17 (a) SEM image of the separated dots capacitively coupled by the coupling metal. (b) Simultaneous measurements of the currents through the dot (SET1, dotted line) and the electrometer (SET2, solid line) as a function of the gate to the dot (V_{g1}) [54]

17.4.2 Single-Electron Inverter and XOR

The CMOS-type single-electron inverter is an inverter with two SETs connected in series, as shown in Fig. 17.18a [11]. The n-MOS and p-MOS transistors in the CMOS inverter are replaced by SETs with the Coulomb peak of each SET adjusted out of phase by the gates line attached to each SET (V_{s1} and V_{s2} in Fig. 17.18a), and these SETs are used as a complementary switch. The inverter has been also fabricated by top-down techniques [55, 56], but the advantage to use the carbon nanotube is that the smaller quantum dots can be fabricated, which is essentially important for robust and high-temperature operations.

The local Ar ion beam irradiation technique was used to form the tunnel barriers, and the two SETs were fabricated in a MWCNT, as shown in Fig. 17.19a [57]. The heavily doped substrate was used for the voltage input. The Coulomb peak of each SET was adjusted by the gates near the SETs (V_{g1} and V_{g2}) to operate the device as an inverter (Fig. 17.19b). The output voltage as a function of the input voltage is shown in Fig. 17.19d. The output is high when the input is low, and it is low when the input is high, an inverter-like behavior. However, the performance is not satisfactory as an inverter in terms of the voltage gain and swing. The voltage gain defined as a slope of the transfer curve in Fig. 17.19d is ~ 0.7 in this device and is smaller than 1. The small gain in the inverter comes from the small gain of each SET which is given by $C_g/C_{s(d)}$, where C_g is the gate capacitance and $C_{s(d)}$ the capacitance at the source (drain) [58]. The capacitances are determined by the geometry of the devices, and in a practical design of the SETs, to realize a large gain is difficult.

The output voltage does not drop to zero when the input is high (small voltage swing). This is because one of the SETs which should have been in the Coulomb blockade was not perfectly blocking the current. This is seen in Fig. 17.19c, where

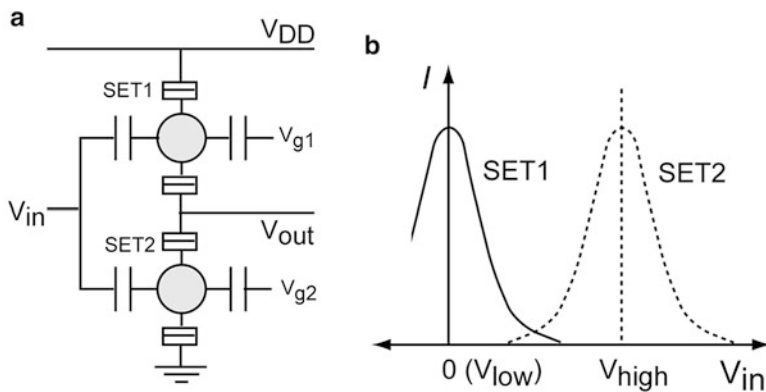


Fig. 17.18 (a) Equivalent circuit of the CMOS-type SET inverter. (b) Operation conditions for the adjusted Coulomb peak of each SET

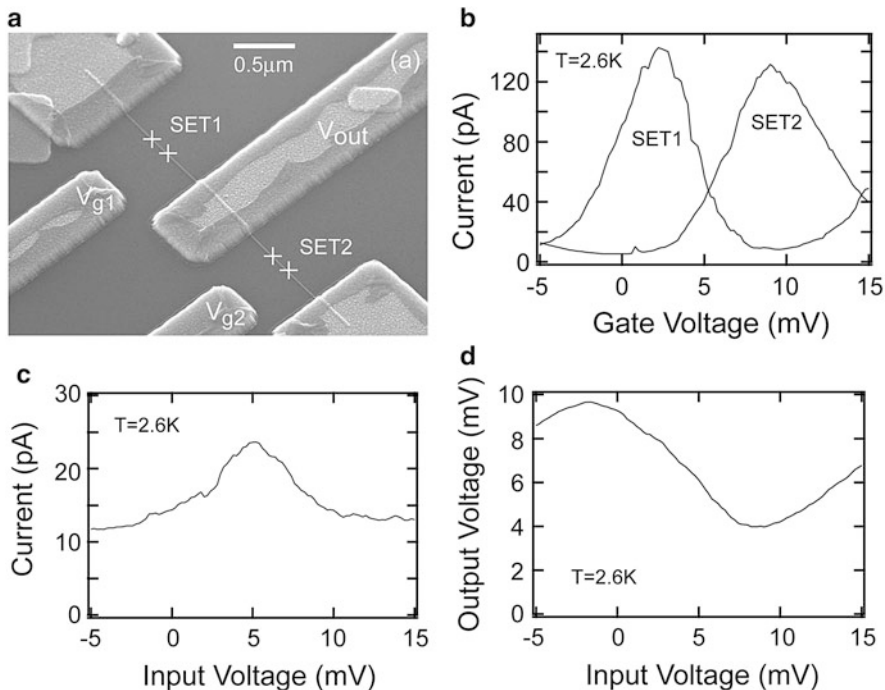


Fig. 17.19 (a) SEM image of the CMOS-type single-electron inverter fabricated in a MWCNT with the local ion beam irradiation technique. (b) Adjusted Coulomb peak of each SET. (c) Current through the two SETs. (d) Input-output curve (transfer characteristic) [57]

the current was measured when the input gate was swept from the low state to the high state. In the CMOS inverter operation, the current does not flow, except it is in the transition between the low state and the high state. The similar behavior is observed in Fig. 17.19c, but the finite current flows in a whole input range.

One of the logic gates that may benefit from the SET is an XOR gate [59]. Using the unique feature of the periodic current oscillation in the SET as a function of a gate voltage, it can be realized by a single SET with two equivalent input gates (Fig. 17.20a). The output is the current in the equivalent circuit shown in Fig. 17.20b. Experimentally, the device can be realized using a SWCNT with the source–drain contacts and the two similar gates, as shown in Fig. 17.20a [60]. The operation principle is shown in Fig. 17.20c. The Coulomb peak as a function of one of the two gates (V_{inA}) is shifted by the other gate (V_{inB}). The Coulomb oscillations due to the V_{inA} are adjusted such that the center position of the two adjacent peaks is positioned at $V_{inA} = 0$ (dotted Coulomb oscillation), which can be done by the third gate (a substrate can be used, for the simplest case). The application of the V_{inB} with the value of the V_{inA} , at which the Coulomb oscillation gives a peak, shifts the peak by a half period (see Fig. 17.20c, solid Coulomb oscillation). Under this condition, the current flows when one of the V_{inA} and V_{inB} is in the “on” or “1” state. When both V_{inA} and V_{inB} are in the “1” or “0” (“off”) state, the current does not flow, showing the XOR operation.

The performances of the device are shown at two different temperatures (1.5 K and 40 K) in Fig. 17.21a and b, respectively. The important requirement for the good performance of the XOR gate is to realize a similar Coulomb peak which is shifted by V_{inB} as the Coulomb peak without the shift ($V_{inB} = 0$). As seen in the upper panel of Fig. 17.21a, this condition is almost met at 1.5 K, and a good XOR operation with enough logic swing is obtained, as seen in the lower panel of Fig. 17.21a. However, at 40 K, the two peaks are no longer equivalent, and the Coulomb blockade is not effective anymore. As a result, the XOR operation is not perfect in terms of the logic swing. But its operation is carried out to some extent even at 40 K with a smaller logic swing, at which temperature the SET does not show the sufficient Coulomb

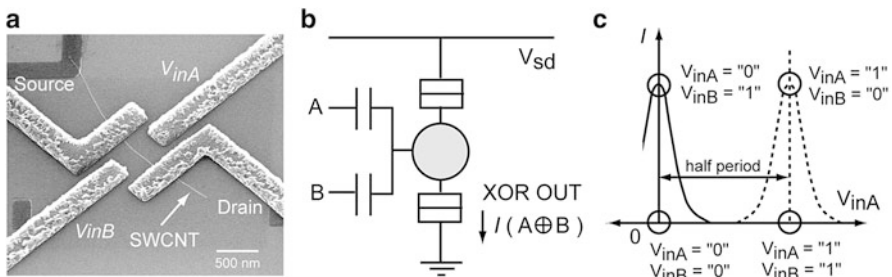


Fig. 17.20 (a) SEM image of the single-electron XOR gate device fabricated in a SWCNT. V_{inA} and V_{inB} are two input voltages. (b) Equivalent circuit of the single-electron XOR gate. (c) Operation principle. Coulomb peaks with $V_{inB} = “1”$ (solid line) and $V_{inB} = “0”$ (dotted line) [60]

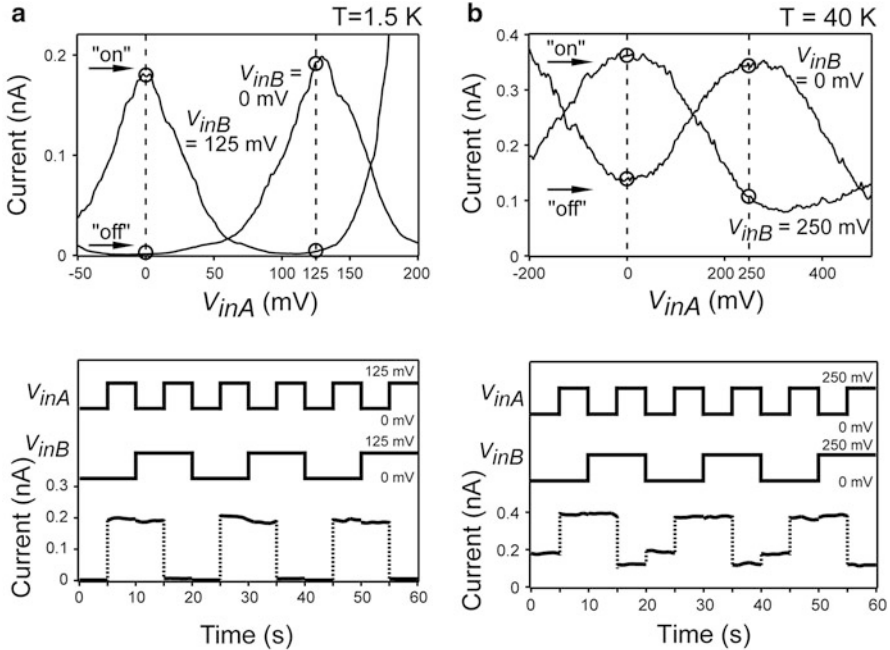


Fig. 17.21 Operation of the single-electron XOR gate at (a) 1.5 K and (b) 40 K. The *top panels* in (a) and (b) show Coulomb peaks with and without the voltage at V_{inB} [60]

blockade. The advantage of fabricating the XOR gate device with the SWCNT may be that several gates are easily incorporated because of the design flexibility with a large space around the dot.

17.4.3 Quantum THz Detection

The quantum dots fabricated with SWCNTs have a charging energy for single electrons (E_c) in a frequency range of THz. With this advantage, the SWCNT SET can be used to detect THz photons [61, 62]. The photon-assisted tunneling (PAT), a basic mechanism of quantum detection of electromagnetic waves, has been demonstrated in a microwave frequency range for the quantum dots formed by the surface gate technique in the GaAs/AlGaAs 2DEG [63, 64]. E_c for the dots fabricated by electron beam lithography is typically in the microwave range. Recently, THz PAT has also been demonstrated in a SET with self-assembled InAs quantum dots [65].

Figure 17.22a shows a Coulomb peak of the SET with and without various THz frequencies [62]. As can be seen in the figure, a new peak emerges on the right-hand side of the main Coulomb peak which shifts away from the main peak as the

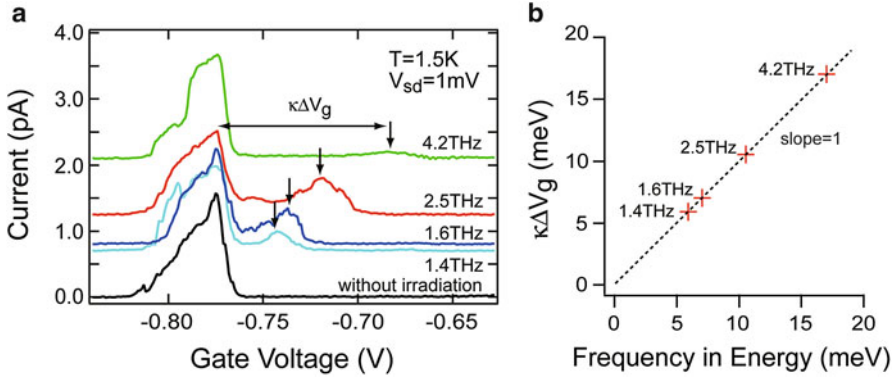


Fig. 17.22 (a) Coulomb peaks with and without THz irradiation with various frequencies. The arrow shows a newly emerged satellite peak (PAT peak) that appears with THz irradiation. (b) Distance in energy between the main Coulomb peak and the satellite peak for various THz frequencies. The distance in the gate voltage is converted by the conversion factor, $\kappa = C_g/C_\Sigma$ [62]

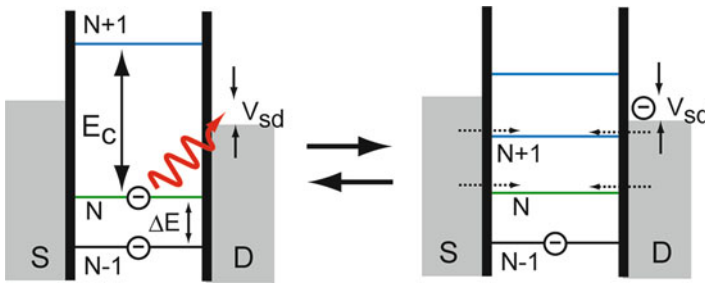


Fig. 17.23 Energy diagram of the dot to explain the PAT mechanism. (a) The dot is in the Coulomb blockade, and (b) it is lifted by the THz photon absorption

THz frequency is increased. The distance between the main peak and the new peak (satellite peak), converted in energy, increases linearly, as shown in Fig. 17.22b, and is equal to the irradiated THz frequency. The mechanism of the satellite peaks is explained by the THz PAT, as shown in Fig. 17.23. An electron residing on the topmost level in the quantum dot tunnels to the right drain bias window (left Fig.) by absorbing a THz photon, and the Coulomb blockade is lifted (right Fig.). When an electron tunnels into the dot from the left source, the process contributes to the current, and the dot comes back to the Coulomb blockade, an initial condition. But an electron tunnels from the right drain, the process does not contribute to the current, and the dot comes back to the Coulomb blockade. The processes are repeated, while the dot is irradiated with the THz waves.

More satellite peaks may appear, which are associated with the excited states. Some peaks move as the THz frequency is changed, but some do not, depending on the process the excited states are involved in [66]. The height of the satellite peaks

depends on the power of the irradiated THz wave through the Bessel functions. The THz PAT mechanism is basically the same with the PAT in a microwave frequency range observed in a superconducting tunnel junction [67]. The mechanism is explained by the Tien–Gordon model in which photon side bands are formed with a separation of hf and amplitude which has the Bessel function behaviors [68]. As the irradiation power is increased, a multiphoton process with absorption and emission of several photons is also possible as well [64, 65].

Next, we show another mechanism to detect the THz photons [69]. A SWCNT SET was fabricated on top of the GaAs/AlGaAs 2DEG wafer [70]. In this case, the THz photons were absorbed by Landau levels formed in the 2DEG in high magnetic fields, and the SWCNT SET was used as an electrometer to detect local charge configurations. Figure 17.24 shows Coulomb peaks of the SET in various magnetic fields under THz irradiation of (a) 1.6 THz and (b) 2.5 THz. In both cases, the peak moves as the magnetic field is changed and comes back again after it makes the maximum shift. The magnetic field which gives the maximum shift depends on the THz frequency, and it was found that the cyclotron resonance condition was met at the magnetic field where the peak showed the maximum shift. The transitions between the Landau levels are most frequent at the magnetic field. Therefore, the reason for the peak shift is a change in the local charge configuration which changes as the magnetic field is changed, and it is detected by the SET electrometer.

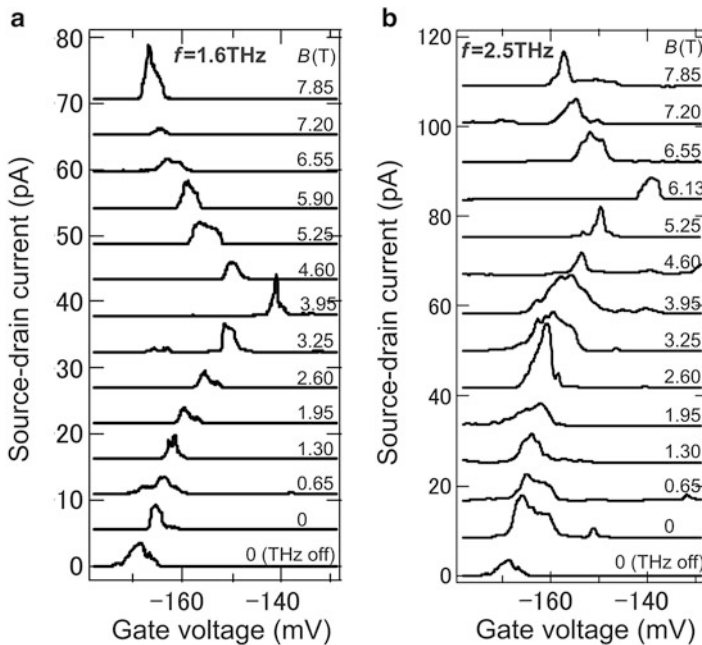


Fig. 17.24 Coulomb peak shifts of the SWCNT SET fabricated on a GaAs/AlGaAs 2DEG wafer for various magnetic fields with THz irradiation of (a) 1.6 THz and (b) 2.5 THz [70]

17.5 Conclusions

As shown in this chapter, there are many advantages in using the carbon nanotubes as a building block of the quantum dot. These come from the large energy scales associated with the nanotube quantum dots. For the single-electron devices that make use of the charging effect, the smaller quantum dots should show the better performance. Various single-electron devices have been proposed, and they could work at higher temperatures when made with carbon nanotubes. They are also advantageous for quantum devices that make use of quantum states because of the larger level spacing between the confined states. They may be also advantageous for quantum computing devices. Various modifications of the nanotube itself, such as peapods and chemically modified nanotubes, would be another advantage for creating new functionalities.

A big challenge for these is to develop reliable, reproducible, and flexible device fabrication processes. Some attempts are shown in the chapter, but they are not satisfactory enough for practical use. So far, semiconductor processing techniques have been applied to the nanotubes to fabricate the devices, but it seems that they are not completely compatible with carbon nanotubes. Unique processes need to be developed for further development of the quantum devices based on the carbon nanotubes.

Acknowledgments The author thanks the following persons who have been in his group for their effort. Those are Dr. Tetsuya Ida, Dr. Masaki Suzuki, Dr. Satoshi Moriyama, Dr. Daijyu Tsuya, Dr. Takahiro Mori, Dr. Hiroshi Tabata, Dr. Tomoko Fuse, Dr. Maki Shimizu, Dr. Tomohiro Yamaguchi, Dr. Yukio Kawano, and Dr. Akira Hida. He also thanks Prof. Takuo Sugano and Prof. Yoshinobu Aoyagi for their continuous encouragement.

References

1. Sohn LL, Kouwenhoven LP, Schon G (1997) Proceedings of the NATO advanced study institute on mesoscopic electron transport, 1996. Kluwer Academic Publishers, Dordrecht
2. Ando T (1997) Excitons in carbon nanotubes. *J Phys Soc Jpn* 66:1066
3. Feng Wang, Gordana Dukovic, Brus LE, Heinz TF (2005) The optical resonances in carbon nanotubes arise from excitons. *Science* 308:838
4. Kamada H, Gotoh H, Temmyo J, Takagahara T, Ando H (2001) Exciton Rabi oscillation in a single quantum dot. *Phys Rev Lett* 87:246401
5. Xiaodong Xu, Sun B, Berman PR, Steel DG, Bracker AS, Gammon D, Sham LJ (2007) Coherent optical spectroscopy of a strongly driven quantum dot. *Science* 317:929
6. Zhiliang Yuan, Kardynal BE, Stevenson RM, Shields AJ, Lobo CJ, Cooper K, Beattie NS, Ritchie DA, Pepper M (2002) Electrically driven single-photon source. *Science* 295:102
7. Saito R, Dresselhaus G, Dresselhaus MS (1998) Physical properties of carbon nanotubes. Imperial College Press, London
8. Koji Ishibashi (2012) Nanoelectronics. In: Cabrini S, Kawata S (eds) Nanofabrication handbook. CRC Press, Boca Raton, pp 451–480
9. Geerligs LJ, Anderegg VF, Holweg PAM, Mooij JE, Pothier H, Esteve D, Urbina C, Devoret MH (1990) Frequency-locked turnstile device for single electrons. *Phys Rev Lett* 64:2691

10. Pothier H, Lafarge P, Urbina C, Esteve D, Devoret MH (1992) Single-electron pump based on charging effects. *Europhys Lett* 17:249
11. Tucker JR (1992) Complementary digital logic based on the "Coulomb blockade". *J Appl Phys* 72:4399
12. Dresselhaus PD, Ji L, Han S, Lukens JE, Likharev KK (1994) Measurement of single electron lifetimes in a multijunction trap. *Phys Rev Lett* 72:3226
13. Amlani I, Orlov AO, Toth G, Bernstein GH, Lent CS, Snider GL (1999) Digital logic gate using quantum-dot cellular automata. *Science* 284:289
14. Postma HWC, Teepen T, Yao Z, Grifoni M, Dekker C (2001) Carbon nanotube single-electron transistors at room temperature. *Science* 293:76
15. Nakahara M, Ohmi T (2008) Quantum computing: from linear algebra to physical realizations. Institute of Physics Pub Inc. 2008, Bristol, UK
16. Elzerman JM, Hanson R, van Beveren LHW, Vandersypen LMK, Kouwenhoven LP (2005) Semiconductor few-electron quantum dots as spin qubits. In: Ruggiero B, Delsing P, Granata C, Pashkin Y, Silvestrini P (eds) *Quantum computation in solid state systems*. Springer, Berlin
17. Petta JR, Johnson AC, Taylor JM, Laird EA, Yacoby A, Lukin MD, Marcus CM, Hanson MP, Gossard AC (2005) Coherent manipulation of coupled electron spins in semiconductor quantum dots. *Science* 309:2180
18. Trauzettel B, Bulaev DV, Loss D, Burkard G (2007) Spin qubits in graphene quantum dots. *Nat Phys* 3:192
19. Shaji N, Simmons CB, Thalakulam M, Klein LJ, Qin H, Luo H, Savage DE, Lagally MG, Rimberg AJ, Joynt R, Friesen M, Blick RH, Coppersmith SN, Erikson MA (2008) Spin blockade and lifetime-enhanced transport in a few-electron Si/SiGe double quantum dot. *Nat Phys* 4:540
20. Ando T (2000) Spin-orbit interaction in carbon nanotubes. *J Phys Soc Jpn* 69:1757
21. Huertas-Hernando D, Guinea F, Brataas A (2006) Spin-orbit coupling in curved graphene, fullerenes, nanotubes, and nanotube caps. *Phys Rev B* 74:155426
22. Kuemmeth F, Ilani S, Ralph DC, McEuen PL (2008) Coupling of spin and orbital motion of electrons in carbon nanotubes. *Nature* 452:448
23. Jespersen TS, Grove-Rasmussen K, Paaske J, Muraki K, Fujisawa T, Nygard J, Flensberg K (2011) Gate-dependent spin-orbit coupling in multielectron carbon nanotubes. *Nat Phys* 7:348
24. Averin DV, Likharev KK (1991) Chapter 6: Single electronics, A correlated transfer of single electrons and Cooper pairs in systems of small tunnel junctions. In: Altshuler B, Lee PA, Webb RA (eds) *Mesoscopic phenomena in solids*. Elsevier Science Publishers, Amsterdam
25. Shaoyun Huang, Naoki Fukata, Maki Shimizu, Tomohiro Yamaguchi, Takashi Sekiguchi, Koji Ishibashi (2008) Classical Coulomb blockade of a silicon nanowire dot. *Appl Phys Lett* 92:213110
26. Beenakker CWJ (1991) Theory of Coulomb-blockade oscillations in the conductance of a quantum dot. *Phys Rev B* 44:1646
27. Fuse T, Moriyama S, Aoyagi Y, Suzuki M, Ishibashi K (2004) Two-electron and four-electron periodicity in single-wall carbon nanotube quantum dots. *Superlattice Microst* 34:377
28. Ralph DC, Black CT, Tinkham M (1997) Gate-voltage studies of discrete electronic states in aluminum nanoparticles. *Phys Rev Lett* 78:4087
29. Huang SY, Shin SK, Fukata N, Ishibashi K (2011) A single-electron transistor and an even-odd effect in chemically synthesized Ge nanowires. *J Appl Phys* 109:036101
30. Liang W, Bockrath M, Park H (2002) Shell filling and exchange coupling in metallic single-walled carbon nanotubes. *Phys Rev Lett* 88:126801
31. Moriyama S, Fuse T, Aoyagi Y, Ishibashi K (2005) Excitation spectroscopy of two-electron shell structures in carbon nanotube quantum dots in magnetic fields. *Appl Phys Lett* 87:073103
32. Moriyama S, Fuse T, Suzuki M, Aoyagi Y, Ishibashi K (2005) Four-electron shell structures and an interacting two-electron system in carbon-nanotube quantum dots. *Phys Rev Lett* 94:186806
33. Oreg Y, Byczuk K, Halperin BI (2000) Spin configurations of a carbon nanotube in a nonuniform external potential. *Phys Rev Lett* 85:365

34. Tarucha S, Austing DG, Honda T, Van der Hage RJ, Kouwenhoven LP (1996) Shell filling and spin effects in a few electron quantum dot. *Phys Rev Lett* 77:3613
35. Jarillo-Herrero P, Sapmaz S, Dekker C, Kouwenhoven LP, Van der Zant HSJ (2004) Electron-hole symmetry in a semiconducting carbon nanotube quantum dot. *Nature* 429:389
36. Noshio Y, Ohno Y, Kishimoto S, Mizutani T (2006) Relation between conduction property and work function of contact metal in carbon nanotube field-effect transistors. *Nanotechnology* 17:3412
37. Tsuya D, Suzuki M, Aoyagi Y, Ishibashi K (2005) Quantum dots and their tunnel barrier in semiconducting single-wall carbon nanotubes with a p-type behavior. *Jpn J Appl Phys* 44:2596
38. Ruzin IM, Chandrasekhar V, Levin EI, Glazman LI (1992) Stochastic Coulomb blockade in a double-dot system. *Phys Rev B* 45:13469
39. Kemerink M, Molenkamp LW (1994) Stochastic Coulomb blockade in a double quantum dot. *Appl Phys Lett* 65:1012
40. Ando T, Nakanishi T (1998) Impurity scattering in carbon nanotubes – absence of back scattering. *J Phys Soc Jpn* 67:1704
41. McEuen PL, Bockrath M, Cobden DH, Yoon Y-G, Louie SG (1999) Disorder, pseudospins, and backscattering in carbon nanotubes. *Phys Rev Lett* 83:5098
42. Bockrath M, Cobden DH, McEuen PL, Chopra NG, Zettl A, Thess A, Smalley RE (1997) Single-electron transport in ropes of carbon nanotubes. *Science* 275:1922
43. Tans SJ, Devoret MH, Dai H, Thess A, Smalley RE, Geeligs BL, Dekker C (1997) Individual single-wall carbon nanotubes as quantum wires. *Nature* 386:474
44. Suzuki M, Ishibashi K, Toratani T, Tsuya D, Aoyagi Y (2002) Tunnel barrier formation using argon-ion irradiation and single quantum dots in multiwall carbon nanotubes. *Appl Phys Lett* 81:2273
45. Takahiro Mori, Shunsuke Sato, Kazuo Omura, Shota Yajima, Yasuhiro Tsuruoka, Yohji Achiba, Koji Ishibashi (2009) Formation of single electron transistors in single-walled carbon nanotubes with low energy Ar ion irradiation technique. *J Vac Sci Technol B* 27:795
46. Kang SJ, Kocabas C, Kim H-S, Cao Q, Meitl MA, Khang D-Y, Rogers JA (2007) Printed multilayer superstructures of aligned single-walled carbon nanotubes for electronic applications. *Nano Lett* 7:3343
47. Kang SJ, Kocabas C, Ozel T, Shim M, Pimparker N, Alam MA, Rotkin SV, Rogers JA (2007) High-performance electronics using dense, perfectly aligned arrays of single-walled carbon nanotubes. *Nat Nanotech* 2:230
48. Tabata H, Shimizu M, Ishibashi K (2009) Fabrication of single electron transistors using transfer-printed aligned single walled carbon nanotubes arrays. *Appl Phys Lett* 95:113107
49. Ishibashi K, Suzuki M, Ida T, Aoyagi Y (2001) Formation of coupled quantum dots in single-wall carbon nanotubes. *Appl Phys Lett* 79:1864
50. Biercuk MJ, Garaj S, Mason N, Chow JM, Marcus CM (2005) Gate-defined quantum dots on carbon nanotubes. *Nano Lett* 5:1267
51. Ono K, Austing DG, Tokura Y, Tarucha S (2002) Current rectification by Pauli exclusion in a weakly coupled double quantum dot system. *Science* 297:1313
52. Koppens FHL, Buizert C, Tielrooij KJ, Vink IT, Nowack KC, Meunier T, Kouwenhoven LP, Vandersypen LMK (2006) Driven coherent oscillations of a single electron spin in a quantum dot. *Nature* 442:766
53. Churchill HOH, Bestwick AJ, Harlow JW, Kuemmeth F, Marcos D, Stwertka CH, Watson SK, Marcus CM (2009) Electron–nuclear interaction in ^{13}C nanotube double quantum dots. *Nat Phys* 5:321
54. Xin Zhou, Koji Ishibashi (2012) Single charge detection in capacitively coupled integrated single electron transistors based on single-walled carbon nanotubes. *Appl Phys Lett* 101:123506
55. Yukinori Ono, Yasuo Takahashi, Kenji Yamazaki, Masao Nagase, Hideo Namatsu, Kenji Kurihara, Katsumi Murase (2000) Si complementary single-electron inverter with voltage gain. *Appl Phys Lett* 76:3121
56. Heij CP, Hadley P, Mooij JE (2001) Single-electron inverter. *Appl Phys Lett* 78:1140

57. Ishibashi K, Tsuya D, Suzuki M, Aoyagi Y (2003) Fabrication of a single-electron inverter in multiwall carbon nanotubes. *Appl Phys Lett* 82:3307
58. Likharev KK (1987) Single-electron transistors: electrostatic analogs of the DC SQUIDS. *IEEE Trans Magn* 23:1142
59. Takahashi Y, Fujiwara A, Yamazaki K, Namatsu H, Kurihara K, Murase K (2000) Multigate single-electron transistors and their application to an exclusive-OR gate. *Appl Phys Lett* 76:637
60. Tsuya D, Suzuki M, Aoyagi Y, Ishibashi K (2005) Exclusive-OR gate using a two-input single-electron transistor in single-wall carbon nanotubes. *Appl Phys Lett* 87:153101
61. Fuse T, Kawano Y, Yamaguchi T, Aoyagi Y, Ishibashi K (2007) Quantum response of carbon nanotube quantum dots to terahertz wave irradiation. *Nanotechnology* 18:044001
62. Kawano Y, Fuse T, Toyokawa S, Uchida T, Ishibashi K (2008) Terahertz photon-assisted tunneling in carbon nanotube quantum dots. *J Appl Phys* 103:034307
63. Kouwenhoven LP, Jauhar S, Orenstein J, McEuen PL, Nagamune Y, Motohisa J, Sakaki H (1994) Observation of photon-assisted tunneling through a quantum dot. *Phys Rev Lett* 73:3443
64. Oosterkamp TH, Fujisawa T, van der Wiel WG, Ishibashi K, Hijman RV, Tarucha S, Kouwenhoven LP (1998) Microwave spectroscopy of a quantum-dot molecule. *Nature* 395:873
65. Shibata K, Umeno A, Cha KM, Hirakawa K (2012) Photon-assisted tunneling through self-assembled InAs quantum dots in the Terahertz frequency range. *Phys Rev Lett* 109:077401
66. Ishibashi K, Moriyama S, Fuse T, Kawano Y, Toyokawa S, Yamaguchi T (2008) Artificial atom and quantum terahertz response in carbon nanotube quantum dots. *J Phys: Condens Matter*, a special issue 20:454205
67. Tucker JR, Feldman MJ (1985) Quantum detection at millimeter wavelengths. *Rev Mod Phys* 57:1055
68. Tien PK, Gordon JP (1963) Multiphoton process observed in the interaction of microwave fields with the tunneling between superconductor films. *Phys Rev* 129:647
69. Tsukamoto T, Moriyama S, Tsuya D, Suzuki M, Yamaguchi T, Aoyagi Y, Ishibashi K (2005) Carbon nanotube quantum dots fabricated on a GaAs/AlGaAs two-dimensional electron gas substrate". *J Appl Phys* 98:076106
70. Yukio Kawano, Takao Uchida, Koji Ishibashi (2009) Terahertz sensing with a carbon nanotube/two-dimensional electron gas hybrid transistor. *Appl Phys Lett* 95:083123

Chapter 18

High-Mobility Thin-Film Transistors for Flexible Electronics Applications

Yutaka Ohno

Abstract Flexible and stretchable electronics are attracting much attention because of the variety of potential applications from flexible e-papers through wearable healthcare devices. Among various kinds of electronic materials, carbon nanotube thin films have advantages in flexibility, stretchability, and performance because of the excellent electronic and mechanical properties. Low-cost manufacturing of flexible devices is also possible with good processability of carbon nanotube films. In this chapter, recent topics and progresses on flexible electronics based on carbon nanotube thin films are introduced, including high-mobility carbon nanotube thin-film transistors (TFTs) and integrated circuits (ICs) on a transparent plastic film, all-carbon ICs demonstrating excellent stretchability and moldability. The high-speed printing process to fabricate CNT TFTs, which enables low-cost manufacturing of large-area flexible devices, is also introduced.

Keywords Carbon nanotube • Flexible electronics • Transparent electronics • Printed electronics • Thin-film transistor • Integrated circuit

18.1 Introduction

Flexible devices made of lightweight flexible plastic are expected to serve as smarter gadgets for information communication such as electronic papers, cell phones, and electronic tags. Since polymer materials are mechanically and biologically compatible with the human body, stretchable smart sensors that can be attached to the skin have also been proposed. In combination with environmentally friendly manufacturing processes based on printing technologies, flexible electronics can be used to produce low-cost disposable devices. With the huge potential market for flexible electronics, intensive research and development are being widely conducted in countries around the world. Flexible electronics have taken on a new reality through the use of organic semiconductor materials, in the form of an

Y. Ohno (✉)

EcoTopia Science Institute, and Graduate School of Engineering, Nagoya University, Furo-Cho, Chikusa-ku, Nagoya 464-8603, Japan

e-mail: yohno@nagoya-u.jp

organic-light-emitting diode (OLED) display [1] or electronic paper that can be wrapped around a rod of several millimeters in diameter, and a microprocessor on plastic film [2].

Flexible devices are constructed by integrating transistors, display elements, sensors, touch screens, wiring, and so forth on a plastic substrate. Thus, not only must the materials be flexible, but they must be workable and capable of being formed on plastic at low temperature. Thin-film transistors (TFTs), which are relatively easy to produce at low temperature, have been examined for use as active devices. Conventional TFTs made of amorphous silicon (a-Si) or polysilicon (poly-Si) are essential for drivers of flat-panel displays, but they require high temperature and vacuum processes and are difficult to produce on inexpensive plastic film such as polyethylene terephthalate (PET) with low glass transition temperature. The latest technology being developed produces TFTs on plastic at low temperature using an oxide semiconductor and organic semiconductor. However, there is still no technique that satisfies all of the practical requirements of operating speed, operating voltage, long-term stability, and productivity, and it is imperative to develop materials and techniques that strike a balance between performance and cost.

Research on flexible devices that use single-walled carbon nanotube (CNT) thin films has been heating up recently because of the high carrier mobility, good flexibility, and processability [3–5]. For example, medium-scale integrated circuits such as a 4-bit decoder have been produced by integrating CNT TFTs on a polyimide film [4]. Intensive efforts have been done to produce an electronic tag via a total printing system as well as a roll-to-roll process using carbon nanotubes [6]. There have also been attempts at making on-demand electronic circuits a reality through ink-jet printing [7].

In this chapter, recent progress on the topic of CNT thin-film devices will be described, which have garnered attention recently as materials that could enable the production of high-performance flexible devices at low cost.

18.2 CNT Thin-Film Technology for High-Mobility TFTs

The growth temperature of CNTs is normally much higher than the softening temperature of plastic substrates, making it impossible to grow CNTs directly on a plastic substrate. On the other hand, high-performance thin films can be obtained by a simple solution method [8] or transfer method [5]. These are the two processes that are primarily used in forming CNT thin films on plastic substrates, i.e., solution process and transfer process.

In the solution process, CNTs grown by chemical vapor deposition (CVD) and so on are dispersed in a liquid such as water or organic solvent and formed into a thin film on a substrate by spin coating or printing. One advantageous feature of the solution process is that the CNTs targeted for the application, i.e., semiconducting CNTs or metallic CNTs separated by density gradient ultracentrifugation [9] or gel

chromatography [10], can be used. One drawback is the degradation of conductivity that arises in processing. In CNTs grown on a substrate or support material (or general soot-like CNT materials), the CNTs aggregate into bundles due to van der Waals forces, and strong ultrasonic treatment is necessary to disperse CNTs individually in liquid. When treated in this manner, the CNTs are often cut and shortened. The conductivity and mobility of a CNT thin film are governed by the contact resistance between CNTs, and when CNTs are shortened, the number of inter-CNT junctions per unit length increases and performance of the CNT thin film decreases substantially. Dispersants such as surfactants are added to stabilize dispersion in liquid, but increased contact resistance between CNTs due to residual dispersant can also cause performance degradation. Surfactants also have a carrier doping effect, making it difficult to control threshold voltage of TFTs if they remain as residue. Under current circumstances, CNT thin-film devices produced using the solution method often exhibit poorer mobility than would be expected from the physical properties of the CNTs. For practical use, it is essential to develop techniques for removing surfactants. In addition, in applications that demand higher performance, gentler dispersion techniques and techniques for extracting only long CNTs are required [11]. Formation of uniform CNT thin film with avoiding aggregation due to surface tension of liquid is also an important issue.

In the transfer method, a CNT thin film is grown on a solid substrate by supported catalyst CVD or deposited on membrane filter by floating-catalyst CVD, and then transferred to a plastic substrate [4, 5]. This method can produce a uniform, high-performance CNT thin film without the problems of CNT shortening and contamination that often occur in the solution process. The transfer technique has fewer process steps and can be used in the roll-to-roll method as well. On the other hand, it is difficult to introduce a semiconductor–metal separation process into this technique.

Figure 18.1a shows the transfer process based on the floating-catalyst CVD technique for TFT fabrication [5]. In this process, CNTs are continuously grown by atmospheric-pressure floating-catalyst CVD and collected by a membrane filter by filtering the aerosol containing CNTs. A uniform CNT film is formed on the membrane filter. The filter is made of a mixture of cellulose acetate and nitrile cellulose and dissolves in acetone. Thus, by attaching the filter onto the desired substrate and immersing in acetone, a CNT thin film can be transferred to the substrate.

Figure 18.1b is an SEM image of a CNT thin film formed on a Si substrate by the transfer method based on the floating-catalyst CVD, showing its characteristic morphology. First, the CNTs have a length of approximately 10 μm and are relatively linear, and second, Y-junctions are frequently seen at inter-CNT junctions. As shown in Fig. 18.1c, the contact area between CNTs is larger in a Y-junction than in an X-junction, and the contact resistance is expected to be lower. In fact, the detailed measurement of contact resistance by conductive atomic force microscopy showed the contact resistance of Y-junctions is lower than that of X-junctions [12, 13]. As mentioned above, the mobility of a CNT thin film is governed by contact resistance between CNTs, and long CNTs and low contact resistance between CNTs can be expected to contribute to high mobility of the film.

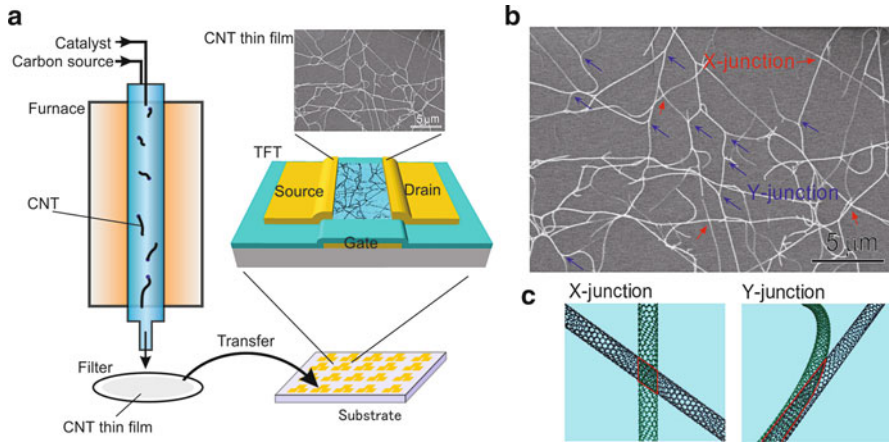


Fig. 18.1 Formation of CNT thin film for TFT applications based on floating-catalyst CVD and transfer process. **(a)** Schematic of growth, filtration, and transfer process. **(b)** SEM image of CNT thin film transferred on Si substrate. **(c)** Schematic of X- and Y-junctions

In the transfer method, however, the semiconductor–metal separation technique of the solution method cannot be employed, and some metallic CNTs (normally 30 %) are present in the TFT channel. However, if CNT density can be precisely controlled, it is possible to obtain a thin film that behaves as a semiconductor, without current paths made only of metallic CNTs being formed [14]. Specifically, when one-dimensional stick-like CNT is randomly arranged in plane, current paths are formed and electrical conduction is obtained when a certain density is exceeded. This density is called the percolation threshold, given by $\rho_{th} = (4.24/L_{CNT})^2/\pi$, where L_{CNT} is CNT length. Approximately two thirds of CNTs grown by conventional methods are semiconducting CNTs and the rest one third are metallic CNTs. Therefore, when its CNT density is approximately ρ_{th} , a CNT thin film behaves as a semiconductor as shown in Fig. 18.2. When CNT density is increased to approximately $3\rho_{th}$, the density of metallic CNTs reaches ρ_{th} , and current paths made only of metallic CNTs are formed, resulting in increased off current or cause of short between the source and drain of TFTs. Therefore, if CNT density can be precisely controlled, it is possible to obtain CNT thin film that behaves as semiconductor, even with metallic CNTs in the film. CNT density can be controlled by the duration of CNT collection on the filter in the case of floating-catalyst CVD.

Transfer and output characteristics of a back-gate CNT TFT fabricated on a p^+ -Si substrate having a thermal oxide film (100 nm) by the transfer process are shown in Fig. 18.3a, b. The channel length and channel width were both 100 μm, which is as large as printing techniques are able to achieve. The device shows p-type transistor characteristics with on/off ratio of 6×10^6 . Carrier mobility μ was estimated to be 634 cm²/Vs by the following formula from characteristics in the linear region:

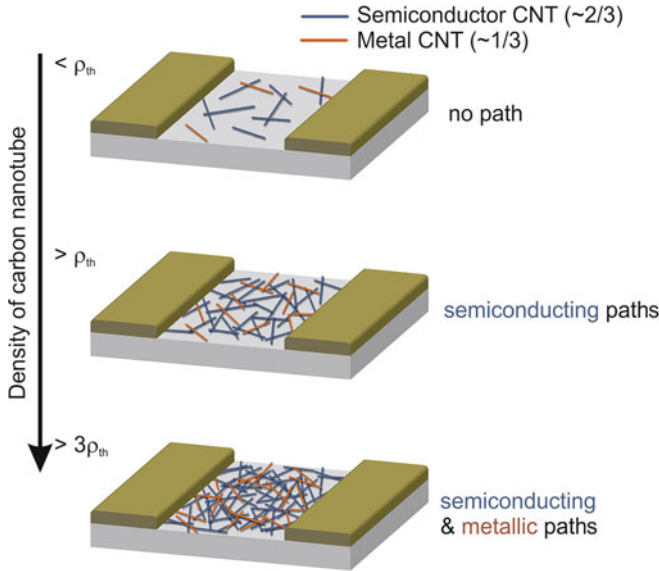


Fig. 18.2 Schematics on formation of percolative conduction channels of CNTs. The conduction property depends on the density of CNTs

$$\mu = \frac{1}{C} \frac{L_{ch}}{W_{ch}} \frac{\partial I_D}{V_{DS}} \frac{\partial I_D}{\partial V_{GS}} \tag{18.1}$$

Here, L_{ch} , W_{ch} , and C are channel length, channel width, and capacitance between gate electrode and CNT thin film, respectively. When the coverage of the CNT thin film is low as shown in Fig. 18.1b, C is approximately given by the following formula [15]:

$$C \sim \frac{2\pi\epsilon}{\Lambda_0 \ln \left\{ \frac{\Lambda_0}{R} \frac{\sinh(2\pi t_{ox}/\Lambda_0)}{\pi} \right\}} \tag{18.2}$$

Here, ϵ and t_{ox} are the dielectric constant and oxide thickness, respectively, of the gate insulating film, and R and Λ_0 are the CNT radius and spacing between CNTs, respectively. This capacitance is smaller than parallel plate capacitance, ϵ/t_{ox} , by a factor of 18 in the present case and approaches the value of parallel plate capacitance with an increasing aspect ratio, t_{ox}/Λ_0 . The rigorous capacitance model expressed by Formula 18.1 is more suitable for mobility evaluation than parallel plate capacitance model when the density of CNTs is low.

Figure 18.3c shows a comparison of on/off ratio and mobility of TFTs produced by the transfer process based on floating-catalyst CVD and various other TFTs. Mobility and on/off ratio are substantially higher than organic, IGZO

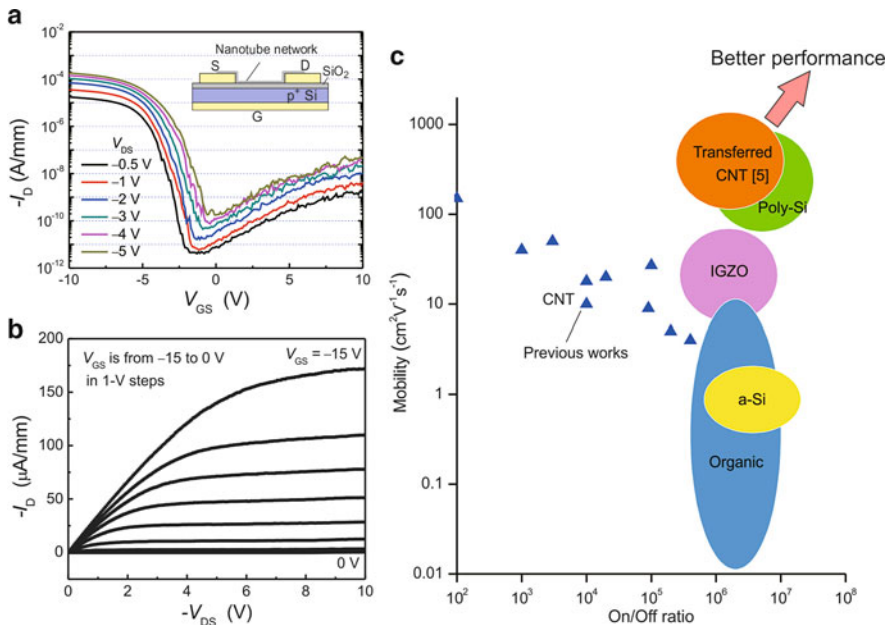


Fig. 18.3 CNT TFT fabricated on Si substrate by transfer process. (a) Transfer characteristics. The *inset* shows schematic device structure. (b) Output characteristics. (c) Mobility and on/off ratio of various kinds of TFTs

(indium–gallium–zinc–oxide), and amorphous Si TFTs and comparable to those of poly-Si, but in the transfer method, they are attained by processing at atmospheric pressure and room temperature.

18.3 CNT Integrated Circuits on Plastic Substrates

The transfer method based on the floating-catalyst CVD is also applicable to fabrication of devices on plastic substrates [5]. As shown in Fig. 18.4a, CNT TFTs and various integrated circuits were fabricated on a transparent and flexible polyethylene naphthalate (PEN) substrate. Figure 18.4b illustrates the structure of the bottom-gate CNT TFT. Because the glass transition temperature of a PEN substrate is approximately 150 °C, the entire process was carried out at 145 °C or below. After the gate electrode was formed by photolithography and evaporation process, an Al_2O_3 gate insulator with a thickness of 40 nm was formed by low-temperature atomic layer deposition at 145 °C. Openings were made in the gate insulating film by reactive-ion etching, and the source/drain electrode was formed. After the CNT thin film was transferred, the CNTs outside the channel were etched

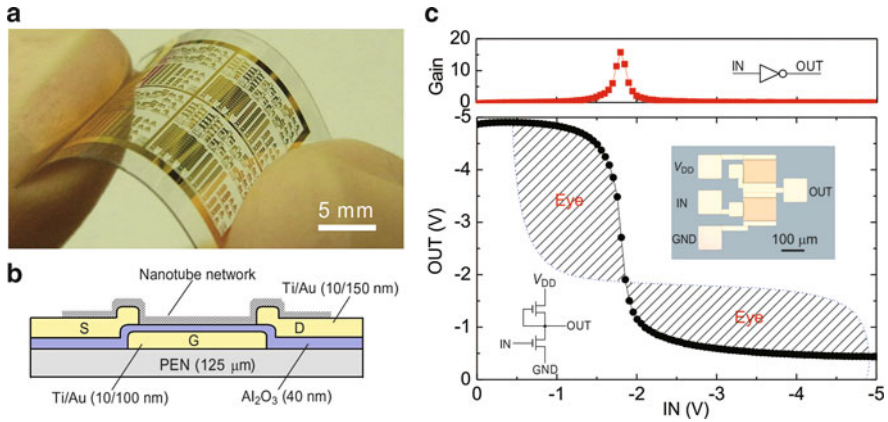


Fig. 18.4 Flexible CNT TFTs and ICs. (a) Photograph. (b) Schematic TFT structure. (c) Transfer characteristics and gain of inverter

by photolithography and oxygen plasma etching. The channel length and channel width of the TFT were both $100\ \mu\text{m}$. Both mobility and on/off ratio of TFTs on a PEN substrate are comparable to those of TFTs produced on a Si substrate.

The control of the threshold voltage of a TFT is essentially required in order to construct integrated circuits. Here, threshold voltage was controlled by chemical doping using F_4TCNQ [16], which has high electron affinity so that electrons (holes) are taken away (doped) from (to) CNTs. Chemical doping was performed by spin coating after dissolving F_4TCNQ in toluene. This technique allows threshold voltage control by means of F_4TCNQ concentration. In the integrated circuits produced in this work, the inverters consisted of enhancement-mode and gate-source-shortened depletion-mode TFTs for driver and load TFTs, respectively. The chemical doping for the load TFT was carried out to determine the logic threshold. Figure 18.4c shows the transfer characteristics of the inverter. When power supply voltage was $-5\ \text{V}$, voltage gain of 16 was obtained. Matching between input and output voltages was achieved, this is important to transfer logic level from one to another in integrated circuits. Additionally, the large eye pattern indicates the large noise margin for logic operations.

A ring oscillator was used to evaluate the operation speed of the integrated circuits. Figure 18.5a–c shows a 21-stage ring oscillator fabricated on a PEN substrate. A total of 44 TFTs were integrated, including an output buffer. The ring oscillator began oscillating at a power supply voltage of $-2\ \text{V}$, and the oscillation frequency at $-4\ \text{V}$ was $2.0\ \text{kHz}$. Delay time per gate ($\tau = 1/2Nf$) was $12\ \mu\text{s}$. Here, N and f are the number of inverter stages and the oscillation frequency, respectively. This delay time is longer than current-gain cutoff frequency of the TFT, which is expected from the carrier mobility, due to the parasitic capacitances attributing to the overlaps between the gate and source/drain electrodes. The parasitic capacitance

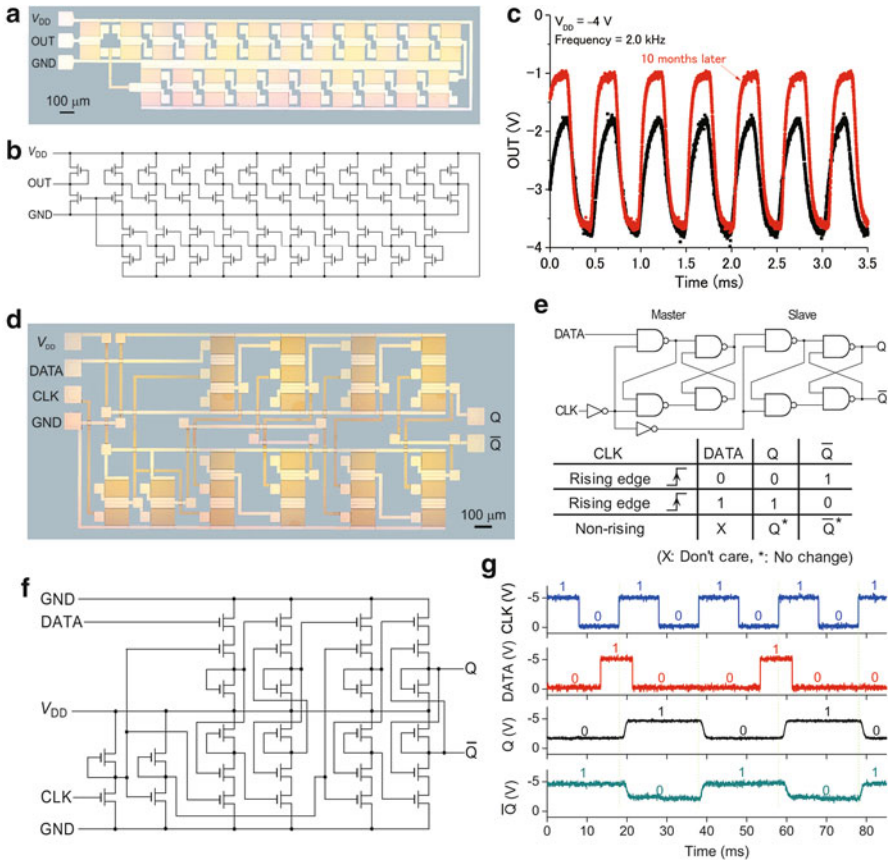


Fig. 18.5 Flexible CNT ICs. (a)–(c) 21-stage ring oscillator. (d)–(g) D-FF

is about 17 times larger than the capacitance of carbon nanotube channel calculated from Formula 18.2. Therefore, the operation speed can be improved by reducing the overlap capacitance.

In addition to basic NOR and NAND logic gates, functional integrated circuits such as reset–set (RS) flip-flop (FF), delay (D)-FF, etc. were realized. It is known that any kind of logic circuit can be built as long as NOR and NAND gates with matched input and output can be produced. Figure 18.5d–g shows a master–slave D-FF fabricated on a PEN substrate. In principle, there are two types of logic circuit: combining circuits and sequential circuits. In a combining circuit, the output is determined only by the present input. In a sequential circuit, on the other hand, the output is determined not only by the present input but also by input history. In short, a sequential circuit has a data storage or memory function. A D-FF is a type of sequential circuit and having two stable states, generally used for 1 bit of memory or delay in logic circuits. In this D-FF, eight NAND gates and two inverters are

integrated. The circuit is constructed of two serially connected D latches, wherein the slave latch changes state in response to a state change of the master latch. In the I/O characteristics of this D-FF, the state of output Q is determined by the input signal when the clock signal rises, and that state is maintained even after the input signal falls, demonstrating the latch operation.

18.4 All-Carbon Integrated Circuits

When a plastic film with a thickness is bent, tensile and compressive strains proportional to the thickness are induced on the surface and back surface of the film, respectively. Therefore, a certain stretching ability is required for the materials composing flexible devices. All-carbon integrated circuits are extraordinarily flexible and transparent by using CNT thin films for the electrodes and interconnections as well as the channel and also using acrylic resin for the insulating film material [17]. Figure 18.6a is a schematic of the all-carbon integrated circuit. The circuit was produced on a PEN film. The CNT thin films were formed by the transfer method [5, 18]. The thickness of the CNT thin film used for electrodes and wiring was about 20 nm.

This all-carbon integrated circuit is particularly flexible and transparent as shown in Fig. 18.6b. As seen from the light transmission spectrum of the integrated circuit, overall transmittance is 78 % in the visible range, but net transmittance excluding absorption and reflection by the PEN substrate is estimated at roughly 90 % (Fig. 18.6c). The transfer characteristics of an all-carbon TFT exhibit a mobility of $1,027 \text{ cm}^2/\text{Vs}$, comparable to that of a metal-oxide-semiconductor field-effect transistor (MOSFET) on a Si single-crystal wafer. Bending property was also good, and no change in TFT characteristics was observed even with a radius of curvature of 8 mm.

In addition to logic gates such as NOR, NAND, and Ex-OR, a ring oscillator (Fig. 18.6d) and SRAM have also been fabricated as all-carbon integrated circuits. Despite using acrylic resin with a thickness of 660 nm as the gate insulator, the integrated circuits can be operated at a relatively low voltage of 5 V. This was achieved by taking advantage of the phenomenon of the gate field concentration to CNTs. In conventional TFTs having sheet-like semiconductor channel, operating voltage normally increases proportionally with gate insulator thickness because the gate capacitance and hence carrier concentration are inversely proportional to the thickness of the gate insulator. With nanoscale structure like that of CNTs, considering the field concentration effect, the gate capacitance is less dependent on the gate insulator thickness as understandable from Formula 18.2. Low-voltage operation achieved by utilizing this field concentration effect could be an important technique for printed electronics as well. When printing techniques are used, it is normally difficult to form ultrathin insulating films, and the rise in operating voltage is problematic. There is such possibility that a low operating voltage can be attained in printed TFTs if low-density CNT film is used in the channel.

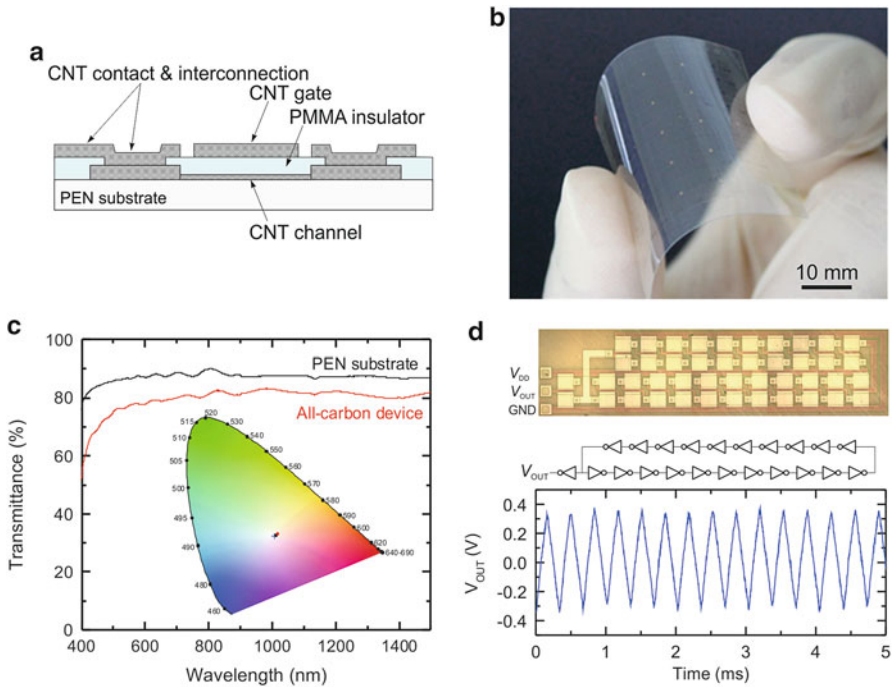


Fig. 18.6 All-carbon ICs. (a) Schematic device structure. (b) Photograph. (c) Optical transmittance spectrum. (d) Ring oscillator

When circuit operating speed was evaluated with a ring oscillator, the delay time per logic gate stage was $8 \mu\text{s}/\text{stage}$. This delay time is comparable to the case where gold electrodes and interconnections are used, indicating that the parasitic resistance of CNT interconnections has only a small effect on the operating speed.

As the all-carbon integrated circuits are constructed from CNT thin films and plastic materials, they are not only flexible but capable of stretching as well. Similar to common plastic materials, they can be formed into three-dimensional shapes by heat-forming techniques as well. For example, when formed into a dome shape as shown in Fig. 18.7, the transistors and interconnections are stretched biaxially, without cracking or peeling of the CNT thin films. The TFTs operated normally even for biaxial strain of 18%. The integrated circuits also operated normally when similarly formed into dome shapes.

Heat forming is widely used in the manufacture of plastic products in a wide range of fields, including household goods, toys, cases for electrical products, and medical devices. If electronic devices can be formed like plastics, electronic functions can be easily built into plastic products, leading to expanded possibilities for the design of electronic parts. Novel devices such as head-up displays on curved glasses, spherical displays, and body of robots integrated with artificial skin can be expected as the potential applications.

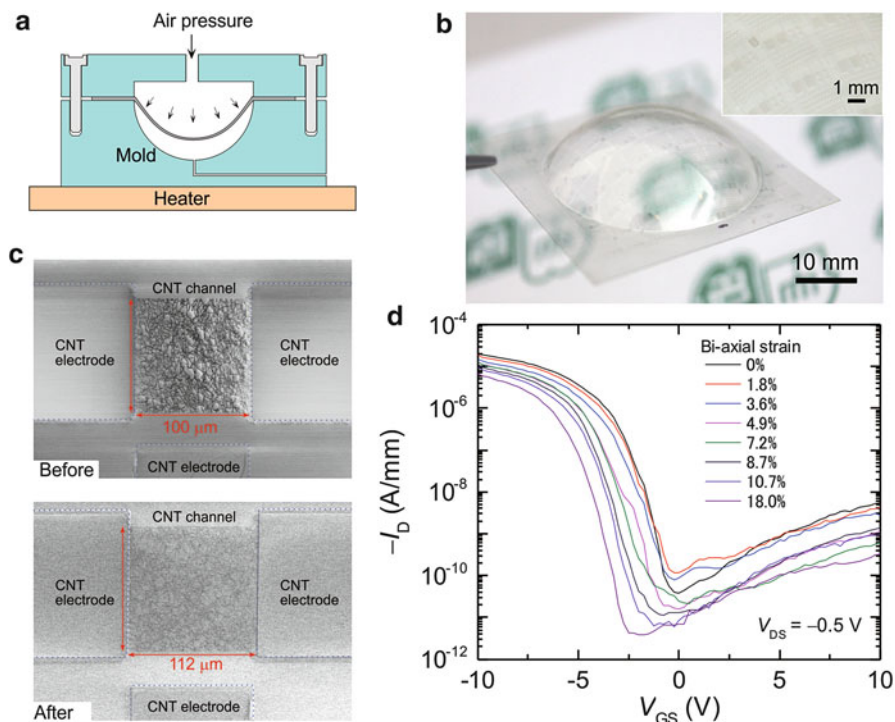


Fig. 18.7 Forming of all-carbon ICs. (a) Schematic of pressure-assisted thermoforming process. (b) Photograph of all-carbon ICs formed into three-dimensional dome shape. (c) SEM images of an all-carbon TFT before and after forming process. (d) Transfer characteristics for various degrees of bi-axial strain

18.5 Printing Fabrication

Due to the simplicity of the carbon nanotube thin-film process, it is possible to produce electronic devices at low cost by a combination of carbon nanotube thin films and a printing process, rather than a semiconductor process based on conventional photolithography technology. For instance, electronic devices may be able to be produced by printing metals, insulators, and semiconductor films on plastic film by a roll-to-roll process like that used in printing newspapers and magazines. The size of device is determined by the resolution and overlay precision of the printing technique, which is currently several tens of microns, but there are various applications which do not require miniaturized high-performance transistors, including displays, RFID tags, and various sensors. Further, the use of ink-jet printing techniques could enable on-demand design and manufacture of devices and circuits, and high-throughput mass production may be possible by using high-speed printing techniques such as gravure printing and offset printing.

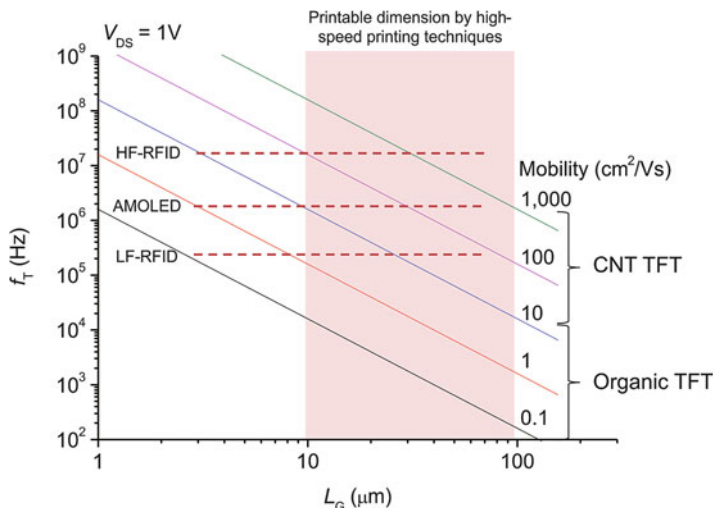


Fig. 18.8 Current-gain cutoff frequency of TFT versus gate length for various carrier mobilities

Ultimately low-cost RFID tags are expected for secure and reliable tracking of physical distribution such as food products. Electronic paper could be inexpensively produced to replace newspapers and magazines, minimizing the distribution costs and carbon dioxide emissions.

The operation speed of a transistor is determined by the channel length electron has to travel. Under constant operating voltage, the current-gain cutoff frequency f_T of a transistor is inversely proportional to the square of channel length L_G , expressed as follows:

$$f_T \sim \frac{1}{2\pi\tau_{\text{trans}}} = \frac{\mu V_{DS}}{2\pi L_G^2}. \tag{18.3}$$

Figure 18.8 is a plot of the relationship between f_T and L_G for various mobilities μ . To obtain a practical operating speed when using a printing process, an improvement of the resolution of the printing technique is necessary as well as high-mobility channel materials. Among the many types of thin-film transistors (TFTs)—including organic TFTs [19], amorphous Si TFTs, and oxide TFTs [20]—that are considered usable for flexible device fabrication, carbon nanotube (CNT) TFTs have attracted increasing attention owing to their high mobility and printability.

Researchers have recently reported on the print fabrication of CNT TFTs. A driving OLED was demonstrated by fully printed CNT TFTs with separated semi-conducting CNTs [21]. A complementary metal–oxide–semiconductor (CMOS) inverter was also developed using an all-ink-jet printing technique that included a dopant printing process [22]. Roll-to-roll fabrication of CNT devices coupled with radio-frequency (RF) antennas for use as ID tags has also been demonstrated by combining gravure with ink-jet printing [23].

More recently, high-mobility CNT TFTs have been realized by combining a transfer technique to form a CNT film and a high-speed flexographic printing technique [24]. Flexographic printing is a type of relief printing method, using a flexible polymer plate. The speed of flexographic printing can be two orders of magnitude faster than that of ink-jet printing and comparable to that of other high-speed printing techniques such as gravure. In addition, the mechanics are simpler than those of offset printing, a feature that leads to low-cost device fabrication. Figure 18.9a, b shows a schematic and photograph of the flexographic printer. In the printing process, the ink is first supplied to the plate by an anilox roll that has fine dimples on its surface to store ink. The amount of ink supplied to the flexo plate is determined by the volume of dimples. The flexo plate normally has a halftone

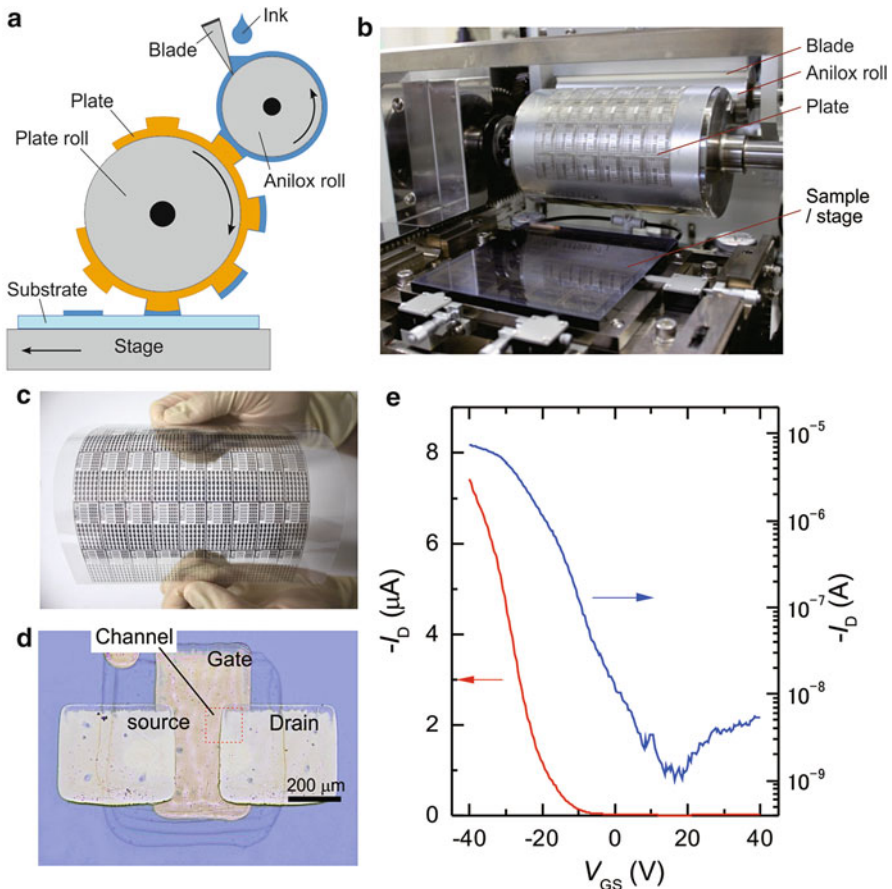


Fig. 18.9 Fabrication of CNT TFTs with flexographic printing technique. (a) Schematic of flexographic printing process. (b) Photograph of prototype flexographic printer. (c) Photograph of an array of TFTs printed on 15-cm square PEN substrate. (d) Photograph of printed TFT. (e) Transfer characteristics

on its surface, allowing it to uniformly hold ink. After its application to the plate, the ink is then transferred to the substrate. Three types of inks were used in the flexographic printing technique: Ag-nanoparticle ink for the electrodes, polyimide ink for the gate insulator, and resist ink for patterning the CNTs.

A photograph of CNT TFTs fabricated by the flexographic printer on a PEN film of $15 \times 15 \text{ cm}^2$ and a micrograph of a CNT TFT are shown in Figs. (c) and (d). The channel length and width are 115 and 130 μm , respectively. The DC characteristics of a CNT TFT are shown in Fig. 18.5. The device exhibits *p*-type conduction and output characteristics displaying ohmic behavior in the linear region, which suggests that good contacts have been formed between the printed Ag electrodes and the CNT film. The gate leakage current is less than 10 pA at $V_{\text{GS}} = 40 \text{ V}$. The carrier mobility evaluated from the transconductance in the linear region (Fig. 18.9e) was $157 \text{ cm}^2/\text{Vs}$. For further development of printed CNT TFTs, there are still challenges to be addressed such as the suppression of hysteresis, doping control, low-voltage operation, and so on.

18.6 Summary

In this chapter, recent progresses on carbon nanotube TFTs and integrated circuits for flexible electronics application, which takes full advantage of the superior electrical and mechanical characteristics provided by CNTs, were described. The simple fabrication process based on the printing techniques was also introduced. CNT thin-film technologies would enable low-cost production of flexible devices.

References

1. Sony Develops a Rollable OTFT-driven OLED Display that can wrap around a Pencil. News Releases. <http://www.sony.net/SonyInfo/News/Press/201005/10-070E/> (2010)
2. Myny K, Veenendaal Ev, Gelinck GH, Genoe J, Dehaene W, Heremans P (2011) An 8b organic microprocessor on plastic foil. In: IEEE international solid-state circuits conference, pp 322–324
3. Snow ES, Novak JP, Campbell PM, Park D (2003) Random networks of carbon nanotubes as an electronic material. *Appl Phys Lett* 82:2145–2147
4. Cao Q, Kim H-s, Pimparkar N, Kulkarni JP, Wang C, Shim M, Roy K, Alam MA, Rogers JA (2008) Medium-scale carbon nanotube thin-film integrated circuits on flexible plastic substrates. *Nature* 454:495–U494
5. Sun DM, Timmermans MY, Tian Y, Nasibulin AG, Kauppinen EI, Kishimoto S, Mizutani T, Ohno Y (2011) Flexible high-performance carbon nanotube integrated circuits. *Nat Nanotechnol* 6:156–161
6. Chen PC, Fu Y, Aminirad R, Wang C, Zhang JL, Wang K, Galatsis K, Zhou CW (2011) Fully printed separated carbon nanotube thin film transistor circuits and its application in organic light emitting diode control. *Nano Lett* 11:5301–5308

7. Takenobu T, Okimoto H, Yanagi K, Miyata Y, Shimotani H, Kataura H, Iwasa Y (2010) Tunable carbon nanotube thin-film transistors produced exclusively via inkjet printing. *Adv Mater* 22:3981–3986
8. Takenobu T et al (2006) High-performance transparent flexible transistors using carbon nanotube films. *Appl Phys Lett* 88
9. Arnold MS, Green AA, Hulvat JF, Stupp SI, Hersam MC (2006) Sorting carbon nanotubes by electronic structure using density differentiation. *Nat Nanotechnol* 1:60–65
10. Tanaka T, Jin H, Miyata Y, Fujii S, Suga H, Naitoh Y, Minari T, Miyadera T, Tsukagoshi K, Kataura H (2009) Simple and scalable gel-based separation of metallic and semiconducting carbon nanotubes. *Nano Lett* 9:1497–1500
11. Miyata Y, Shiozawa K, Asada Y, Ohno Y, Kitaura R, Mizutani T, Shinohara H (2011) Length-sorted semiconducting carbon nanotubes for high-mobility thin film transistors. *Nano Res* 4:963–970
12. Nirmalraj PN, Lyons PE, De S, Coleman JN, Boland JJ (2009) Electrical connectivity in single-walled carbon nanotube networks. *Nano Lett* 9:3890–3895
13. Znidarsic A, Kaskela A, Laiho P, Gaberscek M, Ohno Y, Nasibulin AG, Kauppinen EI, Hassanien A (2013) Spatially resolved transport properties of pristine and doped single-walled carbon nanotube networks. *J Phys Chem C* 117:13324–13330
14. Alam MA, Kocabas C, Pimparkar N, Yesilyurt O, Kang SJ, Rogers JA (2007) Experimental and theoretical studies of transport through large scale, partially aligned arrays of single-walled carbon nanotubes in thin film type transistors. *Nano Lett* 7:1195–1202
15. Cao Q, Xia MG, Kocabas C, Shim M, Rogers JA, Rotkin SV (2007) Gate capacitance coupling of single-walled carbon nanotube thin-film transistors. *Appl Phys Lett* 90:023516
16. Takenobu T, Kanbara T, Akima N, Takahashi T, Shiraishi M, Tsukagoshi K, Kataura H, Aoyagi Y, Iwasa Y (2005) Control of carrier density by a solution method in carbon-nanotube devices. *Adv Mater* 17:2430–2434
17. Sun DM, Timmermans MY, Kaskela A, Nasibulin AG, Kishimoto S, Mizutani T, Kauppinen EI, Ohno Y (2013) Mouldable all-carbon integrated circuits. *Nat Commun* 4:2302
18. Kaskela A, Nasibulin AG, Timmermans MY, Aitchison B, Papadimitratos A, Tian Y, Zhu Z, Jiang H, Brown DP, Zakhidov A, Kauppinen EI (2010) Aerosol-synthesized SWCNT networks with tunable conductivity and transparency by a dry transfer technique. *Nano Lett* 10:4349–4355
19. Gelinck GH, Huitema HEA, Van Veenendaal E, Cantatore E, Schrijnemakers L, Van der Putten J, Geuns TCT, Beenhakkers M, Giesbers JB, Huisman BH, Meijer EJ, Benito EM, Touwslager FJ, Marsman AW, Van Rens BJE, De Leeuw DM (2004) Flexible active-matrix displays and shift registers based on solution-processed organic transistors. *Nat Mater* 3:106–110
20. Sun Y, Rogers JA (2007) Inorganic semiconductors for flexible electronics. *Adv Mater* 19:1897–1916
21. Chen P, Fu Y, Aminrad R, Wang C, Zhang J, Wang K, Galatsis K, Zhou C (2011) Fully printed separated carbon nanotube thin film transistor circuits and its application in organic light emitting diode control. *Nano Lett* 11:5301–5308
22. Matsuzaki S, Nobusa Y, Yanagi K, Kataura H, Takenobu T (2011) Inkjet printing of carbon nanotube complementary inverters. *Appl Phys Express* 4:105101
23. Jung M, Kim J, Noh J, Lim N, Lim C, Lee G, Kim J, Kang H, Jung K, Leonard AD, Tour JM, Cho G (2010) All-printed and roll-to-roll-printable 13.56-MHz-operated 1-bit RF tag on plastic foils. *IEEE Trans Electron Device* 57:571–580
24. Higuchi K, Kishimoto S, Nakajima Y, Tomura T, Takesue M, Hata K, Kauppinen EI, Ohno Y (2013) High-mobility, flexible carbon nanotube thin-film transistors fabricated by transfer and high-speed flexographic printing techniques. *Appl Phys Express* 6:085101

Index

A

Absorption coefficient, 111
Adenine, 146
Air-stable *p*- and *n*-type characteristics, 150
Alkali–fullerene plasmas, 144
Alkali positive ions, 144
All-carbon integrated circuits, 277
Ambipolar, 250
Amorphous carbon (a-C), 22, 30
Anderson localization, 50
Angle-resolved photoelectron spectroscopy (ARPES), 13, 14
Aptamers, 98, 99
Aqueous single-stranded DNA, 162
ARPES. *See* Angle-resolved photoelectron spectroscopy (ARPES)
Atomic force microscopy (AFM), 40
Au chloride (HAuCl₄), 148
Auger, 108
Au nanoparticles (AuNPs), 148
 distance between, 148
 monodispersed, 148

B

Ballistic electron propagation, 155
Biosensor, 91–102
Blocking temperature, 154
Boltzmann equations, 109
Bonded SWNTs, 148
Bottom-up approach, 45
Bundled SWNT layers, 148

C

Calorimeter, 197
Cap, 127

Carbon nanotube (CNT), 45, 180
Carboxyl groups, 148
Carrier–carrier scattering, 108
Carrier density difference, 153
Carrier quasi-equilibration, 108
Ca@SWNTs, 150
Catalyst, 125–128
C₃₀DNA@DWNTs, 160
C₆₀@DWNT, 155
C₇₀@DWNT, 155
C₈₄@DWNT, 155
Charge and spin of electrons, 153
Charge stability diagram, 243
Charge transfer, 60
Charging energy, 243
Chemical doping, 275
Chemical etching, 38
Chemical vapor deposition (CVD), 3–18
Chemisorption group, 55
[C₈H₁₅N₂]⁺[BF₄]⁻, 149
C₆₀ negative ions, 148
C₅₉N radical, 157
C₅₉N@SWNT, 150, 151, 156
Concentrated electric field, 202, 206, 210
Constructive interference, 155
Contact resistivity (ρ_c), 53
Controllable ion irradiation, 144
Correlation coefficient, 168–172
Coulomb blockade, 214, 218, 220, 226, 231, 234, 237, 242
Coulomb charging energy, 219
Coulomb diamond, 214, 218, 219, 223, 224, 226, 227, 232–234, 236
Coulomb diamond-like features, 50
Coulomb gaps, 227, 229

- Coulomb oscillation, 216, 217, 220, 227, 230, 234, 236, 244
- Coulomb oscillation peaks, 151
- Cross-bridge Kelvin (CBK), 64
- Cs and I ion dosages, 151
- Cs/C₆₀@SWNT, 145, 151
- Cs/I@SWNT, 145, 151
- Cs partially-encapsulated SWNT, 149
- Cs@SWNTs, 145, 150
- C₆₀@SWNT, 145, 150, 151, 156
- C₆₀@SWNT film, 158
- C₆₀@SWNT/Si solar cell, 158
- Cu(100), 10, 11
- Cu(111), 7, 10, 11, 13–16
- Current-gain cutoff frequency, 280
- Current-injection, 105
- Current rectification ratio, 152
- CVD. *See* Chemical vapor deposition (CVD)
- Cytosine, 146
- D**
- Damping rate, 109
- DC electric fields with different polarity, 161
- Debye length, 94
- Density of states (DOS), 53
- Depletion layer, 153
- Devices, 105
- Different polarity ions, 144
- Diffusion equation, 42
- Diffusion kinetics, 41
- Dirac points, 108
- Direct growth, 29–34, 37–51
- Dispersion, 106
- DNA negative ion irradiation, 146
- DNA@SWNTs, 160
- Doped CNTs, 149–155
- Doping carrier densities, 153
- Double-quantum dots, 255–259
- Double-walled carbon nanotubes (DWNTs), 146, 147, 152, 155, 160–161
encapsulating C₃₀DNA, T₃₀DNA, A₃₀DNA, and G₃₀DNA, 150
- Drude, 107
- E**
- Edge disorder, 50
- Electrical and magnetic properties, 144
- Electrical double layer, 94–96
- Electrical down-mixing method, 188
- Electrolyte plasmas, 146
- Electron acceptor, 145, 156
- Electron affinity, 60
- Electron beam lithography, 45
- Electron donor, 145, 156
- Electron–hole plasma, 114
- Electronic structure, 149
of C₅₉N, 157
- Electronic transport properties, 149
- Electro-optic fusion devices, 144, 155–159
- Encapsulated DNA molecules, 160
- Encapsulated DNA withdrawal, SWNT interior, 162
- Energy conversion material, 158
- Enhance weak-signal, 171
- Even–odd effect, 245
- Excited state, 156
- F**
- Fabry–Perot interference, 214, 226, 227, 229, 231
- Fabry–Perot oscillation, 214
- Fabry–Perot quantum interference, 218, 219, 223, 224, 226
- Fermi energy, 107
- Fermi level pinning, 60
- Fermi velocity, 109
- Ferromagnetic characteristic, 154
- Ferromagnetic elements, 153
- Fe@SWNTs, 145, 153
- Field cooled (FC) magnetization, 154
- Field-effect mobilities, 51
- Field-effect transistor (FET) devices, 149
- First (E_{11}) and second (E_{22}) van Hove transitions, 158
- Flexible devices, 269
- Flexible electronics, 269
- Flexographic printing technique, 281
- Force sensing, 187
- Fowler–Nordheim tunneling, 204, 210
- Frequency response, 188
- Fullerene-/azafullerene-induced modulation, 151
- G**
- Gas–liquid interfacial plasmas (GLIPs), 148
- Gaussian, 217, 220
- Gold compound H₂AuCl₄·3H₂O, 162
- Grain boundaries, 12, 13, 16
- Graphene, 37–51
nanoribbon, 37–51
resonators, 189
- Graphene-based electrical devices, 37
- Ground state, 156
- Guanine, 146

H

Halogen negative ions, 144
 Heat-forming technique, 278
 Heteroepitaxial, 3, 7–16
 Heterojunctions, 158
 Hexagonal domain, 40–41
 High-energy hydrocarbon ions, 42
 High-energy ion irradiation, 148
 High-sensitivity biosensing, 160
 Hump current feature, 151–152

I

Ideal superlattice structure, 155
 Infrared solar cells, 158
 Ink-jet printing, 279
 Instantaneous polarity change, 145
 Instantaneous (1s) UV light exposure, 156
 Integrated circuits, 274
 Integration, 45, 48
 Intensity modulators, 117
 Interband, 106
 Interconnects, 87
 Internal and surface doping, 144–149
 Internal mechanical loss, 190
 Interstitial nanospaces, 148
 Intraband, 106
 Intrinsic bandgap, 50
 Inverters, 275
 Ionic liquid (IL), 148
 I@SWNTs, 145, 150

J

Junction structure, 145

K

Kondo effect, 214, 232–238
 Kondo peaks, 234, 236, 237
 Kondo resonance, 233–235, 237, 238
 Kondo state, 215, 237
 Kondo temperature, 214, 232, 235–238

L

Large-scale integrations (LSIs), 80, 82, 87
 2D and 3D, 45
 Large-scale site and alignment control, 45
 Laser, 105–107, 109, 111, 112, 114–119
 Laser irradiation, 21–26
 Light illumination, 156
 Localized gap states, 149
 Logic gates, 276

Lorentzian, 216, 217, 220
 Low-energy electron diffraction (LEED), 9–11
 Low-energy electron injection, 148
 Low temperature, 80–83
 measurements, 151
 transport measurements, 50
 LSIs. *See* Large-scale integrations (LSIs)

M

Magnetic semiconductors, 153
 Magnetization *vs.* applied magnetic field, 153
 Metallic CNTs, 155
 Metal nanoparticles (MNPs), 146
 Microelectrodes, 180
 Micro total analysis system (μ TAS), 182
 Minimum detectable force gradient, 196
 MNP–DNA conjugates, 162
 (MNP–DNA)@SWNTs, 160
 Mobility, 272
 Momentum relaxation time, 111
 Multifunctional quantum transistor, 215, 223,
 225–231
 Multilayer graphene, 80–83, 87
 Multiple exciton generation (MEG), 159

N

Nano-bio fusion devices, 143, 145
 Nano-biomedical device, 141
 Nano-biomedical electronics, 160–162
 Nanodevice-applicable transport, 141
 Nanodevices, 143
 Nanomechanical resonators, 187
 Nanothermometers, 158
 Nanotube film, 158
n-dominant ambipolar, 150
 Negative differential conductance (NDC), 256
 Negative differential resistance (NDR)
 characteristic, 155
 Nickel (Ni) nanobar, 38, 45–48
 Noise, 166–176
 Nonlinear, 166
n-type behavior, 150

O

Ohmic contacts, 214
 On/off ratio, 153
 Open-circuit voltage (V_{oc}), 158
 Optical conductivity, 106
 Optically manipulatable drug delivery system
 (DDS), 160
 Optical photon, 108

Optoelectronic devices, 155
 Opto-mechanical heterodyne technique, 193

P

Particle nature, 214–216, 218, 220–223, 226, 231
 Patterned substrates, 132–141
p-dominant ambipolar, 150
 Peak-to-valley current ratio (PVCR = I_p/I_V), 155
 Percolation threshold, 272
 Photoinduced charge transfer, 157
 Photoinduced current vs. temperature, 158
 Photoinduced electrical transport properties, 155
 Photoinduced electron transfer (PET) process, 156
 Photon-assisted tunneling (PAT), 262
 Photosensitive behavior, 156
 Photoswitching effect, 156
 pH sensing, 96–97
 Physisorption group, 55
 π -d coupling, 55
p-i-n photodetectors, 117
 Planar periodic array of graphene plasmonic microcavities (PA-GPMC), 116
 Plasma CVD, 37–51
 Plasma doping, 143–162
 Plasma-ion irradiation method, 144
 Plasma waves, 109
 Plasmon, 105, 106, 109–114, 116–119
 Pneumatic micropumps, 180
p-n junction, 63, 152
 Polymer capping, 38
 Population inversion, 105
 Positive and negative photocurrents rise, 158
 Posttreatment, 45
 Potential barriers, 155
 Potential-structure calculations, 153
 Power conversion efficiency, 159
 Printing process, 279
 Pristine CNTs, 143
 Prostate-specific antigen (PSA), 180
p-type transport characteristic, 150

Q

Q factor, 190
 Quantum capacitance (C_Q), 58
 Quantum computing device, 242
 Quantum confinement, 45
 Quantum dot, 50, 151, 241
 Quantum energy level, 216

Quantum island, 218
 Quantum level, 214, 216, 218, 219, 222, 224
 Quantum nanomemory, 201–210
 Quantum THz detection, 243, 262–264
 Quasi-Fermi energies, 111
 Quasipair ion plasma, 144

R

Radio-frequency, 38
 Raman mapping, 38
 Rapid-heating plasma chemical vapor deposition (RH-PCVD), 38–40, 42–45, 47, 48, 51
 Recoverable photoresponse, 156
 Rectifying behavior, 145
 Release of DNA molecules, 161
 Resist-free process, 58
 Resonant tunneling transistor (RTT), 214–226, 232–238
 RH-PCVD. *See* Rapid-heating plasma chemical vapor deposition (RH-PCVD)
 Ring oscillator, 275
 Roll-to-roll process, 279
 RTT. *See* Resonant tunneling transistor (RTT)

S

Scanning electron microscope (SEM), 38
 Schottky barriers, 60, 214, 216, 219–222, 226, 227, 230, 232, 237, 238
 Schottky contacts, 213, 214
 Shift of threshold voltage, 156
 Short-circuit current (I_{sc}), 158
 SHT. *See* Single-hole transistor (SHT)
 Single-electron device, 242
 Single-electron inverter, 259–262
 Single-electron transistor, 151, 232, 243–245
 Single-hole transistor (SHT), 214–226
 Single-walled carbon nanotubes (SWNTs), 143–152
 functionalized by MNPs, 148
 hetero doping inside, 151
 horizontally aligned, 140, 141
 purely semiconducting, 159
 solar cell, 159
 surface of, 148
 Size-controlled MNP synthesis, 148
 Small graphene islands, 127
 Soluble AuNP–DNA conjugate, 162
 Solution process, 270
 Specific protein sensing, 98–102
 Spintronic devices, 155
 Stimulated emission, 109

STM topographic image, 149
 Stochastic Coulomb blockade, 250
 Stochastic resonance, 165–176
 Stretched DNA, 146
 Superparamagnetic state, 154
 Superradiant, 111
 Surface plasmon polaritons (SPPs), 106
 Surface plasmon resonance, 160
 Suspended CNT, 189
 Suspended resonators, 188–190
 SWNTs. *See* Single-walled carbon nanotubes (SWNTs)

T

Terahertz (THz), 105–119
 Thermal CVD apparatus, 126
 Thermal decomposition of SiC, 45
 Thermal vibration, 196
 Thin-film transistor (TFT), 270
 Threshold gate-voltage shift, 150
 Threshold voltage, 275
 Thymine, 146
 Tien–Gordon model, 264
 Time evolution, graphene growth, 40
 Top-down approach, 45
 Transfer, 271
 Transfer-free method, 37
 Transfer-free processes, 79–88
 Transfer length (d_T), 65
 Transfer length method (TLM), 64
 Transferred electrons, 156
 Transition metal dichalcogenides (TMDCs),
 16, 17
 Transmission electron microscopy (TEM), 40
 Transport gap, 45, 48–51

Tunneling barriers, 151
 2 times the absorption energy gap ($2E_{11}$), 159

U

Ultraviolet photoemission spectroscopy (UPS),
 150
 UV (400 nm) light pulse, 157
 UV–Vis absorbance spectra, 162
 UV–Vis absorption spectra, 160

V

Vapour–liquid–solid (VLS) mechanism, 126

W

Wave nature, 214–216, 218, 220, 222, 223,
 226, 231
 Wide temperature range, 158
 Work function, 60
 measurements, 150

X

X-junction, 271
 XOR gate, 261

Y

Y-junctions, 271
 Young's moduli, 190

Z

Zero-field-cooled (ZFC) magnetization, 154